PETROGENESIS OF BASALT-HOSTED SAPPHIRES FROM THE SIEBENGEBIRGE VOLCANIC FIELD (SVF) IN WESTERN GERMANY

Dissertation
zur
Erlangung des Doktorgrades (Dr. rer. nat.)
der
Mathematisch-Naturwissenschaftlichen Fakultät
der
Rheinischen Friedrich-Wilhelms-Universität Bonn

vorgelegt von
Lisa Christina Baldwin
aus
Luton, England

Bonn 2016

Angefertigt mit Genehmigung der Mathematisch-Naturwissenschaftlichen Fakultät der Rheinischen Friedrich-Wilhelms-Universität Bonn

1. Gutachter: Prof. Dr. Christian Gerhard Ballhaus
2. Gutachter: Prof. Dr. Thorsten Geisler-Wierwille

Tag der Promotion: 08.03.2016

Erscheinungsjahr: 2016

TABLE OF CONTENT

MINERAL FORMULAE

albite	$NaAlSi_3O_8$
alunite	$KAl_3(SO_4)_2(OH)_6$
anatase	TiO_2
anorthite	$CaAl_2Si_2O_8$
anorthoclase	$(Na,K)AlSi_3O_8$
apatite	$Ca_5(PO_4)_3F$
aphthitalite	$K_3Na(SO_4)_2$
aragonite	$CaCO_3$
baddeleyite	ZrO
beryl	$Be_3Al_2Si_6O_{18}$
betafite	$(Ca,U)_2(Ti,Nb,Ta)_2O_6(OH)$
biotite	$K(Mg,Fe)_3[AlSi_3O_{10}(OH,F_2]$
blodite	$Na_2Mg(SO_4)_2H_2O$
burkeite	$Na_4(SO_4)(CO_3)$
calcite	$CaCO_3$
cheralite	$(Ce,Ca,Th)(P,Si)O_4$
chromite	$FeCr_2O_4$
corundum	Al_2O_3
dawsonite	$NaAl[(OH)_2/CO_3]$
diopside	$CaMgSi_2O_6$
dolomite	$CaMg(CO_3)_2$
enstatite	$Mg_2Si_2O_6$

fersmite	$(Ca,Ce,Na)(Nb,Ta,Ti)_2(O,OH,F)_6$
ferrocolumbite	$FeNb_2O_6$
fluorite	CaF_2
goethite	$FeO(OH)$
graphite	C
hematite	Fe_2O_3
hercynite	$FeAl_2O_4$
ilmenite	$FeTiO_3$
ilmenorutile	$(Ti,Nb,Fe)O_2$
margarite	$CaAl_2(Al_2Si_2)O_{10}(OH)_2$
meionite	$Ca_4Al_6Si_6O_{24}CO_3$
molybdenite	MoS_2
monazite	$(La,Ce,Nd,Sm)PO_4$
natroalunite	$NaAl_3(SO_4)_2(OH)_6$
nepheline	$(Na,K)AlSiO_4$
oligoclase	$(Na,Ca)(Si,Al)_4O_8$
olivine	$(Mg.Fe)_2SiO_4$
paravauxite	$FeAl_2(OH/PO_4)_2$
pyrite	FeS_2
pyrochlore	$(Na,Ca)_2Nb_2O_6(OH,F)$
pyrope	$Mg_3Al_2(SiO_4)_3$
pyrophanite	$MnTiO_3$
quartz	SiO_2
rutile	TiO_2

sapphirine	$(Mg,Al)_8(Al,Si)_6O_{20}$
spinel	$MgAl_2O_4$
staurolite	$(Fe,Mg)_2Al_9(Si,Al)_4O_{20}(O,OH)_4$
thenardite	Na_2SO_4
thorianite	ThO_2
thorite	$ThSiO_4$
zircon	$ZrSiO_4$

ABSTRACT

Megacysts of blue sapphires are hosted by alkaline mafic rocks from the Cenozoic Siebengebirge Volcanic Field (SVF) in western Germany. Similar occurrences of sapphires related to intra-continental alkaline mafic volcanism have been reported from many other localities around the world, predominantly from Asia and Australia (e.g. Graham et al., 2008). Markedly, the sapphires are rimmed by a several micrometer thick spinel rim, indicating them to be in disequilibrium with the basaltic melt. Consequently, the sapphires are regarded to be xenocrysts rather than phenocrysts. Yet, in-situ U-Pb dating of a columbite inclusion within one Siebengebirge sapphire using Laser Ablation – Inductively Coupled Plasma – Mass Spectrometry (LA-ICP-MS) revealed that the time of sapphire crystallization (24.73 ± 0.35 Ma) is within the errors the same as the age of alkaline mafic volcanism in the SVF (Przybyla, 2013), indicating a close genetical relationship between sapphire crystallization and alkaline mafic volcanism in the SVF. The sapphires mineral inclusion suite that is comprised amongst others of carbonates, pyrochlore, betafite and columbite, as well as the strong enrichment in the HFSE compared to the primitive mantle and the abundant occurrence of gaseous low-density CO_2 inclusions, indicates that a carbonatitic melt played a major role in the sapphire formation. Glass inclusions of nephelinitic and of carbonated silicate composition probably represent the quenched products of two immiscible liquids in the silicate – carbonatite melt system, indicating that the crystallization of the sapphires was the result of complex magmatic processes in highly evolved SiO_2 undersaturated, CO_2-rich magmatic system, including extensive magma differentiation, the exsolution of two

immiscible melts and the assimilation of the sapphire bearing host rocks by ascending fresh pulses of basaltic magma.

Experiments that were conducted in the carbonatite – silicate melt system revealed that carbonatites are indeed eligible to precipitate corundum, given that the carbonatitic melts are saturated in Al_2O_3 and low in FeO and MgO. Yet, another set of experiments demonstrated that due to much better wetting propertied in a silicate melt, corundum that precipitated from a carbonatitic melt will always migrate into silicate melt if given the chance.

Results from this study infer that the Siebengebirge sapphires probably crystallized from a highly evolved FeO- and MgO-deficient carbonatite that exsolved from a highly evolved phonolite as a consequence of increasing CO_2 partial pressure accompanying melt fractionation. CO_2-rich fluid inclusions have densities up to 0.9 g/cm^3, infering that the sapphires must have formed at a minimum pressure of 0.6 GPa, corresponding to middle crustal levels.

The sapphires were later trapped by fresh pulses of ascending alkaline mafic melts and subsequently transported to the surface. The process of sapphire trapping and transportation to the surface was very rapid on geological time-scales and lasted no longer than a few weeks to months, as indicated by the thickness of the spinel-rims. This petrogenetic scenario implies CO_2 to be the confining variable connecting the genesis of the sapphire megacrysts and the alkaline mafic volcanism in intra-continental volcanic areas.

CHAPTER 1: INTRODUCTION

Along with diamond and emerald, sapphire and ruby belong to the most prominent and precious gemstones. Sapphire and ruby are varieties of corundum (Al_2O_3). Natural corundum (α-Al_2O_3) crystallizes in the trigonal crystallographic system. The oxygen atoms are organized in hexagonal closed packing with Al cations filling the interstitial octahedral sites. From 18 octahedral sites within one hexagonal unit cell, 12 sites are occupied by alumina, the other 6 stay vacant. Specific properties of corundum are the hardness of 9 on the Moh's scale, the high melting temperature of 2040 °C at ambient pressure, and the high heat conductivity of 41.9 W/(m·K) at room temperature. Elements such as Cr, V, Fe, Ni, Ga, Ca, and Mn are common impurities in the corundum structure, giving the minerals their color (Schmetzer and Bank, 1980; 1981; Ferguson and Fielding 1971; 1972). The typical blue color of sapphires is given by Fe^{2+}-O-Ti^{4+} intervalence charge transfer (Lee et al., 2006), whereas Cr^{3+} and V^{3+} give ruby the typical red color. The colors green and yellow are caused by Fe^{3+}, and a pink coloration is given by Ti^{3+}. The combination of several impurities results in intermediate tones. The mineral is colorless if trace elements are lacking in the crystal structure and may then be called leucosapphire.

The word 'sapphire' can be traced back to the Greek sappheiros 'blue stone' or to the Sanskrit 'sanipiya', a dark precious stone, literally meant 'sacred to Saturn' from Sani 'Saturn' + priyah 'precious' (Harper, 2015). Corundum, i.e. sapphire and ruby, have always played an important role for mankind. In ancient and medieval times, sapphire was a symbol for hope, strength, wisdom, and faith and was believed to preserve chastity and to protect people from fraud, treachery, poison, diseases, and from black magic.

Famous people, who are known to have worn a sapphire as talisman, are King Solomon and Abraham. In the Christian Church, sapphires are highly cherished, so these precious stones are commonly the gemstone of choice for a Bishop's ring.

Today, although there is still a large community of people believing in the virtues of sapphires as a healing or protecting stone, sapphires and rubies are mostly popular as precious stone in jewelery. One of the largest and most popular faceted gem-quality sapphires is the Logan Sapphire from Sri Lanka, weighing 422.99 carats (84.6g). The gemstone is currently displayed at the National Museum of Natural history in Washington D.C. Popular for gemstone-sapphires is the so-called asterism, a star-like phenomenon that results from crystallographically oriented needle-like inclusions of rutile (TiO_2) in the sapphire crystal structure. These inclusions cause the appearance of a whitish six-rayed star in the gemstone. Occasionally, when in addition to rutile, hematite (Fe_2O_3) is included in the sapphires, the two types of inclusions superimpose upon each other to form a golden twelve-rayed star asterism. The largest and most popular gem-quality star-sapphires are the Black Star of Queensland (733 carats) and the Star of India (563.4 carats). Due to the high popularity of sapphires for jewels, they emblaze tiaras of many female members of the European royal houses, such as Sweden (Leuchtenberg Sapphire Tiara), Netherland (The Dutch Sapphire Tiara), England (George IV Victorian Suite Tiara; Queen Victoria's Sapphire cronet), France (Queen Marie-Amélie's Sapphire and Diamond Parure Tiara), Italy (Barberini Sapphire Parure Tiara), Luxembourg (Nassau Tiara), Monaco (Océan Tiara), and Denmark (Maria Feodorovna's Sapphire Bandeau).

Corundum is furthermore extremely valuable for industrial usage due to its high melting point of 2040 °C and the hardness of 9 on Moh's scale. Major industrial applications for corundum are the usage as abraisive or as ceramic additive in scratch-proof varnish or as additive to assist the slip-resistivity of materials. Watches are often covered by protective scratch-proof sapphire glass. Furthermore, corundum is commonly added to fire-proof materials. For industrial purposes, synthetic corundum is usually used. The French

chemist Auguste Verneuil was the first person to fabricate synthetic corundum in 1888 via flame fusion. Other methods to grow synthetic corundum are via flux-growth or hydrothermal synthesis.

1.1. DEPOSITS AND GENESIS OF CORUNDUM

Deposits of gem-quality corundum are well distributed all around the world (e.g. Hughes, 1997) and have been described detailed in many publications (see references in this work and references therein). A review of the literature about gem corundum demonstrates the wide distribution of corundum that occurs in various different geological settings and seems to be generated via several different petrogenetical processes, such as metamorphic reactions or through igneous crystallization from alumina-rich magmas. Due to the high variability in the processes leading to the formation of corundum that goes along with chemical and optical variations, a classification of gem-corundum according to their geological occurrence, i.e., the type of deposit, is advantageous. Such a classification basing on the type of corundum deposit has been established by Simonet et al. (2008). Corundum deposits can be either primary or secondary. Primary corundum deposits are those where the corundum is entrained inside the same rock where it crystallized. In secondary deposits, corundum is an inherited mineral that formed in a different petrogenetic setting as where it is deposited.

Primary corundum deposits are either igneous or metamorphic. In-situ occurrences of igneous primary corundum deposits are extremely rare. The only igneous rocks that are reported to bear corundum (sapphire), are syenites (e.g., Deer et al., 1992; Klein and

Hurlbut, 1993; Simonet et al., 2004). Occasionally, corundum is described as accessory mineral in anorthoclasite xenoliths, e.g. in a trachyte dome in Cantal, french Central Massif (Brousse and Varet, 1966), in basalt plugs in central Queensland, Australia (Robertson and Sutherland, 1992), or in alkali basalt sills and dykes from Scotland (Upton et al., 1999). Metamorphic primary deposits are subdivided into three sub-categories: metamorphic stricto sensu (s.s.), metasomatic and anatectic. Metamorphic deposits s.s. are those where corundum crystallized during metamorphism of alumina-rich rocks. Such rocks can be gneisses, granulites, and meta-limestones. These deposits can reach scales of several kilometers. Metasomatic deposits are those where corundum forms via the introduction of fluids into tectonic structures or via contact metamorphism. In these deposits, mineralization of corundum is limited to spatially restricted areas. Typical scales for metasomatic corundum deposits are a few meters. Metasomatic corundum bearing rock types are plumasites, desilicated gneisses, and skarns. In anatectites, corundum may appear as a consequence of desilication during partial melting. Upon melting of meta-pelitic rocks, silica will enter the first melt, leaving an alumina-rich residue (Mehnert, 1968) that may crystallize corundum (Altherr et al., 1982; Cartwright and Barnicoat, 1986).

Secondary corundum deposits are either of sedimentary, basaltic, or lamprophyric type. Sedimentary secondary corundum deposits are either eluvial, colluvial, or alluvial placers. Major gem fields of sedimentary corundum deposits are in Sri Lanka (e.g., Dahanayake, 1980; De Maesschalck and Oen, 1989), east Africa (e.g., Henn and Milisenda, 1997; Simonet et al., 2004; Blauwet and Laurs, 2005), and in Madagascar (e.g., Giuliani et al., 2007; Rakotondrazafy et al., 2008). Basaltic secondary deposits of corundum represent the world's largest corundum suppliers (e.g., Guo et al., 1996; Limtrakun et al., 2001). Corundum associated with basaltic terrains is usually blue, green, or yellow sapphire, and is known as the blue-green-yellow (BGY) sapphire suite (e.g., Sutherland et al., 1998). These types of corundum deposits are located all over the world,

most notably in Asia (e.g., Guo et al., 1996) and Australia (e.g., Coenraads, 1992; Sutherland, 1996; Saminpanya, 2001; Sutherland et al., 2002b; Graham et al., 2004; McGee, 2005), but also in Africa (Kiefert and Schmetzer, 1987; Krzemnicki et al., 1996; Schwarz et al., 2000) or Europe (e.g., Malikova, 1999; Giuliani et al. 2009; Uher et al., 2012). The only reported lamprophyric corundum deposit is the Yogo Gulch sapphire deposit in Montana, USA (e.g., Meyer and Mitchell, 1988; Brownlow and Komorowski, 1988). Sapphires in these lamprophyres are thought to be xenocrysts that were inherited from the metamorphic basement during magma ascent.

In the following section, the main localities and the related genetical hypotheses of metamorphic primary sapphires and of igneous secondary sapphires are reviewed, as these are the world's most abundant and important corundum deposits.

Notably, corundum that formed via metamorphic processes is usually ruby, whereas magmatic corundum usually appears in blue, green, yellow, or transparent colored sapphire. Images of typical magmatic blue sapphires and of metamorphic red rubies are shown in Fig. 1.

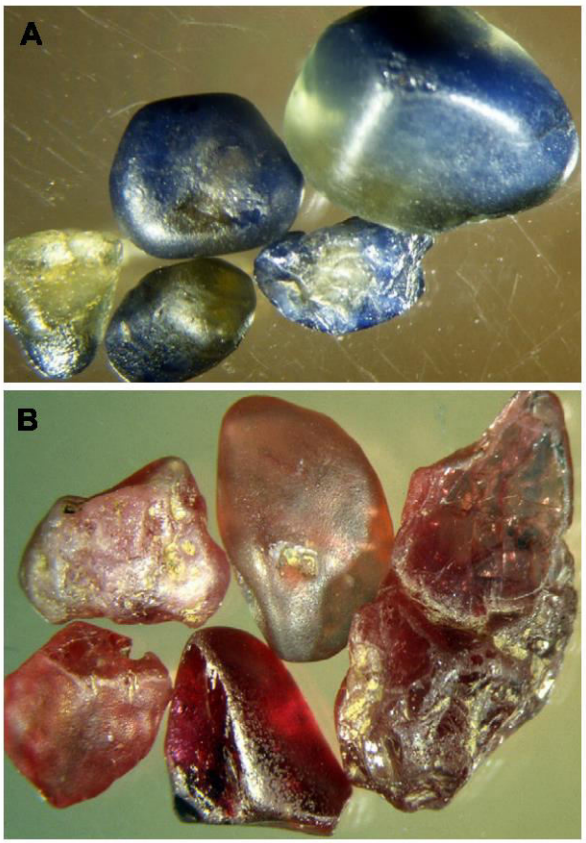

Figure 1:Typical appearance of magmatic and of metamorphic corundum from Graham et al. (2008). (A): BGY 'magmatic' corundum suite, Tumbarumba gemfield, southern New South Wales, Australia (largest grain is 10 mm). (B): Pink-red 'metamorphic' corundum suite, Tumbarumba gemfield, southern New SouthWales, Australia (largest grain is 5 mm in diameter).

Yet, before reviewing the occurrences and petrogenesis of metamorphic and magmatic corundum, I first summarize the distinguishing features between corundum that formed via metamorphic reactions and those that formed via igneous crystallization.

Natural corundum is reported from many different geotectonic settings and may be of magmatic, metamorphic, or metasomatic origin, each differing in terms of trace element geochemistry, the mineral inclusion suite (e.g., Sutherland and Schwarz, 2001; Graham et al., 2004, Peucat et al., 2007), and in the oxygen isotopic composition (Giuliani et al., 2005). Various proposals for the genesis of corundum in each geotectonic setting have been established, many of which are highly conflicting.

The discrimination between sapphires of magmatic and sapphires of metamorphic origin is based on their trace element contents. With the introduction of Laser Ablation – Inductively Coupled Plasma – Mass Spectroscopy (LA-ICP-MS) as a common technique in analytical geoscience, trace element concentrations for solid materials can be obtained down to the ppt level. Most important trace elements to distinguish between sapphires of different origins are Ga, Mg, Fe, Ti, and Cr (e.g., Peucat et al., 2007). These authors show that in a Ga/Mg vs. Fe_{tot} variation diagram, or in a Ga – Mg – Ti ternary diagram, metamorphic and magmatic sapphires form distinct populations confine specific fields (Fig. 2). Others (e.g., Sutherland et al., 1998a; Limtrakun et al., 2001; Saminpanya et al., 2003, Van Long et al., 2004; Garnier et al., 2005; Graham et al., 2008; Uher et al., 2012) preferentially plot sapphire compositions in a wt. % Cr_2O_3/Ga_2O_3 vs. Fe_2O_3/TiO_2 diagram or a wt. % TiO_2/Ga_2O_3 vs. Fe_2O_3/TiO_2 diagram (Fig. 3). These discrimination diagrams are based on the fractionation of the Ga/Al ratio and of Mg in sapphires during crystallization. Magmatic sapphires usually have higher Ga/Al ratios than metamorphic sapphires. The lower Ga/Al ratio for metamorphic sapphires is explained by Whalen et al. (1987) by the extraction of Ga from the metamorphic rocks by circulating F-rich fluids during partial melting of granulites. During fluid circulation, F would complex with Ga to form GaF_6^{3-} ions that are extracted, leaving a restitic granulite depleted in Ga over Al.

In contrast, Mg is usually lower in magmatic than in metamorphic sapphires and is thought to reflect the Mg content of the crystallization environment. LA-ICP-MS investigations to discriminate between sapphires of different origins, have been performed by Upton et al., 1999; Limatrakun et al., 2001; McGee, 2005; Garnier et al., 2005; Peucat et al., 2007; Sutherland et al., 1998a, 2009, and Uher et al., (2012).

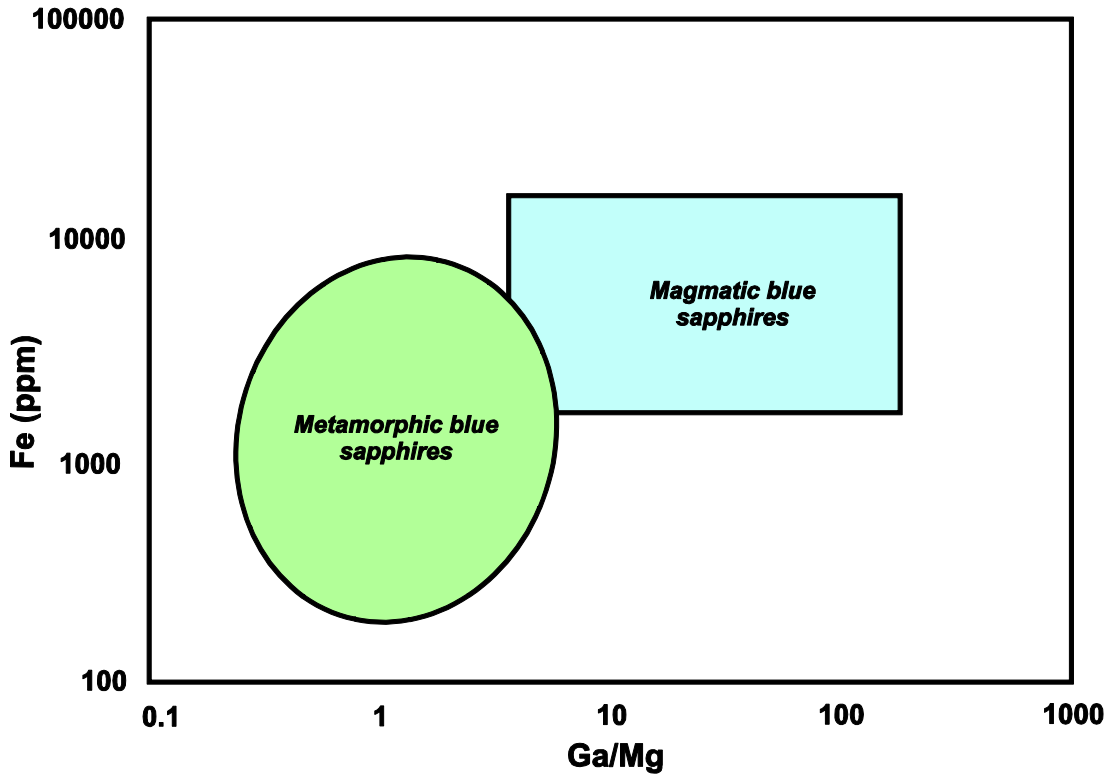

Figure 2: Fe (ppm) vs. Ga/Mg variation diagram for blue sapphires according to their geological origins. Redrawn after Peucat et al. (2007). The blue square represents magmatic blue sapphires, and the green ellipse represents metamorphic blue sapphires.

A further discrimination feature used to distinguish between 'metamorphic' and 'magmatic' sapphires is the mineral inclusion suite (e.g., Coenraads et al., 1992; Guo et al., 1996; Sutherland et al., 1998a, b). Mineral inclusions associated with magmatic sapphires are anatase, albite, anorthite, apatite, baddeleyite, beryl, calcite, cherallite, chromite, euxite, ferrocolumbite, fluorite, graphite, hercynite, ilmenite, margarite, molybdenite, nepheline, oligoclase, olivine, pyrite, pyrochlore, quartz, rutile, spinel,

thorite, and zircon (Bosshart, 1995; Vysotskiy et al., 2002; Khanchuk et al., 2003; Sutherland et al., 2002, 2003; Roberts et al., 2004; Van Long et al., 2004; McGee, 2005; Pisutha-Arnond et al., 2005; Pakhomova et al., 2006). Corundum with a metamorphic association typically carries inclusions of anatase, diopside, Cr-spinel, meionite, pyrope, sapphirine, and spinel (e.g., Sutthirat et al., 2001; Roberts et al., 2004; Sutherland et al., 2005).

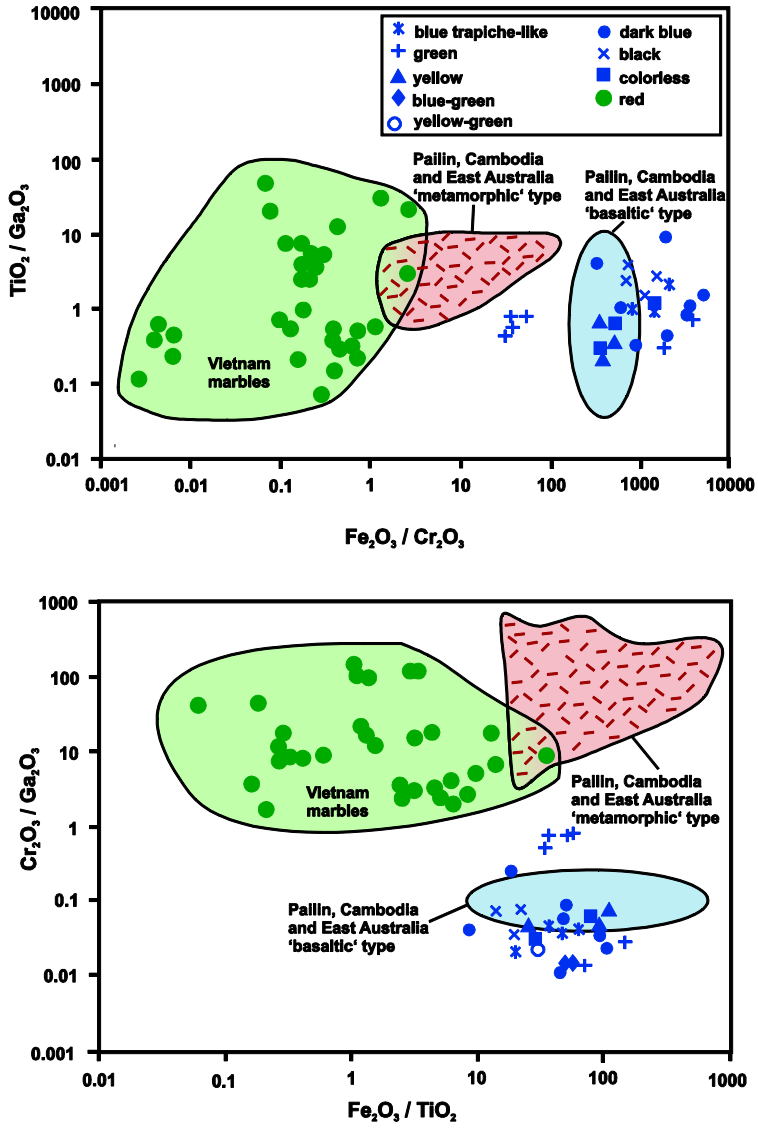

Figure 3: Chemical variation diagram showing the oxide ratios of the trace element contents of green, blue, yellow sapphires from Dak Nong in southern Vietnam (closed blue circles), in northern Vietnam (green circles). Sketch is redrawn after Garnier et al. (2005). For comparison, the authors added the fields for typical 'metamorphic' corundum (red field) and for typical 'basaltic'/'magmatic' corundum (blue field) of Palin (Cambodia) and from Eastern Australia. These fields were defined by Sutherland et al. (1998a).

1.1.1. Metamorphic primary deposits

Metamorphic corundum is usually the Cr and V-rich variety ruby, whereas the Fe and Ti rich corundum variety 'sapphire' usually forms in igneous realms. Many metamorphic rocks such as marbles, skarns, granulites, gneisses, mafic to ultramafic metamorphic rocks, and metapelites (e.g., Okrusch et al., 1976; McColl and Warren, 1980; Kornprobst et al., 1990, Giuliani et al., 2007) are reported to contain metamorphic corundum that crystallized following several different mineral reactions.

Corundum in marbles

The appearance of metamorphic ruby in marbles as a consequence of metasomatism through hydrothermal fluids of magmatic origin has been first described by Moyd (1949) from the Grenville series in Ontario. Okrusch et al. (1976) proposed that ruby in marbles from Hunza (Kashmir) formed during regional metamorphism at 600 – 620 °C and a pH_2O of 0.6 GPa due to the reaction

$$\text{Margarite} \leftrightarrow \text{anorthite} + \text{corundum} + H_2O \quad (1)$$

or

$$8\ \text{diaspore} + 1\ \text{pyrophyllite} + 2\ \text{calcite} \leftrightarrow \text{corundum} + 2\ CO_2 + 3\ H_2O. \quad (2)$$

The formation of ruby in marbles from Central and Southeast Asia has been explained by Garnier et al. (2008) through the destabilization of spinel in the presence of F and Cl rich fluid phases via the reaction

Spinel + calcite + CO_2 → ruby + dolomite. (3)

The role of F and Cl in the genesis of metamorphic corundum was the mobilization of Al from micas that in turn formed during metamorphism of clay minerals and organic matter to spinel. Corundum has also been reported to occur in the reaction zone between marble and corundum-bearing high-grade metapelite from the Alborán Sea basement in the western Mediterranean (Sanchez-Vizcaíno, 2002). The authors describe the appearance of corundum in the reaction zone due to the breakdown of muscovite in the absence of quartz at T > 650 °C and P < 0.5 GPa.

Corundum in metasediments

Granulites preserving corundum that formed by prograde metamorphism are reported from the In Ouzzal granulitic unit from Hoggar in Algeria (Ouzegane et al., 2002), from Central Australia (Warren, 1983; Goscombe, 1992), the Gruf complex in the Italian Central Alps (Droop and Bucher-Nurminen, 1984), the Wilmington complex, USA (Strogi et al., 1993), the Limpopo belt, South Africa (Ackermand et al., 1982; Horrocks, 1983; Windley et al., 1984; Droop, 1989), and from Sri Lanka (Kriegsman and Schumacher, 1999). Grapers and Palmer (1996) investigated so called 'corundumites' - monomineralic rocks consisting of corundum – that are entrained in metamorphic ultrabasic rocks from Westland, New Zealand. These corundumites are thought to be metamorphosed xenolithic quarzo-feldspathic schists. Contact metamorphism of metapelitic country rocks by the Tertiary Skaergaard Intrusion, East Greenland, produced a granitic melt and left the assemblage spinel + cordierite + plagioclase + corundum as residue (Markl, 2005). Corundum has also been found in hornfelses, e.g. from the Cashel-Lough Wheelaun Intrusion, Ireland (Leake and Skirrow, 1960), or from the Land's End

Aureole at Tarter-du, Cornwall (Floyd, 1965). Metamorphic corundum in hornfelses from the central Gran Paradiso Massif, Western Alps, Italy (Gabudianu Radulescu et al., 2011) are the result of the breakdown of spinel and kyanite according to the reaction

$$\text{Spinel} + \text{kyanite} = \text{corundum} + \text{garnet} \quad (4)$$

at 0.5-0.6 GPa and 300-350 °C.

Corundum furthermore occurs in regionally metamorphosed bauxites, e.g. in Namaqualand, S Africa (Coetze, 1940), at Mt. Ismail in the Southern Menderes Massif, SW Turkey (Aydoğan and Moazzen, 2012), in Sonapahar, India (Golani, 1989), and on Naxos, Cyclades, Greece (Feenstra, 1996).

Corundum in metamorphic ultramafic rocks

Ultramafic bodies subjected to high pressure metamorphism during subduction, e.g., amphibolites from the Krivaja-Konjuh ultramafic massif of the Dinaride Ophiolite Zone in Boisnia (Operta et al., 2002) contain corundum in association with pargasitic hornblende and anorthite. Berger et al. (2010) reported corundum-bearing amphibolites from the Variscan French Massif Central that are associated with serpentinites, flaser-gabbros, eclogites, and granulites. The mineral assemblage spinel-corundum-sapphire-kyanite shows that these rocks formed at peak P-T conditions around 0.1 GPa and 800°C.

Corundum + garnet paragenesis

The occurrence of corundum + garnet is known from kimberlite xenoliths as in the Jagersfontein kimberlite (Mazzone and Haggerty, 1989), from aluminous eclogites associated with kimberlites (e.g., Rossman and Smyth, 1990; Jacob, 2004), and from ultrahigh-pressure metamorphic rocks (Zhang et al., 2004). Shimpo et al. (2006) report the assemblage garnet + corundum in Mg-Al-rich rocks from Sevitturangampatti (Namakkal district) in the Palghat-Cauvery Shear Zone System (PCSS), southern India. The assemblage is thought to be formed through the dehydration of staurolite resulting from high-temperature thermal metamorphism following the equation

$$\text{staurolite} \rightarrow \text{garnet} + \text{corundum} + \text{silimanite/kyanite} + H_2O. \quad (5)$$

1.1.2. Magmatic secondary deposits

Gem quality corundum, especially the blue Fe- and Ti-rich modification sapphire, are reported to occur as megacrysts in volcanic terrains associated with rift-related alkali basaltic magmatism all over the world, most notably from Asia and Australia (e.g., Sutherland et al., 1998a; Guo et al., 1996). Sapphires from magmatic secondary deposits are usually found in alluvial or eluvial placer deposits of basalt fields. Reported sapphires from magmatic secondary deposits have diameters up to 2 cm, and may be blue, green, grey, yellow, or transparent. As the colors blue, green, and yellow are most abundant amongst the magmatic secondary sapphires, these type of sapphires are commonly referred to as 'Blue-Green-Yellow' or 'BGY' sapphires in the literature (e.g., Sutherland et al., 1998). Most of the 'BGY' sapphires are less transparent than the metamorphic pendants, decreasing the quality and value as gemstone. Magmatic secondary sapphires commonly exhibit evidence for chemical corrosion at magmatic temperature, including

anhedral crystal shapes, rounded edges, and macroscopically visible spinel rims (e.g., Guo et al., 1996; McGee, 2005).

The petrogenesis of alkaline basalt hosted sapphires was intensively studied from various gem fields in the 90s and early 2000s. These studies compile detailed investigations of the sapphire trace element compositions, mineral inclusions, melt and/or fluid inclusions, as well as oxygen isotope studies.

The first petrological investigation of in-situ occurrences of corundum megacrysts in alkaline basalt was by MacNevin (1972) from the Inverness-Glen Innes region, northern New South Wales, Australia. Further occurrences are in Europe, Asia, Africa, Australia, and South America. Most gemfields containing the magmatic BGY sapphires are monogenetic. Rarely, gemfields contain bimodal suits of magmatic and metamorphic sapphires, e.g. the Barrington gemfield in New South Wales, and various gemfields in Thailand. A polymodal suite of magmatic, metamorphic, and metasomatic sapphires has been reported from the Tumbarumba gemfield in New South Wales (Saminpanya, 2001; Sutherland et al., 2002b; Graham et al., 2004; McGee, 2005). The following list comprises an overview about magmatic secondary corundum deposits:

Europe: Cerová Highlands, W Carpathians (S Slovakia); Massiv Central, France; Jizerská Louka alluvial deposits, Czech Republic (Uher et al., 2012; Lacroix, 1901; Giuliani et al. 2009; Malikova, 1999).

Asia: Chantaburi-Trat AB, Bo Ploi, Khorat, Kanchanaburi, and Denchai gemfields, Thailand; Ban Hui Sai alluvial gemfield, Laos; West Palin, Cambodia; Dak Nong, Gia Lai, Bin Phuoc, Bin Tuan, Lam Dong, Southern Vietnam; China; Primorye, Russia (Barr and

MacDonald, 1981; Keller, 1982; Yui et al., 2003, 2006; Coenraads et al., 1995; Sutherland et al., 1998a; Sutherland et al., 2002a; Garnier et al. 2005; Guo et al. 1996; Izokh et al. 2010; Limatrakun et al., 2001; Graham et al., 2008; Nechaev et al., 2009).

Africa: (Mangari), Kenya; Gimi Valley, Nigeria; Madagascar (Guo et al., 1996; Irving and Price, 1981; Giuliani et al., 2007).

Australia: Weldboroug, NE Tasmania; Barrington; Tumbarumba gemfield, New South Wales; Queensland) (Zaw et al., 2006; McGee, 2005; Sutherland et al., 1998a; Guo et al., 1996).

S America: Merceraderes Rio Mayo area, Colombia (Keller et al., 1985).

The following section provides a detailed description of the most intensely studied 'BGY' sapphires that are derived from magmatic secondary corundum deposits.

Australia

In Australia, gem corundum deposits occur in Mesozoic to Cenozoic intraplate basalt fields in eastern Australia, at the margin to the Pacific Ocean (e.g., Oaks et al., 1996; Sutherland et al., 1996; Graham et al., 2008), with the most prominent deposits being located in Tasmania and in New South Wales. The Tasmanian sapphire deposits are alluvial deposits within a Miocene basalt field in Weldborough and were intensively studied by McGee (2005) and Zaw et al. (2006). The New South Wales sapphires are from the Tumbarumba field in southern NSW, the Barrington field in eastern NSW, and

the Yarrowitch field in northeast NSW. The sapphires from the Tumbarumba field lie within placer deposits of Miocene age. The Yarrowitch sapphires lie within the placer deposits of Mesozoic to Cenozoic basalts, and are associated with megacrystic zircon and spinel. Most strikingly, the Tumbarumba gemfield contains polygenetic corundum suites comprised of a metamorphic pink-red ruby suite and a magmatic BGY sapphire suite.

Asia

The most abundant gem quality magmatic corundum fields are located in Asia with the most prominent gemfields in Thailand at Bo Ploi (Guo et al., 1996; Pisutha-Arnond et al., 1998; Srithai and Rankin, 1999; Abduriyim and Kitawaki, 2006), Denchai (Limatrakun et al., 2001; Zaw et al., 2002; Yui et al., 2003), Phrae (Wathanakul et al., 2004), and Chanthaburi-Trat (Sutthirat et al., 2001; Saminpanya et al., 2003; Chualaowanich et al., 2005; Yui et al., 2006). Whereas the Bo Ploi, Denchai, and Phrae gemfields host only magmatic BGY sapphire, the Chanthaburi-Trat gem-corundum suite is comprised of magmatic sapphire and of metamorphic ruby. The Thailand sapphires are recovered from placer deposits of Cenozoic alkali basalts.

Sapphires from the Ban Huai Sai gemfield in northwest Laos (Sutherland et al., 2002a) are mined from alluvial deposits of Cenozoic basalt fields. The age of sapphire crystallization in this region has been estimated by Sensitive High Resolution Ion Microprobe (SHRIMP) U-Pb dating of a zircon inclusion to be 1.2-1.3 ± 0.3 Ma and hence matches the age of basaltic volcanism in that area.

Sapphire gemfields in Vietnam are the Dak Nong gemfield in south Vietnam (Garnier et al., 2005, and Izokh et al., 2010), as well as the Binh Thuan, Lam Dong, Dong Nai, and the Dac Lac provinces in northern Vietnam (Smith et al., 1995). Gem sapphires from this region are recovered from eluvial and alluvial placers of late Cenozoic to Quarternary alkaline basalts of the Dak Lak Province (Garnier et al., 2005).

Cambodian sapphires are from the Palin basalt field where magmatic sapphires and metamorphic ruby form a bimodal corundum suite (Sutherland et al., 1998; 2008b; 2009).

In eastern Russia, sapphire and zircon are found in placer deposits of the Late Cenozoic intra-plate alkaline basalt fields in the Marevka and the Kedrovka river basins in the Marevka district in the north and in Shkotovo Plateau in the south (Nechaev et al., 2009).

Alkaline basalt hosted sapphires in China are found in the Changle district of Shandong Province (Giuliani et al., 2015). The host rocks are Miocene aged alkali basalts that contain in addition to sapphire, xenoliths of spinel lherzolite, wehrlite and pyroxenite. These blue and yellow sapphires from Changle occur along with diopside, anorthoclase, magnetite, zircon and garnet megacrysts (Guo et al., 1996; Song et al., 2008; Song and Hu, 2009).

Africa

The most prominent gem-quality sapphire deposits in Africa are from Madagascar which is one of the major gem-producing countries of the world (Rakotondrazafy et al., 2008). Many gem-corundum deposits in Madagascar are primary, and corundum may be hosted by metamorphic rocks, such as gneisses, cordieritite, metamorphic mafic and ultramafic rocks, marbles, and in metamorphic calc-silicate rocks (e.g., Giuliani et al., 2009), or in magmatic rocks (syenites or alkali basalts). Secondary placer deposits contain ruby and sapphires that are associated with alkaline basaltic volcanism in the northern and central part of Madagascar. Well studied corundum placer deposits are at Vatomandry, Andilamena, and the Ilakaka basalt fields.

Europe

Sapphires from the French Massif Central occur in alluvial and eluvial deposits of Cenozoic alkali basalts, and in anortholcasite xeoliths from the Menet trachyte cone in Cantal (Giuliani et al., 2009). The localities are within the volcanic areas of the Chaîne de la Sioule, Chaîne des Puys, Mont Dore, Cantal, Devès, and Velay (Simonet, 2000) with the main localities being in the Devès area, which is the southern prolongation of the Limagne graben that is part of the European Rift System.

In Slovakia, magmatic blue sapphires were found in Neogene volcanic areas in the Cerová Highland, Western Carpathians (Uher et al., 2012). The sapphires occur within placer deposits of Pliocene to Pleistocene intra-plate mafic volcanics.

Genetic implications for basalt hosted sapphires

Although corundum from secondary magmatic deposits often occurs in alluvial or eluvial placer deposits and are thus detached from their host rocks, they are generally thought to be carried to the surface by ascending basaltic melts which is strongly supported by rare in-situ occurrences of corundum in alkaline mafic rocks (e.g., MacNevin, 1972; Stephenson, 1976; Vichit, 1978). These sapphire megacrysts from secondary magmatic deposits are frequently accompanied by megacrystic zircon, spinel, ilmenite, olivine, clinopyroxene, garnet, biotite, apatite, magnetite or feldspar (e.g., Upton et al., 1999; Coenraads et al., 1990; Garnier et al., 2005). The megacrystic 'BGY' sapphires commonly exhibit evidence for chemical corrosion (xenomorphic crystal habitus, rounded edges, and spinel rims at the interface towards the basalt), indicating disequilibrium with the basaltic carrier magma and suggesting a non-cogenetic origin of the corundum and the hosting basalt. Further evidence for a xenogenetic relationship between the sapphires and their host basalts is given by the oxygen-isotope disequilibria between the sapphires and olivine phenocrysts in the host basalt (e.g., Yui et al., 2003;

2006). Yet, the most striking evidence for a non-cogenetic origin of the sapphires and their host-rocks is given by the phase relations in the CMAS system (Fig. 4), at pressures of 1 GPa and 2 GPa. A melt with the composition of an alkaline mafic rock (red star in Fig. 4) will follow the red cooling path (2 GPa), or the blue cooling path (1 GPa). Upon cooling, the melt will start to crystallize olivine and orthopyroxene, followed by spinel. Fractional crystallization of olivine, opx, and spinel will lead to an increase in the Al content in the melt. Upon further cooling, plagioclase will start to crystallize, leading to a decrease in the Al content in the melt. Plagioclase crystallization thus functions as a chemical buffer, controlling the alumina content in the melt. The final eutectic composition is given by the small stars at the enstatite-anorthite-quarz triple point. The diagram shows that, even at high pressure, an alkaline mafic melt will never intersect the corundum stability field boundary in order to stabilize corundum as a liquidus phase. Hence, the sapphires that are frequently reported to occur in association with alkaline mafic rocks, must have formed in an environment that was chemically significantly different from an alkaline mafic melt.

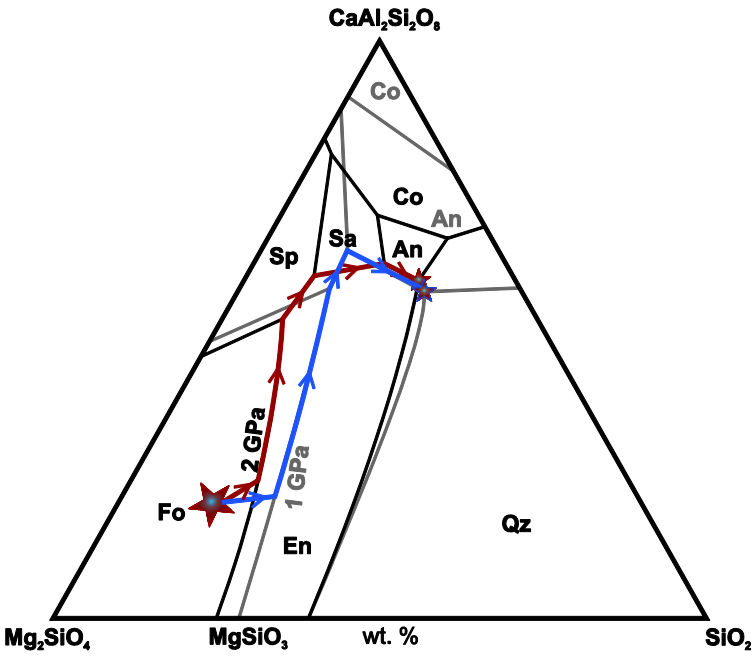

Figure 4: Phase relations in the CMAS system at 1 GPa (Sen and Presnall, 1984) and 2 GPa (Liu und Presnall, 1990) pressures. Abbrevations are: Fo: Forsterite; En: Enstatite; Qz: Quartz; Sp: Spinel; Sa: Sapphirine; An: Anorthite; Co: Corundum. The star in the forsterite field represents an exemplaric composition of an alkali basalt. Upon cooling, the melt will follow the blue path at 1 GPa, and the red path at 2 GPa pressure. The final eutectic composition of the melt is given by the small stars at the anorthite-enstatite-quarz triple point.

The impossibility of crystallizing corundum directly from a basaltic melt has been proven experimentally by Green et al. (1978).

The contentious occurrence of corundum megacrysts in a carrier magma containing no normative corundum triggered an extensive research in order to explain the enigmatic origin of the corundum. There seems to be a consensus in the literature that the basalt-hosted corundum megacrysts are xenocrysts rather than phenocrysts with the basaltic magma serving as transport medium, carrying the sapphires from a deeper situated reservoir to the surface. Still, there is no common theory about the petrogenesis of the sapphire xenocrysts. In the following sections, the main results from alkali basalt hosted magmatic sapphire studies are summarized and compared in terms of optical features, trace element composition, mineral inclusion suite, fluid/melt inclusions, and the oxygen isotopic composition.

Trace element composition

Magmatic sapphires can show significant core to rim variations of trace elements. Upton et al. (1999) reported magmatic sapphires from Scotland to be enriched in Fe, Ti, Be, and Nb in the core compared to the rim, contributing this to noticeable changes of the physical conditions in the melt during crystal growth. This differs marginally from core to rim variations reported by McGee (2005) who showed for the Weldborough sapphires (Australia) that Fe, Ga, V, and Mg do not partition preferentially into either core or rim of the sapphire, whereas Be and Ti are preferentially incorporated into the core. Nb and Ta are reported to be predominantly enriched in the core, but some samples show a depletion of Nb and Ta in the core. Zaw et al. (2006) reported that in the Weldborough sapphires, Fe, Ti and Ga are preferentially incorporated into the core.

Mineral inclusions

Syngenetic mineral inclusions in alkaline basalt hosted gem sapphires provide important information about the origin of their host corundum. Reported mineral inclusion suites of gem fields in Australia, East Asia and Russia, Europe, and South America, are summarized in Table 1. Most abundant mineral inclusions associated with magmatic sapphires are those of the columbite-group, zircon, spinel, rutile, and feldspar. These Nb, Ta, Zr, and Ti bearing mineral inclusions have been suggested to be derived from highly evolved felsic melts such as syenites (e.g., Sutherland et al., 1998b). Other mineral inclusions such as plagioclase, nepheline, or calcite suggest crystallization from undersaturated alkaline melts. Some sapphires are reported to have bimodal mineral inclusion suites, indicating a complex petrogenesis involving magmas of different compositions. Guo et al. (1996), for example, attribute the syngenetic inclusions feldspar, zircon, uraninite, ilmenorutile, and Fe-, Cu-sulphide to evolved alkaline felsic melts, and titaniferrous columbite, uranpyrochlore, and fersmite to carbonatitic melts. Based on these bimodal characteristics of mineral inclusions, the authors suggested the sapphire formation to be the result of the interaction of a highly evolved alkaline felsic melt and a carbonatitic melt. Later, Sutherland et al. (1998) argued that, chemically, the columbite inclusions rather resemble columbites from pegmatites than carbonatitic columbites and that no carbonatitic melt is necessarily required to explain the mineral inclusion suite. Izokh et al. (2010) came to a similar conclusion. CO_2 played a significant role in the formation of magmatic sapphires hosted by alkaline mafic rocks, although their model does not include a carbonatitic melt. They rather suggest that the sapphires crystallized from highly evolved syenitic melts that were saturated in CO_2 and had a free CO_2-H_2O bearing fluid, as indicated by the abundance of CO_2-H_2O bearing fluid inclusions.

In addition to estimating the composition of the parental melt, mineral inclusions – especially zircon – are widely used for geochronological applications. Applying U-Pb geochronology to syngenetic zircon inclusions in sapphires using LA-ICP-MS or

Sensitive High Resolution Microprobe (SHRIMP) techniques were frequently used to quantify the petrogenetical relationship between the sapphire megacrysts and their host basalts. Several studies revealed - based on zircon inclusion ages - that the time of sapphire crystallization falls into the same age as basaltic volcanism in that area, indicating a strong genetical link between both events (e.g., Coenraads et al., 1990; Sutherland et al., 1998b; McGee, 2005; Sutherland et al., 2002, 2009). Only Garnier et al. (2005) reported from the Dak Nong gemfield in Vietnam that the sapphires predate the basaltic volcanism by a few Ma.

Table 1: Mineral inclusions in magmatic sapphires.

Gemfield	Inclusions
Australian Fields	
Weldborough[1]	anorthite, apatite, beryl, chromite, ferrocolumbite, graphite, hercynite, molybdenite, oligoclase, olivine, pyrite, pyrochlore, quartz, rutile, zircon
Tumbarumba[2]	anatase, ferrocolumbite, rutile, spinel, zircon
Barrington[3]	hematite, rutile, spinel
Wellington[4]	anorthoclase, nepheline
Central Province[5]	alkali feldspar, columbite, thorite, uranium pyrochlore, zircon
East Asian-Russian Fields	
Kanchanaburi[7,6]	Alkali feldspar, biotite, calcite, columbite, enstatite, garnet, hercynite, Mn-ilmenite, monazite, nepheline, pyrochlore, sapphirine, staurolite, thorite, zircon
Ban Huai Sai[8,9]	albite, cheralite, columbite, euxenite-Y, zircon
Dak Nong[10]	apatite, baddeleyite, columbite, ilmenite, margarite, plagioclase, pyrochlore, zircon
Kedrovka[11,12]	albite, columbite, fluorite, monazite, rutile, zincian spinel, zircon
Podgelbanochny[13]	albite, chlorapatite, nepheline
Vietnam[10,14]	apatite, baddeleyite, columbite, goethite, ilmenite, margarite, plagioclase, pyrochlore, zircon
Thailand[15]	alkali feldspar (sanidine), hercynite-spinel, magnetite-hercynite, nepheline, zircon
European Fields	
Massiv Central[16]	columbite-group minerals, hercynite, ilmenite, magnetite, Nb-bearing rutile, pyrochlore, rutile, thorite, zircon
South American Fields	
Rio Mayo, Colombia[17]	apatite, plagioclase, rutile, zircon

Fluid/melt inclusions

Fluid/melt inclusion investigations provide important information about the composition of the parental melt and about the thermobarometric conditions at the time of mineral crystallization. Many sapphires are reported to contain polyphase fluid inclusions consisting of vapor + fluid ± solid. The frequent abundance of CO_2-rich fluid inclusions in alkaline basalt hosted sapphires (Coenraads et al., 1990; Limatrakun et al., 2001; Zaw et al., 2006; Van Long et al., 2004; McGee, 2005; Pakhomova et al., 2006; Song and Hu, 2009; Izokh et al., 2010) is strongly indicative for CO_2 to play a major role in the sapphire formation. Song and Hu (2009) report that CO_2 bearing fluid inclusions from the Changle basalts in China contain carbonate and sulfate daughter minerals, implying that these fluid inclusions derived from a carbonatitic melt. Thermobarometric conditions for sapphire formation yielded from fluid inclusion studies are extremely variable. For the Weldborough sapphires, McGee (2005) estimated 0.45 GPa and 1000 – 1200 °C as sapphire formation conditions. Significantly lower temperatures (780 – 820 °C) and pressures (0.17 – 0.3 GPa) were reported for the Kedrovka River sapphires by Pakhomova et al. (2006). Sutherland et al. (1998) report similar crystallization temperatures (720 – 880 °C) but higher pressures of 0.7 – 1.1 GPa for the Barrington sapphires. According to Limtrakun et al. (2001), the Denchai sapphires crystallized at temperatures between 770 and 1200 °C.

Primary melt inclusions in sapphires from alkali basalt terrains are all silica-rich and resemble a syenitic/ granosyenitic melt composition (McGee, 2005; Pakhomova et al., 2006; Izokh et al., 2010). Pakhomova et al. (2006) for example report following melt inclusion compositions from the Nezametnoye corundum deposit in the Primorsky region in Eastern Russia: SiO_2: 59 – 62 wt.%, Al_2O_3: 14 – 20 wt.%, Na_2O: 4 – 10 wt.%, K_2O: 2 - 6 wt.%, Fe_2O_3: 0.4 – 1.2 wt.%. Some melt inclusions contain also CaO (0.3 – 3.7 wt.%), P_2O_5 (0.92 – 1.28 wt.%), Cl (0.18 – 0.66 wt.%) and V_2O_3 (0.2 – 1.5 wt.%).

Oxygen isotopic composition

Oxygen isotope studies of sapphire xenocysts are aimed at investigating the origin of the sapphires, as the Earth's mantle and crust have distinctive oxygen isotopies. Typical magmatic sapphires have a $\delta^{18}O$ of +4.4 to +6.9 ‰ (Giuliani et al., 2005; McGee, 2005; Yui et al., 2003, 2006; Graham et al., 2008; Giuliani et al., 2009; Sutherland et al., 2009; Uher et al., 2012). Most sapphires are found to be not in oxygen isotopic equilibrium with olivines from the hosting basaltic melt, supporting a xenogenetic relationship. All reported oxygen isotopic studies agree in that the sapphires originated from evolved sub-continental mantle magmas. Only Yui et al. (2003) suggested that those sapphires with $\delta^{18}O$ values greater than +5.5 ‰ must have had a crustal component involved in their genesis. They thus suggest a hybridization model where sapphires formed via the reaction of a felsic melt from the metasomatized mantle and a peraluminous rock at lower/mid-crustal level. They also dismissed an alleged involvement of a carbonatitic melt, as carbonatitic melts in equilibrium with mantle silicates would have $\delta^{18}O$ values between +7 and +8 ‰.

Petrogenetic models

Based on detailed investigations of the sapphires major and trace element geochemistry, the mineral inclusion suite, on melt and/or fluid inclusions, and on the oxygen isotopic compositions, several hypotheses about the petrogenesis of alkaline basalt hosted sapphires have been proposed in the past. Although there is a consensus about the xenocrystic nature of the sapphires, there is still a debate about the origin of the sapphires and the parental melt composition. There seems to be also a consensus that highly fractionated alkaline silicate melts play a major role in the sapphire

formation with the different petrogenetic models only differing in details such as the depth of formation, or the exact role of the syenitic melt. The major theories about the crystallization of alkaline basalt hosted sapphires can be summarized as follows:

(1) Crystallization from highly evolved melts such as syenites that are partial melts of the mantle/lower crust, and subsequent assimilation by ascending basaltic magma (e.g., Irving, 1986, Coenraads et al., 1990, Aspen et al., 1990, Garnier, 2005, Giuliani et al., 2009).

(2) Crystallization from alkaline Si- and Al-rich melts from partial melting of amphibole bearing lithospheric mantle (Sutherland et al., 1996; 1998).

(3) Hybrid formation via reaction between a silicate and a carbonatitic melt at mid-crustal levels (Guo et al., 1996). This hybrid model is based on the occurrence of a very complex mineral inclusion suite that must have precipitated from melts of two different compositions, most probably a carbonatitic melt and a highly evolved silicate melt. These authors propose that intruding carbonatitic melts response an Al-oversaturation of highly evolved silicic (syenitic) melts, resulting in local precipitation of corundum. The alumina oversaturation in the silicate melt is thought to be caused by CO_2 that changes the crystallization path towards the precipitation of Al-free silicates such as wollastonite, so the Al/Si ratio in the melt increases until corundum becomes a stable liquidus phase.

Crystallization at shallow crustal levels from an iron-rich syenitic melt with the participation of a carbonate - H_2O – CO_2 fluid phase (Izokh et al., 2010). This model is similar to the model proposed by Guo et al., (1996), but does not include the participation of a carbonatitic melt. Izokh et al. (2010) rather suggest that the syenitic melt must have had high CO_2 contents from the beginning, as it was presumably formed under the influence of CO_2 rich basaltic magmas. Differentiation of these CO_2 rich syenitic magmas led to the formation of alkali-carbonate complexes, so that the residual melt becomes oversaturated in alumina. Corundum may precipitate in the most fractionated magma chambers.

1.2. AIM OF THE THESIS

Occurrences of gem quality sapphire megacrysts associated with alkaline mafic rocks have been reported from many regions all around the world, most notably in Asia and Australia (e.g., Sutherland et al., 1998a; Guo et al., 1996). These sapphires occur predominantly in alluvial or eluvial placer deposits of basalt fields. In-situ occurrences are rare. The petrogenesis of these secondary magmatic sapphire deposits is yet unconstrained. Many theories have been proposed in order to explain the enigmatic origin of these sapphires. There is a consensus in the literature that the sapphires did not crystallize from the host basalt, but are xenocrystic in origin, and that the basalts only served as a medium to carry them to the surface. Yet, most petrogenetic models that were previously proposed to explain the formation of these sapphires only agree in some points, such as the involvement of highly evolved silicate melts and of CO_2 - either as fluid phase or in the form of a carbonatite (e.g., Irving, 1986; Coenraads et al., 1990, Aspen et al., 1990; Guo et al., 1996; Sutherland et al., 1998; 2002a; b; 2008; Garnier et

al., 2005; Giuliani et al., 2009, Izokh et al., 2010). The details such as the actual role and origin of CO_2 and the depth of crystallization differ significantly among the models. But as these sapphires always occur in the same petrogenetic realm – alkaline mafic intra-plate volcanic settings - it seems rather unlikely that all sapphires formed via different petrogenetic processes. Another puzzle is the selective sampling of the sapphires by the alkaline mafic melts, as the basalts only carry single crystals but never show schlieren or fragments of the former host rocks from which the sapphires were supposed to be derived. Furthermore, the association of alkali basalt and sapphire is poorly understood, yet (e.g., Izokh et al., 2010; Uher et al., 2012) because primitive alkali basalts are never corundum-normative when they leave the mantle source (Liu and Presnall, 1990). Still, there must be a genetical link between the sapphires and the host-rock, as these xenocrystic sapphires occur exclusively in primitive continental alkali basalts, but never in basaltic melts from other geotectonic settings, and never in derivative melts. Such a genetical relationship between the sapphires and their host basalts has never been explained in any of the models.

Aim of this study is to develop a model for the genesis of sapphires that are hosted by alkaline mafic rocks associated with intra-plate volcanism using sapphires from the Cenozoic Siebengebirge Volcanic Field (SVF) in western Germany. The SVF is part of the Cenozoic Central European Volcanic Province (CEVP) that forms a 200 – 300 km broad volcanic belt north of the Alpine Orogen. Alkaline mafic rocks from the SVF are long known to host sapphire megacrysts (e.g., Braun, 1922), that reach sizes up to 2 cm. The sapphires of the SVF are extremely valuable for scientific purposes, as the SVF sapphire deposit is one of the world's rare in-situ occurrences where the sapphires are still entrained in their host-rocks. Hence, the direct contact between sapphire and host-rock can be studied.

In order to investigate the petrogenesis of the Siebengebirge sapphires, detailed petrological and geochemical investigations of the sapphire, of syngenetic mineral

inclusions, and of fluid inclusions were conducted using the Electron Probe Micro Analyzer (EPMA), Laser Ablation – Inductively Coupled Plasma – Mass Spectrometry (LA-ICP-MS), Transmission Electron Microprobe (TEM), and a Raman spectroscope. The crystallization age of the sapphires was obtained by in-situ U-Pb dating of a syngenetic ferrocolumbite inclusion using LA-ICP-MS. This age allowed to directly link the sapphire genesis to the alkaline basaltic volcanism in the study area. Based on the results of the microchemical investigations, a carbonatitic melt could be identified to be the most probable candidate for the melt that precipitated the sapphires.

The petrogenetic implications that were derived from the microchemical investigations were tested in a set of three experiments. Time-series of experiments were employed to quantify the residence time of the sapphires in the basaltic melt and thus to conclude about the depth of sapphire entrapment which is probably the same as the sapphire crystallization depth. Two further experimental series were designed to investigate the feasibility of corundum to crystallize from a carbonatitic melt and to conclude about the alleged composition of a carbonatitic melt that is capable of crystallizing corundum. The experiments that were performed in this study provide a unique insight into the igneous formation of sapphires from carbonatitic melts, and into the behavior of sapphires upon the interaction of carbonatitic melt with silicic melt. The model proposed in this study for the first time explains the petrogenetic relationship between the sapphires and their host-rocks. In addition to the constraints on the sapphire petrogenesis, results from this study provide new insights into the magmatism in the SVF. Glass inclusions of nephelinitic and of carbonated silicate composition demonstrate that in the SVF, the differentiation of the SiO_2 undersaturated volcanic suite proceeded to more evolved compositions than it was implicated to date (e.g., Kolb et al., 2012), and that the mantle source of the alkaline mafic rocks from the SVF must have been enriched in CO_2, so that upon late stage differentiation, a carbonatitic melt could be expelled from the silicate melt.

CHAPTER 2: PETROLOGICAL AND GEO-CHEMICAL INVESTIGATIONS OF THE SIEBENGEBIRGE SAPPHIRES

2.1. GEOLOGICAL OVERVIEW

2.1.1. Central European Volcanic Province

The Central European Volcanic Province (CEVP) is a Cenozoic intra-continental volcanic belt north of the Alpine Orogen. The CEVP is a 200 to 300 km broad belt of volcanic fields that trends from the northern Rhône Depression in the south, to the North Sea in the north. Volcanic fields belonging to the CEVP are the Siebengebirge, Hocheifel, Westerwald, Vogelsberg, Rhön, Heldburg, Hessian Depression and the Urach-Hegau regions in Germany (Fig. 5), the Bohemian Massif in the Czech Republic, the Eger Rift System in the Czech Republic and Poland, the Pannonian Basin in Hungary, and the french Massif Central. Igneous activity in the CEVP lasted during the whole Cenozoic (Wilson and Downes, 1991). The petrogenetic processes that triggered volcanism in the CEVP, as well as the mantle source of the magma, are still in dispute. The geochemical resemblance of the volcanic rocks from the CEVP with Ocean Island Basalts (OIB) supports a deep asthenospheric/ plume like mantle source (e.g., Wörner

et al., 1986; Hoernle et al., 1995; Wedepohl and Baumann, 1999; Haase et al., 2004). Evidence for the existence of a finger-like mantle plume under the CEVP is given by seismic tomography studies that allowed the identification of thermal anomalies in the lower mantle (e.g., Granet et al., 1995; Goes et al., 1999; Ritter et al., 2001). Alternatively, volcanism in Central Europe is explained to be the consequence of the Alpine Orogeny. The Alpine Orogeny is a consequence of the collision of the Afican and Eurasian tectonic plates in the Cenozoic. As a result of this collision, the lithosphere below the Alps was depressed down to 200 km depth (Babuska et al., 1990). This alpine lithospheric depression is compensated by lithospheric thinning in the northern Mediterranean Sea and in Central Europe to depths as low as 50 km (Wedepohl et al., 1994), inducing melting as a consequence of adiabatic decompression (Illies et al., 1981; Illies and Baumann, 1982; Lippolt, 1982; Ahorner et al., 1983; Ziegler, 1992; Regenauer-Lieb, 1998). A significant uplift of the MOHO discontinuity is supported by probative geophysical data. Although the maximum crustal thinning is located at the northernmost part of the Northern Rhine Graben (Wilson and Patterson, 2001), this area is lacking extensive volcanism, arguing against extension alone to having caused volcanic activity in the CEVP.

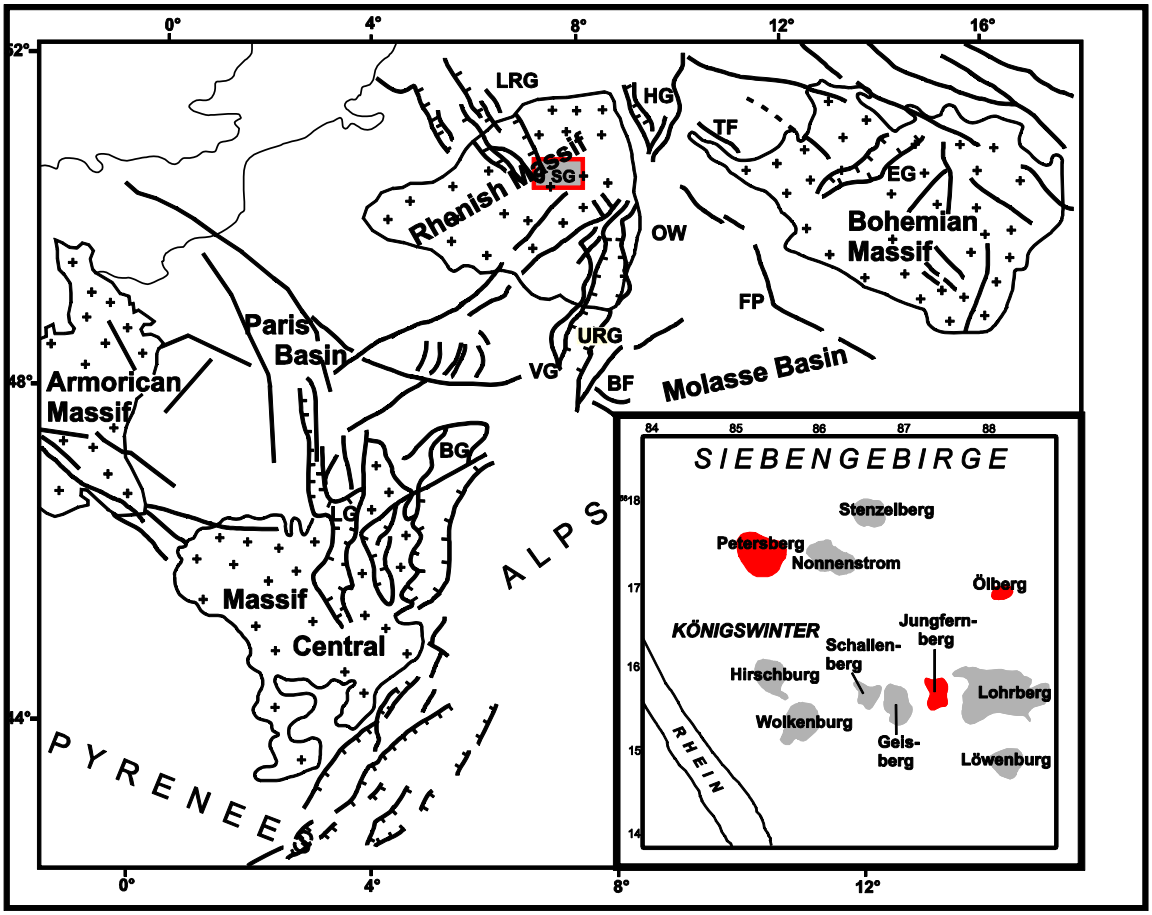

Figure 5: Location of the SVF within the European Cenozoic Rift System in the alpine foreland. Modified after Ziegler and Dèzes (2005). Cross pattern: Variscan Massifs; Black lines: Cenozoic faults. BF Black Forest, BG Bresse Graben, EG Eger Graben, FP Franconian Platform, HG Hessian grabens, LG Limagne Graben, LRG Lower Rhine (Roer Valley) Graben, SG Siebengebirge, TF Thuringian – Francian Schiefergebirge, URG Upper Rhine Graben, OW Odenwald, VG Vosges. The Siebengebirge overview map in the bottom right part is from the Geological Map Nordrhein Westfalen, 1:25000, Bl. 5309 Königswinter (1995); Krefeld. The main localities from which the Siebengebirge sapphires derived from are colored in red.

In addition to the causes of the tertiary volcanism in the CEVP, the mantle source is also highly disputed. It is still poorly understood whether the mantle source of the CEVP volcanics is asthenospheric (Wedepohl et al., 1994; Hegner et al., 1995; Jung et al., 2005), lithospheric (Blusztajn and Hart, 1989; Blusztajn and Hegner, 2002; Meyer et al., 2003), or both (e.g., Wilson and Downes, 1991; Jung and Hoernes, 2000; Wilson and Patterson, 2001; Bogaard and Wörner, 2003).

The main argument for a lithospheric source for the CEVP magmatism is provided by the osmium isotope systematics of melilitites from SW Germany that overlap with those of the lithosphere (Blusztajn and Hegner, 2002) and exceed those of the asthenospheric mantle. An asthenospheric source is supported by the striking geochemical resemblance between continental alkaline mafic rocks and Ocean Island Basalts (OIBs), in terms of the radiogenic isotope composition, mainly Sr, Nd, and Pb (e.g., Wedepohl et al., 1994), supporting a common mantle source for both rocks types and similar mantle dynamics controlling partial melting and melt extraction. Nevertheless, a broad range in the Sr, Nd, and Pb isotopic composition, as well as the enrichment of some basanites in Ti, Al, Sc, and V, measured by Wilson and Downes (1991) rather supports a combined source of primitive asthenospheric and of depleted lithospheric mantle material. Crustal contamination (e.g., Jung, 1999; Bogaard and Wörner, 2003, Haase et al., 2004, and Jung et al., 2006) during melt ascent, has been reported to have modified the composition of the primary melt making it even more difficult to determine the original mantle source/s.

2.1.2. Siebengebirge Volcanic Field

The Siebengebirge Volcanic Field (SVF) in western Germany forms part of the CEVP. It is located at the SE margin of the Lower Rhine Graben which is part of the Rhine Graben rift system that formed in Eocene to Oligocene times as a consequence of syn- to post-orogenic extension in the Alpine foreland (Ziegler, 1992). The NNE-SSW-trending Rhine Graben rift system transects the Rhenish Shield that is a Variscan tectonic block within the Rhenohercynian Zone and is being uplifted since Pliocene times (e.g., Illies et al., 1979; Oncken et al., 1999; Meyer and Stets, 2002). Mengel et al. (1991) and Prodehl et al. (1992) estimated a depth of the MOHO underneath the Rhenish Shield of 28 to 32 km. For the lilthosphere – asthenosphere boundary underneath the Rhenish Shield, Babuska and Plomerová (1992) estimated a depth of 60 km. In a more recent study,

Babuska and Plomerová (2006) estimated the lithosphere – asthenosphere boundary to be rather located at 90 km depth. The hercynian basement below the SVF consists of metabasites, orthogneisses, and of greenschist- to amphibolite-facies metapelites of the Mid German Crystalline Rise. The metamorphic rocks are overlain by Paleozoic and Cenozoic sediments and clays, sandstones, carbonates, and limestones (Mengel et al., 1991).

The total volcanic area of the SVF has a size of about 1500 km^2. The volcanic activity in the Siebengebirge occurred over several eruptional phases. This periodical volcanic activity resulted in the eruption of a very broad spectrum of SiO_2 saturated and SiO_2 undersaturated mafic and felsic melts that now outcrop in various locations around the SVF. Mafic rocks are basanites to alkali basalts; felsic rocks are latites to trachites as SiO_2 saturated suites and phonotephrites to tephriphonolites as SiO_2 undersaturated suites (Frechen and Vieten, 1970a,b; Kolb et al., 2012; Jung et al., 2012). The period of active volcanism in the SVF ranges from 30 Ma to 19 Ma (Todt & Lippolt, 1980; Vieten et al., 1988; Linthout et al., 2009; Przybyla, 2013) with the main magmatic activity culminating between 26 Ma and 24 Ma. Age determinations for the Siebengebirge volcanism are based on K/Ar radiometric dating of whole rocks and of sanidine and biotite mineral separates (Todt and Lippolt, 1980), as well as on whole rock Ar/Ar dating (Linthout, 2009) and on whole rock and sanidine Ar/Ar dating (Przybyla, 2013). These age data, supported by field evidence given by the relationship of intrusions, indicate that in the earliest stage of the Siebengebirge Volcanism, felsic melts were erupted and were then followed by intermediate lavas. In the latest stage of the Siebengebirge Volcanism, the alkaline mafic rocks were produced.

Alkaline basalts from the Siebengebirge are long known to host megacrystic sapphires (Laspeyres, 1900). They were first noticed by Nöggerath, (1827) and were then scientifically described by Lasaulx (1885), Dannenberg (1895), Zirkel (1903), Wildschrey (1911) and Brauns (1922). Until now, no effort has been made to investigate

the sapphires entrained in alkaline mafic rocks from the SVF with modern techniques and to identify possible genetic links to their host basalts

2.2. SAMPLES

2.2.1. Origin of samples and localities of their host rocks

Most of the sapphires studied in this work belong to the mineralogical collection of the Geological and Mineralogical department of the University of Bonn and were recovered in the early 20th century when the basalt occurrences (now protected) were still subject to quarrying. More sapphires were donated from local collectors, so that for many of these sapphires the exact localities in the Siebengebirge cannot be reconstructed with certainty. The principal localities in the Siebengebirge from which sapphires are reported are the Petersberg and Ölberg alkaline mafic rocks (Red marking in Fig. 5). Other known localities are the Jungfernberg, Heisterbacher Rott at the northern part of the Siebengebirge, and Unkel at the south-western extension of the Siebengebirge.

2.2.2. Petrographical description

Study objects are 11 sapphires with an anhedral to subhedral crystal shape and sizes of 5 to 20 mm. Colors vary from a milky pale-blue to a clear dark blue. A detailed petrographical description of the sapphires and of their host-rock locality is given in Tab. 2. Two sapphires (Fig. 6) have large brown to gray areas, distinguishing them macroscopically from the other samples. A graphical interpretation of the sapphire that is

shown in Fig. 6, is presented in Fig. 7. In contrast to many sapphires from basaltic placer deposits, the Siebengebirge sapphires are in-situ occurrences, and are thus still attached to their host basalt, allowing to study the relationship between the sapphires and the hosting basalt.

Table 2: Petrographical description of the Siebengebirge sapphires, and the host locality within the Siebengebirge.

sample	host-rock locality	color	reaction rim	inclusions
3	Jungfernberg	light-blue, milky	70 - 80 µm,	calcite, ilmenorutile, alkalifeldspar, spinel, apatite, ilmenite
15	Ölberg		40 - 100 µm	calcite
26	Ölberg	dark blue	50 - 100 µm, partly missing	calcite, plagioclase, alkalifeldspar, columbite, thorite, thorianite, apatite
KS21	Heisterbacher Rott	a) light blue, milky; b)dark blue, clear	10 - 50 µm, partly missing	-
ÖL25	Ölberg	light blue, milky	100 - 200 µm	calcite, ilmenorutile, ilmenite-pyrophanite
ÖL60	Ölberg	light blue, milky	100 - 150 µm, one area with 500 µm	plagioclase, spinel, calcite
ÖL61	Ölberg	dark blue, clear	ca. 100 µm	plagioclase
UN31	Unkel	light blue, milky and dark blue areas	40 - 100 µm	-
PE21	Petersberg	light blue, milky with gray area in the center	100 - 200 µm	Nb-rich microinclusions in reaction rim
PE25	Petersberg	light blue, milky with gray area in one edge	100 - 200 µm	alkalifeldspar, Nb-rich microinclusions in reaction rim
S52	Unknown	dark blue	10 - 300 µm	plagioclase, alkalifeldspar, calcite

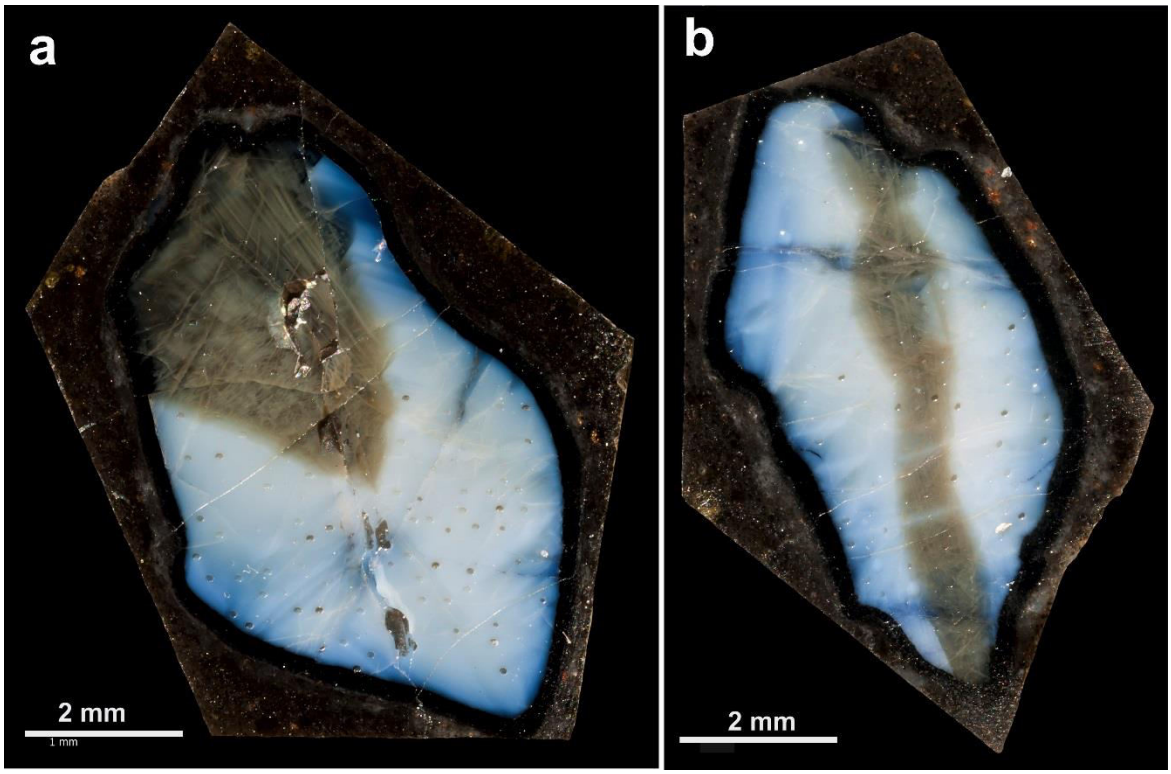

Figure 6: Photography of two Siebengebirge sapphires. a: Sample PE25, b: sample PE21. The sapphires have a pale milky blue color in the center and become more transparent and dark blue towards the rims. Both sapphires show brownish areas. At the interface with the basalt, the sapphires have visible black coronas. The basalt at the interface towards the corundum is lighter than the rest of the basalt.

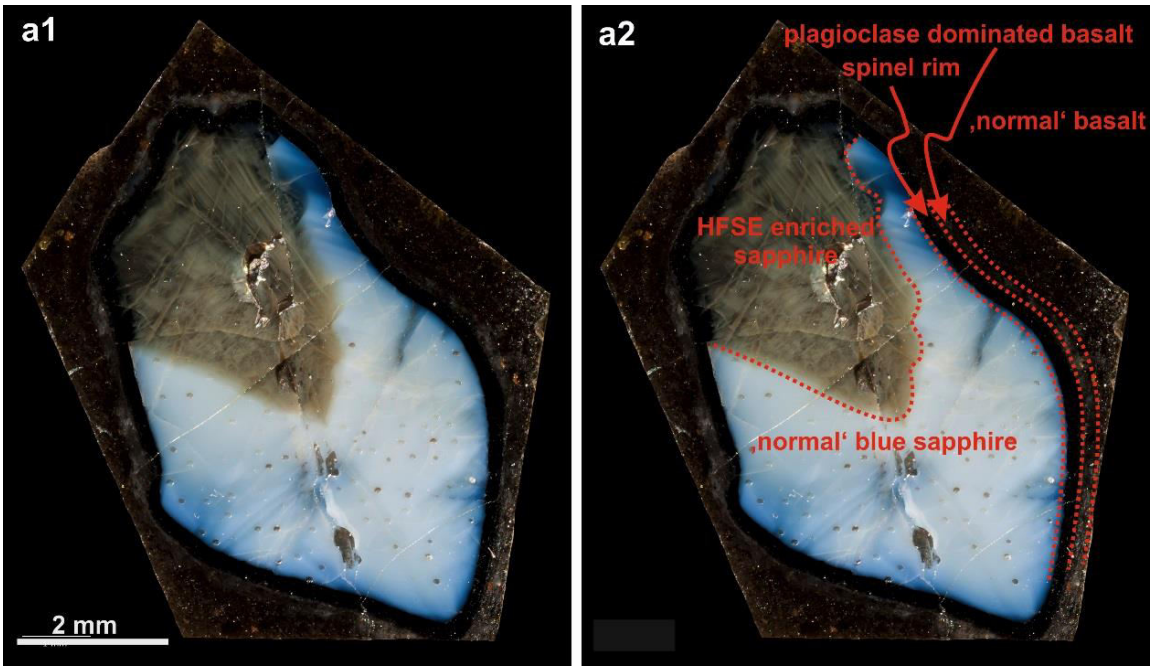

Figure 7: Graphical interpretation of Figure 6a. a1: Photograph of sapphire PE25. a2: Graphical interpretation of Figure 7a1. The brownish are is chemically characterized by a higher enrichment in the HFSE (Nb, Ta, Zr, and Hf) compared to the blue area. The transition from the brown towards the blue are is extremely sharp. The black rim surrounding the sapphires is spinel. The spinel rim is surrounded by a corona of plagioclase rich basalt that has about the same thickness as the spinel rim. The plagioclase enriched basaltic matrix is surrounded by 'normal' basaltic matrix constituted of plagioclase, pyroxene, and Ti-phases.

All sapphires show evidence for chemical disequilibrium with their host basalt. Many grains are rounded with resorbed edges, and all grains are rimmed by tens to hundreds of µm wide spinel coronas (Fig. 8a). The contact of sapphire with spinel is quite sharp, but as the basalt is approached, the spinel coronas become more ragged and more porous, and tend to disintegrate to discrete grains (Fig. 8a). Noticeably, the basalt in contact with the spinel corona is predominantly constituted by plagioclase. Pyroxene or Ti-phases are scarce in the close ambience of spinel (Fig. 8b, c) and only occur in further distances from the basalt-spinel interface. Figure 9 shows a representative graphical interpretation of the contact zone between the sapphire and the host-rock.

Mineral inclusions typically found exposed on the polished surfaces of the Siebengebirge sapphires are plagioclase and alkali feldspar, calcite, and Nb-Ta-Th-oxides and silicates. The spinel coronas are virtually free of inclusions. Only samples PE21 and PE25 show tiny micron-sized inclusions of Nb-Ta phases in their spinel rims (Fig. 8d). Many inclusions appear to be primary, i.e., were trapped during growth of the sapphires. They thus provide the opportunity to characterize the environment of sapphire crystallization. Other inclusions are located at cracks within the sapphire and may thus be regarded as secondary in origin.

Upon examination in transmitted light, most of the samples exhibit complex fluid inclusions that are either aligned along certain crystallographic orientations that are most likely healed secondary cracks, or occur randomly distributed without any preferred orientation.

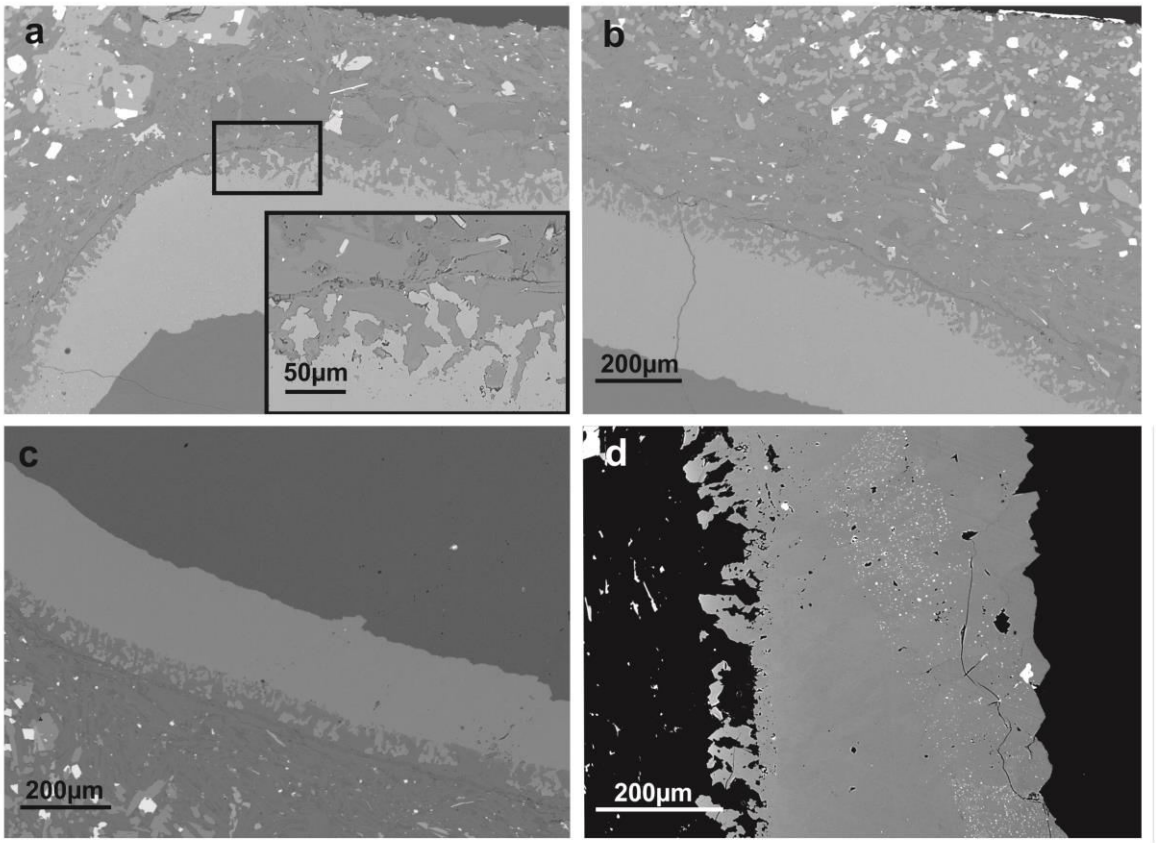

Figure 8: Backscattered electron images of Siebengebirge sapphires. a: spinel corona (light gray) surrounding the sapphire (dark gray). The close up shows the ragged contact from the spinel rim towards the basalt. b and c: Transition zone from sapphire to host basalt of sample PE21 (b) and PE25 (c). The contact sapphire (dark gray) – spinel (light gray) is sharp, whereas the contact from spinel to basalt is ragged and very diffuse. The contact zone of the basalt with the spinel is depleted of Fe-, Mg-, and Ti-phases. Only after a zone that is about the same thickness as the spinel corona, pyroxene and rutile crystallized from the basalt. d: Spinel corona of sapphire PE21. The corona has tiny Nb-Ta –phases (white dots) of a micrometer or less in size.

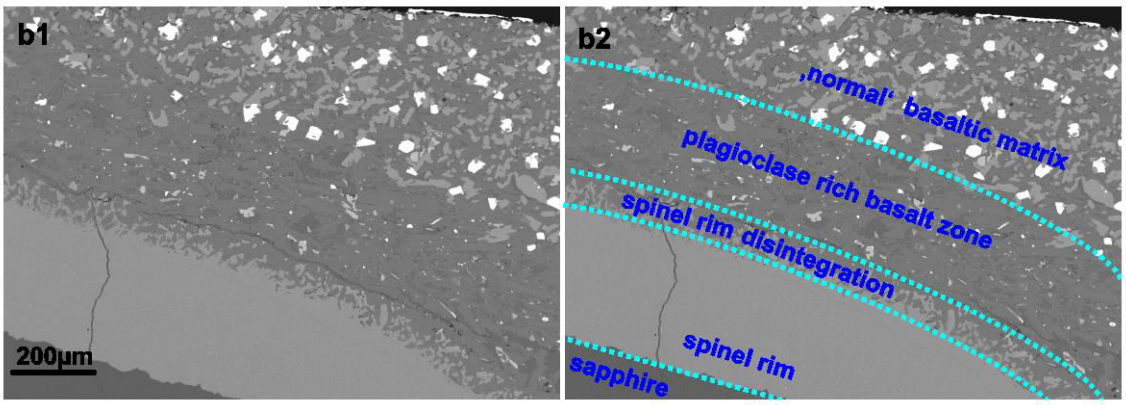

Figure 9: Graphical interpretation of Fig. 8b. B1: Backscattered electron image of the transition from the sapphire to the basaltic matrix. B2: Graphical interpretation of b1. The transition from the sapphire to the basalt follows a zonar structure. The interface of the sapphire to the spinel rim is well defined, whereas the transition zone from the spinel towards the basaltic melt occurs via a zone of disintegrated spinels that mingle in more or less equal fractions with the basaltic matrix. The basaltic matrix in direct contact with the spinel rim is constituted by almost pure plagioclase. Fe-Mg phases such as pyroxene are missing. The plagioclase rich zone has about the same thickness as the spinel rim. The plagioclase rich basaltic matrix is followed by the 'normal' basaltic matrix with abundant plagioclase, pyroxene, and Ti-phases.

2.3. ANALYTICAL METHODS

2.3.1. XRF

Some sapphires were still inside their host rocks, offering the opportunity to classify the basalts that carried them to the surface. After removal of visible alteration rims, around 100 g sample material was crushed and ground in an agate mill. Major elements were analyzed from fused lithium fluoride-based glass disks using a PANalytical Axios wavelength dispersive XRF.

2.3.2. EPMA

The sapphires, their reaction rims, and the mineral inclusions were analyzed for major and minor elements with a Jeol JXA 8900 electron microanalyzer equipped with a tungsten cathode. All measurements were performed at 15 kV acceleration voltage and

a probe current of 15 nA. Major elements were quantified on the Kα lines. Where possible, the trace elements Nb, Ce, Y, Ta, and Zr were quantified on the L lines, while Th, U, and Pb were quantified on the M lines. Synthetic and natural materials were used as standard reference materials. Matrix corrections were done online using the ZAF correction routine.

2.3.3. LA-ICP-MS

The trace elements were measured using a Resonetics Resolution M50E 193 nm laser ablation system coupled to a Thermo Scientific X Series II quadrupole inductively coupled plasma mass spectrometer (Q-ICP-MS). The laser was operated at a repetition rate of 15 Hz and a fluence of 7 J/cm². For all samples, 20 – 30 spots with a size of 100 µm were set, depending on grain size and homogeneity of the sapphire. Count rates were normalized using ^{27}Al as an internal standard. The NIST610 and NIST612 standard reference materials were used for calibration as external standards.

Monitored isotopes were ^{9}Be, ^{23}Na, ^{24}Mg, ^{25}Mg, ^{39}K, ^{47}Ti, ^{51}V, ^{52}Cr, ^{53}Cr, ^{55}Mn, ^{57}Fe, ^{66}Zn, ^{68}Zn, ^{69}Ga, ^{88}Sr, ^{89}Y, ^{90}Zr, ^{93}Nb, ^{118}Sn, ^{120}Sn, ^{178}Hf, ^{180}Hf, ^{181}Ta, ^{182}W, ^{184}W, ^{186}W, ^{232}Th, and ^{238}U.

Later, experiments were conducted to investigate the origin of the sapphires and the nature of the parental melts (See chapter 3 for experimental details). As there is striking evidence for the participation of a carbonatitic melt in the sapphire petrogenesis, some experiments were conducted in the silicate-carbonatite melt system. Due to the enrichment in the HFSE of the Siebengebirge sapphires compared to the Primitive Mantle, the experiments were doped with Nb, Ta, Zr, and Hf. To determine the partition coefficients of Nb, Ta, Zr, and Hf between silicate and carbonatite melt, as well as between silicate melt and nepheline, the isotopes ^{93}Nb, ^{181}Ta, ^{90}Zr, ^{91}Zr, ^{94}Zr, ^{178}Hf, ^{179}Hf,

and ^{180}Hf were monitored in the experimental products. As internal standards, ^{43}Ca and ^{29}Si were measured. Laser operation conditions were 15 Hz and ~ 5 J/cm², and a spot size of 58 µm.

2.3.4. Raman spectroscopy

The vibrational spectrum received from Raman spectroscopy is an exceptional method for identifying fluid or mineral phases that are trapped inside another mineral, or to distinguish between polymorphic minerals. In this study, Raman spectroscopy was used to identify the composition of fluid inclusions and their daughter minerals, to investigate the nature of completely entrained mineral inclusions, to distinguish between calcium carbonate polymorphs, and to analyze the fluid inclusions and their daughter minerals.

Raman spectra from mineral and from fluid inclusions were obtained using a confocal Horiba HR800 equipped with an Olympus BX41 optical microscope in 180° backscatter geometry. As excitation source, a Nd-YAG Laser (532.18 nm) was used. The laser beam was focused using a X 50 objectice lense. Spectra were accumulated with an exposure time of 30 s on each point with a laser power of 200 mW. The measurements were performed in the frequency range of 100 to 4000 cm^{-1}.

For the fluid inclusion study with Raman spectroscopy, the sapphires that were previously already mount in epoxy, were cut into ~ 500 micrometer thick sections that are transparent, allowing to study the mineral's interior with transmitted light to detect fluid inclusions that are completely entrained within the sapphires. Unfortunately, not all sapphires were suitable for this type of preparation, as the samples are still inside their host-rock so that they are not transparent and hence could not be regarded under transmitted light. In addition, some of the sapphires were extremely thin, so it was not possible to cut transparent thick sections of the samples without breaking them.

2.3.5. Transmission electron microscopy (TEM)

Sapphire PE25 was investigated with the Transmission Electron Microscope (TEM) at the GeoForschungsZentrum (GFZ) in Potsdam, Germany, in order to identify potential nanometer sized inclusions inside the sapphires. A thin electron-transparent foil (15 µm X 10 µm X 0.15 µm) was cut from the brownish area (Fig. 6a) from the polished sapphire by the focused ion beam technique (FIB). In a final step, the FIB-section was thinned to a thickness of 25 – 30 nm. The FIB technique is based on sputtering atoms from the target material by the bombardment with accelerated Ga ions. A detailed description of the principles of the FIB technique is given by Wirth (2004) and Wirth (2009). The section was subsequently analyzed with a FEI Tecnai G2 X-TwinTEM. The instrument is equipped with a Fishione high-angle annular dark field (HAADF) detector, an EDAX energy dispersive X-ray spectroscopic system (EDS) for the identification of the chemical composition from the excited characteristic X-rays of the sample, a Gatan Tridiem energy filter, and an electron energy loss spectrometer (EELS).

2.4. MINERAL CHEMISTRY

2.4.1. Host-rock composition

Except for sample S52 where the host-rock material was not sufficient for quantitative analysis, the composition of the sapphire host rocks could be determined via XRF analysis. Bulk compositions and CIPW norms of the host basalts are given in Table 3. In the total alkali vs. silica (TAS) diagram that is recommended by the IUGS Subcommission on the Systematics of Igneous Rocks for the chemical classification of

volcanic rocks (e.g., LeMaitre, 1984, 2002), the samples plot well above the line of SiO_2 undersaturation (Fig. 10). Most host rocks are alkali basalts. One sapphire is entrained in basanite and some samples lie in the field for trachybasalts (hawaiite). Compared to the whole compositional range of volcanic rocks from the SVF (e.g., Frechen & Vieten, 1970a, b; Vieten, 1983; Vieten et al., 1988; Kolb et al., 2012; Jung et al., 2012), the samples that host the sapphire megacrysts investigated in this study belong to the most primitive rocks. Sapphires are not known to occur in volcanic rocks with more than 47.6 wt.% SiO_2.

For the calculation of CIPW-normative minerals, the Fe^{3+}/Fe_{tot} ratio was assumed to be 0.1. The host basalts are nepheline-normative and are predominantly alkali basalts. In the following work, when referring to the sapphire host rocks, the terms 'alkaline mafic rocks' or 'alkali basalts' are used for simplification. Of course, these terms include the basanites and trachybasalts as host rocks.

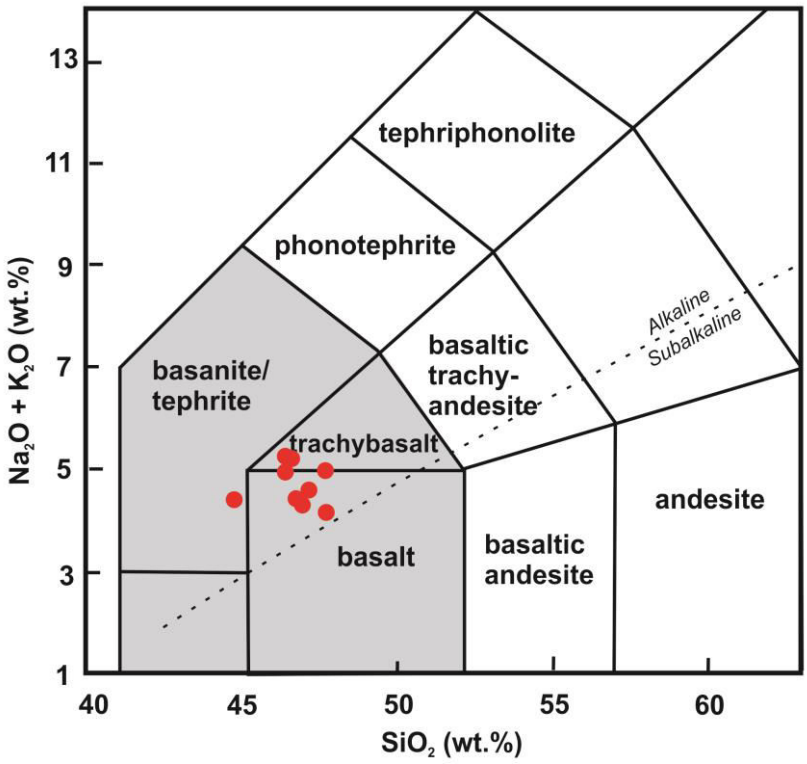

Figure 10: Position of the host rocks of the Siebengebirge sapphires in the Total Alkali vs. Silica (TAS) diagram after Le Maitre et al., 1984; 2002. The compositional range between the host rocks is very small. Host rocks are predominantly alkali basalts, two samples plot in the basanite field, and some samples are trachybasalts.

Main minerals comprising the host basalts are diopside and plagioclase. Some samples contain rare alkali feldspar (samples 3, 15, ÖL25, and PE25) or olivine (samples 3, ÖL60, ÖL61, S52, and UN31). A common accessory phase in all host rocks is pseudobrookite (Fe_2TiO_5). Olivine ranges in composition from Fo_{69} to Fo_{80}. Plagioclase is dominantly labradorite (An_{53-63}) and occasionally andesine (An_{53-48}). The composition of the main minerals comprising the host basalt is given in Appendix A).

Table 3: XRF analyses of the host rocks of the Siebengebirge sapphires. The CIPW norm was calculated on the assumption that the Fe^{3+}/Fe_{tot} ratio of the basalt is 0.1.

	ÖL 61	ÖL 60	ÖL 25	26	15	3	KS 21	UN 31	PE 25	PE 21
SiO_2	46.0	46.3	46.9	45.4	46.1	43.7	46.5	46.2	46.6	46.2
Al_2O_3	14.2	14.3	14.2	13.8	14.3	12.6	14.8	14.2	14.0	13.9
Fe_2O_3	11.1	11.4	11.2	11.3	11.4	12.0	11.5	11.4	12.4	12.4
MnO	0.18	0.18	0.18	0.20	0.18	0.19	0.19	0.18	0.19	0.20
MgO	9.24	9.07	8.68	9.72	9.41	12.1	8.01	9.27	8.92	9.09
CaO	9.80	9.87	10.1	10.6	9.84	10.7	9.62	9.87	9.40	9.32
Na_2O	3.66	3.80	3.60	3.03	3.35	3.10	2.75	3.58	3.26	3.05
K_2O	1.43	1.44	1.40	1.37	1.38	1.21	1.37	1.35	1.19	1.15
TiO_2	2.23	2.24	2.25	2.21	2.23	2.28	2.35	2.26	2.20	2.19
P_2O_5	0.45	0.45	0.46	0.52	0.46	0.55	0.41	0.46	0.44	0.45
SO_3	0.07	0.18	0.13	0.10	0.17	0.16	0.15	0.15	0.19	0.17
L.O.I.	0.47	0.53	0.16	0.62	0.73	0.45	1.34	0.63	0.90	0.77
Sum	98.8	99.8	99.3	98.9	99.6	99.0	99.0	99.6	99.7	98.9
Rock type	Hawaiite	Hawaiite	Hawaiite	Alkali Basalt	Alkali Basalt	Basanite	Alkali Basalt	Alkali Basalt	Alkali Basalt	Alkali Basalt
CIPW Norm										
plagioclase	34.7	34.5	37.4	34.7	37.9	25.2	48.1	34.5	42.9	44.2
orthoclase	8.69	8.69	8.45	8.33	8.33	7.33	8.39	8.16	7.21	6.97
nepheline	8.4	8.49	6.54	6.46	5.9	10.03	0.21	7.08	2.82	1.83
diopside	22.8	22.9	23.4	24.1	21.0	26.7	17.4	22.2	19.2	18.3
olivine	18.2	18.0	16.9	19.0	19.4	22.1	18.4	18.7	20.3	21.1
ilmenite	4.35	4.33	4.35	4.31	4.33	4.44	4.62	4.39	4.27	4.29
magnetite	1.65	1.68	1.65	1.68	1.70	1.78	1.73	1.68	1.84	1.86
apatite	1.07	1.07	1.09	1.23	1.09	1.32	0.97	1.09	1.04	1.09
Na_2SO_4	0.12	0.32	0.23	0.18	0.3	0.3	0.28	0.27	0.35	0.32

2.4.2. Sapphire major and trace element composition

The Siebengebirge sapphires are almost pure Al_2O_3 with Fe and Ti as main chromophores. The major and trace element composition of the sapphires, as well as the major element composition of the spinel coronas, are listed in Table 4. A complete compilation of all single spot analyses is given in Appendix B. Most sapphires are intrinsically inhomogeneous in terms of trace element abundances and ratios. Compared to Primitive Mantle (PM) abundances (McDonough and Sun, 1995), some sapphires are locally up to five orders of magnitude enriched in Ta, up to four magnitudes in Nb and Th, and up to three in W.

Notably, the highest Nb and Ta concentrations are measured in the gray colored zones of the sapphires PE21 and PE25 shown in Fig. 2, indicating that next to Fe^{2+} and Ti^{4+}, niobium and tantalum act as further chromophores in the Siebengebirge sapphires. Except for samples PE21 and PE25 which are those that show the highest Nb and Ta enrichment, all samples are depleted in Zr and Hf relative to PM values. All sapphires have strongly subchondritic Nb/Ta and Zr/Hf ratios with CI normalized $(Nb/Ta)_N$ of 0.32 ($2\sigma = 0.19$) and $(Zr/Hf)_N$ of 0.26 ± 0.17. Values for CI normalization are taken from Münker et al. (2003).

Table 4: Main element (EPMA) and trace element (LA-ICP-MS) composition of the Siebengebirge sapphires and the spinel coronas. The Nb/Ta and the Zr/Hf ratios are normalized to CI chondrite values (Münker et al., 2003).

	3		15		26		PE21		PE25		ÖL25	
	corundum	**spinel**	**corundum**	**spinel**	**corundum**	**Spinel**	**Corundum**	**Spinel**	**corundum**	**spinel**	**corundum**	**spinel**
wt.%												
MgO	bdl	16.4	0.01	16.1	bdl	15.8	bdl	14.2	0.01	14.1	bdl	15.2
Na_2O	bdl	bdl	0.01	0.02	0.01	0.01	0.01	bdl	0.01	0.02	bdl	bdl
FeO	1.17	16.8	2.02	18.5	0.87	18.9	0.86	20.7	0.92	21.3	1.57	20.6
K_2O	n.d.	bdl	bdl	0.01	0.01	n.d.	0.01	0.01	0.01	0.01	bdl	n.a.
TiO_2	0.10	0.11	0.13	0.09	0.12	0.07	0.75	0.27	0.25	0.15	0.11	0.12
SiO_2	0.02	0.03	0.02	0.1	0.02	0.02	0.02	0.01	0.02	0.05	n.a.	bdl
Al_2O_3	97.6	65.4	98.1	65.6	99.5	65.6	98.1	63.7	99.4	65.1	99.4	65.5
MnO	0.01	0.27	0.01	0.28	0.02	0.3	0.01	0.26	0.02	0.3	0.01	0.33
CaO	bdl	0.02	bdl	0.02	0.01	0.01	0.01	0.03	0.01	0.02	bdl	bdl
Cr_2O_3	bdl	0.03	bdl	0.02	bdl	0.01	n.d.	0.02	0.02	0.02	0.01	0.01
Total	98.9	99.0	100.3	100.6	100.6	100.7	99.8	99.2	100.7	101.0	101.1	101.7
n	3	4	3	5	3	7	3	5	3	2	20	10
Spinel		63		60		60		56		54		57
Hercynite		37		40		40		54		56		43
ppm	(*n* = 32)		(*n* = 30)		(*n* = 31)		(*n* = 30)		(*n* = 36)		(*n* = 30)	
Be	0.06 - 2.3		0.06 - 7		0.1 - 2		bdl - 10		0.7 - 11		bdl - 2	
Na	15 - 198		4 - 144		8 - 373		bdl - 79		bdl - 149		bdl - 359	
Mg	22 - 10803		39 - 150		5 - 253		10 - 34		13 - 243		7 - 90	
K	6 - 94		10 - 1152		12 - 283		bdl - 52		bdl - 109		bdl - 222	
Ti	158 - 2880		171 - 1182		78 - 1292		1045 - 6231		876 - 6226		76 - 5154	
V	8 - 15		7 - 17		2 - 12		13 - 37		12 - 29		5 - 19	
Cr	bdl		1 - 15		2 - 8		bdl - 20		bdl - 21		bdl - 2	
Mn	1.2 - 212		2 - 29		4 - 92		bdl - 196		bdl - 5		bdl - 49	
Fe	5559 - 18295		8565 - 14958		2967 - 16746		3301 - 6693		3853 - 6168		3177 - 12122	
Zn	1.9 - 212		2 - 10		2 - 9		bdl - 5		bdl - 7		bdl - 10	
Ga	127 - 238		91 - 138		149 - 256		113 - 193		116 - 188		87 - 147	
Sr	bdl		bdl		bdl		bdl - 0.2		bdl - 0.2		bdl	
Y	bdl		bdl		bdl		bdl - 0.5		bdl - 0.5		bdl - 0.2	
Zr	0.1 - 1.94		bdl		bdl		0.4 - 22		0.3 - 22		bdl - 0.6	
Nb	0.75 - 706		0.2 - 57		0.5 - 710		3 - 3998		12 - 2771		0.6 - 96	
Sn	0.13 - 9		0.1 - 1.8		0.1 - 2		2 - 21		0.4 - 14		0.1 - 2	
Ta	0.43 - 362		bdl - 26.4		0.1 - 25		4 - 1699		8 - 1011		bdl - 46	
ppb												
Hf	10 - 600		10 - 70		10 - 130		113 - 4825		33 - 4085		bdl - 0.1	
W	10 - 290		10 - 130		10 - 560		995 - 41 (ppm)		117 - 23 (ppm)		bdl - 750	
Th	10 - 7030		10 - 850		bdl - 890		1 - 166 (ppm)		0.6 - 226 (ppm)		10 - 5310	
U	bdl - 10		bdl - 200		bdl - 470		bdl - 419		bdl - 0.6		bdl - 120	
	ratios	**2 σ**	**ratios**	**2 σ**	**ratios**	**2 σ**	**ratios**	**2 σ**	**ratios**	**2 σ**	**ratios**	**2 σ**
Nb/Ta	1.6	1.5	4.1	10.0	1.9	2.0	2.3	1.0	2.4	0.9	2.1	2.0
$(Nb/Ta)_N$	0.09	0.08	0.21	0.55	0.24	1.22	0.13	0.06	0.14	0.05	**0.17**	0.42
Zr/Hf	3.4	2.0	-	-	-	-	4.6	2.3	5.0	2.5	6.1	7.6
$(Zr/Hf)_N$	0.04	0.10	-	-	-	-	0.13	0.06	0.14	0.14	0.07	0.15
Ga/Mg	3.6	4.1	1.5	0.8	17.1	16.2	5.8	3.3	6.6	4.1	6.3	7.9

Table 4 (continued): Main element (EPMA) and trace element (LA-ICP-MS) composition of the Siebengebirge sapphires and the spinel coronas. The Nb/Ta and the Zr/Hf ratios are normalized to CI chondrite values (Münker et al., 2003).

	ÖL60		ÖL61		KS21		UN31		S52	
	corundum	**spinel**	**corundum**	**spinel**	**corundum**	**spinel**	**corundum**	**spinel**	**corundum**	**spinel**
wt.%										
MgO	bdl	16.7	0.01	16.1	bdl	14.2	0.01	15.6	0.01	15.9
Na_2O	0.03	0.01	0.01	0.01	0.02	bdl	bdl	0.01	bdl	0.02
FeO	0.43	17.8	1.31	17.0	1.52	21.1	1.46	18.8	1.67	18.2
K_2O	0.01	bdl	0.01	bdl	bdl	bdl	bdl	bdl	0.01	n.d.
TiO_2	0.06	0.08	0.03	0.1	0.18	0.23	0.2	0.14	0.1	0.08
SiO_2	0.02	0.02	0.02	0.01	0.01	0.02	0.01	0.01	0.02	0.02
Al_2O_3	99.7	65.4	97.8	64.7	98.6	64.8	98.2	65.0	97.8	65.1
MnO	bdl	0.24	0.02	0.21	0.01	0.27	bdl	0.26	bdl	0.28
CaO	0.01	0.01	0.01	0.01	0.02	0.04	0.01	0.01	0.01	0.02
Cr_2O_3	0.02	0.01	0.01	0.01	0.01	0.01	n.d.	n.d.	0.01	0.01
Total	100.2	100.3	99.2	98.1	100.4	100.6	99.9	99.8	99.7	99.6
n	3	5	2	3	2	3	3	4	3	5
Spinel		64		63		55		60		61
Hercynite		36		37		45		40		39
ppm	(*n* = 16)		(*n* = 30)		(*n* = 32)		(*n* = 30)		(*n* = 31)	
Be	0.3 - 26		bdl - 0.7		bdl - 3		bdl - 1		bdl - 0.8	
Na	8 - 1007		bdl - 469		bdl - 144		bdl - 60		bdl - 1644	
Mg	2 - 860		10 - 45		4 - 39		61 - 174		42 - 152	
K	14 - 39		bdl - 732		bdl		bdl		bdl - 427	
Ti	60 - 659		75 - 1205		158 - 1316		641 - 2149		150 - 490	
V	2 - 12		6 - 10		3 - 15		28 - 66		6 - 12	
Cr	0.8 - 2		bdl - 4		bdl - 2		bdl - 22		bdl - 5	
Mn	3 - 18		bdl - 10		1 - 13		bdl - 3.7		bdl - 33	
Fe	1875 - 8549		4598 - 10728		4599 - 15967		6545 - 12701		6519 - 10434	
Zn	2 - 11		2 - 14		bdl - 714		2 -11		bdl - 5	
Ga	135 - 210		107 - 167		135 - 252		133 - 205		48 - 90	
Sr	bdl		bdl - 8		bdl		bdl		bdl - 11	
Y	bdl		bdl		bdl		bdl		bdl - 4	
Zr	bdl		bdl - 0.6		bdl - 4		bdl - 3		bdl - 1	
Nb	0.3 - 814		bdl - 9		bdl - 806		bdl - 748		bdl - 18	
Sn	bdl - 10		bdl - 0.6		0.2 - 20		0.3 - 9		bdl - 0.1	
Ta	0.2 - 370		0.1 - 4		0.03 - 342		0.1 - 169		bdl - 1992	
ppb										
Hf	bdl - 200		bdl - 35		bdl - 600		bdl - 552		bdl - 14	
W	bdl - 600		bdl - 376		bdl - 1735		bdl - 1770		bdl - 388	
Th	10 - 9960		bdl - 74		bdl - 14 (ppm)		bdl - 21.3 (ppm)		bdl - 3264	
U	bdl - 20		bdl - 24		bdl - 20		bdl - 40		bdl - 741	
	ratios	**2 σ**	**ratios**	**2 σ**	**ratios**	**2 σ**	**ratios**	**2 σ**	**ratios**	**2 σ**
Nb/Ta	1.1	3.6	2.1	5.0	2.3	2.3	3.1	3.7	44.7	66.9
$(Nb/Ta)_N$	1.83	3.63	0.12	0.28	0.11	0.20	0.15	0.23	1.39	6.11
Zr/Hf	-	-	-	-	5.7	4.3	-	-	-	-
$(Zr/Hf)_N$	-	-	-	-	0.15	0.16	-	-	-	-
Ga/Mg	23.4	57.8	1.3	2.0	16.0	31.4	1.6	0.7	1.0	0.3

The high variability in the sapphires Nb/Ta and Zr/Hf ratios are probably analytical artifacts, that becomes obvious when plotting the Nb/Ta ratio versus total Nb (ppm) and Zr/Hf ratio versus total Zr (ppm). These plots demonstrate clearly that the spread in the Nb/Ta and Zr/Hf ratios is larger at lower element concentrations where the detection limit is being approached (Fig. 11). At higher concentrations, the Nb/Ta ratio is approaching a value of ~ 2.5, probably reflecting the true Nb/Ta ratio in the sapphires. A Nb/Ta ratio of 2.5 corresponds to $(Nb/Ta)_N$ of 0.13. The same trend is less distinctive, but still recognizable for the Zr/Hf ratios. This ratio is settling at values of ~ 4.5 for high Zr concentrations, corresponding to $(Zr/Hf)_N$ of 0.13. This implies that although Nb/Ta and Zr/Hf ratios of the Siebengebirge sapphires are strongly subchondritic, no fractionation of Nb and Ta from Zr and Hf occurred during sapphire crystallization.

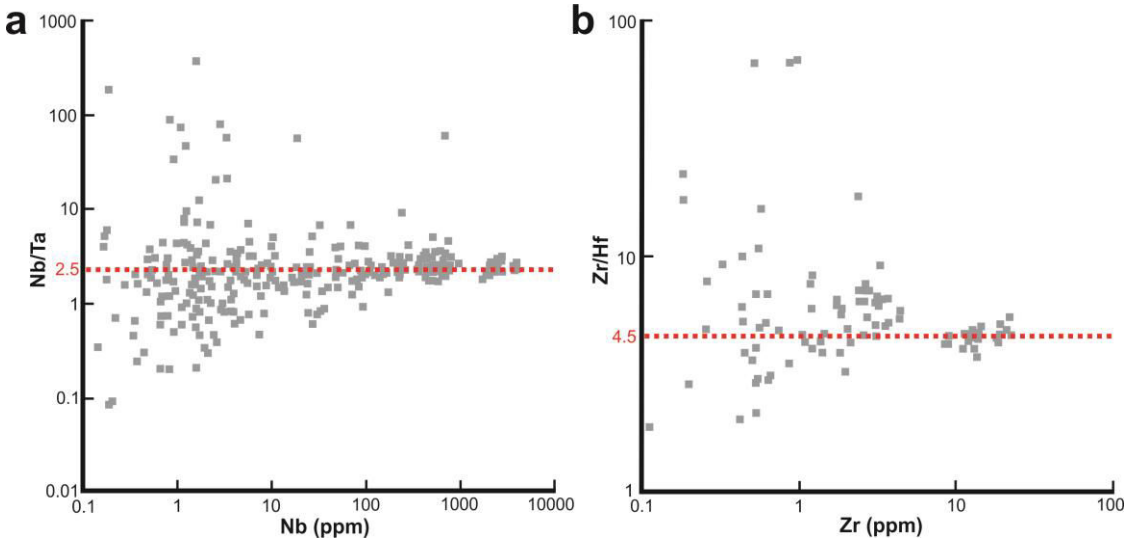

Figure 11: a: Nb/Ta vs. Nb (ppm) and b: Zr/Hf vs. Zr (ppm) plots. The higher the Nb, or the Zr concentrations are, the closer the Nb/Ta and the Zr/Hf ratios converge towards a specific value of 2.5 for the Nb/Ta ratio, and 4.5 for the Zr/Hf ratio, indicating that the high variability in the two element ratios is an analytical artifact reflecting the loss of precision on approach to the detection limit.

In all samples, the elements Nb, Ta, Hf, W, and to a minor extent Sn and Be are positively correlated (correlation coefficient $R \geq 0.85$). The elements Ga, Ti, V, Fe, Mg, and Zn are apparently uncorrelated in most samples. A complete list of correlation coefficients for the relevant trace elements is given in Appendix C.

In the Introductory chapter, discrimination diagrams to distinguish between corundum of magmatic and of metamorphic origin basing on their Ga, Mg, Ti, and Fe concentrations (Peucat et al., 2007) were introduced. In terms of their Ga/Mg ratio and the total Fe concentration, the Siebengebirge sapphires can be divided into two different groups: (I) Sapphires with low Ga/Mg ratios and high Fe_{tot}, and (II) sapphires with high Ga/Mg ratios and lower Fe_{tot}. In the Mg – Fe – Ti ternary diagram that has been proposed by Peucat et al. (2007) to distinguish sapphires of metamorphic from those of magmatic origins, the sapphires of group I plot in the field for metamorphic sapphires, whereas those of group II plot in the field for magmatic sapphires (Fig. 12).

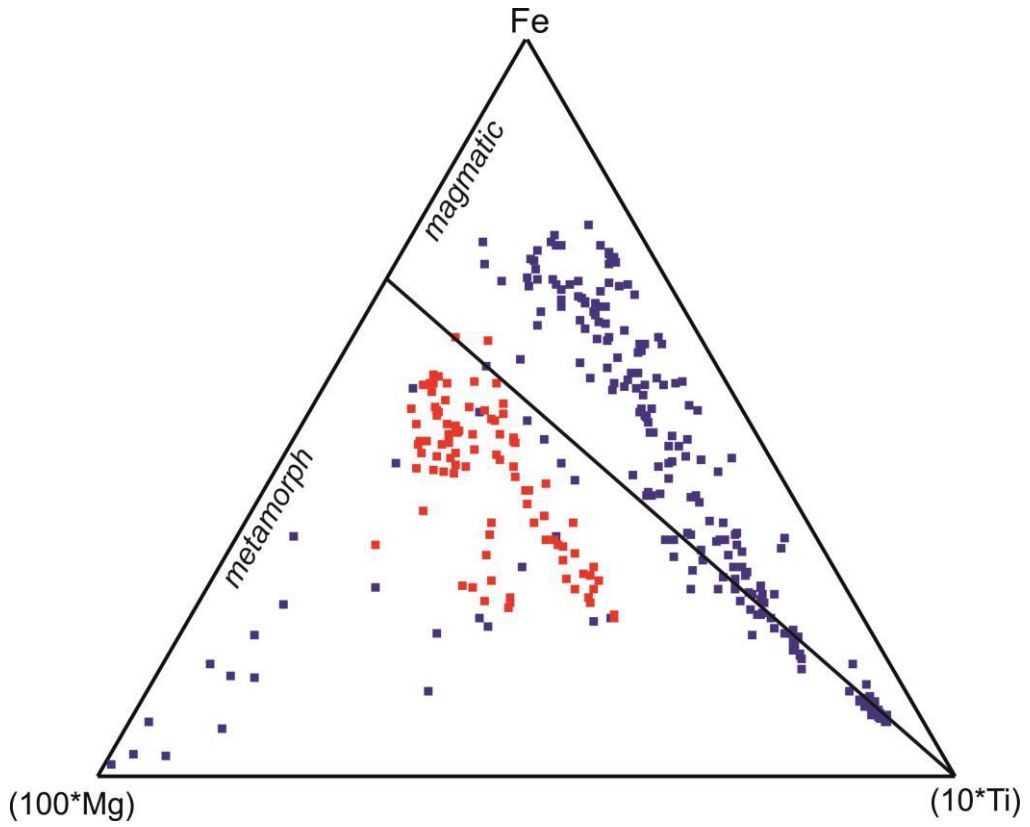

Figure 12: Fe-Mg-Ti discrimination diagram for the Siebengebirge sapphires (after Peucat et al., 2007). Some sapphires (Group II: blue squares) plot in the field of magmatic sapphires, and others (Group I: red squares) plot in the field for metamorphic sapphires.

The same distribution along metamorphic/magmatic fields is given for the Ga/Mg vs. Fe_{tot} distribution (Peucat et al., 2007), only that the Siebengebirge sapphires have higher

total Fe concentrations than the reference sapphires used by Peucat et al. (2007) to confine the fields for the magmatic and the metamorphic sapphires (Fig. 13). The strong variability of the Ga/Mg ratio in our samples that is ranging from ~0.01 up to 100, is largely controlled by Mg that is strongly negative correlated with the Ga/Mg ratio (Fig. 14a). The influence of Ga on the Ga/Mg ratio is minor (Fig. 14b). The dominant role of Mg as the element controlling the sapphires' Ga/Mg ratios, strongly suggests that the high Ga/Mg scatter is not caused by metamorphism, as the decrease in the Ga/Al, and thus in the Ga/Mg ratio in metamorphic sapphires is thought to be caused by the extraction of Ga from the metamorphic rocks by F-rich fluids (Wahlen et al., 1987). Hence, it would be expected that Ga rather than Mg controls the Ga/Mg ratio in the sapphires. It is thus extremely unlikely that the sapphires form a polygenetic suite of magmatic and of metamorphic origin. Evidence given by the mineral inclusion suite rather supports a magmatic origin for all sapphires from the SVF, regardless of where they plot in the discrimination diagrams.

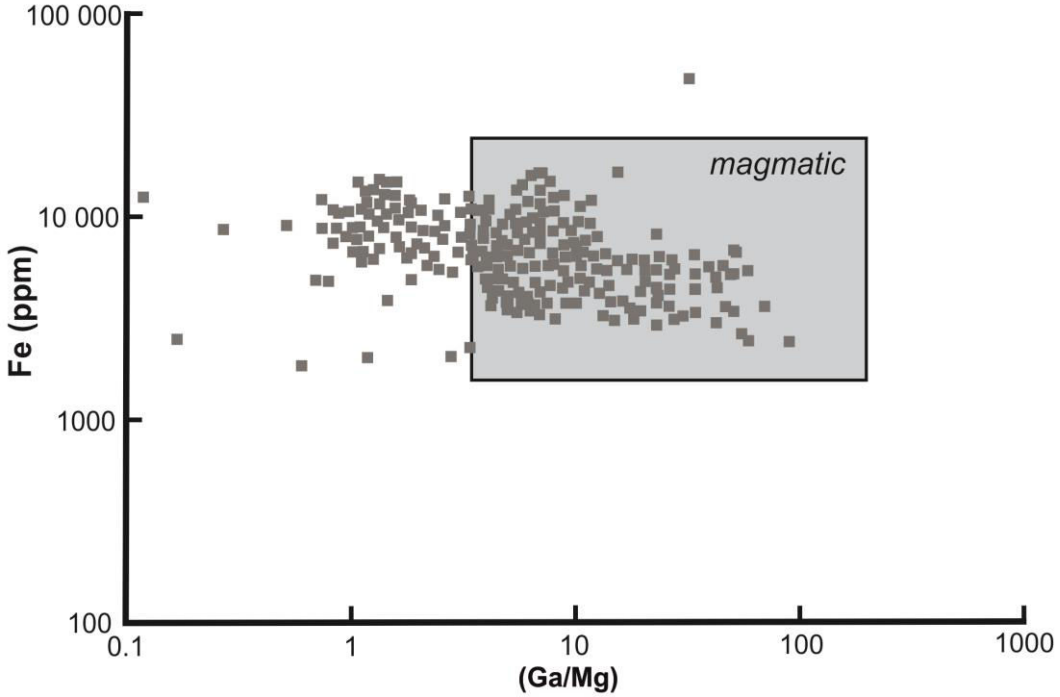

Figure 13: The Ga/Mg vs. Fe_{total} discrimination diagram for the Siebengebirge sapphires (after Peucat et al., 2007). Most analyses plot in the field for magmatic sapphires. Some samples have much lower Ga/Mg ratios defined for magmatic sapphires, though the Fe concentration is the same as for the magmatic sapphire field.

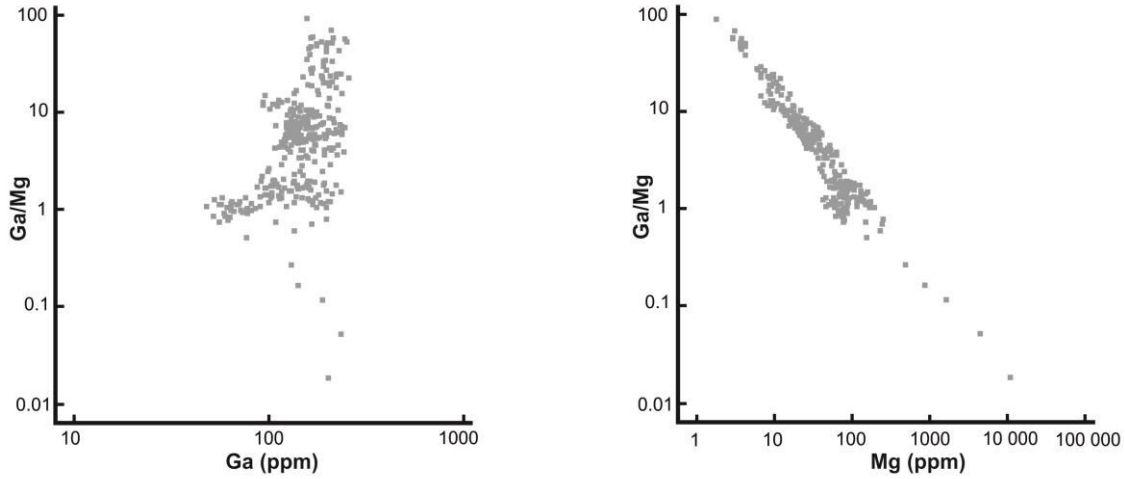

Figure 14: a) Ga/Mg vs. Ga (ppm) and b) Ga/Mg vs. Mg (ppm) plots. The effect of Ga on the Ga/Mg ratio is low, whereas the total Mg content in the sapphires is highly correlated with the Ga/Mg ratio, indicating that the strong variability of the Ga/Mg ratio in the Siebengebirge sapphires is controlled by changes in the Mg concentration, and largely unaffected by changes in the Ga content.

2.4.3. Mineral inclusions

The Siebengebirge sapphires have two kinds of mineral inclusions: Primary and secondary inclusions. Primary inclusions are trapped during crystal growth of their host minerals and are therefore completely entrained in the host phase, not located along visible cracks. These primary - or syngenetic – mineral inclusions have a high potential for providing important information about the melt composition of the parental magma of the host mineral, as they are potential samples of the parental magma. Secondary mineral inclusions are those that form along healed cracks that develop during crystal growth. In this case, the inclusions are still derived from the same parental melt as the host mineral. Secondary inclusions may also be trapped during late-stage magmatic evolution in which case the inclusion would not be a sample of the parental melt. These secondary inclusions are located at visible cracks in the host minerals.

In addition to providing information about the parental melt composition, U-bearing primary inclusions such as columbite have a potential for dating the event of crystallization, and thus on providing information about the temporal relationship between sapphire growth and basaltic

volcanism, as the age of basaltic volcanism in the SVF is well constrained (Todt & Lippolt, 1980; Vieten et al., 1988; Linthout et al., 2009; Przybyla, 2013).

The Siebengebirge sapphires contain a broad spectrum of mineral inclusions such as silicates, carbonates, and Nb, Ta, and Th phases. While some sapphires are virtually free of inclusions, other samples contain a high number of mineral inclusions covering a broad compositional spectrum. Notably, there is no correlation between the geochemical group of the sapphires, i.e., the Ga/Mg vs. total Fe ratio, and the mineral inclusion suite.

In this study, special attention was paid to the carbonate inclusions, as carbonate inclusions have only been reported – but not further described - for sapphires associated with alkaline basaltic volcanism from the Bo Phloi gemfield in Kanchanaburi, western Thailand (Khamloet et al., 2014). They are thus very rare for sapphires from magmatic secondary deposits and highly characteristic for the Siebengebirge sapphires.

Silicates

Silicate inclusions are potassic feldspar and plagioclase. The composition of the feldspar inclusions in the Siebengebirge sapphires is given in Table 5. In ÖL25, feldspar is associated with calcite and is either located next to it or forming a thin rim around it (Fig. 15a). Feldspar in sample 26 is commonly located in vesicles along cracks within sapphire and is associated with alteration products as clay minerals and zeolites. These are presumably secondary inclusions. Frequently, vesicular calcium carbonate is entrained in secondary alkalifeldspar (Fig. 15b). These spherular calcium carbonate inclusions will be described in the section of the carbonate inclusions in more detail. A plagioclase inclusion in ÖL60 is intensively altered to zeolite, and is partly rimmed by spinel (Fig. 15c). The fact that only part of the inclusion is rimmed by spinel rules out a

spinel-formation due to reaction with the hosting sapphire at magmatic temperatures. Sample ÖL61 has one xenomorphic plagioclase inclusion.

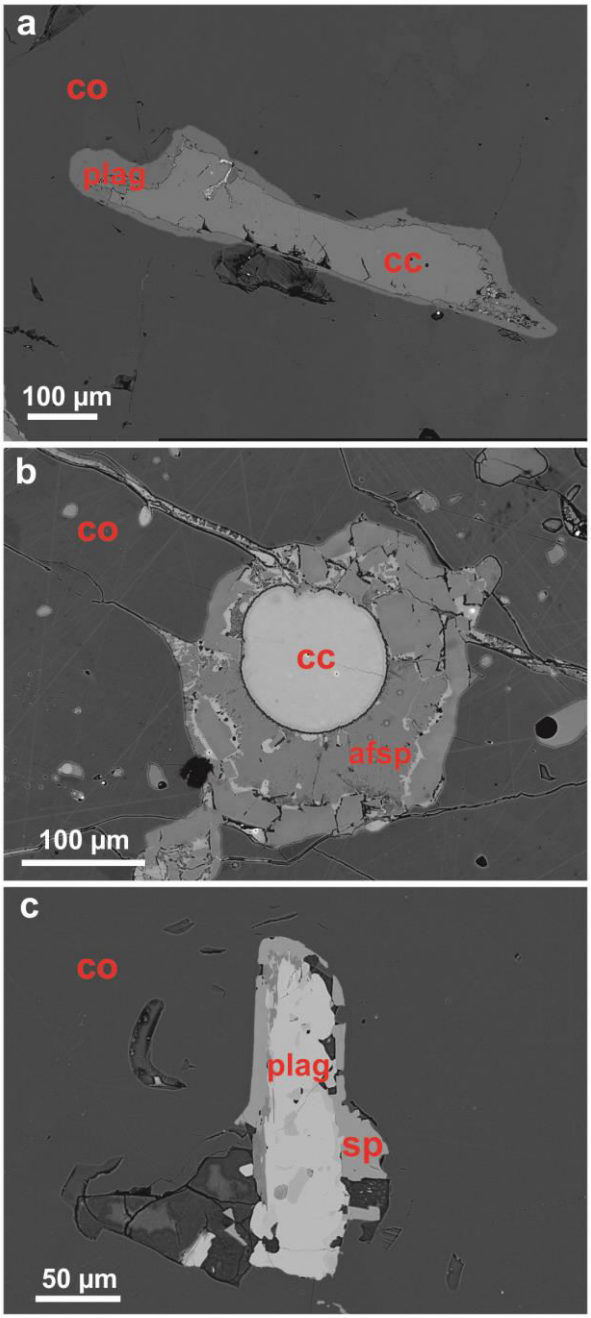

Figure 15: Composite silicate – carbonate inclusions in Siebengebirge sapphires. a: carbonate inclusion rimmed by plagioclase in sample ÖL25. b: Large secondary alkali feldspar inclusion with a globular carbonate inclusion in sample 26. c: plagioclase inclusion rimmed by spinel in sample ÖL60.

Table 5: Composition of feldspar inclusions in the Siebengebirge sapphires. Often, feldspar inclusions are inhomogeneous and consist of alkaline feldspar and plagioclase (compositions a and b in one mineral grain correspond to the composition of coexistent alkali feldspar and plagioclase).

	1a	1b	2a	2b	3	4a	4b	5	6	7	1a	1b	2	3	1	1
SiO_2	60.9	59.8	59.5	58.2	59.2	57.4	58.1	55.8	59.2	59.2	52.9	62.6	49.5	55.5	52.3	58.7
TiO_2	0.05	n.d.	0.29	0.21	0.26	0.24	0.48	0.26	0.01	0.01	0.31	0.16	0.33	0.09	0.03	n.d.
Al_2O_3	24.9	25.1	27.0	26.7	27.2	27.4	24.5	29.0	27.0	27.1	31.0	21.1	33.5	29.2	32.3	25.5
FeO	0.50	0.83	0.89	0.06	0.11	0.17	1.20	0.10	0.06	0.02	0.12	0.03	0.31	0.14	0.22	0.06
MnO	0.08	0.10	0.32	0.01	0.05	0.11	0.10	0.03	0.01	n.d.	0.04	0.02	0.02	0.05	n.d.	0.04
MgO	0.07	0.08	0.13	n.d.	0.01	0.01	1.02	0.02	n.d.	0.03	0.01	0.01	0.02	0.01	0.01	n.d.
CaO	0.05	5.16	0.11	5.79	5.87	7.41	2.10	8.26	6.26	6.21	10.97	0.41	13.73	8.89	12.37	4.85
Na_2O	5.30	7.67	5.90	7.34	5.69	6.27	6.38	6.54	7.50	7.36	4.93	1.84	3.65	6.17	4.28	6.36
K_2O	6.56	1.92	5.80	1.58	1.46	1.09	5.63	0.75	1.36	1.40	0.49	14.02	0.15	0.67	0.33	2.72
Cr_2O_3	0.01	0.23	0.02	n.d.	n.d.	n.d.	n.d.	n.d.	0.01	0.03	n.d.	n.d.	n.d.	n.d.	n.d.	0.01
NiO	n.d.	0.16	0.02	n.d.	0.01	0.04	n.d.	0.01	0.05	0.01	n.d.	n.d.	n.d.	0.06	n.d.	n.d.
Total	98.5	101.1	100.0	99.9	99.9	100.1	99.5	100.7	101.5	101.3	100.7	100.1	101.2	100.8	101.8	98.3
An	17	24	22	35	35	40	21	46	35	35	59	8	72	48	64	30
Ab	43	62	43	58	52	53	45	51	59	58	39	11	27	49	34	54
Ksp	38	15	33	9	8	6	33	4	8	8	3	82	1	4	2	16

Carbonates

Carbonate inclusions are observed in samples 3, 15, 26, ÖL25, and S52. Compositions range from calcium carbonate to magnesian calcium carbonate, or dolomite. Grain textures and mineral associations differ strongly between the different carbonate inclusions (Fig. 16). Vibrational spectroscopic studies of the carbonate inclusions in sample 26 using Raman spectroscopy revealed that these carbonates - mostly calcium carbonates - occur in various modifications and may be dolomite, calcite, or aragonite. Figures 16e and 16f show that calcite may also form spherular inclusions within silicate glass of phonolitic composition (see section about melt inclusions).

Calcite and dolomite inclusions can be regarded as primary which is supported by the occurrence of calcite and dolomite grains that are completely entrained in the host sapphire, as revealed by Raman spectroscopy. In contrast, the vesicular aragonite inclusions entrained in alkali feldspar filled blebs, are probably of secondary origin, as they are associated with veins and cracks in the sapphire.

Sample 3 has a 200 – 300 µm sized, homogeneous calcite inclusion (Fig. 16a) and one composite mineral aggregate containing calcite and plagioclase that is surrounded by a spinel rim.

Sample 15 has one ~ 100 µm sized homogeneous calcite inclusion located at a tiny crack, indicating it to be a secondary inclusion. The electron dispersive element map (Fig. 17) reveals a slight oscillatory zonation of Mg that becomes most evident at the left side of the mineral. This zonation is probably a preserved magmatic imprint.

Carbonate inclusions are most abundant in sample 26. The carbonate inclusions in this sample differ significantly in their appearance (Fig. 16). Those carbonates that are directly included in the sapphire, are calcite (Fig. 16a) or dolomite (Fig. 16b), whereas the vesicular calcium carbonates within the feldspar inclusions that are entrained along cracks (e.g., Fig. 16 c, d) are aragonite, as shown by Raman spectroscopy. The electron

dispersive element map of the vesicular aragonite inclusion entrained in feldspar (Fig. 18) shows a complex internal structure becoming most evident in the Mg and Mn maps, and a slight enrichment in Mg at the lower part of the mineral. As the aragonite must have formed due to late stage low-temperature alteration, a magmatic zonation can be ruled out. One Mn bearing calcite inclusion in sample 26 (Fig. 19) shows a fine rim of spinel. Due to the lack of Fe in both, the carbonate, and in the hosting sapphire, the spinel may not have formed via interaction of the carbonate with the sapphire. It seems rather likely that the spinel is a precipitate from an Fe-bearing silicate melt that communicated with the carbonate inclusions via a crack in the crystal which can also be seen in the electron dispersive element map. The rim-like appearance of the spinel is thus probably only a visual effect resulting from sample sectioning.

In sample ÖL25, carbonate inclusions reach sizes up to 700 µm and occur either associated with spinel and Fe-Ti-Mn oxides (ilmenite – pyrophanite solid solution) or with plagioclase and/or alkali feldspar. One calcite grain showing a truncated slight oscillatory zoned Mg pattern (Fig. 20) is rimmed by labradorite. As the zonation is a mineral feature that was imprinted upon the mineral during growth, the fragmentation must predate the trapping by the sapphire, i.e., the inclusion must be primary. As described for the spinel-rimmed carbonate in sample 26, the plagioclase was probably inherited from a silicate melt that entered the crystal along cracks.

In sample S52, one calcite grain is located in the central part of hydrous altered plagioclase.

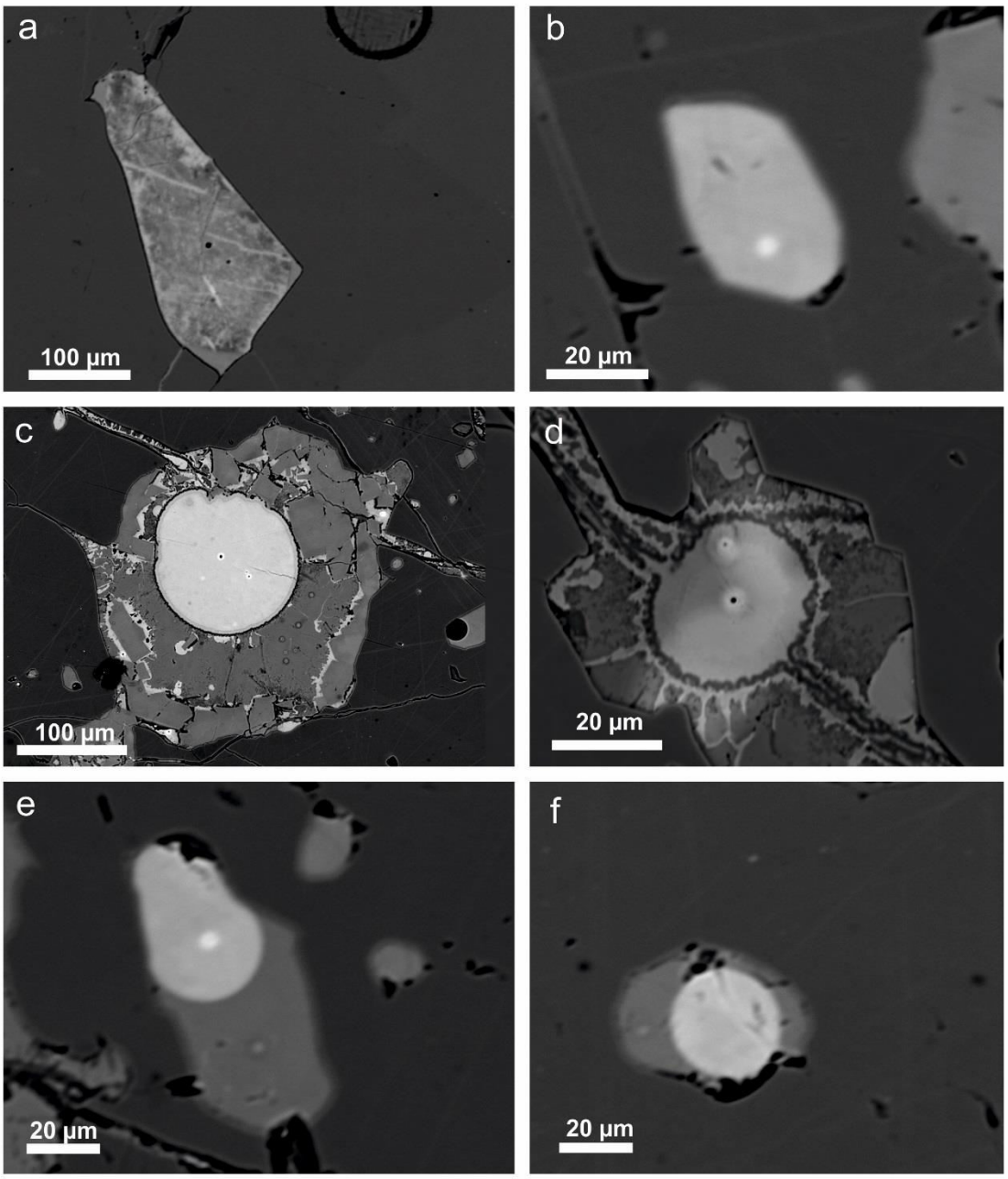

Figure 15: Backscattered electron images of selected carbonate inclusions in some Siebengebirge sapphires. a: calcite inclusion in sample 3. b: dolomite inclusion in sample 26. c and d: vesicular secondary aragonite in alkali feldspar located at cracks in sample 26. e and f: spherular calcite inclusions in phonolitic silicate glass in sample 26.

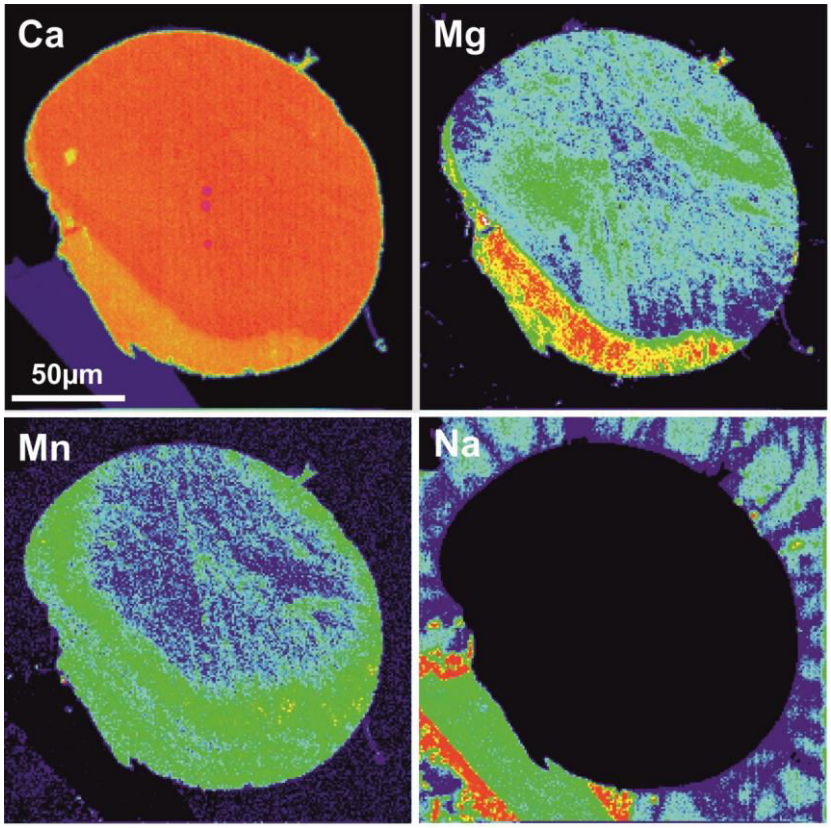

Figure 16: Element map of an aragonite inclusion in sample 26. The vesicular aragonite is entrained in alkalifeldspar (Min 1a and b in Table 5) and shows a complex internal structure.

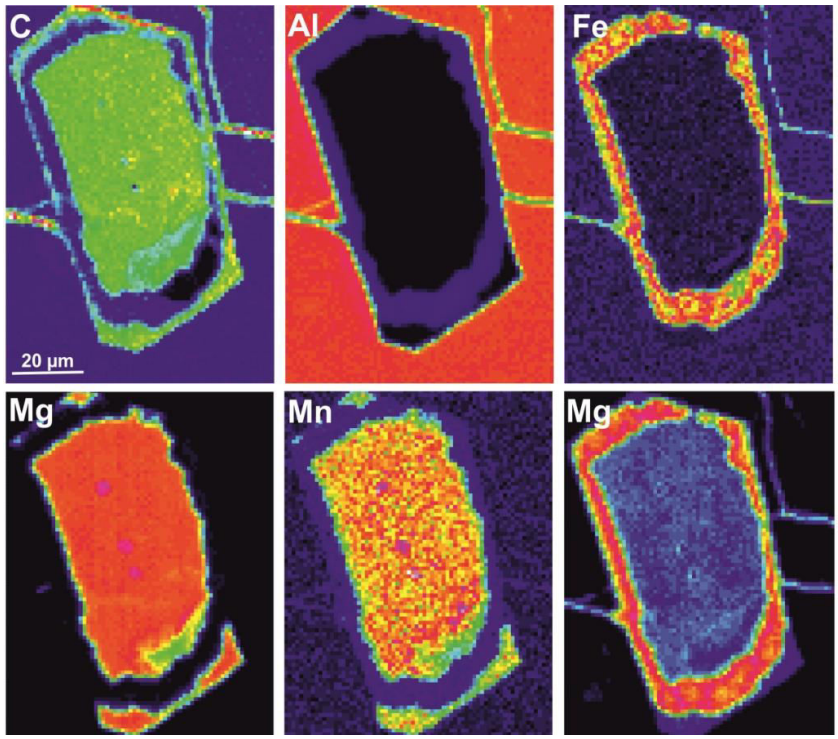

Figure 17: Element map of a Mg-bearing calcite inclusion in sample 26. The mineral shows a negative crystal shape which is evidence for the primary nature. The carbonate shows a spinel corona towards the interface of the corundum.

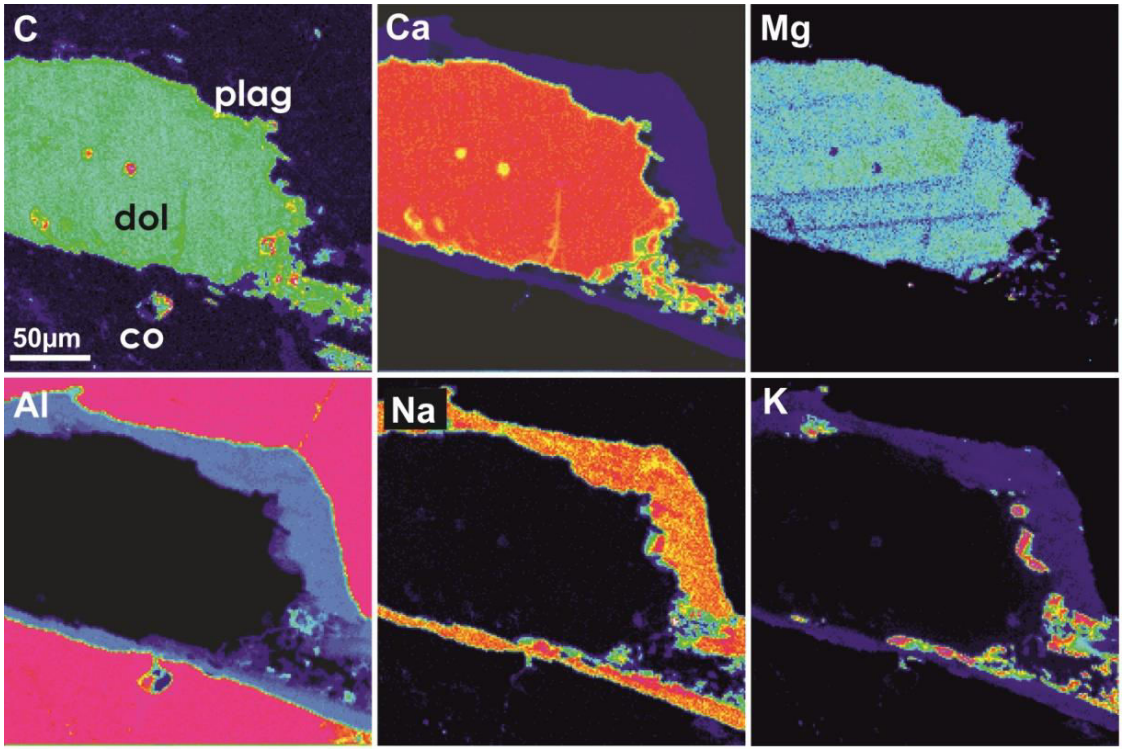

Figure 18: Element map of a Mg-bearing carbonate inclusion in sample ÖL25. The carbonate inclusion is rimmed by plagioclase (See table 5, mineral 3 for the composition). The carbonate inclusion has a slight oscillatory zonation that becomes most evident in the Mg map. The truncation of the magmatic zonation is strongly indicative for the primary nature oif the carbonate inclusions.

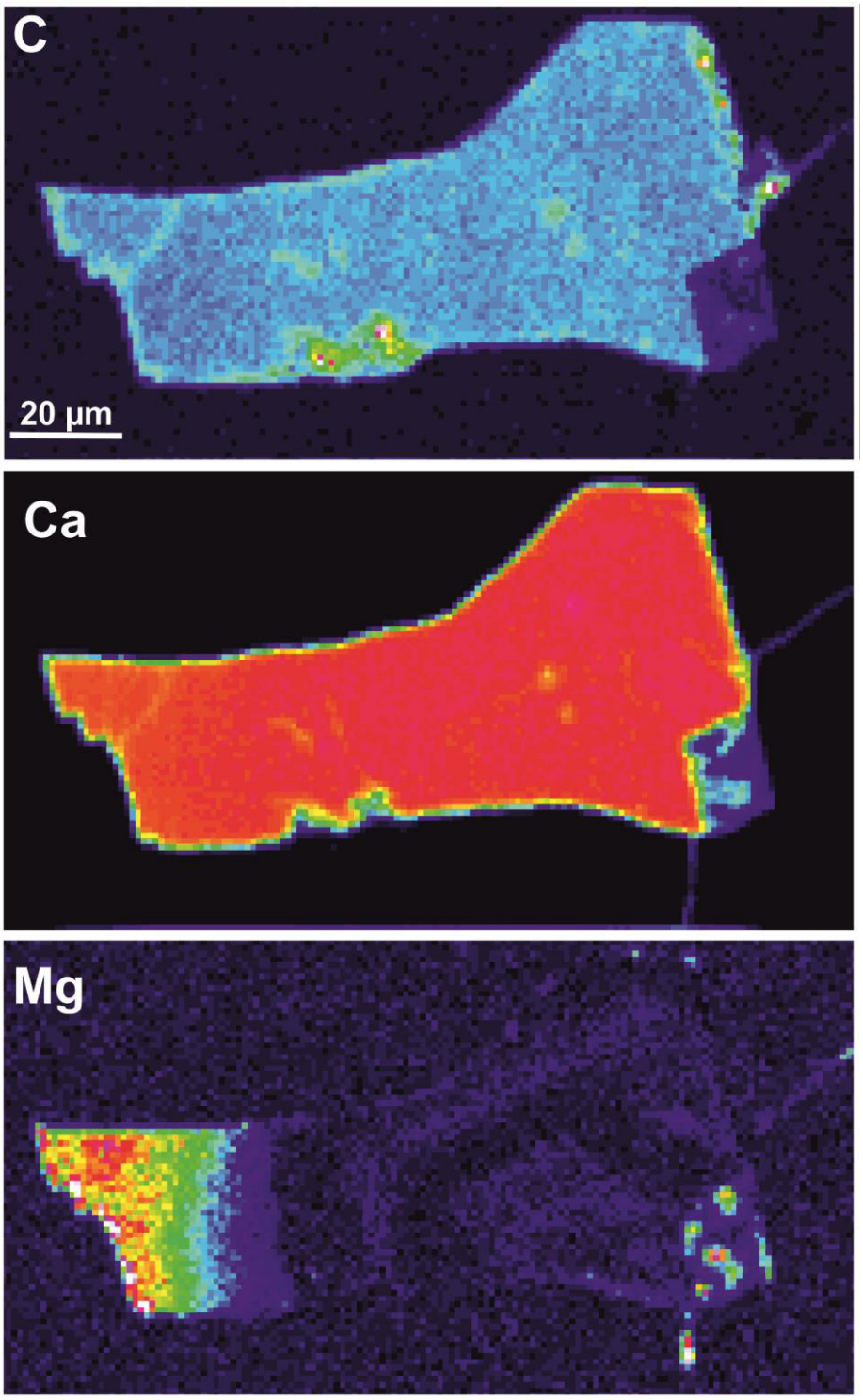

Figure 19: Element map of a Magnesium bearing carbonate inclusion in sample 15. This carbonate inclusion also shows an oscillatory zonation that is most evident in the Mg map.

Oxides

Sapphire samples 3, 15, 26, and ÖL25 have various oxide inclusions of different compositions. All oxide inclusions are completely entrained in the sapphire, and there are no visible cracks near them. Hence, they can be regarded as primary inclusions that formed cogenetically with the sapphires. Strikingly, most oxide inclusions are minerals of the HFSE, most notably of Nb, and Ta, but also of Th and U. The inclusions were identified using EPMA. Base metal oxides are from the spinel – hercynite solid solution series that are found within alkali feldspar inclusions in sample 3, along with ilmenorutile [$(Nb,Ti,Fe)O_2$]. Submicron to micron sized ilmenite ($FeTiO_3$) inclusions are widely distributed in sample 15. Sample 26 furthermore contains a 400 µm sized columbite [$(Mn)(Fe,Nb)_2O_6$] inclusion (Fig. 14a) which in turn encloses a cluster of thorite (ThO_2) and thorianite ($ThSiO_4$) embedded in a matrix of pyrochlore ($Ca_2Nb_2O_7$) (Fig. 14b). Sample ÖL25 carries several complex composite oxide inclusions (Fig. 14c). These complex oxide assemblages are hercynite-rimmed ilmenite-pyrophanite solid solutions [$(Fe,Mn)TiO_3$] with exsolved hercynite and ilmenorutile, that are each oriented in different crystallographic orientations. The hercynite rim surrounding the ilmenite-pyrophanite$_{ss}$ is probably the consequence of the reaction of the solid solution with the enclosing corundum along the reaction:

$$FeTiO_{3\,(ilmenite)} + Al_2O_{3\,(corundum)} \rightarrow FeAl_2O_{4\,(hercynite)} + TiO_{2(rutile)}, \qquad (6)$$

indicating that the inclusion is of primary magmatic origin.

Strikingly, the base metal oxides are usually incorporated in the sapphires that carry carbonate inclusions. Another inclusion in sample 26 is betafite [$(Ca,U)_2(Ti,Nb,Ta)_2O_6(OH)$], neighbouring ilmenorutile (Fig. 20d). As detected by a

Raman map from sample 26, sapphires contain abundant rutile (TiO_2) inclusions of 1-3 micrometer size that are evenly distributed within the sapphire.

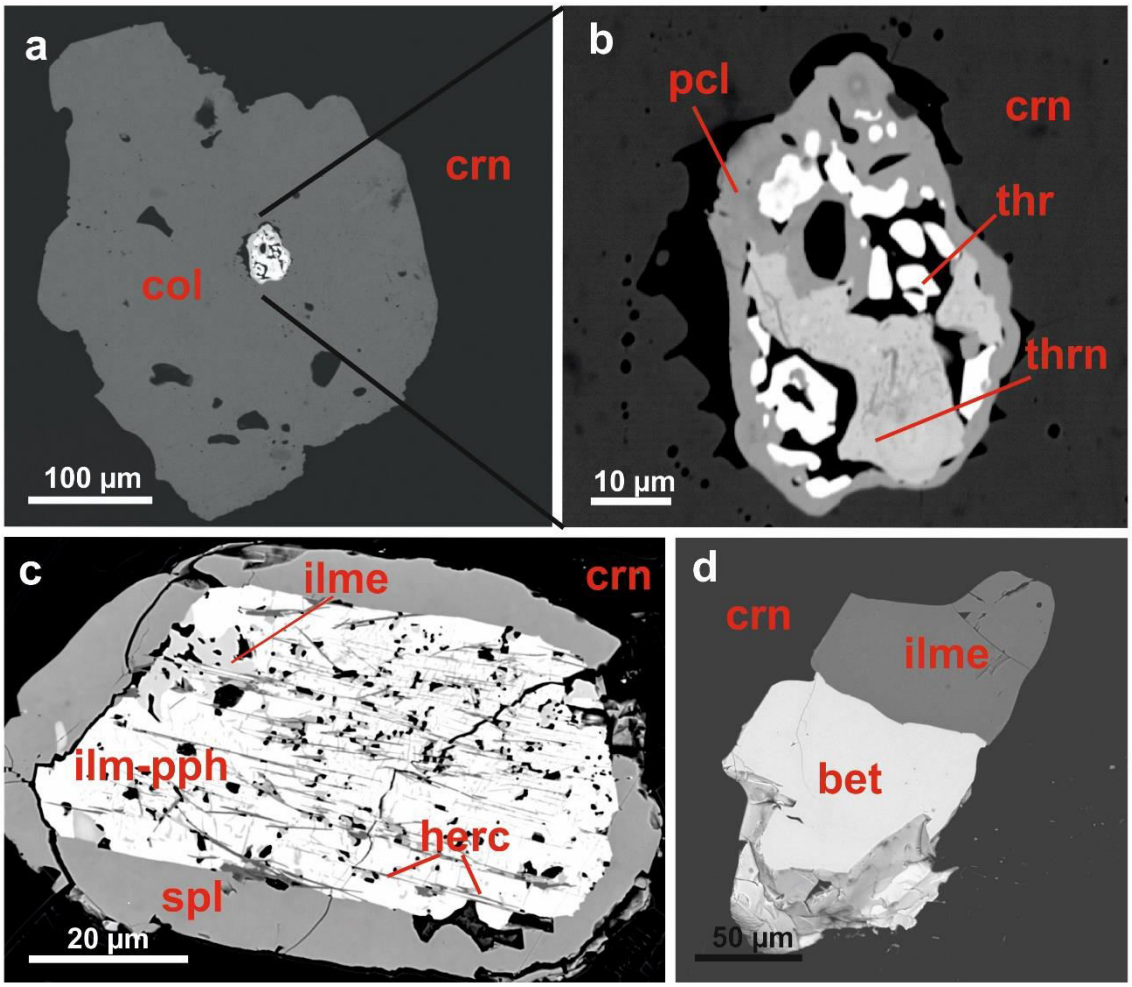

Figure 20: Complex composite oxide inclusions in the Siebengebirge sapphires. a and b are inclusions in sample 26, c and d are inclusions in sample ÖL25. Abbrevations are: bet: betafite; crn: corundum; col: columbite; herc: hercynite; ilm: ilmenite; ilme: ilmenorutile; pcl: pyrochlore; pph: pyrophanite; spl: spinel; tho: thorite; thor: thorianite.

2.4.4. Nanoinclusions

Nanoinclusions were observed in the brownish area enriched in the HFSE of sample PE25 via TEM. Transmission electron microscopy has been proven to be a powerful tool for the identification and chemical characterization of nanophases (see review about nanophase investigations using transmission electron microscopy by Wang (2000)). The TEM investigation visualized that the studied area comprises hundreds of phases that

reach sizes of a few tens of nanometers (Fig. 21a, and b). These phases are all crystallographically arranged in the same direction and grow along the (0001) basal plane, parallel to the c axis. Remarkably, the crystallization of nanophases periodically ceases at some stage, leaving the corundum to grow almost free of inclusions. These nanophase deficient bands occur repeatedly in irregular distances along the whole studied area and have thicknesses of a few hundreds of nanometers (Fig. 21c,d). The crystallinity of the phases has been proven by Fast Fourier Transformation (FFT) of High Resolution images (Fig. 21e, f). Electron dispersive X-Ray analysis (EDX) of the nanoinclusions revealed that these are Nb, Ti, (and Fe) bearing oxides (Fig. 22). These are most likely ilmenorutile $(NbTi,Fe)O_2$, as this is the only known oxide to contain only Nb, Ti, and Fe as main cations. In addition, ilmenorutile has been observed as macroscopic mineral inclusion in sapphire ÖL25. As the other HFSE (Ta, Zr, and Hf) are similarly enriched in the brownish areas, it is most probable that not all nanoinclusions are ilmenorutile but that other HFSE bearing minerals may also contribute to the compositional suite of the nanoinclusions, but were only not detected in the frame of the work that has been done on this sample.

The occurrence of ilmenorutile as ‘normal’ micrometer sized inclusions in some sapphires, as well as nanoinclusions within the brownish areas of other sapphires (PE21 and PE25) indicates that the mineral inclusion suite is probably the same on the ‘large’ scale (detectable by the electron microprobe) and on the nanometer scale (detectable by TEM). This observation is additionally supported by the fact that those sapphires having the brownish HFSE enriched areas (areas comprising HFSE-bearing nanoinclusions) do not contain visible ‘large mineral inclusions’, and those sapphires that do contain ’large mineral inclusions’ lack nanoinclusions.

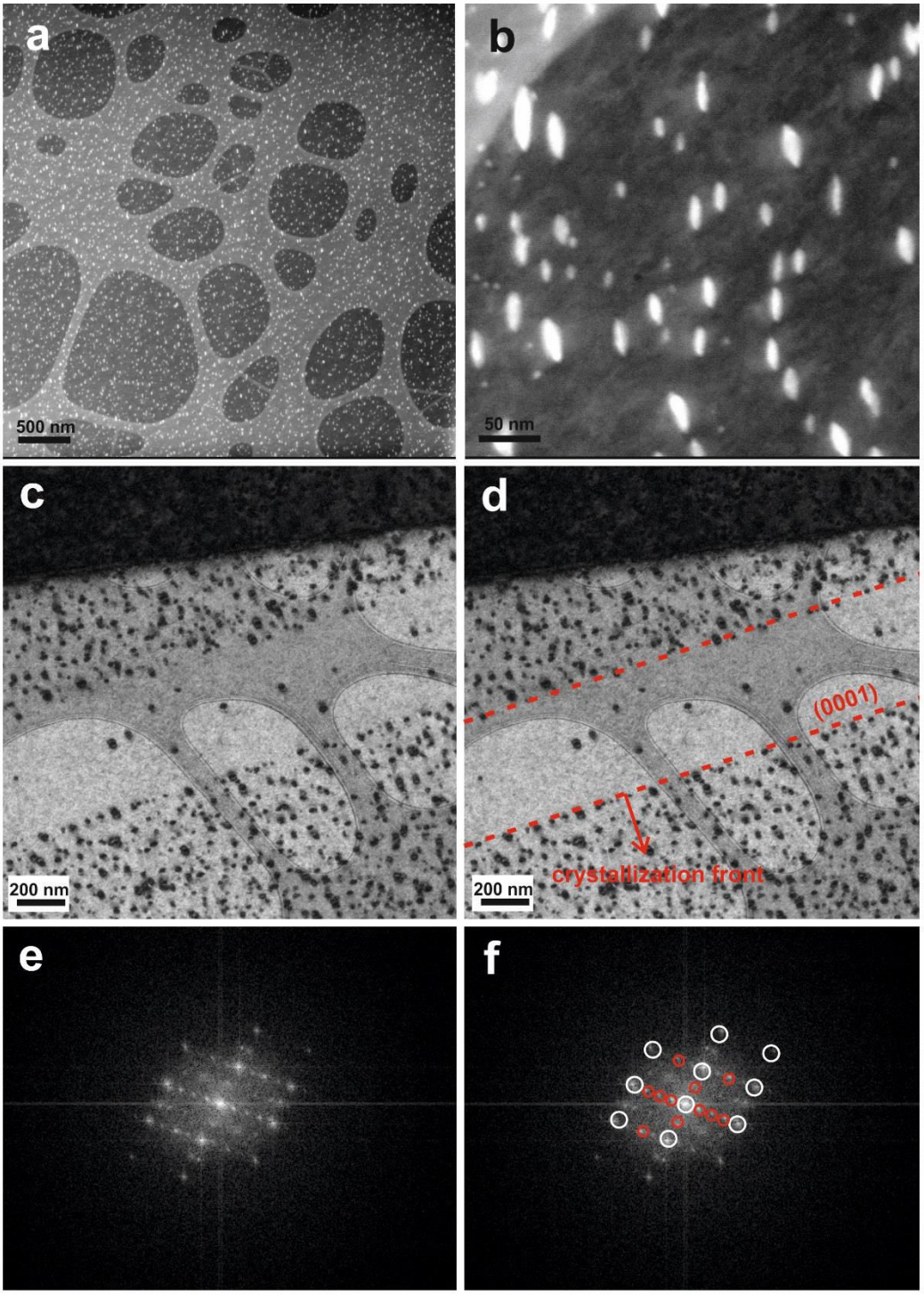

Figure 21: Nanoinclusions in sapphire PE25 detected by TEM. a and b: High-angle annular dark field (HAADF) images. The color contrasts reflect the contrast in the atomic number with brighter colors representing higher atomic numbers than darker colors. c: Bright Field image of the nanoinclusions within the sapphire. One band with a thickness of ~ 400 nm that has very few nanoinclusions lies between two areas with high abundances of nanoinclusions. d: Graphical interpretation of image c. e and f: Fast Fourier Transformation (FFT) of a High Resolution image of one nanoinclusion. The FFT shows the superposition of the corundum crystal lattice (white circles in Fig 21f) and of the inclusion crystal lattice (red circles in Fig. 21f).

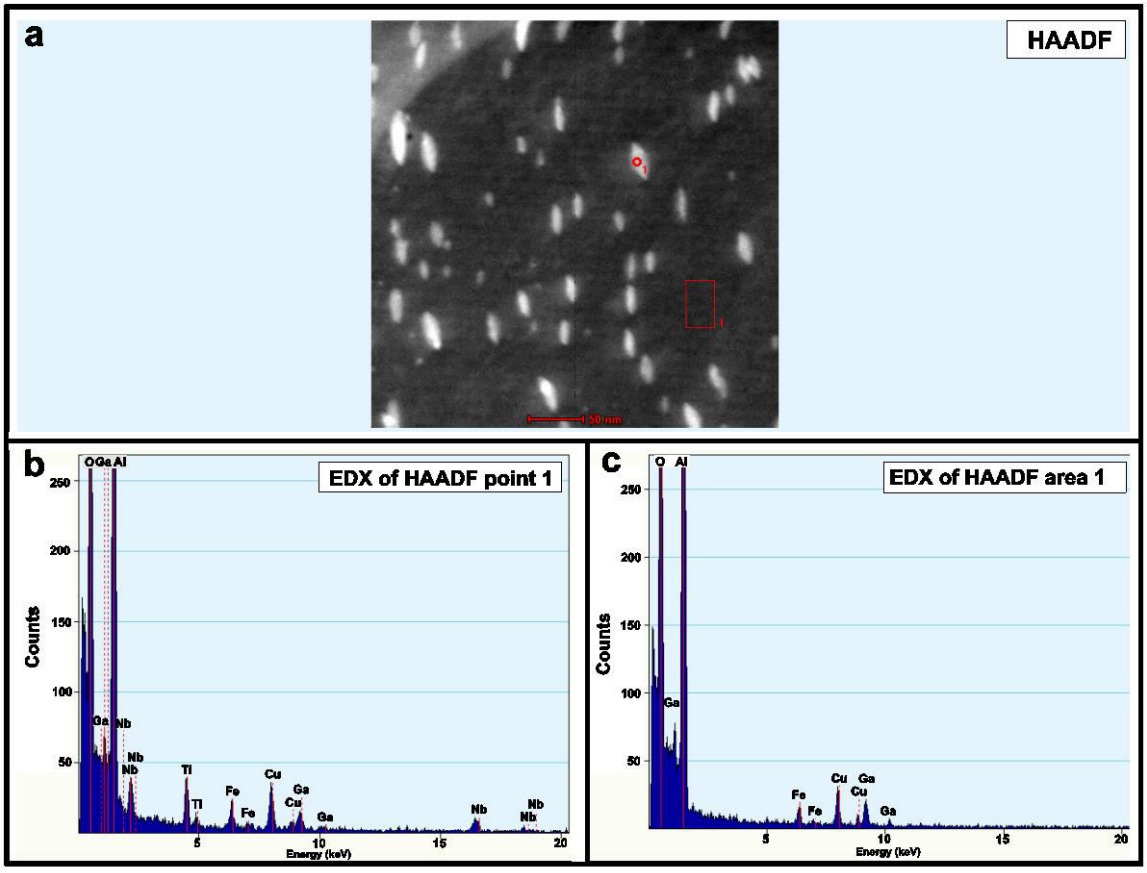

Figure 22: Electron dispersive X-ray spectra of one nanoinclusion and of the sapphire matrix. a: HAADF image showing the spot where the EDX spectrum of the inclusion was taken from (red circle) and the area where the EDX spectrum of the corundum was taken for comparison (red square). b: EDX spectrum of one nanoinclusion. The Ga peaks are from the Ga ion beam that was used for FIB sectioning, and the Cu peak is from the Cu metal sample carrier. Figure 22c shows that the Al, and at least parts of the Fe peaks belong to the spectrum of the surrounding corundum.

2.4.5. Fluid inclusions

Fluid inclusion studies may provide exceptionally valuable information about the composition of the melt that crystallized the host minerals. Most important information provided by the fluid inclusions are not only the chemical composition hinting to the composition of the parental melt but also barometric information that can be derived from the fluid inclusions by estimating the internal pressure, as the internal pressure within a fluid inclusion is supposed to equal the lithostatic pressure during mineral crystallization. Hence, fluid inclusion studies may provide critical information about the pressure, and

thus the depth of mineral crystallization which is an important factor for the development of a petrogenetic model.

In the Siebengebirge sapphires, fluid inclusions were identified in samples 26, 15, S52, and KS21 using the method described above. Fluid inclusions may occur either randomly distributed along the whole sapphire without any preferred crystallographic orientation, or crystallographically arranged, as it is shown in Fig. 23a for CO_2 inclusions with thenardite as daughter minerals in sample S52. Pure CO_2 fluid inclusions are common and are usually arranged along fluid trails that transect the whole sapphire (Fig. 23b). The sizes of the fluid inclusions are highly variable and range from < 1 µm to several tens of micrometers. Fluid inclusions often show negative crystal structures, indicating a primary origin. Whereas the identification of CO_2 from a vibrational spectrum of a fluid inclusion is simple, as CO_2 has two strong bands at 1285 cm^{-1} and at 1388 cm^{-1} (Rosso and Bodnar, 1995), the identification of daughter minerals in the fluid inclusions from the Siebengebirge sapphires was not unambiguously possible. The limiting factor for the identification of the daughter phases in the fluid inclusions is given by the band positions of their vibrational spectra. The typical Raman spectra of the fluid inclusions in the Siebengebirge sapphires show many peaks in the wavelength range between 100 cm^{-1} and 1000 cm^{-1} which is probably reflecting the superposition of the vibrational spectra of multiple phases, including the spectrum of the hosting sapphire. One strong band at 992.4 cm^{-1} repeatedly occurs in the vibrational spectrum of many fluid inclusions. This band is characteristic for minerals such as (natro-)alunite ($(Na,K)Al_3[(OH_6)/SO_4]_2$), thenardite ($Na_2SO_4$), aphthitalite [$K_3Na(SO_4)_2$], blodite [$Na_2Mg(SO_4)_2H_2O$], and paravauxite [$FeAl_2[OH/PO_4]_2$ (Fig. 24). A further daughter mineral has been identified to be burkeite ($Na_4(SO_4)(CO_3)$) (Fig. 25). As these minerals have their main band at about the same position (~992 cm-1), the distinction between them occurs via their minor bands at lower wavenumbers where the superposed peaks are located. Thus, although an unambiguous identification of the daughter minerals is

not possible from the vibrational spectrum, it can be stated with certainty that the daughter mineral/s in the CO_2 bearing fluid inclusions must be alkali rich sulfates, and probably contain ± Al and OH/H_2O. Most probably, the daughter minerals are mineral aggregates of several of the mentioned sulfates/phosphates. A further mineral that was identified as a daughter phase in the CO_2 inclusions is dawsonite ($NaAl[(OH)_2/CO_3]$). A typical Raman spectrum for fluid inclusions in Siebengebirge sapphires is presented in Fig. 26, showing a CO_2 inclusion with alunite as daughter mineral.

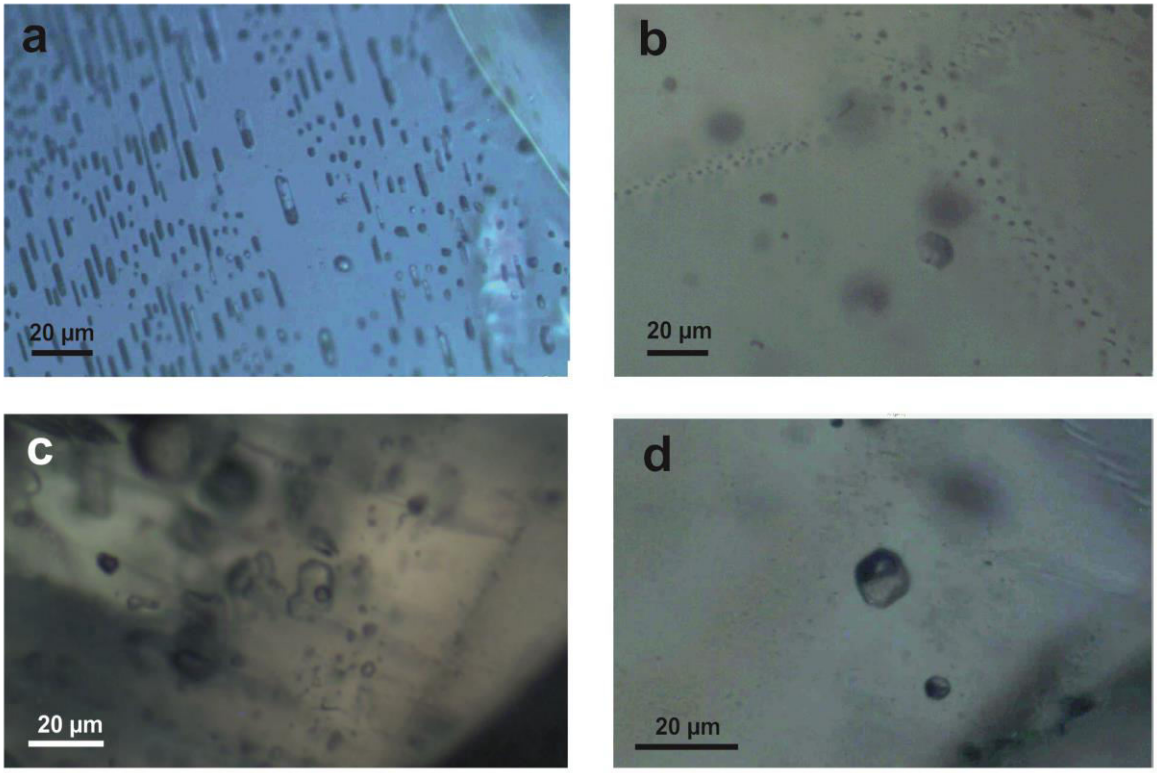

Figure 23: Fluid inclusions in Siebengebirge sapphires. a: Crystallographically oriented elongated fluid inclusions in sample S52. b: trails of fluid inclusions in sample 26. c and d: multiple phase fluid inclusions in sample 26.

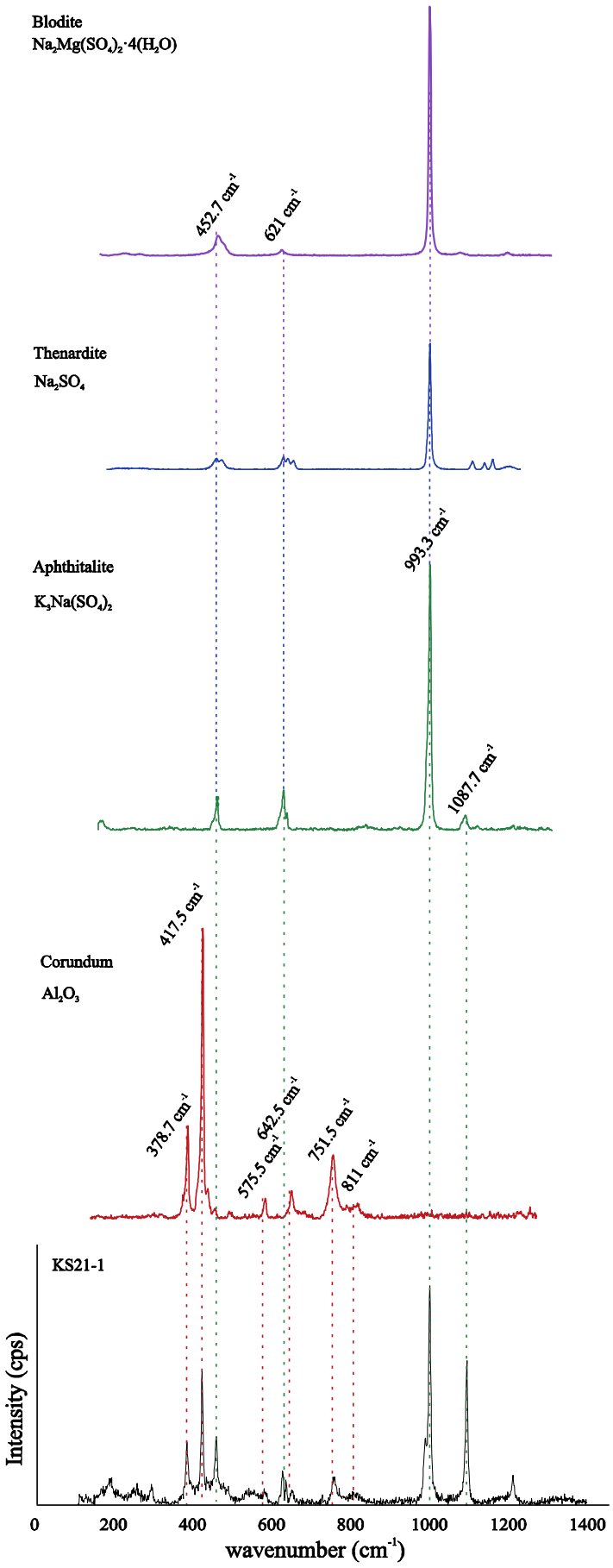

Figure 24: Raman spectrum of fluid inclusion KS21-1 with the reference spectra of possible daughter phases. The Raman spectrum of KS21-1 is a mixed spectrum of several mineral. Many bands represent the corundum matrix. Other bands cannot be unambiguously assigned to a certain mineral. But certainly, the daughter phase must be a sodium-sulfate. The reference spectra are from the RRUFF Database.Following reference spectra were used: blodite: R050341; thenardite: R040178; aphthitalite: R050651; corundum: R060020.

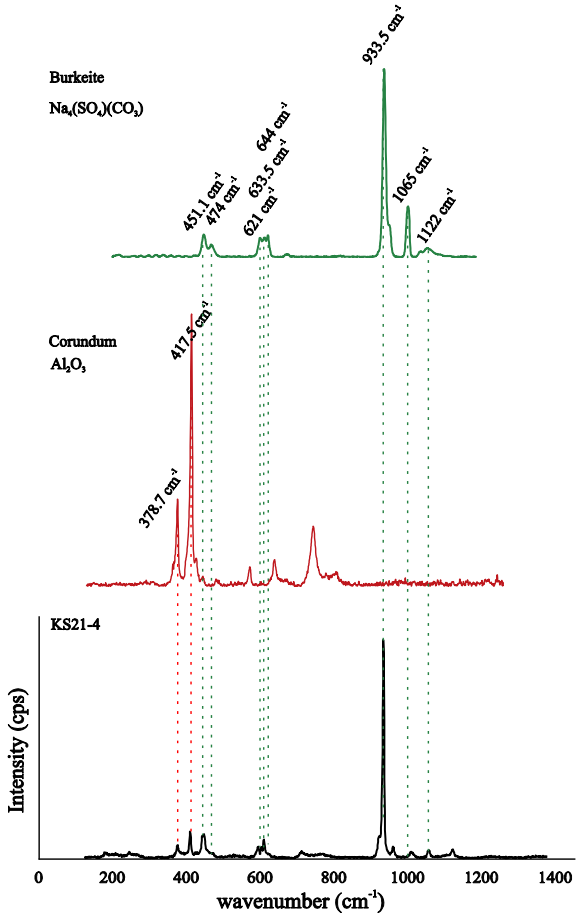

Figure 25: Raman spectrum of fluid inclusion KS21-4 with the reference spectra of possible daughter phases. The Raman spectrum of KS24-1 is a mixed spectrum of the corundum matrix and burkeite. The reference spectra are from the RRUFF Database.Following reference spectra were used: burkeite: R060112; corundum: R060020.

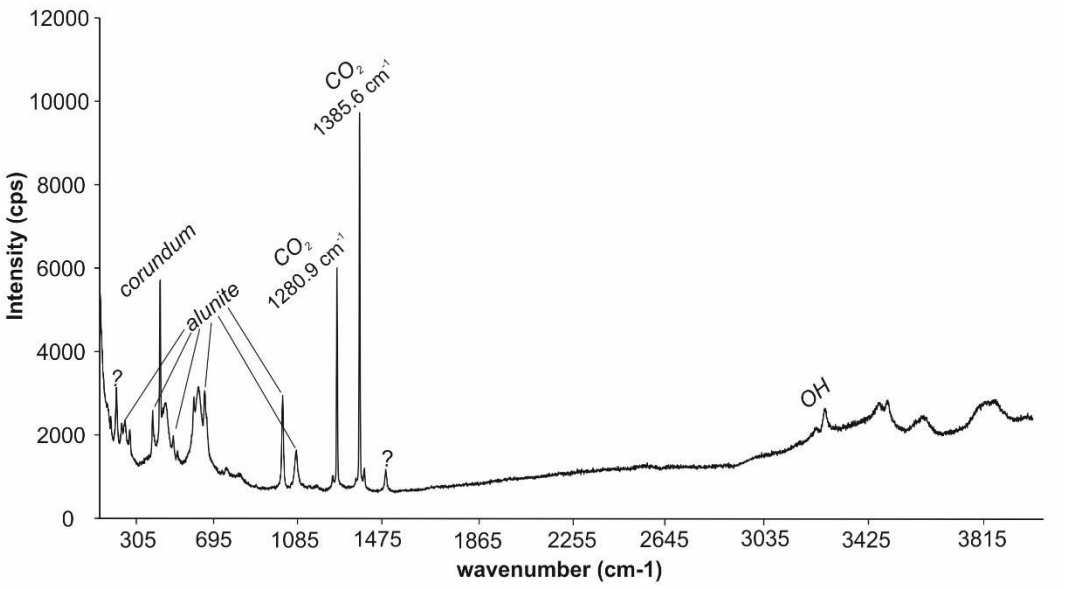

Figure 26: Typical not background corrected vibrational spectrum of a fluid inclusion in sample 26. The two CO_2 bands are visible at 1285 cm^{-1} and 1388 cm^{-1}. The bands at lower wavenumbers are a mixture of the vibrational spectra of alunite and corundum.

2.4.6. Melt inclusions

By electron microprobe analysis only, inclusions of glass cannot be distinguished from mineral inclusions, as EPMA only returns the chemical composition of a phase, but may not provide information about the structural state of the phase, i.e., whether the analyzed phase is crystalline or amorphous. Some phases that were analyzed with the electron microprobe in sample 26 have round crystal shapes that are untypical for crystalline phases, so their structures were investigated using Raman spectroscopy to determine the structural state of the phase. The Raman spectroscopic investigations on these vesicular inclusions confirmed that they are amorphous glasses that most likely represent quenched liquids that were trapped during sapphire growth. These glasses are all composite aggregates that are comprised of two different compositions. All composite glass inclusions show the same structure. The glass with composition 1, henceforth referred to as melt 1 always forms a globular structure within the glass with composition 2, which is henceforth referred to as melt 2. (Fig. 27). The results of the electron microprobe analyses of the glasses are given in Table 7. Melt 2 has the composition of a high alumina phonolite, with the average composition: SiO_2: 59.8 wt. %, Al_2O_3: 25.6 wt. %, Na_2O: 7.72 wt. %, K_2O: 6.97 wt. %, MnO: 0.11 wt. %, FeO: 0.52 wt. %. Melt 1 has a more complex composition and can be regarded as an inhomogeneous carbonated silicate melt with extremely variable CO_2 concentrations of 5 to 52 wt. % (as the presence of carbon in melt 1 was confirmed via energy dispersive element mapping, the shortfall of the microprobe totals were taken as CO_2 concentrations). Energy dispersive element maps of the glasses are displayed in Figures 28, 29, and 30. The vesicular glasses included in the Siebengebirge sapphire strongly support that liquid immiscibility in a magmatic system involving silicate melts that are highly enriched in CO_2, played a major role in the sapphire genesis. In addition, these glasses provide the first direct evidence for that the magma differentiation in the SVF led to more evolved – phonolitic

– compositions than those that are observed from the outcrops, where the highest known differentiates are tephritic phonolites (cf. with Kolb et al., 2012).

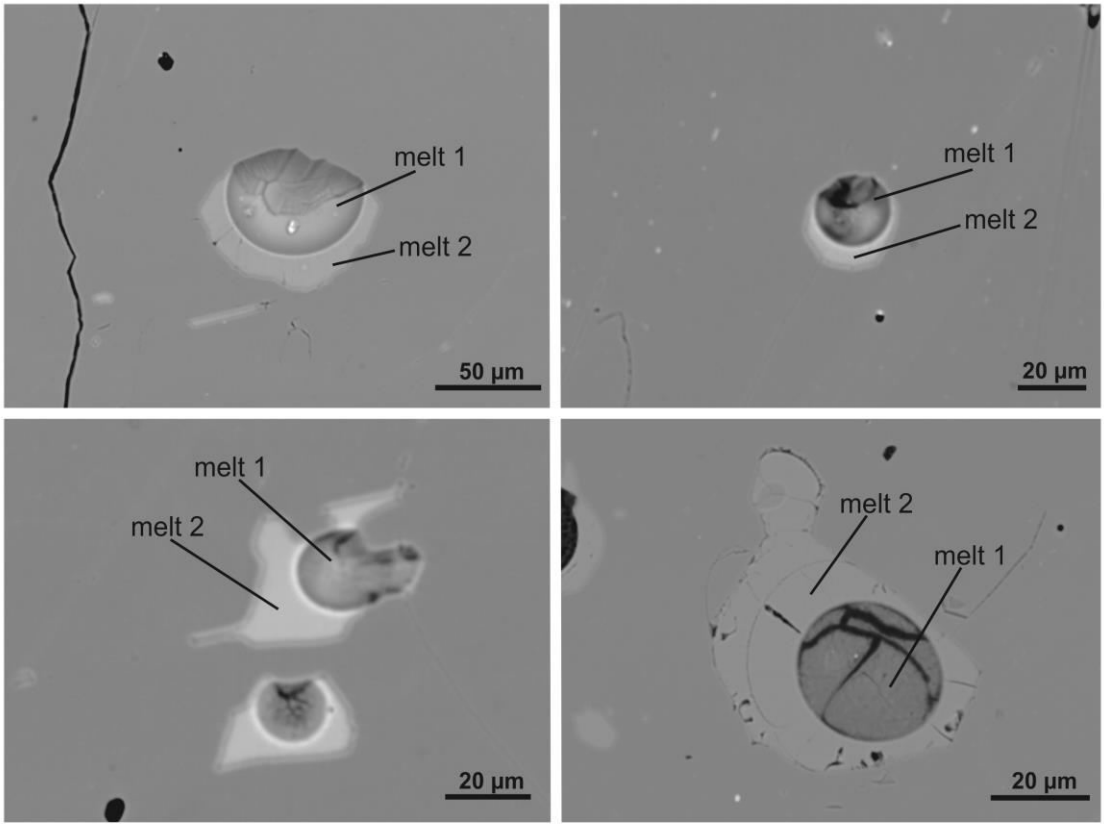

Figure 27: Inclusions of glasses that represent quenched products of two immiscible melts in sample 26. Melt 1 which has the composition of an inhomogeneous carbonated silicate melt, forms spherular droplets in melt 2 which has a high-alumina phonolitic composition.

Table 7: Results of EMP analyses of the immiscible melt inclusions in sample 26.

	melt 1-1a	melt 1-1b	melt 1-1c	melt 1-1c	melt 1-2a	melt 1-2b	melt 1-3a	melt 1-3b	melt 1-3c	melt 1-4a	melt 1-4b	melt 1-4c	melt 1-5a	melt 1-5b	melt 1-5c
n															
MgO	0.05	0.01	0.01	0.06	0.18	0.02	0.15	0.16	0.19	0.11	0.27	0.17	9.19	8.63	9.93
Na_2O	0.17	5.82	5.89	0.70	1.57	9.32	6.17	7.13	9.00	9.52	7.77	2.41	0.94	1.50	1.66
FeO	0.63	0.53	0.63	0.56	0.65	0.44	0.67	0.72	0.49	0.64	0.66	0.56	0.35	0.32	0.30
K_2O	5.11	6.89	6.73	6.47	6.57	6.66	3.05	6.90	6.63	6.81	6.70	6.31	0.92	1.16	1.24
SiO_2	56.6	17.0	2.45	48.8	47.3	4.9	58.4	43.4	32.2	32.5	38.5	61.5	38.6	39.5	43.8
Al_2O_3	11.9	28.1	31.9	15.0	11.1	31.7	25.9	26.4	29.6	32.0	27.2	13.9	17.4	16.7	16.5
MnO	0.17	0.08	0.10	0.17	0.08	0.07	0.12	0.19	0.08	0.08	0.11	0.12	0.12	0.12	0.24
CaO	0.64	0.65	0.66	0.64	0.57	0.60	0.34	0.61	0.61	0.55	0.66	0.54	1.40	1.40	1.40
Total	**75.2**	**59.0**	**48.3**	**72.4**	**68.0**	**53.7**	**94.7**	**85.5**	**78.8**	**82.2**	**81.8**	**85.6**	**68.9**	**69.3**	**75.1**
CO_2	24.8	41.0	51.7	27.6	32.0	46.3	5.3	14.5	21.2	17.8	18.2	14.4	31.1	30.7	24.9
Na_2O+K_2O	5.28	12.71	12.62	7.17	8.14	15.97	9.21	14.03	15.63	16.33	14.47	8.72	1.86	2.65	2.90

Table7 (continued)

	melt 2-1	melt 2-2	melt 2-3	melt 2-4	melt 2-5
n	2	2	3	3	5
MgO	0.06	0.06	0.07	0.06	0.06
Na_2O	7.15	8.40	8.25	8.04	6.78
FeO	0.61	0.42	0.56	0.55	0.47
K_2O	6.58	7.18	6.95	7.12	7.02
SiO_2	58.8	59.6	60.6	60.3	59.6
Al_2O_3	25.9	25.5	26.0	25.3	25.2
MnO	0.10	0.07	0.15	0.11	0.12
CaO	0.67	0.45	0.50	0.49	0.48
Total	**99.9**	**101.6**	**103.0**	**102.0**	**99.7**
CO_2					
Na_2O+K_2O	13.73	15.58	15.20	15.16	13.80

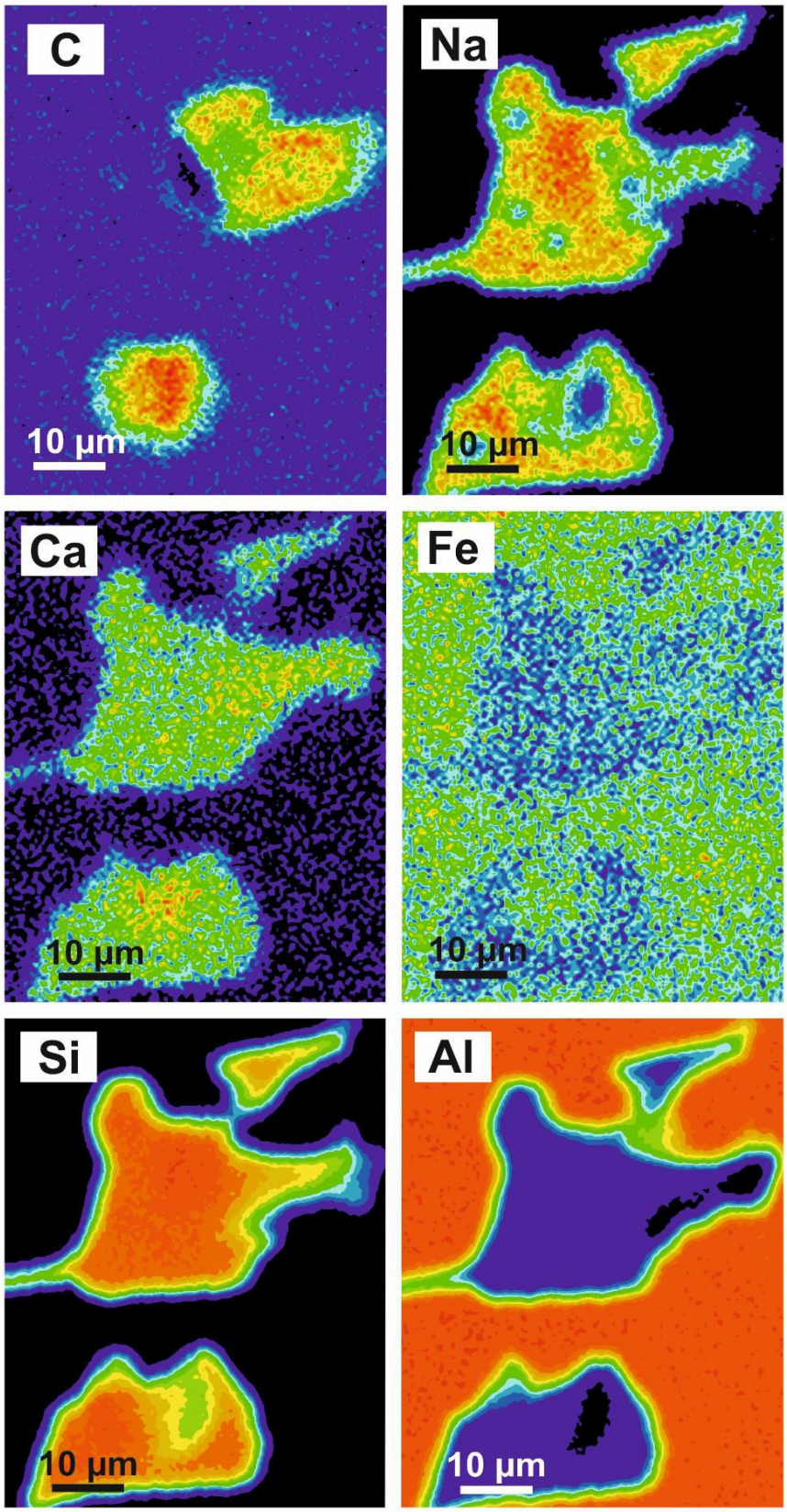

28: Backscattered electron map of a two-phase melt inclusion in sample 26 corresponding to analyses melt 1-1a to melt 1-1d and melt 2-1 in Table 6. Compared to melt 2, melt 1 contains C, and has lower concentration of Na, and Al.

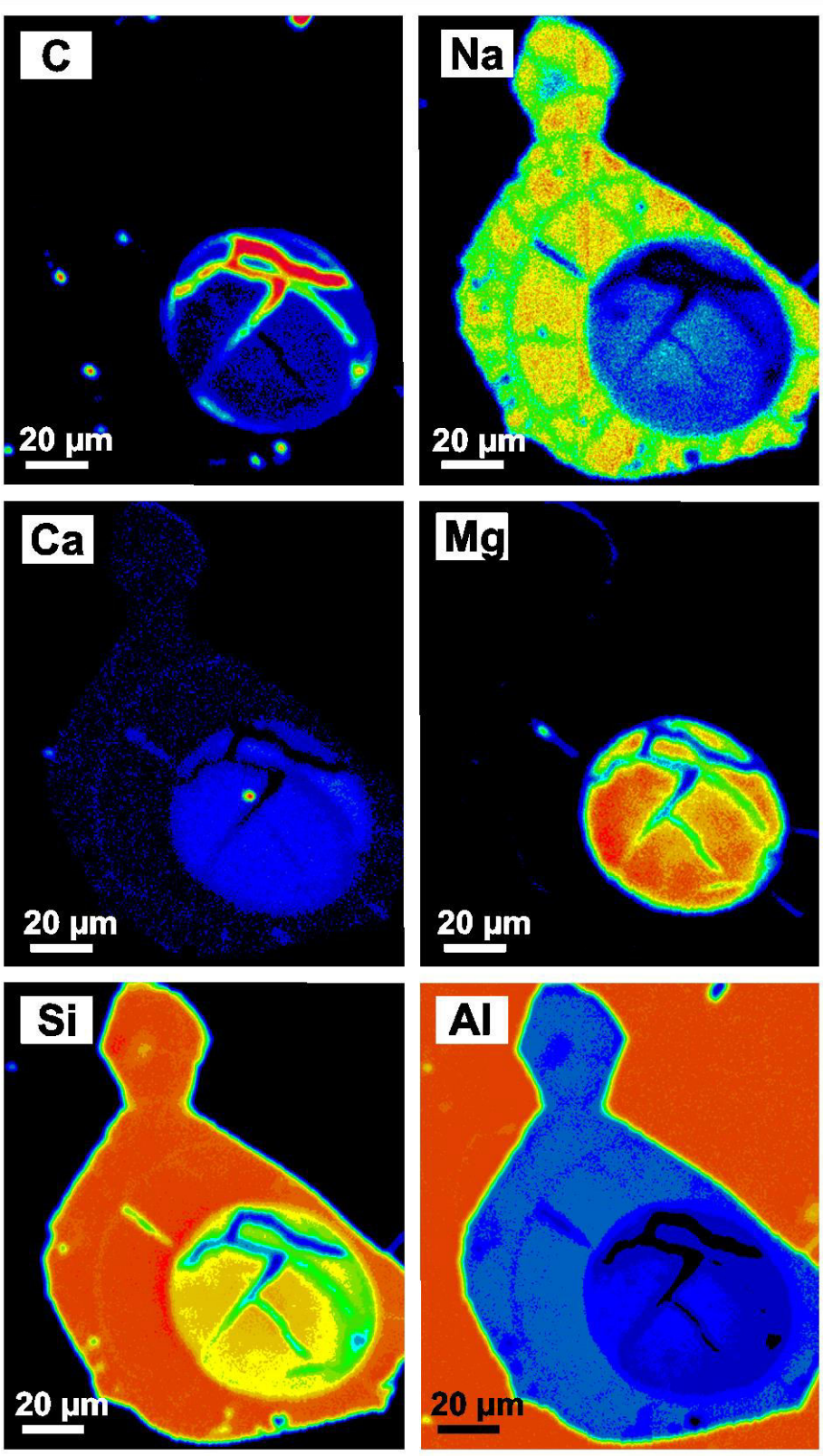

Figure 29: Backscattered electron map of a two-phase melt inclusion in sample 26. The map corresponds to analyses melt 1-3a to melt 1-3c (upper part), melt 1-4a to melt 1-4c (lower part) and melt 2-3 (upper part) and melt 2-4 (lower part) in Table 6. Compared to melt 2, melt 1 contains C, and has lower concentration of Na, and Si but is slightly richer in Ca.

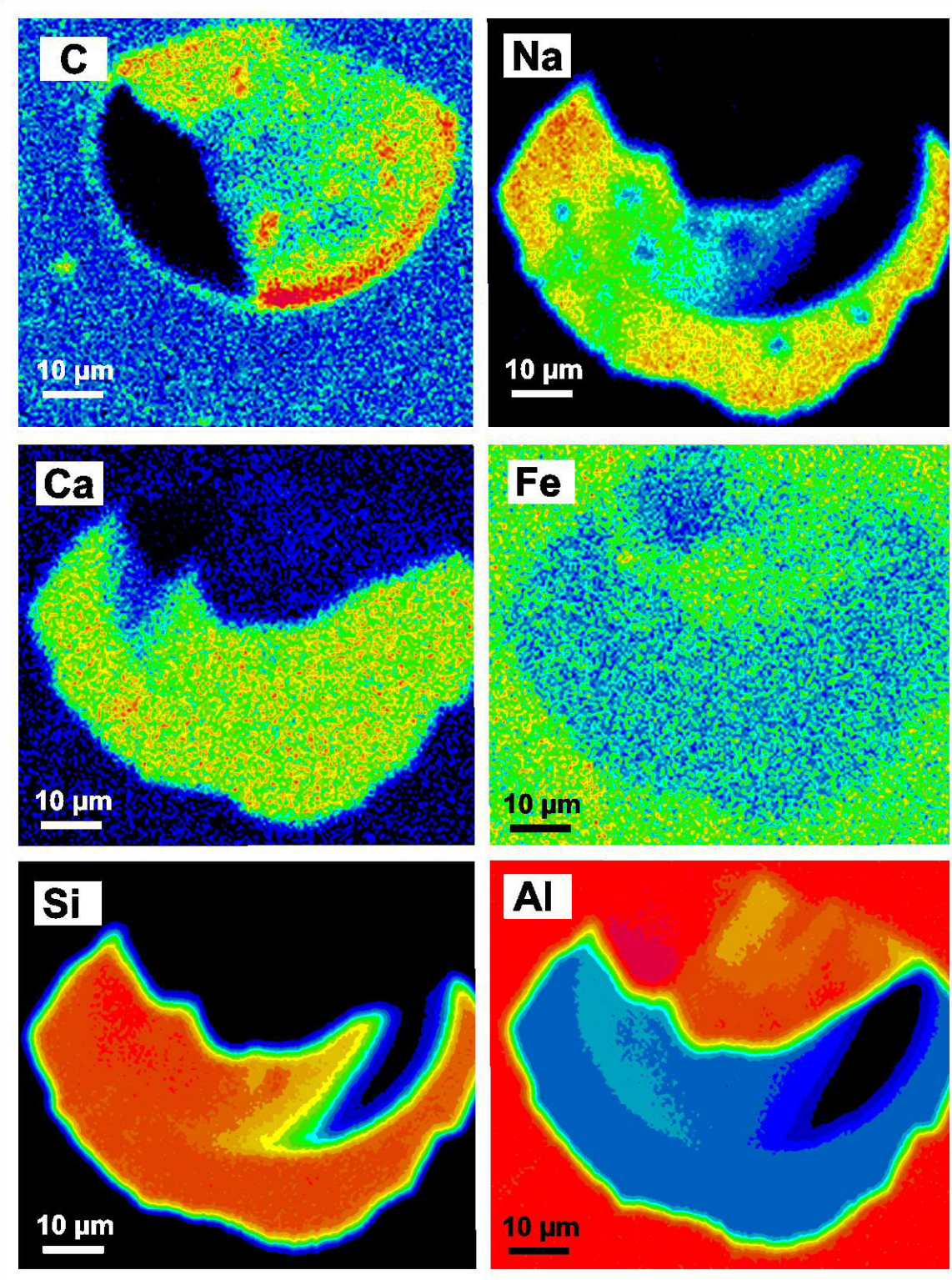

Figure 30: Backscattered electron map of a two-phase melt inclusion in sample 26. The map corresponds to analyses melt 1-5a to melt 1-5c and melt 2-5 in Table 7. Compared to melt 2, melt 1 has C, and higher concentrations of Ca and Mg, but lower Na and Si concentrations.

The liquid miscibility relations in the carbonatite - silicate system has been intensively studied in the past decades, with the most pioneering work by e.g. Koster VanGroos and Wyllie (1963, 1966), Hamilton and Freestone (1979), Freestone and Hamilton (1980), Kjarsgaard and Hamilton (1988), Brooker and Hamilton (1990), Lee and Wyllie (1997, 1998), Brooker (1998), Brooker and Kjarsgaard (2010). In the Hamilton pseudoternary phase diagram (projected from CO_2) (Fig. 31), both melt 1 and melt 2 plot on the silicate liquidus surface close to the $SiO_2 + Al_2O_3$ apex. The average composition of melt 2 is given by the red star, and the green stars represent the single spot analyses of melt 1. From the phase relations, it becomes obvious that these two melts do not represent primary exsolved melts, as two liquids that lie in the field of liquid immiscibility would exsolve along the cotectic lines, so that one composition would lie at the lowermost (SiO_2 and Al_2O_3 rich) two field boundary, and the coexisting composition would lie at the opposite (Na_2O and K_2O / CaO rich) two field boundary. Yet, although the glasses may not represent primary unmixed liquids, the glasses show striking evidence for liquid immiscibility, such as the vesicular shape of the innermost glass. Consequently, if these glasses do represent quenched products of two melts that formed via liquid immiscibility, then there must have been a further, Na_2O and K_2O rich liquid that probably separated from the coexisting SiO_2 and Al_sO_3 rich liquids and is now not present in the sapphire, anymore. This melt would have a composition that lies somewhere on the 'a – b' two liquid field boundary. Upon cooling, the melt will evolve from a to b via crystallization of silicate phases, and will then evolve along the silicate – carbonate field boundary 'b – c' with the coprecipitation of silicate and carbonate phases (Lee and Wyllie, 1998). Such a melt would be a carbonatite containing ≤ 5 wt. % $SiO_2 + Al_2O_3$. The prerequisite for a liquid that lies along the a - b two liquid field boundary to cross the silicate liquidus surface and reach the silicate – carbonate field boundary in order to precipitate carbonate minerals is that the melt has physically separated from the coexisting silicate melt (e.g., Kjarsgaard and Peterson, 1991; Lee and Wyllie, 1998). Now, combining this necessity of the presence of a now absent

carbonatitic melt with the abundance of carbonate mineral inclusions and CO_2 rich fluid inclusions in the sapphires, it seems most probable that the sapphires crystallized from the 'missing' carbonatite that separated from the melts now present as glass inclusions within the sapphires.

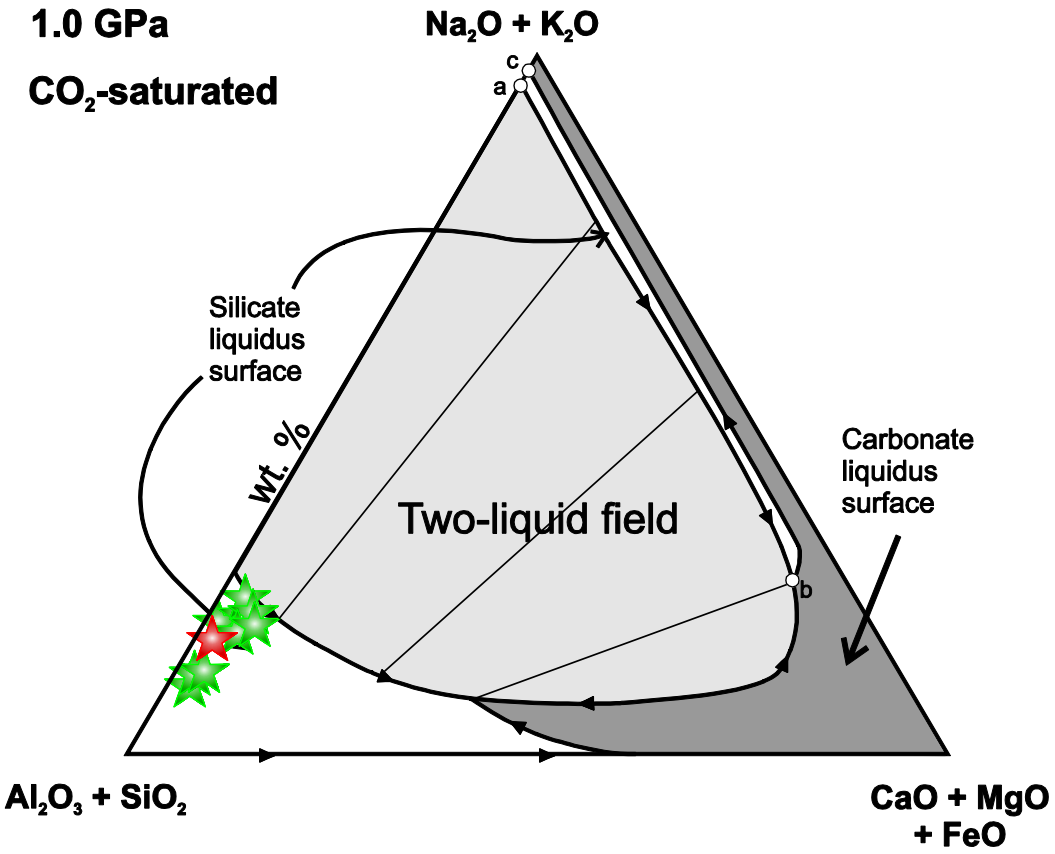

Figure 31: Location of the glass compositions (melt 1: green stars; melt 2: red star) in the schematic pseudoternary phase diagram of the Hamilton projection at 1 GPa (Lee and Wyllie, 1998). The line 'a – b' represents the two liquid field boundary at the Na_2O, K_2O rich side, and line 'b – c' represents the silicate – carbonate field boundary. The composition of both glasses plot in the same field (silicate liquidus surface at the SiO_2, + Al_2O_3 rich apex), ruling out that they formed solely via liquid immiscibility.

2.5. U-Pb DATING OF A COLUMBITE INCLUSION

The columbite dated in this study (Fig. 14a) is a manganocolumbite with the formula $Fe_{0.2}Mn_{0.5}Nb_{2.3}O_6$ and is an inclusion in sample 26 which is entrained in an alkali basalt from the Ölberg. The columbite is virtually free of inclusions. The large size of 200 – 500

µm and the absence of visible mineral inclusions make it highly suitable for in-situ LA-ICP-MS dating. The reliability of in-situ U-Pb dating with LA-ICP-MS has been previously demonstrated by e.g., Smith et al., 2004; Dill et al., 2007; Melcher et al. 2008, 2015, and Che et al., 2015.

2.5.1. Analytical conditions

The columbite inclusion was analyzed for U, Th, and Pb isotopes by LA-ICP-MS at the Institute of Geosciences, Johann Wolfgang Goethe-University Frankfurt, using a Thermo-Scientific Element II sector field ICP-MS coupled to a New Wave Research UP-213 ultraviolet laser system. Data were acquired in the analogue mode for ^{238}U and in the counting mode for all other isotopes with 20 s measurement on the background followed by sample ablation of 20 s. The sample surface was cleaned with 3 pulses of pre-ablation. Square laser spots with an edge length of 28 µm were used. The laser operated at a repetition rate of 6 Hz and an energy fluence of 2 J/cm^2 with an energy output of 50 %. The signal was tuned to obtain maximum sensitivity for ^{238}U and ^{206}Pb, and to keep the oxide production monitored as $^{254}UO/^{238}U$ below 3 %. Measured masses were: ^{202}Hg, ^{204}Hg, ^{204}Pb, ^{206}Pb, ^{207}Pb, ^{208}Pb, ^{232}Th, ^{235}U, and ^{238}U. Mercury was measured as it is commonly a minor component of the Ar carrier gas and may cause isobaric interferences on ^{204}Pb which is usually used for common lead correction.

A coltan (columbite-tantalite) standard from Madagascar, Africa (Coltan 139), as well as Zircon GJ-1 (Jackson et al., 2004) were used as primary standards. The usability of Coltan 139 as a matrix matching standard for columbite LA-ICP-MS U-Pb dating has been recently shown by Che et al. (2015). Coltan 007 from Kokobin, Ghana (Melcher et al., 2008; 2015) was used as a secondary standard to control the accuracy of the measurements. For Coltan 139, Melcher et al. (2015) reported TIMS ages of 505.4 ± 1.0 Ma (BGR, Hannover) and 506.6 ± 2.4 Ma (University of Toronto), and a LA-ICP-

MS age of 506.2 ± 5.0 Ma (University of Frankfurt). The GJ-1 zircon has a TIMS age of 608.5 ± 0.4 Ma (Jackson et al., 2004), and Coltan 007 has an age of 2079.6 ± 3.1 Ma (Melcher et al., 2008, 2015). Ages of primary and secondary standards are summarized in Table 8. A total number of 45 unknowns were analyzed, using the standard bracketing method. Acquired data were then processed independently using two different approaches to test the accuracy of the calculated age as a function of the data processing method. One way of data procession was the use of the VizualAge Data Reduction Scheme from Petrus and Kamber (2012) for Iolite 5.4 (Paton et al., 2011), using Coltan139 as primary standard. Iolite is a software package that visualizes the full analytical session in a data versus acquisition time plot, allowing the user to process the data individually timeslice - by - timeslice. The raw data were corrected for the ablation-induced elemental fractionation, and then normalized to the standard using a spline that interpolates the correction factor through the analytical session. Final error propagation is done by treating each individual analysis as unknown, producing a population of pseudo-secondary standards. A $^{207}Pb/^{206}Pb$ correction was done offline using the model after Stacey and Kramers (1975).

The second way to calculate the U-Pb age was the use of an in-house MS Excel© spreadsheet (Gerdes and Zeh, 2006; 2009). Zircon GJ-1 was used as a primary standard. The mass bias was subsequently corrected for Coltan139. Later, a ^{208}Pb based common lead correction was applied, as there is very low Th in the sample. The data were then corrected for the ablation induced element fractionation offset between zircon matrix and columbite matrix, as suggested by Che et al. (2015). The accuracy and reproducibility was checked by repeated analyses of Coltan 139 (n=9) and Coltan 007 (n=8) which yield intercept ages of 507.1 ± 4.8 Ma (MSWD = 0.42) and 2074.1 ± 7.5 Ma (MSWD = 2.9), respectively (Fig. 32). These ages are in excellent agreement with the published values.

Table 8: Ages for primary and secondary standards used for the columbite dating.

Standard	Mineral	Age (Ma)	Dating method	Reference
GJ-1	Zircon	608.5 ± 0.4	TIMS	Jackson et al. 2004
Coltan 007	Ferrocolumbite	2079.6 ± 3.1	TIMS	Melcher et al. 2008, 2015
Coltan 139	Ferrocolumbite	505.4 ± 1.0	TIMS	Melcher et al. 2015
		506.6 ± 2.4	TIMS	Melcher et al. 2015
		506.2 ± 5.0	LA-ICP-MS	Melcher et al. 2015

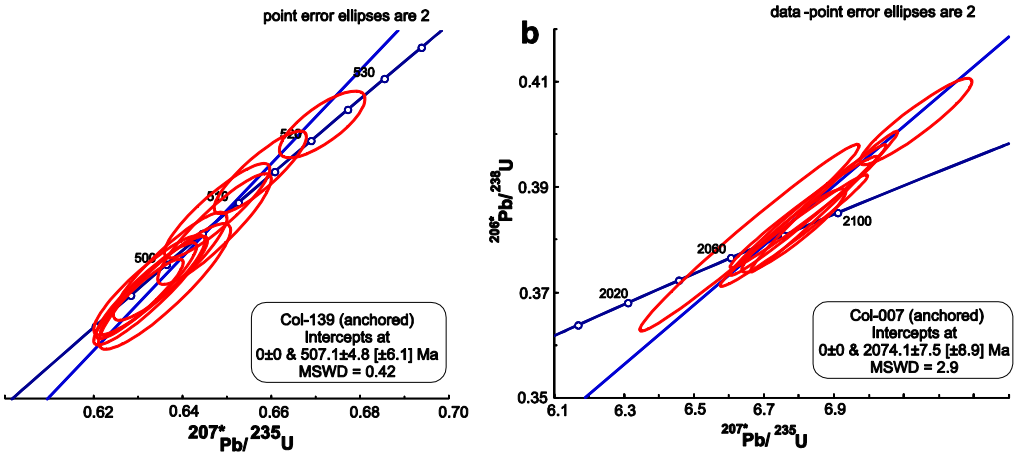

Figure 32: Ages for the (a) Col 139 and (b) Col 007 secondary standards plotted in a Wetherill diagram. The ages are obtained with the MS Exel© spreadsheet data reduction approach after Gerdes and Zeh, 2006, 2009. *206: ^{206}Pb corrected for common Pb.

2.5.2. Results

Although the two methods for data reduction (Iolite vs. MS Excel© spreadsheet) use completely different approaches for the procession of the LA-ICP-MS raw data, the returned date is the same within the errors (Table 9 for data processed with Iolite, and Table 10 for data processed with the in-house MS Excel© spreadsheet). The reported uncertainties (2σ) are the propagated errors that include the external reproducibility obtained from the standards Coltan 139, and zircon GJ-1 during the analytical session. Although data processed with Iolite plot on the Concordia (Fig. 33a) in the Wetherill diagram, an age could not be calculated directly from the position on the Concordia, as the single spot analyses have different anchored ^{206}Pb/^{238}U ages (^{207}Pb/^{206}Pb ratio for 25

Ma was obtained from the model of Stacey and Kramers, 1975). Therefore, weighted mean ages of the single spot analyses were calculated. The weighted mean age for the columbite inclusion in sapphire 26 from the SVF is 24.51 ± 0.44 Ma (MSWD = 3.9) (Fig. 33b). Data processed with the MS Excel© calculation spreadsheet returned weighted mean ages of 24.76 ± 0.23 Ma (MSWD = 3.4) for $^{206}Pb/^{238}U$, and of 24.93 ± 0.38 Ma (MSWD = 1.2) for $^{207}Pb/^{235}U$ (Fig. 23a, b), respectively (Fig. 34). Hence, the calculated ages are within the errors identical for both data processing methods.

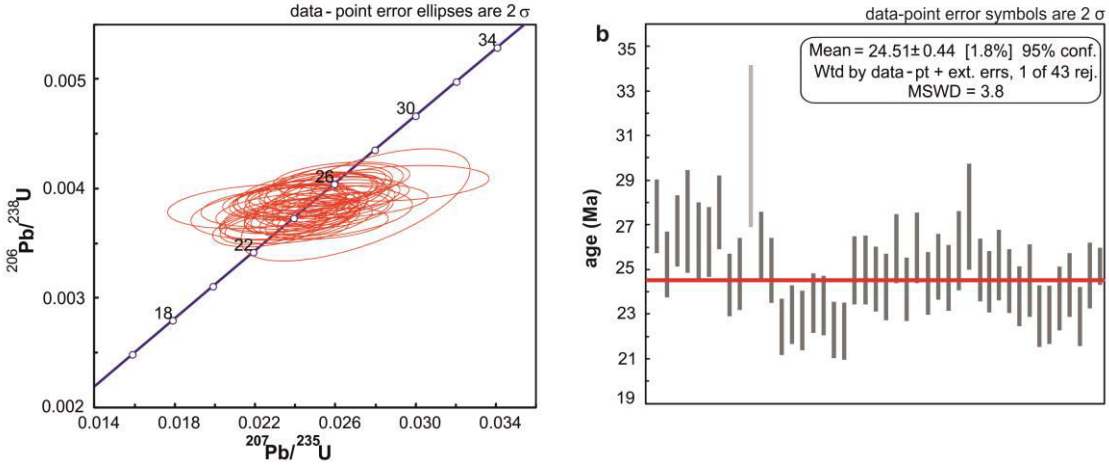

Figure 33: Age calculations for the columbite inclusion in the Siebengebirge sapphire sample 26 based on the data processed using *Iolite*. a: Data plotted in a Wetherill concordia diagram. b: Weighted mean age of the columbite inclusion based on the $^{206}Pb/^{238}U$ ratio. The gray bars are the errors of the calculated age, the red line represents the mean age of all analyses.

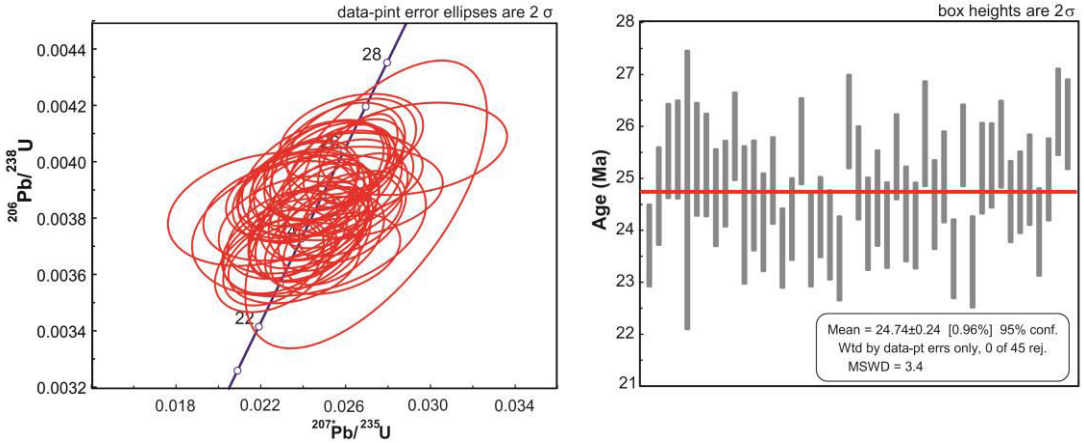

Figure 34: Age calculations for the columbite inclusion in the Siebengebirge sapphire sample 26 based on the data processed using an MS Excel© spreadsheet. a: Weighted mean age based on the calculated $^{206}Pb/^{238}U$ ratio. b: Weighted mean age based on the calculated $^{207}Pb/^{238}U$ ratio. The gray bars are the errors of the calculated age, the red line represents the mean age of all analyses.

Table 9: Results for the columbite dating using Iolite for data procession.

	U[a] (ppm)	Th[a] (ppm)	Th/U	$^{206}Pb/^{238}U$	±2s (%)	$^{207}Pb/^{235}U$	±2s (%)	$^{207}Pb/^{206}Pb$	±2s (%)	rho[b]	$^{206}Pb/^{238}U$[c]	±2s (Ma)
Unknown												
1	289	122	0.42	0.00438	5.9	0.0039	11	0.0686	9.3	0.318	27.4	1.6
2	525	327	0.62	0.00397	5.8	0.0029	11	0.0549	9.5	0.063	25.2	1.4
3	325	150	0.46	0.00424	5.9	0.0034	11	0.0620	10	0.122	26.7	1.6
4	359	235	0.65	0.15280	6.5	0.7200	6.7	0.7700	1.4	0.954		
5	213	68	0.32	0.00486	7.6	0.0240	23	0.1500	17	0.816	27.2	2.2
6	545	486	0.89	0.00458	6.3	0.0100	13	0.1320	9.1	0.728	26.3	1.7
7	411	254	0.62	0.00429	5.8	0.0043	9.8	0.0854	8.8	-0.047	26.2	1.5
8	483	394	0.82	0.00444	5.9	0.0048	12	0.0739	8.8	-0.150	27.6	1.6
9	846	936	1.11	0.00384	5.7	0.0022	8.8	0.0586	6.7	0.281	24.3	1.4
10	501	369	0.74	0.00392	6.4	0.0057	18	0.0590	19	-0.304	24.8	1.6
11	447	342	0.76	0.01433	8.4	0.1200	11	0.5750	3.8	0.956		
12	300	113	0.38	0.00414	5.8	0.0033	10	0.0636	9.0	0.016	26.1	1.5
13	409	117	0.29	0.00397	5.8	0.0032	10	0.0643	9.0	0.011	25.0	1.4
14	702	410	0.58	0.00360	5.6	0.0029	9.3	0.0714	7.6	0.172	22.5	1.2
15	844	324	0.38	0.00375	5.6	0.0029	8.4	0.0828	6.8	-0.028	23.0	1.3
16	761	307	0.40	0.00379	5.8	0.0037	8.5	0.1013	5.9	0.390	22.7	1.3
17	650	439	0.68	0.00390	5.6	0.0028	7.3	0.0969	5.3	0.227	23.5	1.3
18	588	375	0.64	0.00373	5.6	0.0028	9.8	0.0654	8.3	0.130	23.4	1.3
19	686	360	0.52	0.00356	5.6	0.0022	8.3	0.0664	6.6	0.092	22.3	1.3
20	712	387	0.54	0.00352	5.7	0.0025	9.6	0.0604	8.3	0.069	22.2	1.2
21	361	245	0.68	0.00397	6.0	0.0037	12	0.0641	10	0.023	25.0	1.5
22	354	197	0.56	0.00395	6.1	0.0036	12	0.0598	11	0.034	25.0	1.5
23	351	236	0.67	0.00389	5.9	0.0033	11	0.0609	9.9	-0.045	24.6	1.4

[a] U and Pb content and Th/U ratio were calculated relative to coltan 139. b rho is the $^{206}Pb/^{238}U/^{207}Pb/^{235}U$ error correlation coefficient. [c] corrected for background, within-run Pb/U fractionation (in case of $^{206}Pb/^{238}U$) and common Pb using Stacy and Kramers (1975) model Pb composition.

Table 9 (continued): Results for the columbite dating using Iolite for data procession.

	U[a] (ppm)	Th[a] (ppm)	Th/U	$^{206}Pb/^{238}U$	±2s (%)	$^{207}Pb/^{235}U$	±2s (%)	$^{207}Pb/^{206}Pb$	±2s (%)	rho[b]	$^{206}Pb^{c}/^{238}U$	±2s (Ma)
24	391.7	269.6	0.69	0.0038	6.0	0.0032	11.5	0.0555	9.7	0.208	24.2	1.4
25	449.5	260	0.58	0.0041	5.9	0.0027	9.8	0.0568	8.6	-0.009	25.9	1.5
26	369.7	223.2	0.60	0.0040	5.8	0.0041	10.1	0.0866	8.9	0.266	24.1	1.4
27	322.8	213.7	0.66	0.0041	6.0	0.0029	9.2	0.0657	7.6	0.127	26.0	1.5
28	980	869	0.89	0.0038	5.7	0.0018	8.0	0.0550	6.0	0.270	24.4	1.4
29	304.1	167.3	0.55	0.0040	5.8	0.0033	10.7	0.0630	9.4	0.073	25.1	1.4
30	319.3	107.1	0.34	0.0039	5.9	0.0028	9.6	0.0609	8.7	-0.005	24.6	1.4
31	252.3	133.6	0.53	0.0043	6.5	0.0081	15.5	0.0960	15.6	-0.020	25.9	1.7
32	223.8	113.2	0.51	0.0071	6.9	0.0320	10.3	0.3630	6.9	0.641		
33	352.7	169.1	0.48	0.0040	5.5	0.0030	9.6	0.0646	8.0	0.083	25.0	1.4
34	506	258	0.51	0.0038	5.5	0.0022	8.8	0.0598	7.5	-0.118	24.0	1.3
35	422.7	196.4	0.46	0.0044	5.9	0.0093	11.0	0.1400	8.6	0.524	24.8	1.5
36	460.4	238.9	0.52	0.0039	5.7	0.0028	8.7	0.0719	7.4	0.074	24.1	1.4
37	483.4	220.5	0.46	0.0038	5.5	0.0035	9.0	0.0897	7.1	0.117	23.4	1.3
38	570	282	0.49	0.0043	6.4	0.0093	11.1	0.1420	7.7	0.785	24.0	1.5
39	419	151.4	0.36	0.0036	5.9	0.0026	10.0	0.0611	8.0	-0.013	22.5	1.3
40	509	240.3	0.47	0.0036	5.5	0.0025	8.2	0.0762	6.6	0.159	22.6	1.2
41	312.6	98.7	0.32	0.0037	5.9	0.0030	10.2	0.0661	9.1	-0.041	23.3	1.4
42	333.9	101.5	0.30	0.0038	5.8	0.0034	10.6	0.0691	9.4	-0.145	23.9	1.4
43	676	513	0.76	0.0035	5.7	0.0019	8.4	0.0575	6.4	0.273	22.5	1.2
44	351.2	114.5	0.33	0.0039	5.9	0.0030	9.3	0.0728	7.7	0.115	24.3	1.4
45	404.8	222.2	0.55	0.0051	7.7	0.0250	16.2	0.2100	10.5	0.896		

[a] U and Pb content and Th/U ratio were calculated relative to coltan 139. b rho is the $^{206}Pb/^{238}U/^{207}Pb/^{235}U$ error correlation coefficient. [c] corrected for background, within-run Pb/U fractionation (in case of $^{206}Pb/^{238}U$) and common Pb using Stacy and Kramers (1975) model Pb composition.

Table 10: Results for the columbite dating using the MS Excel© calculation spreadsheet after Gerdes and Zeh (2006, 2009) for data procession.

Spot	$^{207}Pb^{a}$ (cps)	U^{b} (ppm)	Pb^{b} (ppm)	$\frac{Th^{b}}{U}$	$^{206}Pbc^{c}$ (%)	$\frac{^{206}Pb^{d}}{^{238}U}$	±2σ (%)	$\frac{^{207}Pb^{d}}{^{235}U}$	±2σ (%)	$\frac{^{207}Pb^{d}}{^{206}Pb}$	±2σ (%)	rho[e]	$\frac{^{206}Pb}{^{238}U}$	±2σ (Ma)	$\frac{^{207}Pb}{^{235}U}$	±2σ (Ma)
A06	569	685	2.9	0.66	1.4	0.00368	3.3	0.0229	9.5	0.0451	8.9	0.35	23.7	0.8	23.0	2.2
A07	367	363	1.5	0.47	1.8	0.00383	3.8	0.0248	8.0	0.0470	7.1	0.47	24.7	0.9	24.9	2.0
A08	513	687	3.0	0.61	0.9	0.00397	3.5	0.0253	9.1	0.0462	8.3	0.39	25.5	0.9	25.3	2.3
A09	402	419	1.8	0.44	2.1	0.00397	3.7	0.0250	9.2	0.0457	8.5	0.40	25.6	0.9	25.1	2.3
A10	26135	384	20.7	0.58	25.9	0.00385	11	0.0270	17.3	0.0509	13	0.63	24.8	2.7	27.1	4.6
A11	375	249	1.1	0.34	4.0	0.00394	4.3	0.0248	12.0	0.0456	11	0.35	25.4	1.1	24.9	3.0
A12	1230	616	3.5	0.85	10.1	0.00393	3.9	0.0255	12.1	0.0471	11	0.32	25.3	1.0	25.5	3.1
A13	813	570	2.7	0.50	7.0	0.00383	3.8	0.0232	13.8	0.0440	13	0.27	24.6	0.9	23.3	3.2
A14	727	623	3.0	0.69	3.9	0.00387	3.3	0.0240	8.6	0.0450	8	0.38	24.9	0.8	24.1	2.0
A15	849	946	4.8	1.02	0.3	0.00401	3.2	0.0266	5.8	0.0481	4.8	0.56	25.8	0.8	26.7	1.5
A16	7954	544	7.9	0.68	25.0	0.00378	5.4	0.0243	18.6	0.0467	18	0.29	24.3	1.3	24.4	4.5
A17	282	269	1.1	0.28	5.1	0.00383	4.3	0.0221	16.6	0.0419	16	0.26	24.7	1.1	22.2	3.6
A18	373	365	1.5	0.34	1.4	0.00375	3.9	0.0245	8.9	0.0473	8.1	0.43	24.2	0.9	24.5	2.2
A19	507	230	0.9	0.25	3.0	0.00388	3.3	0.0238	11.7	0.0445	11	0.28	25.0	0.8	23.9	2.8
A20	865	402	1.6	0.49	3.3	0.00368	3.2	0.0256	9.8	0.0504	9.3	0.33	23.7	0.8	25.6	2.5
A21	1198	492	2.0	0.29	4.4	0.00376	3.2	0.0251	7.3	0.0484	6.5	0.44	24.2	0.8	25.2	1.8
A22	1251	422	1.9	0.34	6.2	0.00400	3.2	0.0264	7.4	0.0480	6.6	0.44	25.7	0.8	26.5	1.9
A23	1242	371	1.7	0.56	7.2	0.00370	3.7	0.0234	11.2	0.0459	11	0.33	23.8	0.9	23.5	2.6
A24	694	325	1.4	0.51	2.4	0.00377	3.2	0.0241	8.9	0.0463	8.3	0.35	24.3	0.8	24.2	2.1
A25	771	387	1.6	0.43	1.7	0.00372	3.6	0.0247	8.3	0.0482	7.4	0.43	23.9	0.9	24.8	2.0
A26	719	406	1.6	0.44	1.7	0.00365	3.4	0.0226	8.6	0.0450	7.9	0.40	23.5	0.8	22.7	1.9
A27	444	457	2.1	0.57	1.1	0.00406	3.4	0.0263	9.5	0.0471	8.9	0.36	26.1	0.9	26.4	2.5
A28	422	451	1.9	0.44	2.4	0.00390	3.6	0.0238	9.7	0.0442	9	0.37	25.1	0.9	23.9	2.3
A29	417	428	1.8	0.57	1.2	0.00375	3.7	0.0242	9.4	0.0469	8.6	0.39	24.1	0.9	24.3	2.3

Spot size = 19 and 28 µm, respectively; depth of crater ~20µm. $^{206}Pb/^{238}U$ error is the quadratic additions of the within run precision (2 SE) and an estimated repeatibility of 2% (2 SD). $^{207}Pb/^{206}Pb$ error propagation (^{207}Pb signal dependent) following Gerdes & Zeh (2009). $^{207}Pb/^{235}U$ error is the quadratic addition of the $^{207}Pb/^{206}Pb$ and $^{206}Pb/^{238}U$ uncertainty. [a]Within run background-corrected mean ^{207}Pb signal in cps (counts per second). [b] U and Pb content and Th/U ratio were calculated relative to GJ-1 reference zircon. [c] percentage of the common Pb on the ^{206}Pb. b.d. = below dectection limit. [d] corrected for background, within-run Pb/U fractionation (in case of $^{206}Pb/^{238}U$) and common Pb using Stacy and Kramers (1975) model Pbcomposition and subsequently normalised to GJ-1 (ID-TIMS value/measured value); $^{207}Pb/^{235}U$ calculated using $^{207}Pb/^{206}Pb/(^{238}U/^{206}Pb*1/137.88)$. [e] rho is the $^{206}Pb/^{238}U/^{207}Pb/^{235}U$ error correlation coefficient. [f] degree of concordance = $^{206}Pb/^{238}U$ age / $^{207}Pb/^{206}Pb$ age x 100. [g] Accuracy and reproducibilty was checked by repeated analyses (n = 7 to 13) of reference columbite 139 and 007 and tantalite Ta-1; data given as mean with 2 standard deviation uncertainties.

Table 10(continued): Results for the columbite dating using the MS Excel© calculation spreadsheet after Gerdes and Zeh (2006, 2009) for data procession.

Spot		$^{207}Pb^{a}$ (cps)	U^{b} (ppm)	Pb^{b} (ppm)	$\frac{Th^{b}}{U}$	$^{206}Pbc^{c}$ (%)	$\frac{^{206}Pb^{d}}{^{238}U}$	±2σ (%)	$\frac{^{207}Pb^{d}}{^{235}U}$	±2σ (%)	$\frac{^{207}Pb^{d}}{^{206}Pb}$	±2σ (%)	rho^{e}	$\frac{^{206}Pb}{^{238}U}$	±2σ (Ma)	$\frac{^{207}Pb}{^{235}U}$	±2σ (Ma)
A30		448	505	2.2	0.52	0.9	0.00383	3.7	0.0248	9.2	0.0470	8.5	0.40	24.6	0.9	24.9	2.3
A31		591	566	2.4	0.52	1.7	0.00375	3.4	0.0236	7.3	0.0456	6.4	0.47	24.1	0.8	23.6	1.7
A32		567	491	2.2	0.47	4.3	0.00395	3.2	0.0257	12.8	0.0471	12	0.25	25.4	0.8	25.7	3.3
A38		483	441	2.0	0.62	2.1	0.00378	3.7	0.0236	12.3	0.0453	12	0.30	24.3	0.9	23.7	2.9
A39		995	666	2.8	0.74	3.0	0.00374	3.4	0.0233	9.9	0.0451	9.3	0.34	24.1	0.8	23.4	2.3
A40		441	208	0.9	0.48	1.9	0.00402	3.9	0.0257	10.0	0.0464	9.2	0.39	25.9	1.0	25.8	2.5
A41		473	233	0.9	0.28	1.0	0.00381	3.5	0.0264	7.8	0.0502	7	0.44	24.5	0.8	26.4	2.0
A42		725	177	0.9	0.46	14.4	0.00389	3.5	0.0258	15.4	0.0480	15	0.23	25.0	0.9	25.8	3.9
A43		556	273	1.1	0.42	1.9	0.00364	3.2	0.0236	10.8	0.0470	10	0.30	23.5	0.8	23.7	2.5
A44		769	368	1.6	0.51	1.8	0.00399	3.0	0.0259	7.9	0.0471	7.3	0.39	25.6	0.8	26.0	2.0
A45		1158	338	1.5	0.45	10.2	0.00364	3.7	0.0226	9.9	0.0451	9.2	0.38	23.4	0.9	22.7	2.2
A46		866	379	1.7	0.47	4.4	0.00392	3.4	0.0258	9.1	0.0478	8.4	0.38	25.2	0.9	25.9	2.3
A47		1007	400	1.8	0.44	5.4	0.00393	3.2	0.0241	8.8	0.0445	8.2	0.36	25.2	0.8	24.2	2.1
A48		2132	478	2.5	0.45	12.6	0.00399	3.2	0.0252	9.7	0.0458	9.1	0.34	25.7	0.8	25.3	2.4
A49		625	343	1.4	0.37	1.1	0.00382	3.2	0.0259	8.7	0.0493	8.1	0.36	24.6	0.8	26.0	2.2
A50		942	432	1.8	0.45	3.1	0.00384	3.1	0.0252	7.7	0.0476	7.1	0.41	24.7	0.8	25.3	1.9
A51		614	276	1.1	0.32	3.3	0.00388	3.5	0.0238	10.7	0.0445	10	0.32	25.0	0.9	23.9	2.5
A52		693	313	1.2	0.29	3.0	0.00373	3.5	0.0255	7.6	0.0496	6.8	0.46	24.0	0.8	25.5	1.9
A53		1023	643	2.8	0.70	1.3	0.00388	3.1	0.0266	7.3	0.0497	6.5	0.43	25.0	0.8	26.7	1.9
A54		865	345	1.5	0.33	4.0	0.00409	3.1	0.0263	10.5	0.0467	10	0.30	26.3	0.8	26.4	2.7
A55		1920	385	2.1	0.61	11.2	0.00405	3.3	0.0292	12.4	0.0524	12	0.27	26.0	0.9	29.3	3.6
A56		41353	1981	145.2	0.02	0.0	0.07940	2.6	0.6281	2.8	0.0574	0.99	0.93	492.6	12.3	494.9	10.9
Tantalite [g]	n=13	56343	1366	104.3	0.02	0.57	0.08059	7.6	0.6382	7.5	0.05744	0.9	0.88	500	37	501	30
Coltan 139 [g]	n=9	61066	1384	105	0.05	0.14	0.08126	4.1	0.6433	4.3	0.05742	0.5	0.87	504	20	504	17
Coltan 007 [g]	n=8	176241	366	136	0.02	0.46	0.3818	3.9	6.7501	4.2	0.12825	1.1	0.96	2085	69	2079	37

2.6. SUMMARY AND DISCUSSION

2.6.1. Xenocrystic vs. Phenocrystic origin

Macroscopic sapphire phenocrysts occur in SiO_2 saturated and undersaturated mafic rocks from the SVF. All sapphires are rimmed by tens to several hundred micrometer sized spinel rims. The spinel coronas around the sapphires indicate a chemical disequilibrium with the host basalt, as primitive alkali basalts are never corundum-normative. In the CMAS system (Sen and Presnall, 1984; Milholland and Presnall, 1998; Liu and Presnall, 1990; 2000) a hypothetical cooling path of a basaltic model melt will never intersect the corundum stability field. In the presence of MgO (in CMAS) or MgO + FeO (in basalt), stable aluminous phases coexisting with near-liquidus melts are spinel at 1 to 2 GPa, garnet at ~ 3 GPa, or anorthite at pressures < 1 GPa. Hence, the stability of corundum is not only a function of the alumina content of a melt, but is also sensitive to the presence of MgO and FeO. In a primitive melt with high MgO and FeO contents, corundum will never be a stable alumina phase. The sapphires of the alkaline basalts from the SVF must therefore be of a xenocrystic nature, which is well in accord with the literature on other alkaline basalt hosted sapphires, as pointed out in the introductory chapter of this work. The basaltic melts only functioned as a transport medium that carried the sapphires from a deeper situated reservoir to the surface.

2.6.2. Magmatic vs. metamorphic origin

Accepting a xenogenetic relationship between the sapphires and the host basalt, the first question to be answered is the geological nature of the sapphires, i.e., whether they formed via igneous or metamorphic processes. According to Peucat et al. (2007), the

geological origin of basalt hosted sapphires can be constrained by the Ga/Mg ratio. In terms of their Ga, Mg, Fe, and Ti concentrations, the sapphires from the SVF can be assigned to two different groups with Group I sapphires having low Ga/Mg ratios at high Fe_{tot} and Group II sapphires having high Ga/Mg ratios at lower Fe_{tot}. In the Ga/Mg vs. total Fe and the Fe – Mg – Ti discrimination diagrams that have been established by Peucat et al. (2007) as a tool to distinguish between magmatic and metamorphic sapphires, sapphires of Group I plot in the field for metamorphic sapphires and those of Group II plot in the field for magmatic sapphires. Peucat et al. (2007) claim that magmatic sapphires have rather high Ga/Mg ratios (>10 to >>10) and metamorphic or metasomatic sapphires have rather low Ga/Mg ratios (<10 to <<10). According to the discrimination diagrams by Peucat et al. (2007), the Siebengebirge sapphires would represent a bimodal suite of magmatic and metamorphic origin. Yet, the Ga, Mg, Fe, and Ti trace element signatures are not the only variables referring to the origin of the sapphires. Metamorphic corundum is usually richer in Cr and V and represented by the red variety ruby (cf. with Sutthirat et al., 2001; Sutherland et al., 2003; 2005; Roberts et al., 2004). These authors report typical mineral inclusions for metamorphic corundum to be spinel, sapphirine, diopside, pyrope, meionite, and anatase. Except for spinel, none of these mineral inclusions typical for metamorphic corundum were found in the Siebengebirge sapphires. The occurrence of an unambiguously magmatic mineral inclusion suite comprising amongst other minerals pyrochlore, columbite, calcite and feldspar rather supports a magmatic origin for all sapphires that were investigated within the frame of this study. A further argument for a magmatic origin of the sapphires are the glass inclusions that are definitely magmatic in origin and were not incorporated from the basaltic melt during magma ascent, but were rather trapped by the sapphire during crystal growth. Yet, the most significant evidence for a magmatic origin of the Siebengebirge sapphires is given by their Cenozoic age. The metamorphic basement underneath the SVF is of Devonian age. Had the sapphires been metamorphic in origin, the columbite inclusion would have returned Devonian ages.

2.6.3. Constraints on the parental melt

Important indicators for the parental melt of the Siebengebirge sapphires are the trace element composition and the composition of syngenetic mineral-, fluid-, and glass inclusions, as these directly sample the parental melt. Geochemically, the sapphires are characterized by a strong enrichment in the HFSE up to five orders of magnitude compared to the PM and by extremely subchondritic Nb/Ta and Zr/Hf ratios of 0.13. A transmission electron microprobe study of one area that showed an exceptional enrichment in the HFSE up to five orders of magnitude compared to the PM, revealed that the HFSE are not incorporated in the corundum crystal lattice but rather form tiny, nanometer sized phases that lie crystallographically aligned within the corundum and grew along the (0001) basal plane. Via EDX, only Nb phases (ilmenorutile) could be detected as nanoinclusions, but the other HFSE (Ta, Zr, and Hf) are most probably also carried by nanophases. Importantly, they do not substitute for alumina in the corundum crystal lattice. The HFSE-nanoinclusions most probably formed during crystallization from a melt that was oversaturated in the HFSE. The recurring areas lacking of nanophases represent phases of crystal growth that are associated with an increasing element concentration in the melt that goes along with the increase of the Gibs free energy (ΔG). Only when the critical size of the nucleus is reached in order to trigger crystal growth, nanophases start to precipitate along a well defined crystallization front which is parallel to the c axis of the sapphires.

The mineral inclusion suite comprises feldspar, calcitic and dolomitic carbonate, and Nb, Ti, Mn, Th, and U-rich oxides such as pyrochlore, betafite, columbite, ilmenite-pyrophanite solid solution, and ilmenorutile. Most of these minerals are also reported as inclusions in alkali basalt hosted sapphires from other locations around the world (Coenraads et al., 1990; Guo et al., 1996; Sutherland et al., 1998; Graham et al., 2008; Giuliani et al., 2009).

Both, the mineral inclusion suite as well as the trace element composition of the Siebengebirge sapphires indicate that the parental melt was highly enriched in the HFSE. Only a melt that was oversaturated in the HFSE would precipitate phases such as pyrochlore, ilmenorutile, columbite, and betafite. Such high concentrations in the HFSE are well known from highly evolved silicate melts, and from carbonatitc melts. Most authors (cf. introductory chapter of this work) relate the HFSE enrichment of the sapphires and the presence of columbite, pyrochlore, and of ilmenorutile mineral inclusions to highly evolved silicate melts such as syenites or nepheline syenites. A further observation supporting to favor syenites as parental melts is that repeatedly melt inclusions of syenitic composition were reported from magmatic sapphires (e.g., Pakhomova et al., 2006; Zaw et al., 2006; Izokh et al., 2010). Carbonatites were to date not considered as potential parental melts that crystallized the magmatic sapphires, although many authors (e.g., Coenraads et al., 1990; Van Long et al., 2004; McGee, 2005; Izokh et al., 2010) claimed that CO_2 must have played a significant role in the formation of these sapphires, as CO_2-rich fluid inclusions are commonly observed in most magmatic sapphires. Only Guo et al. (1996) and Limatrakun et al. (2001) assign carbonatitic melts a role in the sapphire petrogenesis. Yet, the only role that was assigned to carbonatites in these studies was their function as CO_2 source, but no possible role as parental melt. The reason to discard carbonatites as parental melts or to disclaim carbonatites to play a significant role in the sapphire genesis is usually based on lack of primary evidence for a carbonatitic melt such as carbonate inclusions. Furthermore, Sutherland et al. (1998) claimed that the columbite inclusions found in carbonatites rather resemble the composition of columbites that were found in syenites than those that were found in carbonatites.

The Siebengebirge sapphires by contrast do show direct evidence for the participation of a carbonatitic melt in the sapphire petrogenesis which is given by the several primary carbonate inclusions in most of the samples, as carbonates only precipitate from magmas

that are CO_2 saturated and that are located at the silicate melt – carbonatite melt two liquid interface in the Hamilton projected (Na_2O + K_2O) – (Al_2O_3 + SiO_2) – (FeO + MgO + CaO) pseudoternary system. Such melts are carbonatites rather than silicate melts. Further striking evidence for a parental melt of carbonatitic composition is given by the silicate glasses in sample 26. These glasses have two different compositions and are either a carbonated silicate or a nephelinitic glass, and probably represent quenched liquids that formed via liquid immiscibility from a carbonated silicate melt, as supported by the recurrence of the vesicular shape that melt 1 (carbonated silicate) forms within melt 2 (nephelinite). If theses glasses formed via liquid immiscibility from a carbonated silicate melt, then a Na_2O and K_2O rich carbonatite melt must have exsolved simultaneously which becomes evident from the phase relations in the Hamilton projection (Fig. 29) showing that both glasses plot in the same field, so they can impossibly be coexisting liquids that exsolved from a common parental melt. Yet, the vesicular structure implies that liquid immiscibility was the process leading to the formation of these structures. After physical separation of the putative carbonatitic melt from the coexisting silicate melt, the carbonatitic melt will evolve separately. Once separated from the silicate melt, the carbonatitic melt will cool via crystallization of silicate minerals until it intersects the silicate – carbonate field boundary (line 'b – c' in Fig. 29). Further cooling along the silicate – carbonate field boundary occurs via the coprecipitation of silicate and carbonate minerals. It is highly favourable that the sapphires from the SVF crystallized from these "missing" exsolved carbonatitic melts. During crystal growth, the exsolved silicate melts were trapped. The fluid inclusion daughter phases that are mostly Na and K sulphate minerals, indicate a high sulphate enrichment of the carbonatitic melt.

Assigning highly evolved carbonatitic melts a potential parentage to the Siebengebirge sapphires is advantageous for further reasons. One problem arising with silicate rocks being the initial host rocks of the sapphires is the necessity of a traceless assimilation of the host rock to selectively incorporate the sapphires into the basaltic melt. This is

considered unlikely for rocks of a silicate composition. In contrast, carbonatites are highly reactive and would thus be immediately consumed and decomposed by the assimilating basaltic melt. A further benefit of carbonatites as parental melts is provided by the extremely low viscosity of carbonatitic melts of ~ $1.5x10^{-2}$ – $5x10^{-3}$ Pa·s (Dobson et al., 1996) which would promote rapid ion transportation through the melt that is needed to form megacrystic corundum at low degree of alumina oversaturation.

2.6.4. Barometry

The estimation of the lithostatic pressure during crystallization is crucial for generating a petrogenetical model as the pressure may be easily converted to a depth of formation, given that the geological context, i.e., the density of the overlying rocks, is well constrained. Two widely used methods for geobarometry are (1) Pressure dependent phase transitions, e.g. the transition of calcite to aragonite (e.g., Johannes and Puhan, 1971), of quartz to coesite (Bohlen, 1982) or of albite to jadeite and quartz (Holland, 1980), or pressure dependent element partitioning, such as the solubility of Al_2O_3 in orthopyroxene coexisting with garnet (Harley and Green, 1982). (2) The internal pressure of CO_2 fluid inclusions in minerals.

As CO_2 rich fluid inclusions are abundant in the Siebengebirge sapphires, these are used to estimate the pressure of mineral crystallization. Fluid inclusions in the Siebengebirge sapphires are mostly aligned along trails or randomly distributed within the whole sample. They are pure CO_2 fluids with predominantly sodium sulfate daughter phases such as (natro-)alunite, thenardite, aphthitalite, blodite, paravauxite, and dawsonite.

The internal pressure of fluid inclusions can be estimated from their vibrational spectra using Raman spectroscopy, and reflects the barometric conditions during fluid trapping, i.e. during host phase crystallization. The determination of the internal pressure from CO_2

fluid inclusions in natural samples using Raman spectroscopy has been successfully conducted for the first time by Bertrán (1983). The Raman spectrum of CO_2 has two main peaks at $\nu_+ = 1388.0\ cm^{-1}$ (upper band) and $\nu_- = 1285.5\ cm^{-1}$ (lower band) which are called a Fermi diad. The distance between the upper and the lower band is called the Fermi diad split. The exact position of the upper and lower band, and thus the width of the CO_2 Fermi diad split, is density dependent. With increasing density, the bands shift to lower frequencies (wavenumbers). As the frequency shift of the lower band is more susceptible to density changes as the upper band frequency shift (Garrabos et al., 1980), the width of the CO_2 Fermi diad split will increase with increasing density, and is thus a direct measure of the density of the CO_2 bearing fluid inclusion. The relationship between the density of a CO_2 bearing fluid inclusion and the Fermi diad split is intensively studied in detailed works by Rosso and Bodnar (1995), Kawakami et al. (2003), Yamamoto and Kagi (2006), Song et al. (2009), Fall et al. (2011) and Wang et al. (2011). For the Siebengebirge sapphires, the equation (7) by Wang et al. (2011):

$$\rho = 47513.64243 - 1374.824414\Delta + 13.25586152\Delta^2 - 0.04258891551\Delta^3 \qquad (7)$$

was used to quantify the density of the fluid inclusion with ρ being the density of the fluid, and Δ being the width of the CO_2 Fermi diad split (Figure .35).

The pressure during entrapment of the fluid into the host crystal can be calculated from the volumetric properties of the fluid inclusion, given that the composition and the trapping temperature is known as in a closed system, pressure and temperature vary isochoric. Raman spectroscopy characterizes the fluid inclusions to be pure CO_2. The P-T-V relationship for pure CO_2 has been calculated by Yamamoto (2002) basing on data for the equation of state for CO_2 by Pitzer and Sterner (1994). Assuming that the Siebengebirge sapphires crystallized from carbonatitic melts, and taking average

liquidus temperatures for carbonatites of 700 to 1000 °C (Dobson et al., 1996; Genge et al., 1995; Wolff, 1994) for modeling, the pressure of sapphire crystallization lies between 0.1 and 0.6 GPa (Fig. 36), corresponding to depths of 3 to 15 km. Yet, the pressure of 0.6 Gpa must be regarded as minimum pressure during crystallization. The fluid inclusions with the lower densities probably decrepitated during ascend, and hence only represent pseudosecondary fluid inclusions. Hence, the crystallization of the Siebengebirge sapphires must have occurred at least at mid-crustal levels.

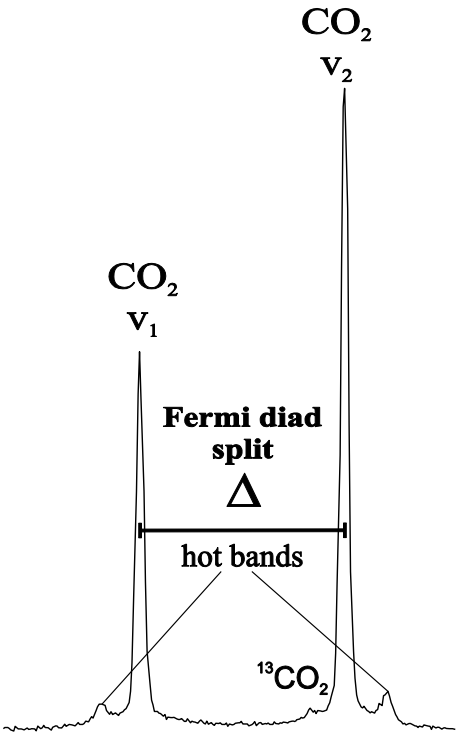

Figure 35: Typical vibrational spectrum of CO_2. The width of the Fermi diad split is controlled by the fluid density.

The pressures estimated for the Siebengebirge sapphires from their CO_2 bearing fluid inclusions are well in accord with pressures estimated for sapphires from Weldborough sapphire, Australia (McGee, 2005), and from the Nezametnoye deposit in the Primorsky Region, Far East Russia (Pakhomova et al., 2006) which are 0.45 GPa, and 0.17 to 0.3 GPa, respectively. Only pressure estimates for the Barrington sapphires, Australia (Sutherland et al., 1998a) exceed the estimates for the Siebengebirge sapphires, although

the estimated pressures of 0.7 to 1.1 GPa correspond to a depth of ~ 20 to 35 km, which is consistent with a crystallization at crustal depths. The temperature estimates for the Barrington (720 – 880 °C) and the Nezametnoye (780 – 820 °C) sapphires are also well in accord with a putative crystallization from carbonatites at low magmatic temperatures. Hence, the pressure and temperature estimates for the Siebengebirge sapphires of 0.3 to 0.6 GPa, and 700 to 1000 °C agree with either the pressure estimates (Barrington and Nezametnoye) or the temperature estimates (Nezametnoye and Weldborough) from the literature, indicating similar petrogenetic settings for crystallization. All P-T estimates from the literature, and from this study are well in accord with a crystallization of the magmatic sapphires from carbonatitic melts at mid crustal levels.

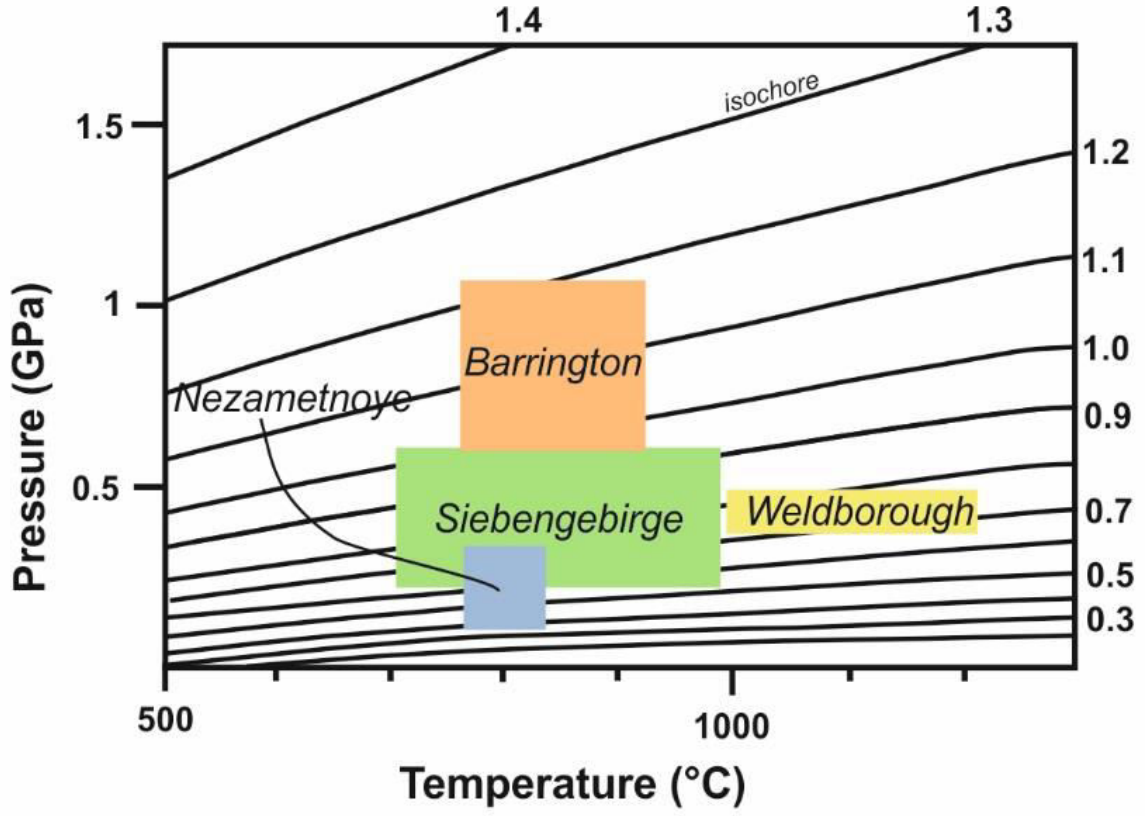

Figure 36: P-T-δ relationships for CO_2 calculated by Yamamoto (2002) after data of the equation of state by Pitzer and Sterner (1994). Shown is the field for CO_2-bearig fluid inclusions from the Siebengebirge sapphires, assuming average temperatures of 700 to 1000 °C (Dobson et al., 1996; Genge et al., 1995; Wolff, 1994) for the carbonatites that crystallized the sapphires. For comparison, the fields for the Barrington (Sutherland et al., 1998a) and Weldborough (McGee, 2005) sapphires in Australia, and the sapphires from the Nezametnoye deposit in the Primorsky Region, Far East Russia (Pakhomova et al., 2006).

2.6.5. Genetical relationship between the sapphires and their host rocks

In-situ LA-ICP-MS U-Pb dating of a syngenetic columbite inclusion within a xenocrystic sapphire hosted by alkaline basalt from the Ölberg in the SVF yielded an age of 24.73 ± 0.35 Ma. This age matches perfectly the age of alkaline mafic volcanism in that area. The alkali basalts from the Ölberg have an ^{40}Ar-^{39}Ar isochron age of 24.91 ± 0.45 Ma (Przybyla, 2013) and can thus be regarded as cogenetic with the Siebengebirge sapphires. The Oligocene age of the sapphires confirms a magmatic origin, as a sapphire that originated from the basement below the SVF would have a Variscan age. The accordance between the age of the Siebengebirge sapphires and the alkaline basaltic volcanism in that area provides a crucial evidence for a genetical link between the processes triggering alkaline basaltic magmatism and the crystallization of sapphire megacrysts.

In summary, the microchemical investigations of the Siebengebirge sapphires, including the study of mineral inclusions with the electron microprobe, the study of nanoinclusions with TEM, and the study of fluid inclusions with Raman spectroscopy strongly support that the Siebengebirge sapphires crystallized from a highly evolved carbonatitic melt that in turn formed via liquid immiscibility from a carbonated silicate melt. The potential role of a carbonatitic melt in the genesis of alkaline basalt hosted sapphires is quantified in a set of three experiments that are presented in the chapter 3 of this work.

CHAPTER 3: EXPERIMENTAL STUDIES

3.1. INTRODUCTION

Sapphires hosted by alkaline mafic rocks from the SVF show an extensive reaction with the host rock as a consequence of chemical disequilibrium between the sapphire and the basaltic melt. This reaction resulted in the formation of a spinel corona around each sapphire, strongly supporting a xenogenetic relationship between the sapphires and the hosting basalt. As demonstrated in the previous chapter, it is evident that the sapphires are of an igneous origin. A metamorphic origin can be ruled out mainly because of the Cenozoic age of the sapphire crystallization that was ascertained by U-Pb dating of a syngenetic columbite inclusion. Regarding the question about the nature of the melt parental to the sapphires, the sapphires show significant evidence for a carbonatitic melt to be a likely melt from which the sapphires crystallized. Primary evidence for the participation of a carbonatite is given by the sapphires' strong enrichment in the HFSE and by the presence of abundant carbonate inclusions in some of the samples. These carbonate inclusions, some of which are primary, present a hitherto missing link to the involvement of carbonatitic melts in the sapphire petrogenesis. There are two putative scenarios how a carbonatitic melt could have participated in the crystallization of magmatic sapphires; either via reaction with a highly evolved silicate melt where CO_2 from the carbonatitic melt decreases the alumina solubility in the silicate melt, triggering the precipitation of corundum (Guo et al., 1996), or via direct crystallization of sapphire from a carbonatitic melt that is oversaturated in Al_2O_3.

In the following chapter, a set of three experiments is presented. These experiments were aimed at investigating the physicochemical relationship between the sapphire withs and the hosting basalts and to evaluate the potential role of a carbonatitic melt in the sapphire petrogenesis. The first set of experiments is a time series where corundum was equilibrated with powder of natural basalt at magmatic temperature and lower mantle pressure for durations between 1.5 and 48 hours. These experiments aimed at determining the residence time of the sapphires in the basaltic melt on the basis of the thickness of the spinel reaction corona. The second experimental serie are reconnaissance experiments that were designed to estimate the possibility of the direct crystallization of corundum from carbonatitic melts of different compositions. The third experimental series was conducted in the corundum - silicate melt – carbonatite melt system to investigate the behavior of corundum in contact with both melts.

3.2. RESIDENCE TIME OF SAPPHIRE IN BASALT: TIME-SERIES EXPERIMENTS

The sapphire and the basaltic melt are in chemical disequilibrium, expressed by the spinel corona surrounding each sapphire. The reaction of the sapphires with the basaltic melt to form the spinel rim is a consequence of the adaption of corundum to the changing chemical conditions imposed by the basaltic melt and follows the equation:

$$Al_2O_{3\ (corundum)} + MgO_{\ (melt)} + FeO_{\ (melt)} = (Mg,Fe)Al_2O_{4\ (spinel)}. \qquad (8)$$

This reaction will continue to take place until chemical equilibrium is attained. For corundum in the basaltic melt this means that the reaction will continue until either the corundum is completely consumed, or until the basaltic melt is so depleted in FeO and MgO that the reaction stagnates. First case is not likely, as there would be no more corundum left in the basalt and latter case is unlikely, as the FeO and MgO reservoir is too large to significantly decrease the MgO and FeO content in the melt by the reaction with the sapphire to form spinel. In nature, an intermediate solution between both scenarios is observed, where the reaction arrests in situ. The reason for this may be given either by the porous spinel rim at the interface between sapphire and melt that may protect the sapphire from being completely consumed, or maybe the melt cooled so rapidly that the reaction kinetics are too slow and the reaction ceased before the sapphire could be consumed completely. If latter is the case, then the width of the spinel rim may be a function of the magmatic temperature and of the residence time of the sapphire in the basaltic melt. The sapphires from the SVF have homogeneous thicknesses that range between 50 and 300 micrometers from sample to sample (See table 2 for average spinel rim thicknesses) and thus may provide crucial information about the residence time of the sapphire in the basaltic melt, given that the kinetics of the reaction is known.

To simulate the reaction of the basaltic melt with corundum to form spinel, the reaction experiments were conducted. The main questions to be answered in these experiments are first, if it is possible to derive the residence time of sapphires in a basaltic melt just from the thickness of the spinel rims, and second which factors control the spinel formation reaction rate: the amount of MgO and FeO, or rather the deficiency in Al_2O_3 in the melt?

3.2.1. Experimental procedure

For the experiments, dried powder of alkaline basalt hosting sample PE25 (for composition see Tab. 3) was used as starting mix. The basalt was ground in acetone in an agate mortar. Ten wt. % corundum splitters in form of synthetic Al_2O_3 were mixed to the basalt powder and filled into Pt capsules with an outer diameter of 4 mm that was subsequently shut under Ar atmosphere with a tungsten spot welder. The sealed Pt-capsules were loaded into inner boron-nitride sleeves. Talc-pyrex assemblies were used as pressure media and graphite heaters were used as heating elements. Temperatures were monitored using a C-Type $W_{95}Re_5/W_{74\%}Re_{26}$ thermocouple positioned at the top of the capsule and are maintained to ± 5 °C of the designed run-temperature. The experimental assemblies were loaded into a ¾ inch pressure vessel. The experiments were conducted with a Bristol type Piston Cylinder Press, using the piston-in technique. The run temperature was kept at 1250 °C and a pressure of 1 GPa. 1250 °C were used as run temperature, as the liquidus temperature for a melt with 8.9 wt. % MgO (MgO content in the starting mix) is 1193 °C at 1 bar (Helz and Thornber, 1987). At 1 GPa, the liquidus temperature is slightly higher (1266 °C, Sugawara, 2000). The experiments were equilibrated for 1.5, 4, 8, 12, 24, and 48 hours. The time series experiments were complemented by one decompression experiment that aimed to estimate the effect of pressure on the stability of the spinel corona. Therefore, the same stating mix and experimental assemblies were used as for the time series. After the experiment was equilibrated at 1 GPa and 1250 °C for 24 h, the experiment was decompressed to a pressure of 0.6 GPa where it was equilibrated for another 4 h before quenching. The experiments were terminated by thermal quenching and subsequent depressurization and recovery of the sample assembly from the pressure vessel.

After each experiment, the Pt capsules were opened and the quench product was mound in epoxy and polished with diamond-polish to ensure that the corundum fragments are plane. Run products were then analysed with the Electron Microprobe. Of each run

product, electron dispersive element distribution maps were made to visualize the change of element distribution as a function of time. The thicknesses of the newly formed spinel rims were estimated from backscattered electron images obtained with the Electron Microprobe. The inhomogeneous rim size of the spinel rims complicated the measurement of the thickness. Therefore, the spinel rims of the run products were measured at 20 to 30 different localities for each run and then averaged out, to get a precise as possible estimate of the average spinel rim thickness.

3.2.2. Results

Petrography of the run products

Backscattered electron images of selected run products are presented in Figure 37. In all experiments, the corundum splitters reacted with the basaltic melt to form spinel coronas at the corundum – basalt interface. The most important observation is that the spinel rim thickness increases with increasing run duration. Yet after the shortest run time of 1.5 hours, the spinel rim has an average thickness of 5 to 6 µm and increases to an average thickness of 31 µm after a run time of 48 h. A further striking observation is that after a time of 24 h, the spinel rim starts to recrystallize and to form nearly euhedral disintegrated grains (Fig. 37 b and c) which detach from the reaction rim surrounding the sapphire, as soon as they reach a composition in equilibrium with the melt.

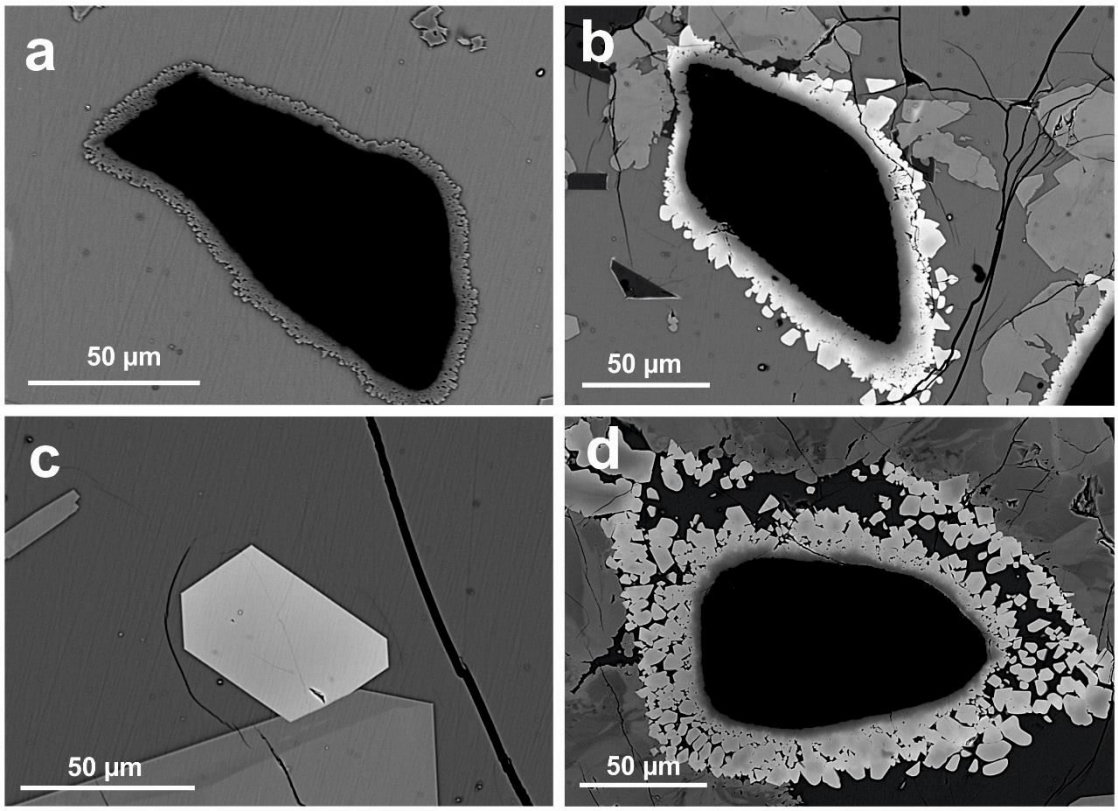

Figure 37: Backscattered electron images of selected run products of the experimental time series. a: Run product of the 4 h run. Spinel forms a homogeneous rim of almost equal thickness at the interface between corundum and the melt. b and c are images of run products after 24 hours. Image b shows that the spinel rim thickness more than doubled compared to the 4 hours run. At the spinel – melt interface, single spinel grains detach from the spinel rim as soon as they are in chemical equilibrium with the melt. Image c shows one completely replaced corundum fragment that now present as a euhedral spinel within the melt. d: Run product after 48 h equilibration. Compared to the 24 h run product, more spinel grains attained equilibrium with the basaltic melt and separated from the spinel rim to migrate into the melt.

The spinel – corundum interface is very sharp and well defined whereas the interface of the spinel rim towards the basaltic glass is diffuse. With increasing run time, the porosity of the newly formed spinel rim at the spinel – basalt interface increases until at the highest run times, single spinel grains in contact with the basaltic melt start to disintegrate and to form single homogeneous spinel grains that are detached from the spinel rim. The chemical composition of the spinel rims tends to reorganize with increasing run time. This chemical reorganization becomes most evident in the electron dispersive element maps showing the distribution of Fe, Mg, Al, and Cr of the experimental run products (Fig.38). After 1.5 hours run time, Fe, Mg, and Cr are homogeneously distributed within

the newly formed spinel rim, but with proceeding run time, Mg and Al become richer at the spinel – corundum interface, whereas Fe and Cr show the reverse pattern and tend to become richer with increasing distance from the spinel – corundum interface, resembling the chemical gradient that was observed in the natural sapphires from the SVF. Similar observations have been made by Watson and Price (2002) for the reaction of periclase with corundum to form spinel. These authors report that the spinel rim developing at the interface between the two disequilibria phases may show a significant Mg excess at the spinel – corundum interface compared to the spinel – periclase interface. The decompression experiment did not show any difference compared to the experiments that were conducted at constant pressures.

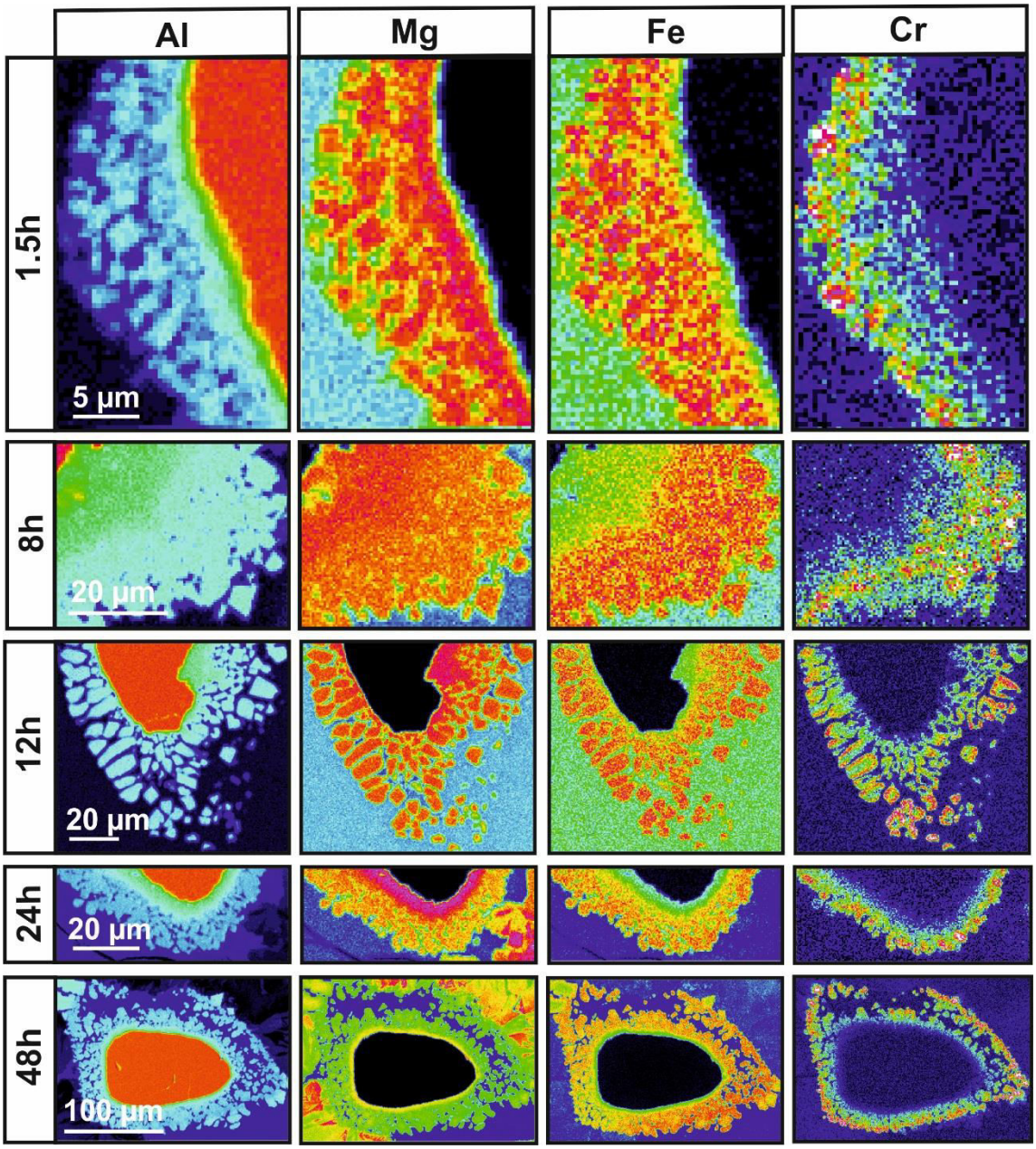

Figure 38: Element maps of the run products of the time-series experiments. The warm colors represent higher concentrations and the cold colors represent lower concentrations. The maps show the progressive reaction of corundum with the basaltic melt to form spinel. With increasing run duration, the spinel rim grows and disintegrates to single grains that detach from the spinel rim. Also, with increasing run time, the spinel rim becomes Mg-richer towards the spinel - corundum interface and Fe- and Cr-richer at the spinel – basalt interface.

Summary and interpretation

The time-series experiments where corundum was equilibrated in alkaline basaltic melt demonstrated that yet after a very short residence time, the corundum gets resorbed and

reacts with MgO and FeO in the melt to form a spinel rim at the corundum – melt interface according to equation 8. The spinel composition changes with time, so that the spinel at the interface towards the corundum becomes richer in Mg and Al, whereas Fe and Cr increase towards the spinel – basalt interface. The same chemical element distribution can be made for the natural spinel coronas surrounding the Siebengebirge sapphires. Remarkably, in the experiments spinel in contact with the basaltic melt detaches and migrates away from the spinel rim as soon as it equilibrated with the basaltic melt. The natural spinel rims enclosing the Siebengebirge sapphires show that the process of spinel detachment was initiated but not completed (see Fig. 8), inferring that the spinel rims surrounding the Siebengebirge sapphires did not reach equilibrium with the basaltic melt at the time when the reaction ceased. This observation is crucial towards the understanding of the spinel rim formation, as it evidences that the spinel rims surrounding the Siebengebirge sapphires did not reach equilibrium with the basaltic melt, so that the reaction was forced to cease, probably due to cooling below solidus temperatures. This is the first hint to that the sapphires probably resided only for a very short time in the hosting basalt.

A further question is the possibility to derive information from the experiments about the pressure at which the sapphires reacted with the basaltic melt to form the spinel coronas. As mentioned in the petrographical description of the sapphires, the basalt that is directly in contact with the spinel coronas surrounding the Siebengebirge sapphires is dominated by plagioclase. Fe and Mg bearing minerals that are commonly found in a basalt such as pyroxene and olivine are only scarcely present. As the nature of the stable alumina phase is a function of pressure, the plagioclase zone at the contact towards the spinel rim may be the result of decompression during ascend following the reaction

$$((2-x)/2)(Mg_yFe_{1-y})Al_2O_3 + xCaO + ((1-x)/2)Na_2O + (2+x)SiO_2$$

$$= (Ca_xNa_{1-x})Al_{2-x}Si_{2+x}O_{8} + yMgO + (1-y)FeO + (-0.25+x/2)O_2. \quad (9)$$

Yet, the decompression experiment showed that there is no reaction of spinel with the melt to form plagioclase at decreasing pressure, indicating that independent from the pressure in the system, as long as there is FeO and MgO present in the melt corundum will react to form spinel, and this spinel corona will not decompose to form plagioclase at decreasing pressure. These observations support that the factors controlling the reaction of corundum with are melt is the MgO and FeO contents in the melt rather than the Al_2O_3 content. The decompression experiment furthermore demonstrates that the plagioclase rich zone at the contact to the spinel rim most probably represents a zone that is depleted in MgO and FeO due to leaching by the reaction with corundum to form spinel.

Reaction kinetics

The thickness of the spinel rim increases with increasing run time and follows a parabolic time dependence, as shown in Fig. 39. The larger error bar for the longest run time is the result of the problematics of measuring the spinel rim thickness, as the spinel grains start to disintegrate so it is hard to determine the exact position of the spinel – melt interface. The parabolic time dependence of the spinel layer thickness indicates that the reaction is a diffusion controlled process. Similar growth relations were observed for the reaction of corundum with periclase (MgO) to form spinel by e.g., Whitney and Stubicam (1971), Zhang et al. (1996), and Watson and Price, (2002).

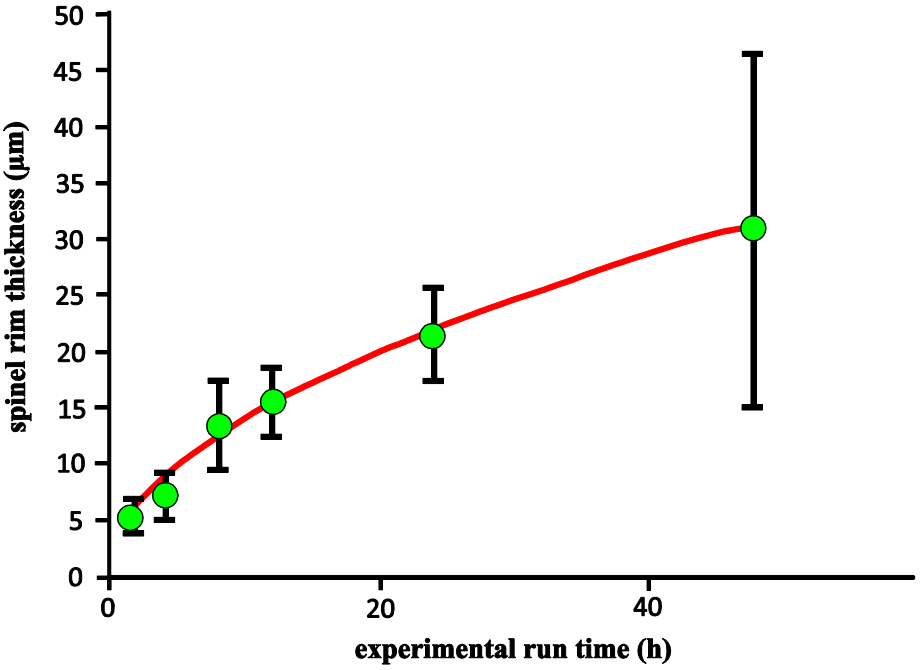

Figure 39: Relation between the spinel rim thickness and the experimental run time. Each point represents one experiment. The vertical bars are 1 sigma errors on the average of the measured spinel rim thicknesses.

Valuable clues to the processes controlling the reaction of the basaltic melt with the sapphire to form a spinel corona, i.e. if the reaction follows a dissolution-precipitation process or diffusion controlled coupled cation exchange, can be obtained from the reaction product itself, i.e. the spinel rim. There are two major observations that support dissolution-precipitation to be the process predominantly controlling the reaction of corundum with the basaltic melt to form spinel. Firstly, the porosity of the spinel corona that increases towards the spinel – basalt interface which is a very characteristic phenomenon for materials dissolved by fluids (e.g., Békri et al., 1995; Putnis, 2002). The second observation is less obvious than the porosity increase, but still striking. As mentioned in the previous chapter, two sapphires have patchy zones that are enriched in Nb and Ta up to five orders of magnitude compared to the PM (McDonough and Sun, 1996). The TEM study revealed that these HFSE that are not represented in equation 8, do not substitute for Al in the sapphire crystal lattice but rather form tiny nanophases

that are crystallographically aligned. In the spinel rim, the HFSE minerals are significantly larger (1-2 micrometer) and are detectable with the Electron Microprobe. This observation implies that the HFSE-nanophases in the sapphires were dissolved into the melt during resorption of the sapphire by the basaltic melt. When the basaltic melt encounters the sapphire, the sapphire is being dissolved at the crystal - melt interface as a consequence of chemical disequilibrium. Subsequently, spinel that is now in equilibrium with the basaltic melt is re-precipitated at the crystal – melt interface. Upon dissolution of the sapphire, the HFSE-nanophases will get dissolved and enter the basaltic melt, so that the melt is enriched in the HFSE at the corundum-melt interface. Owing to the extremely low distribution coefficients between spinel and basaltic melt for the HFSE with $D_{HFSE}^{spinel/liquid}$ between 0.05 and 0.08 (Horn et al., 1994), these highly incompatible elements will not enter the newly precipitated spinel but will rather form distinct phases that precipitate from the melt and are later encorporated as inclusions into the growing spinel rim. These observations both support that the reaction of the sapphires with the basaltic melt followed a dissolution-precipitation process. Surely, dissolution-precipitation reactions are coupled to diffusion controlled cation exchange, as supported by the parabolic time dependence of the mineral reaction: Once the sapphire that is in disequilibrium with the basaltic melt is completely enclosed by a spinel rim, there is no longer a direct interface between the two phases in disequilibrium. Thus, the chemical exchange between the sapphire and the basaltic melt occurs via the spinel rim that has a common interface with both phases. The chemical exchange takes place via intracrystalline cation diffusion. Cation diffusion is a process that runs at a constant rate. Consequently, the time that a cation from the basaltic melt needs to cross the spinel in order to react with the sapphire, is a function of the thickness of the spinel rim. With proceeding reaction and thus with increasing rim thickness, the time that is needed for the cations to cross the spinel increases, so that the reaction slows down with increasing time.

In order to quantify the growth of the spinel rim as a function of time to estimate the residence time of the sapphire in the basaltic melt, the parabolic time – spinel rim thickness relation must be converted into a linear relationship. For that reason, the spinel rim thickness (dx) was plotted against the square root of the experimental run time (√t), so that the two variables follow a linear rate law (Fig. 40).

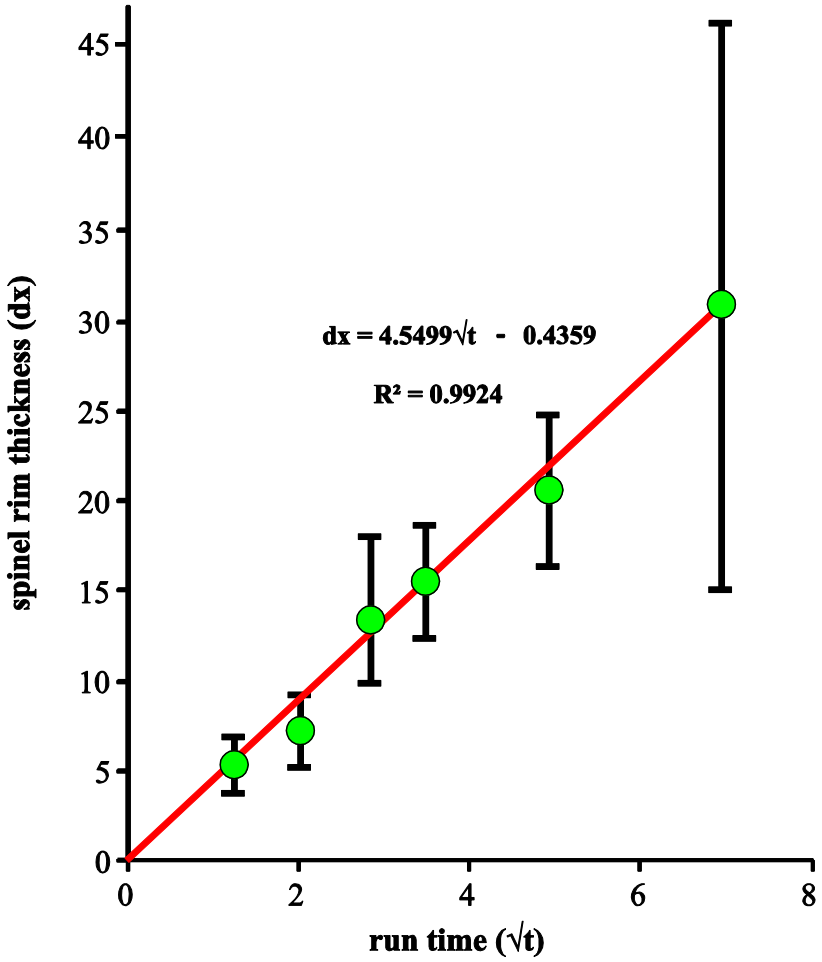

Figure 40: Correlation of the spinel rim size (dx) and the square root of the run time (√t). Each point represents one experiments. The vertical bars are 1 sigma errors on the average of the measured spinel rim thicknesses. The slope of the line is given by the reaction rate constant k.

The thickness of the newly formed spinel layer dx as a function of time obeys a simple rule. Analogue to the procedure of Tammen (1920), the velocity of the increase of the reaction rim thickness $v = \frac{dx}{dt}$ depends on the amount of MgO and FeO reaching the corundum surface and on the amount of Al_2O_3 reaching the spinel – basalt interface. As

the MgO and FeO supply in an open system diverges towards infinity, the amount of MgO and FeO reaching the corundum surface and the amount of Al_2O_3 reaching the corundum – melt interface is reverse proportional to the thickness of the reaction rim, so that

$$\frac{dx}{dt} = \frac{2k}{dx} \tag{10}$$

with k being the reaction rate constant, dx being the thickness of the reaction rim, and dt being the reaction time. Consequently, dx and t obey following relation:

$$dx^2 = 2kt \tag{11}$$

The spinel rim thicknesses of the run products of the experimental time series can thus be transferred into a reaction rate constant *k* that has the unit of diffusivity, following equation 12:

$$k = \frac{dx^2}{2t} (m^2/s) \tag{12}$$

with dx being the spinel rim thickness and t the experimental run time. Values for the reaction rate constant k calculated from each time-series experiment are given in Table 11. The reaction rate constant calculated for the spinel formation includes a kinetic and a thermodynamic component (compare with Watson and Price, 2002). The kinetic

component is derived from the diffusion of MgO and FeO through the spinel layer and the thermodynamic component originates from the composition of spinel at the interfaces with corundum and the melt.

Table 11: Calculated reaction rate constants for the reaction of corundum with the basaltic melt to form spinel. The rim thickness dx are averages of 20 – 30 single thickness measurements. The reaction rate constant was calculated using equation 12. For residence time modeling, the average value for the calculated reaction rate constant k was used.

run time	dx (µm)	k (m^2/s)
1.5	5.4	2.7E-15
4	7.3	1.9E-15
8	13.6	3.2E-15
12	15.6	2.8E-15
24	21.6	2.7E-15
48	31	2.8E-15
Average		2.7E-15

The reaction rate constant calculated from the experimental time-series can be used to derive an equation to calculate the residence time of the natural sapphires in the basaltic melt on the basis of the spinel rim thickness. The equation for the residence time of the sapphires in the basaltic melt can be obtained by the reorganization of equation (12), and by using the average calculated reaction rate constant k = 2.7 * 10^{-15} m^2/s (see Table 11), so that the residence time can be calculated using following equation:

$$t_R = \frac{dx^2}{2k} = \frac{dx^2}{5.4 \cdot 10^{-15}} \quad (13)$$

with t_R being the residence time of the sapphire in the basaltic magma, and dx being the thickness of the spinel rim surrounding the sapphires.

3.2.3. Discussion

Residence time of sapphires in alkali basalt

Applying equation (13) to the natural sapphires from the SVF that have average spinel rim thicknesses of 100 – 300 µm, the corresponding residence times are ~22 days for a spinel thickness of 100 µm, ~86 days for a thickness of 200 µm, and ~195 days for a thickness of 300 µm. The Siebengebirge sapphires hence resided on geological time scale only a very short time of a couple of weeks to months within the basaltic melt. Note that these calculated residence times are only valid for the pressure and temperature conditions of the experimental run, i.e. 1 GPa, and 1250 °C. A change in temperature or pressure will change the reaction rate constant k and will thus influence the residence time estimation. An increase in temperature would result in higher reaction rate constants, following Van't Hoffs equation that describes the change in the equilibrium constant as a function of time in thermodynamic systems. Higher magmatic temperatures than 1250 °C would hence result in faster running reactions, hence the sapphires would have even lower residence times than those estimated by equation (13). Consequently, for lower magmatic temperatures the residence time would be higher than estimated. The effect of pressure on the reaction probably follows the same tendency as the temperature effect (e.g., Wood and Price, 2002), though these authors infer that the increase in the reaction rate constant with increasing pressure is not due to the effect of pressure on the diffusivities, but rather due to the pressure dependency on the phase relations in the Al_2O_3-MgO system. Yet, the experimental run conditions of 1 GPa, and 1250 °C that were chosen for the time-series experiments reflect realistic estimates as they are well in accord with pressures and temperatures estimated for the generation of the Siebengebirge alkaline mafic rocks (e.g., Schubert et al., 2015, and this work).

Magma ascent velocities

From the estimated residence times of the sapphires within the basaltic melt, minimum and maximum ascent velocities of the alkaline mafic melts from the SVF can be obtained. Minimum velocities are given by the settling velocity of the sapphires in the basaltic melt, as given by Stokes law:

$$V = \frac{2gr^2 (\delta s - \delta l)}{9\eta} \quad (14)$$

with V = velocity of magma ascend (cm/s); g = acceleration due to gravity (980 cm/s^2); r = radius of the particle (under assumption of a spherical particle shape); δs = density of the particle (g/cm^3), δ_l = density of the liquid (g/cm^3) and η = viscosity of the liquid (10 Pa·s = 1 poise).

For the Siebengebirge sapphires and a basaltic melt, the parameters used for modeling are δs = 3.93 g/cm^3; δ_l = 2.65 g/cm^3, and η = 1000 poise. Depending on the sapphire size (0.5 to 1 µm, this yields an average mineral settling velocity v_s of 60 to 242 m/d which is the minimum ascent velocity of the basaltic melt that is required in order to carry the sapphires to the surface.

The absolute magma ascent rate can be obtained from combining the estimated depths of sapphire crystallization with the estimated residence time of the sapphires in the basaltic melt and with the calculated settling time for the sapphires. From the barometric investigations in this study, the depth of sapphire formation could be estimated to be between 3 and 18 km, corresponding to the Earth's mid- to upper crust. For the highest magma residence time of 200 days (300 µm thick spinel rim) that was estimated for the Siebengebirge sapphires, maximum relative ascent velocities for the Siebengebirge

sapphires of $v_{a\ (sapphire)}$ of 17 to 78 m/d can be retained. Hence, the carrying basalt must have had an absolute ascend velocity of $v_{a\ (basalt)} = v_s + v_{a\ (sapphire)}$, corresponding to 78 to 320 m/d.

3.3. INVESTIGATIONS OF CORUNDUM IN THE CARBONATITE AND THE CARBONATITE – SILICATE SYSTEM

The microchemical investigations of the Siebengebirge sapphires showed that these did not precipitate from the hosting alkaline basalts but rather crystallized from a different, yet unconstrained parental melt. Although in the literature, a parentage is preferentially assigned to highly evolved syenitic melts (see introductory chapter), the Siebengebirge sapphires show crucial evidence such as carbonate inclusions, CO_2 bearing fluid inclusions and carbonated silicate glass inclusions, for that carbonatitic melts were involved in the petrogenesis of the sapphires. Though carbonatites were previously designed to having played a role in the genesis of alkaline basalt hosted sapphires (e.g., Guo et al., 1996 and Izokh et al., 2010), no one ever tested the feasibility of carbonatites to be the parental melt of the sapphires.

The following two experimental series are aimed to answer two major questions about the sapphire genesis. First, crystallization experiments were performed to estimate the feasibility to crystallize corundum directly from a carbonatitic melt, and which compositional features are controlling the feasibility of the crystallization of corundum from a carbonatitic melt. The wetting experiments in the liquid immiscible basalt – carbonatite system were performed to investigate the behavior of corundum upon interaction with both melts.

3.3.1. Crystallization experiments

The feasibility of crystallizing corundum directly from a carbonatitic melt has been tested in the crystallization experiments. In these experiments, the solubility of Al_2O_3 in a carbonatitic melt of two different compositions was estimated. Furthermore, it has been investigated which effect the MgO and FeO content in a carbonatitic melt that is oversaturated in Al_2O_3 has on the composition of the stable alumina phase that precipitates from the carbonatitic melt upon cooling.

Experimental setup

For the crystallization experiments, five wt. % colloidal Al_2O_3 were added to synthetic carbonatite powders of two different compositions. The starting compositions were one evolved, FeO – MgO deficient carbonatite, and one primitive, FeO and MgO bearing carbonatite. The starting compositions of the FeO - MgO free system is a synthetic pure alkaline carbonatite (Na_2CO_3 : K_2CO_3 : $CaCO_3$ = 70 : 25 : 5) (Experiment SGS 15). For the FeO - MgO-rich run, a carbonatitic composition was synthesized that is in equilibrium with phlogopite lherzolite at 3 GPa and 1100 °C (Thibault et al., 1992) (Experiment SGS 17). The colloidal Al_2O_3 powder was retained by drying down a colloidal Al_2O_3 solution with 50% Al_2O_3 and 50 % H_2O, supplied from Alpha Aesar, and then grinding the residue in an agate mortar. The colloidal nature of the dried Al_2O_3 powder was verified before experimental runs with X-ray diffraction analysis. The starting mixes were filled into Pt capsules with an outer diameter of 4 mm that was subsequently shut under Ar atmosphere with a tungsten spot welder. The sealed Pt-capsules were loaded into inner boron-nitride sleeves. Talc-pyrex assemblies were used as pressure media and graphite heaters were used as heating elements. The experimental procedure followed the same as described for the time-series experiments. The experiments were each equilibrated for 5 h at 1 GPa and 1200 °C. The preparation of

the quenched carbonatites required special attention as first, carbonatites do not quench to glass and are thus not easy to recover from the platinum capsule and second, carbonatites are highly soluble in water, so cutting and polishing needs do ne done under water-free conditions. The sealed Pt capsules were completely embedded in epoxy, and then cut into two halves along the long axis of the capsule. The bisected capsule was then again embedded in epoxy under vacuum to guarantee that the pore spaces are completely soaked with epoxy so that the porous carbonatite remains inside the mound. The run products were subsequently analysed with the Electron Microprobe.

Results and Discussion

In the Fe-Mg bearing system, the only alumina phase that crystallized from the silicate melt was spinel (Fig. 41a). The Fe-Mg free run yielded evenly distributed 10 – 40 µm sized euhedral corundum grains embedded in a matrix of lath like quenched carbonate crystals (Fig. 41b) resembling spinifex textures. Due to the inhomogeneity of the quench phases, the conduction of quantitative analyses with the electron microprobe is difficult, resulting in inhomogeneous element distributions. Hence, the error on element concentrations is larger as for glasses of homogeneous silicate melts. Of great importance is the alumina solubility in the carbonatitic melt, as the solubility of Al_2O_3 determines the amount of alumina that is required to oversaturate the melt so that alumina phases precipitate.

The solubility of Al_2O_3 in the carbonatitic melt differs insignificantly between the two different carbonatite compositions (Fig. 42). To estimate the solubility of Al_2O_3 in the quenched carbonates, 20 to 30 single spots were analyzed. The Fe-Mg free carbonatite yielded a median of 0.3 wt. % Al_2O_3 ($2\sigma = 1.99$) and the Fe-Mg-bearing composition yielded a median of 0.52 wt. % Al_2O_3 ($2\sigma = 0.78$).

The crystallization experiments show clearly that it is indeed possible to crystallize corundum directly from a carbonatitic melt, given that the carbonatitic melt is free of FeO, and MgO. The low solubility of Al_2O_3 in a carbonatitic melt shows that only minor amounts of alumina are required to stabilize Al-bearing phases at liquidus conditions.

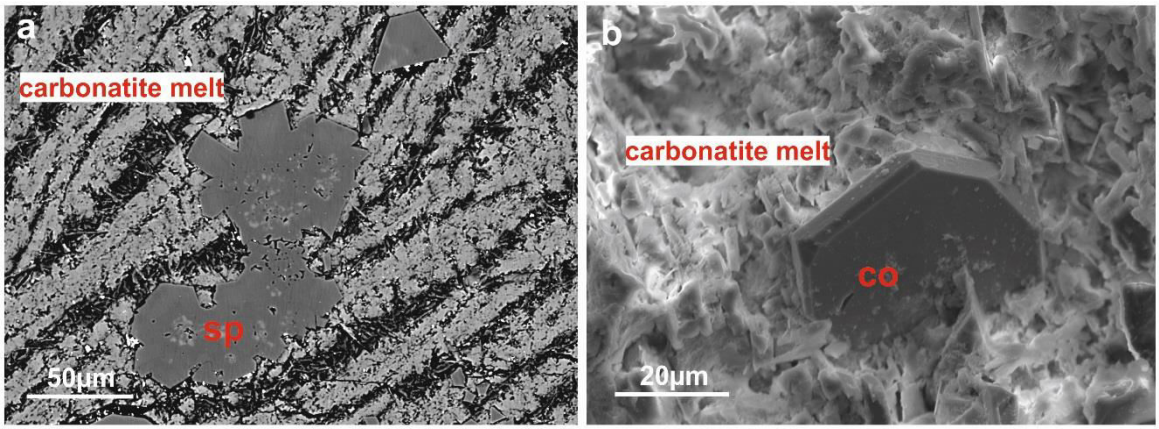

Figure 41: Run products of the crystallization experiments. a: Spinel crystallized from the experiment with the Fe- Mg – bearing starting composition, whereas the experiment with the Fe- Mg –deficient starting composition (b) precipitated euhedral corundum grains.

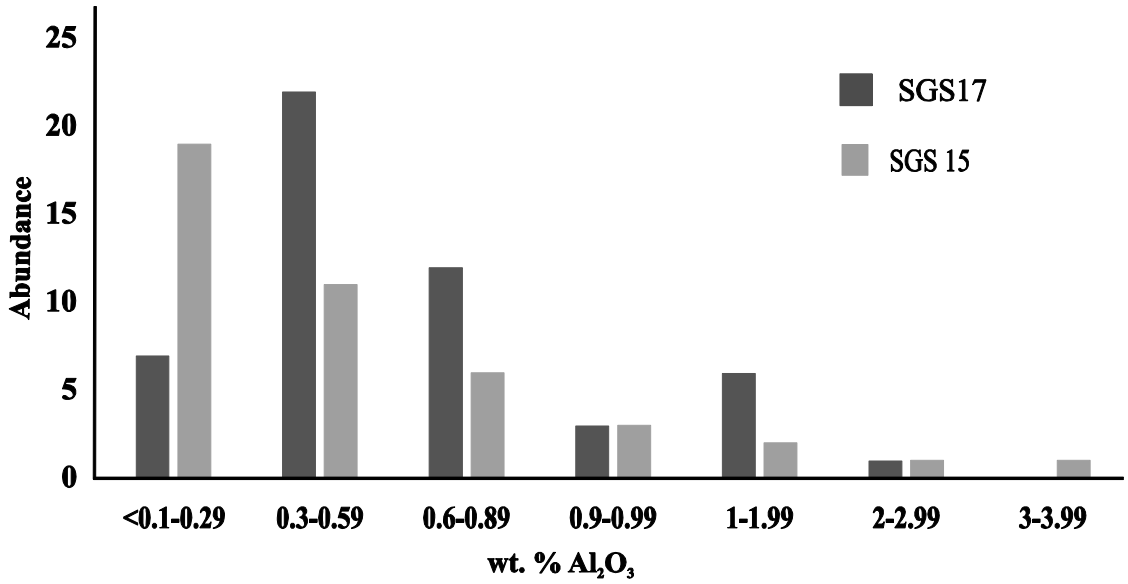

Figure 42: Distribution of the alumina solubility in carbonatitic melt. The distribution comprises 41 single analyses for the Fe-Mg bearing carbonatite and 51 single analyses for the FeO - MgO – deficient carbonatite composition.

3.3.2. Wetting experiments

The wetting experiments were designed to investigate the behavior of corundum in a silicate – carbonatite melt system. The strategy behind this investigation is to evaluate if corundum may have crystallized as a consequence of the interaction of a carbonatitic melt with a silicate melt, as it is implicated by Guo et al. (1996). According to these authors, corundum crystallizes upon the interaction of a highly evolved alumina rich silicate melt such as a syenite with a carbonatitic melt. Injection of the latter into the silicate melt would trigger the crystallization of Al-free silicate phases such as wollastonite ($CaSiO_3$) from the silicate melt and consequently procure an increase in the Al/Si ratio and thus a local Al-oversaturation in the silicic melt fraction at the two-liquid interface. Corundum would then crystallize as a liquidus phase within the silicate melt fraction of the hybridization zone. If such a scenario is applicable for the petrogenesis of magmatic sapphires, then in experiments where a carbonatitic and a highly evolved silicate melt are equilibrated, a significant increase in the Aluminum Saturation Index (ASI = molar Al_2O_3 / [$CaO + Na_2O + K_2O$]) should be observable in the exsolved silicate melt fraction in equilibrium with the carbonatitic melt fraction, compared to the ASI of the silicate powder prior to the interaction with the carbonatitic melt. The ASI in the silicate melt fraction in equilibrium with carbonatitic melt should be greater than 1, so that corundum forms a stable liquidus phase. The HFSE enrichment in the sapphires crystallized in such a hybridization zone should also be explained by the interaction of carbonatitic and silicate melts. Hence, partition coefficients for the HFSE between silicate melt and carbonatite melt ($D_{HFSE}^{carb/sil}$) should be well below 1, so that the HFSE concentration in a silicate melt increases upon interaction with a carbonatitic melt that is rich in HFSE.

Experimental setup

The wetting experiment series is comprised of two single experiments. One reconnaissance experiment and one reversal experiment that was aimed to control and verify the result of the reconnaissance experiment. In the reconnaissance experiment (SGS2), ten wt. % of 100 – 200 µm sized corundum fragments were added to a synthetic silicate-carbonatite mix (starting composition is Mix Ca from Brooker, 1998), that lies within the field of liquid immiscibility in the CO_2-projected (SiO_2+Al_2O_3+TiO_2) – (Na_2O+K_2O) – (CaO+MgO+FeO) ternary diagram (Lee and Wyllie, 1997). For the starting mixes, Si, Al, Ti, Na, and K were added as oxides and Ca, Mg, and Fe were added as carbonates. The powders were ground and mixed in an agate mortar for 1 h, so that a homogeneous mixture was obtained. The starting mix powder was then doped with 200 ppm HFSE (each 50 ppm Nb, Ta, Zr, and Hf), using a 1000 ppm solution. The doped powder was then dried down for 24 h, and then ground and mixed again. The powder was then filled into a Pt capsule that was subsequently arc welded. In a reversal experiment (SGS3), a synthetic FeO - MgO free starting composition (trachytic silicate) was used, in order to prevent the formation of spinel rims. This time, the carbonatite powder was not mixed with the silicate powder but both fractions were loaded separately into the Pt-capsules. The corundum splinters were added solely to the carbonate fraction. The experimental charges were the same. The experiments were each equilibrated in a Piston Cylinder Apparatus at 1 GPa and 1200 °C for 6 h (SGS2) and 4h (SGS3), following the same procedure as described for the time-series experiments.

Results

The starting compositions of the experiments, as well as the resulting silicate and carbonatite melt compositions, and the carbonatite melt – silicate melt partition coefficients for the HFSE ($D_{HFSE}^{carb/sil}$) are summarized in Tab. 12.

In the reconnaissance experiment, a carbonatitic melt exsolved from a silicate melt, as predicted by the starting composition that lies in the field of liquid immiscibility in the Hamilton projected pseudoternary (SiO_2+Al_2O_3+TiO_2) – (Na_2O+K_2O) – (CaO+MgO+FeO) phase diagram. The corundum fragments that were added to the starting mix migrated exclusively into the silicate melt fraction where they reacted with the melt to form broad spinel rims (Fig. 43). At the time of quenching, the silicate melt was CO_2 saturated, as shown by abundant CO_2 gas bubbles in the glass. The carbonatite melt fraction remained virtually free of corundum. This affinity of corundum to migrate into the basaltic melt demonstrates that the wetting ability for corundum is much higher in a silicate melt than in a carbonatitic melt.

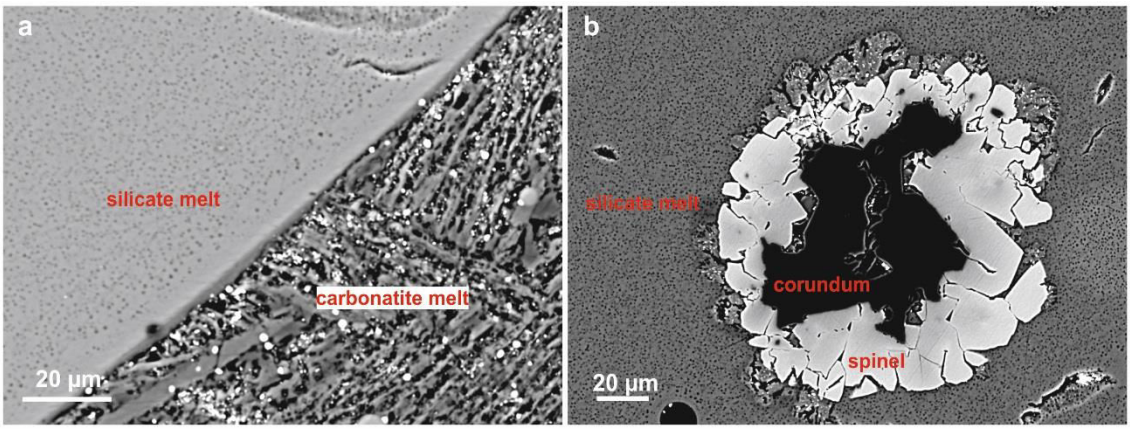

Figure 43: Run product of the wetting experiment SGS2. The corundum grains that were added to the bulk starting mix migrated solely into the silicate melt fraction where it immediately reacted with the basaltic melt to form a spinel rim. The carbonatite melt fraction remained free of corundum. The silicate glass shows tiny bubbles of exsolved CO_2 gas, indicating that the melt was saturated in CO_2 when it was quenched.

The reversal experiment (SGS3) confirmed that the wetting ability for corundum is much better in a silicate melt than in a carbonatite melt. The corundum fragments that

were added only to the carbonate fraction migrated into the silicate liquid during experimental run, leaving the carbonatite virtually corundum free (Fig. 44). Hence, these wetting experiments demonstrate strikingly and unambiguously that corundum hosted by carbonatitic melts will immediately migrate into a silicate melt if given the chance, even if the corundum is highly unstable in the silicate melt and will immediately get resorbed to form spinel coronas.

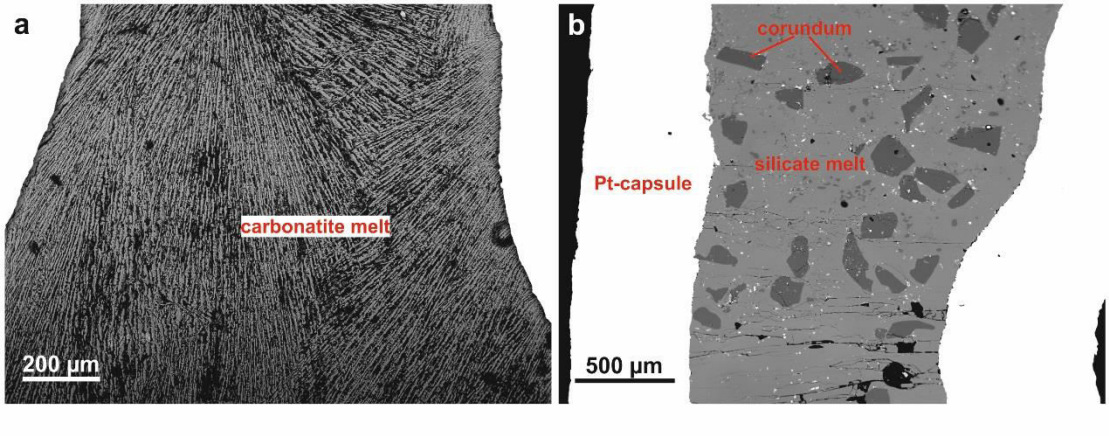

Figure 41: Run product of the wetting experiment SGS3. The carbonatite melt fraction (a) remained free of corundum. The corundum grains that were added to the carbonatite fraction migrated exclusively into the silicate melt fraction (b).

The carbonatite – silicate melt partition coefficients for the HFSE show a decreasing trend from Nb > Ta > Zr > Hf for both, the nephelinitic (SGS3) and the trachytic (SGS2) silicate melt composition, only that the values for the trachytic silicate melt are a magnitude higher than those for the trachytic melt.

In experiments SGS2 (trachytic silicate starting composition), both the ASI and the Al/Si ratio increase in the exsolved silicate melt fraction compared to the starting composition, whereas the coexisting carbonatitic melt shows a decrease in the ASI and an increase in the Al/Si ratio. In experiment SGS3 (nephelinitic silicate melt starting composition), the ASI increases in the silicate melt fraction, and strongly decreases in the carbonatitic melt fraction, whereas the Al/Si ratio remains unchanged in the silicate melt fraction and slightly decreases in the carbonatitic melt fraction. Although in the

experiment with the nephelinitic silicate composition the ASI increases to a value > 1, the glass does not contain normative corundum.

Table 12: Overview of the wetting experiments. SGS2 and SGS3. Given are the starting compositions, as well as the run products and the partition coefficients $D^{carb/sil}$ for the HFSE.

	SGS2							SGS3							
	Starting composition	Run producs		$D^{carb/sil}$				Starting composition		Run producs		$D^{carb/sil}$			
		silicate	carbonatite	Nb	Ta	Zr	Hf	silicate batch	carbonatite batch	silicate	carbonatite	Nb	Ta	Zr	Hf
SiO_2	17.07	36.09	2.51	0.80	0.30	0.21	0.13	62.3	1.96	65.7	0.7	0.09	0.04	0.02	0.01
TiO_2	1.16	1.26	0.52					0.51		0.38	n.d.				
Al_2O_3	4.85	28.15	2.44					19.6		19.5	0.2				
Fe_2O_3	3.97	n.a.	n.a.					1.63		n.a.	n.a.				
FeO	3.16	3.36	2.79					1.53		1.96	0.3				
MgO	6.70	2.03	8.31					0.41		0.38	0.2				
CaO	4.91	1.42	8.17					1.23		1.51	31.9				
Na_2O	27.4	20.6	28.0					6.76		7.20	20.2				
K_2O	0.42	1.07	1.55					5.99		2.97	3.9				
$CaCO_3$	-								24.5						
Na_2CO_3	-								68.6						
K_2CO_3	-								4.90						
CO_2	30.4														
Total	100.0	94.0	54.3					100.0	100.0	99.6	57.4				
ASI	0.09	0.75	0.04					0.99		1.10	0.002				
Al/Si	0.16	0.44	0.55					0.18		0.17	0.14				

Discussion

The wetting experiments were conducted to investigate the behaviour of corundum in the silicate – carbonatite melt system. Both experiments that were designed for that purpose - the reconnaissance and the reversal experiment – markedly demonstrate that upon interaction of a corundum bearing carbonatite with a silicate melt of any composition, the corundum will immediately migrate into the silicate melt due to better wetting properties.

The experiments furthermore provided crucial information about the change of the aluminium saturation of silicate melts that interact with a carbonatitic melt. Guo et al. (1996) proposed that magmatic corundum may crystallize from a silicate melt in which the Al/Si ratio increased upon interaction with a carbonatitic melt, as the CO_2 from the carbonatitic melt would trigger the precipitation of alumina free silicates (e.g., wollastonite). Yet, such a scenario can be excluded from the results of the reconnaissance experiments. For the experiment with the nephelinitic starting composition, an increase of the ASI to > 1 can indeed be observed, indicating that relative to alumina, alkalis were leached out of the melt. Yet, an increase in the Al/Si ratio in the silicate melt that reacted with a carbonatitic melt as implicated by Guo et al. (1996) cannot be observed. It thus seems unlikely that magmatic corundum may form in the hybridization zone of a silicate melt and a carbonatite melt.

The partitioning coefficients for the HFSE between carbonatite and silicate melt obtained from the experiments show that upon interaction of a silicate melt with a carbonatitic melt, the silicate melt will get enriched in the HFSE, and the carbonatitic melt will consequently get depleted. The decrease of $D^{carb/sil}_{HFSE}$ from Nb > Ta > Zr > Hf results in a decrease in the Nb/Ta and the Zr/Hf ratios in the silicate melt compared after interaction with a carbonatitic melt, and the carbonatitic melt will hence bear higher Nb/Ta and Zr/Hf ratios.

3.4. SUMMARY AND CONCLUSIONS

In this chapter, a set of three experiments are presented that were designed to investigate the relationship between the sapphires and the host basalt, and to investigate a potential role of carbonatitic melts in the formation of magmatic sapphires. From these experiments, four major conclusions can be drawn:

(1) Corundum that is being entrained into a basaltic melt will be immediately resorbed by the melt to form a spinel rim. The resorption is kinetically controlled by a dissolution-precipitation process that is bound to intracrystalline coupled cation exchange. The thickness of the spinel corona that formed at the corundum – melt interface (dx) is linearly correlated with the square root of the experimental run time ($\sqrt{t}$), allowing to calculate the reaction rate constant *k* for the reaction of corundum and basaltic melt to form spinel at 1250 °C and 1 GPa. Using the reaction rate constant, a formula could be derived to calculate the residence time of the Siebengebirge sapphires in the hosting basaltic melt as a function of the spinel rim thickness. The results show that the sapphires from the SVF resided only a few weeks to months in the basaltic melt before the magma erupted and crystallized. This short residence time of the sapphires in the basaltic melt is in accord with the close temporal relationship between sapphire formation and basaltic volcanism in the SVF that has been demonstrated in the previous chapter. The formula derived for the residence time of the sapphires in the basaltic melt is universally applicable to all sapphires that are found *in-situ* within basaltic rocks, where the thickness of the spinel rim can be measured.

(2) The ascent velocities of the alkaline mafic melts from the SVF were between 78 m/d and 320 m/d, and are thus lower than typical estimates for alkaline mafic melts of 860 to 8600 m/d (Spera, 1984).

(3) Corundum can crystallize from a carbonatitic melt, given that the carbonatitic melt is saturated in Al_2O_3. The solubility of Al_2O_3 in a carbonatitic melt is extremely low (< 1 wt. %), thus only minor amounts of alumina are required to saturate the melt with a stable alumina phase The prerequisite for corundum to precipitate from a carbonatitic melt is that latter is free of FeO and MgO, i.e. is highly evolved. An FeO-MgO bearing, Al_2O_3 saturated carbonatitic melt would rather precipitate spinel as a liquidus phase.

(4) The wetting experiments demonstrate that the corundum will always migrate into a silicate melt if the carbonatite coexists with the silicate melt, even if the corundum is not stable in this melt and will immediately be resorbed. There is no chance that corundum which precipitated from a carbonatitic melt remains longer in that carbonatitic melt if this carbonatitic melt gets in contact with a silicate melt.

CHAPTER 4: PETROGENETIC MODEL FOR THE CRYSTALLIZATION OF THE SIEBENGEBIRGE SAPPHIRES

4.1. INTRODUCTION

Sapphires that are hosted by alkaline mafic rocks from the SVF are proven to be of a xenocrystic nature. This becomes most evident by the spinel coronas around the sapphires. There is no doubt that the sapphires were entrained into ascending alkaline mafic melts when they encountered the sapphire-bearing parental melt during ascend.

An experimental time-series where corundum was equilibrated with basaltic melt (Chapter 3 in this work) showed that yet after a very short residence time of 1.5 hours, the corundum becomes resorbed by the basaltic melt and forms spinel coronas at the corundum - melt interface. From CO_2-bearing fluid inclusion studies, the depth of sapphire crystallization could be estimated to lie between about 3 and 18 km, corresponding to middle to upper crustal levels. The sapphires were then trapped by fresh pulses of ascending alkaline mafic melts which carried them to the surface. The time-series experiment allowed calculating residence times for the sapphires in the basaltic melt basing on the thickness of the surrounding spinel rim. From these calculations, it becomes obvious that the sapphires resided no longer than a few weeks to months in the basaltic melt before latter erupted ~ 25 Ma ago in the SVF.

As to the xenocrystic nature of the sapphires, the yet unconstrained issue is the true nature of the melt that crystallized the sapphires. Although many authors (e.g., Irving, 1986; Coenraads, 1990; Aspen et al., 1990; Garnier et al., 2005; Giuliani et al., 2009) favor highly evolved silicate melts such as syenites to be the potential parental melt, the Siebengebirge sapphires provide strong evidence for precipitation from a carbonatitic melt. Such evidence is given by the strong enrichment in the HFSE that is reflected by the abundance of HFSE bearing mineral inclusions on a micrometer and nanometer scale, by the occurrence of CO_2-bearing fluid inclusions, and of glasses of nephelinitic and of carbonatitic silicate composition that probably represent quenched liquids that were trapped during crystal growth. Indeed, several studies (e.g., Coenraads et al., 1990; Limatrakun et al., 2001; Zaw et al., 2006; Van Long et al., 2004; McGee, 2005; Pakhomova et al., 2006; Izokh et al., 2010) revealed that the formation of magmatic sapphires hosted by alkaline mafic rocks – the so called blue-green-yellow or BGY sapphires - must be linked in some way to CO_2, as many of these sapphires contain CO_2-rich melt and/or fluid inclusions. Whereas Guo et al. (1996) imply that the sapphires probably crystallized from a highly evolved silicate melt that interacted with a carbonatitic melt, Izokh et al. (2010) discard a direct participation of a carbonatitic melt in the formation of BGY sapphires but imply that the sapphires crystallized from a syenitic melt that is saturated in CO_2 and contains a CO_2-H_2O-rich fluid phase. According to Izokh et al. (2010), the CO_2-rich fluid phase neutralizes the alkali effect of the syenitic melt by binding the alkalis to alkaline carbonate complexes, so that alumina will not participate into alkali feldspar or nepheline but rather precipitates as corundum. In both models (Guo et al., 1996, and Izokh et al., 2010), the role of CO_2 in the sapphire genesis is proposed to cause an alumina excess in a syenitic melt by leaching the alkalis out of the melt. Yet, the authors fail to prove the effectivity of the alkali neutralization effect that is supposed to be caused by the injection of CO_2 from a carbonatitic melt into a neighbouring syenitic melt. The wetting experiments that were conducted (Chapter 3) demonstrate that the alkali neutralization effect via CO_2 injection is not efficient enough

to stabilize corundum as a liquidus phase in a syenitic melt upon interaction with a carbonatitic melt. The interaction of a silicate melt with a carbonatitic melt indeed raises the Alumina Saturation Index (ASI) in the silicate melt fraction, but the increase in the ASI is not sufficient to retain normative corundum. The crystallization experiments rather showed that corundum can crystallize directly from a carbonatitic melt, provided that latter is saturated in alumina. As the solubility of alumina in a carbonatitic melt is extremely low (< 1 wt. %), only minor amounts of excess Al_2O_3 are required to trigger the crystallization of corundum as a liquidus phase, given that the carbonatitic melt has low FeO and MgO contents.

In the following chapter, a petrogenetic model for the genesis of the Siebengebirge sapphires is proposed, based on the assumption that a carbonatitic melt is parental to the sapphires. The focus of the presented petrogenetical model lies on the putative composition and the nature of the carbonatitic melt that precipitated the sapphires, i.e., if the carbonatitic melt is a primary mantle melt or a derivative melt that formed during evolution of a preexisting parental melt. A further focus of the following constraints is to reveal the yet unconstrained genetical relationship between the carbonatites that crystallized the sapphires and the alkaline basalts that later encountered the carbonatitic melt during ascend and incorporated the sapphires to carry them to the surface.

4.2. NATURE OF THE CARBONATITE THAT PRECIPITATED THE SIEBENGEBIRGE SAPPHIRES

4.2.1. Carbonatite petrogenesis

Carbonatites are magmatic rocks with a modal abundance of more than 50 wt. % carbonate minerals (calcite, dolomite, magnesite, etc.) and low silica content (0 to 10 wt. %). They are commonly enriched in Ba, P, Sr, and in the Light Rare Earth Elements (LREE) (Nelson et al., 1988). Carbonatites are often associated with intra-continental alkaline silicate magmatism (e.g., Harmer, 1999; Andersen, 2008) and are commonly part of intrusive bodies. Most carbonatites are calcite-carbonatites (sövites or alvikites). Dolomite-carbonatite (rauhaugite or beforsite) and natrocarbonatites are far less frequent. Typical silicate rocks associated with carbonatites are nephelinites, phonolites, nepheline syenites, ijolites and urtites (e.g., Wallace and Green, 1988; Beccaluva et al., 1992; Harmer, 1998; Srivastava et al., 2005). The genesis of carbonatitic melt has been extensively studied in the past decades. There are three major scenarios that have been established to explain the formation of carbonatitic magmas: (1) Low degree partial melting of a carbonated mantle peridotite (e.g., Cooper et al., 1975; Koster van Groos, 1975; Wallace and Green, 1988; Sweeney, 1994; Harmer and Gittins, 1998; Harmer et al., 1998; Ying et al., 2004), (2) Exsolution of a carbonatitic melt from a CO_2-saturated silicate melt by liquid immiscibility in the carbonate – silicate system (e.g., Koster van Groos and Wyllie, 1963, 1966; Middlemost, 1974; Cooper et al., 1975; Mitchell and Brunfelt, 1975; Freestone and Hamilton, 1980; Kjarsgaard and Hamilton, 1988, 1989; Brooker and Hamilton, 1990; Kjarsgaards and Peterson, 1991; Church and Jones, 1995; Lee and Wyllie, 1997; Dawson, 1998; Halama et al., 2005; Brooker and Kjarsgaard,

2011), and (3) carbonatites as residual melts of highly fractionated carbonated nephelinite or melilitite (Gittins 1989; Gittins and Jago, 1998).

A distinction between primary carbonatites and carbonatites that formed via liquid immiscibility can be made based on major and trace element compositions. Significant factors controlling the composition of a melt are the volatile inventory of a magma source and the degree of melting. Increasing volatile content in a melt decreases the silica content (Kushiro, 1975), so that the melt becomes silica-deficient. The melting degree influences the incompatible trace element composition of a melt. Low degree partial melting produces melts that are more enriched in incompatible elements compared to melts that formed at higher melt degrees. Consequently, the near-solidus liquid of a CO_2-bearing source, e.g., a carbonated peridotite or a carbonated eclogite, will be a SiO_2-deficient melt, enriched in incompatible elements compared to the source. With the onset of melting, the melt will become less enriched in incompatible elements, the CO_2 content in the melt will be diluted, and the melt will be more silica rich. Dasgupta et al. (2007) demonstrated that at melting degrees of < 1 %, a peridotite containing 0.1 – 0.25 wt. % CO_2 will produce a carbonatitic melt which will become more silica rich with increasing melting degree until carbonated silicate melts are produced. With increasing melting degree and thus decreasing CO_2 concentration in the melt, the partial melt of a carbonated peridotite will be carbonatitic at lowest melt degrees, and then melilititic, nephelinitic, and finally basanitic or alkali basaltic at melt degrees above ~ 30 %. Primary carbonatites have calcic dolomite compositions whereas immiscible carbonatite melts tend to be calciocarbonatitic (Lee and Wyllie, 1998).

4.2.2. Constraints on the carbonatite composition parental to the sapphires

A primary nature of the carbonatite that precipitated the sapphire seems unlikely, as carbonatitic melts in equilibrium with mantle peridotites at high pressures have too high MgO and FeO contents (cf. Wallace and Green, 1988; Thibault et al., 1992; Lee and Wyllie, 1998) for corundum to be the stable alumina phase. Instead, spinel would form, as demonstrated in the crystallization experiments in Chapter 3. The carbonatitic melt parental to the Siebengebirge sapphires must rather have formed via exsolution from a CO_2-saturated, highly fractionated alkaline silicate melt. Such nephelinitic or phonolitic melts intersect the silicate-carbonatite liquid immiscibility field during ascent, as the CO_2 solubility in the melt decreases with decreasing pressure. The resulting carbonatitic melt would be rich in CaO, Na_2O and K_2O, but low in MgO and FeO. Support for liquid immiscibility to be the main process generating the carbonatite that precipitated the Siebengebirge sapphires is given by the immiscible silicate – carbonatite melt inclusions in sample 26, which could only have formed, provided that simultaneously a conjugate carbonatitc melt formed. These glasses provide strong evidence that sapphire crystallization is the result of a serie of processes involving fractionation of alkaline basaltic melt to phonolite/ syenites and liquid immiscibility in a multi-component system including silicate, carbonatite, and carbonated silicate melts. High concentrations of volatiles in a silicate melt will promote the two-melt liquid immiscibility in the silicate-carbonatite system. Upon intersection of the silicate-carbonatite miscibility gap, a carbonated silicate melt will split into a silicate melt fraction and a carbonatite melt fraction, with the majority of the volatile components partitioning into the carbonatitic melt. The different physicochemical properties such as density and viscosity will trigger the physical separation of the two immiscible melts. After spatial separation, the melts will evolve and differentiate independently. The carbonatite melt now enriched in

volatiles, will expel alkali-sulfates, alkali-phosphates, and alkali-halide melts upon cooling (evidence for the presence of sulfate and halide melts are given by the daughter minerals in the CO_2 rich fluid inclusions of the Siebengebirge sapphires), leaving a residual calcium-rich carbonatitic melt that may precipitate magmatic calcite. Thus, the occurrence of calcium carbonate inclusions and of sulfate daughter minerals in the CO_2-bearing fluid inclusions indicates that the sapphires formed at a late-stage evolution of a volatile-enriched carbonated silicate melt.

4.3. Petrogenetic model for the Siebengebirge sapphires

The formation of the alkaline basalt hosted sapphires from the SVF is a result of a complex sequence of magmatic processes that elapsed on a very short time-scale. During Miocene times, extensive active volcanism started in the SVF, producing a broad spectrum of SiO_2 saturated and undersaturated primitive and evolved volcanic rocks. The alkaline mafic melts probably formed due to melting of amphibole and phlogopite-bearing peridotite in the spinel peridotite stability zone (Jung et al., 2012; Jung et al., 2015), at pressures between 1 and 2.5 GPa and temperatures between 1150 and 1350 °C. These P-T conditions correspond to the lithospheric mantle (Fig. 45a). It has been repeatedly suggested that the alkaline mafic rocks were formed from a carbonatite-metasomatized mantle source (Jung et al., 2012; Pfänder et al., 2012). As a result, the melts must have been enriched in volatiles including CO_2, sulfates, phosphates, and chlorides. With ensuing fractionation of the primitive melts towards more evolved phonolitic compositions, the partial pressure of CO_2 (pCO_2) in the melt increases (Fig. 45b) until at high differentiation degrees and high pCO_2, a carbonatitic melt exsolves from the phonolite (Kogarko, 1997). The carbonatitic melt exsolving from a highly evolved phonolite will be rich in CaO and in volatiles but low in SiO_2, MgO, and FeO (Kogarko, 1997). The carbonatite will cool and start to crystallize carbonate phases when

it is physically separated from the coexisting silicate melt (Lee and Wyllie, 1998). The physical separation of the carbonatitic melt from the silicate melt will probably occur rapidly after exsolution due to the significant viscosity and density difference of both melts. The low viscous carbonatitic melt will rise much more rapidly than the strongly polymerized and more viscous phonolite. Cooling of the immiscible carbonatitic liquid after physical separation from the high-temperature silicate will occur via crystallization of silicate minerals, until the silicate-carbonate field boundary is reached. Only then, cooling proceeds via the crystallization of carbonate phases. The occurrence of carbonate inclusions in the sapphires indicates that the physical separation and carbonate precipitation must have occurred prior to the crystallization of the sapphires from the carbonatites. At a concentration of 0.1 wt. % Al_2O_3 in a carbonatitic melt, only 10^3 cm^3 melt are required to obtain one sapphire with a size of 1 cm (assuming the sapphire to be a square). The growth of large sapphires is promoted by the low viscosity of the carbonatite, so that ion transport is very rapid. The crystallization of the sapphires from highly fractionated carbonatite occurred at middle- to upper crustal levels (Fig. 45c). A fresh pulse of hot ascending alkali basalts later encounters the carbonatite melt pocket in the crust on their way upwards, decomposes the carbonatitic melt and incorporates the sapphires to transport them to the surface (Fig. 45d). The entrapment of the sapphires by the alkaline basaltic melt is an unavoidable self-assisting process as shown in the wetting experiments which demonstrate that corundum which crystallized from a carbonatitic melt will immediately migrate into a silicate liquid, if given the chance, even when it is not stable in the silicate melt where it becomes resorbed. The transport of the sapphire megacrysts to the surface by alkaline mafic melt is a rapid process on a geological time scale, requiring only a few weeks to months, depending on the depth of entrapment.

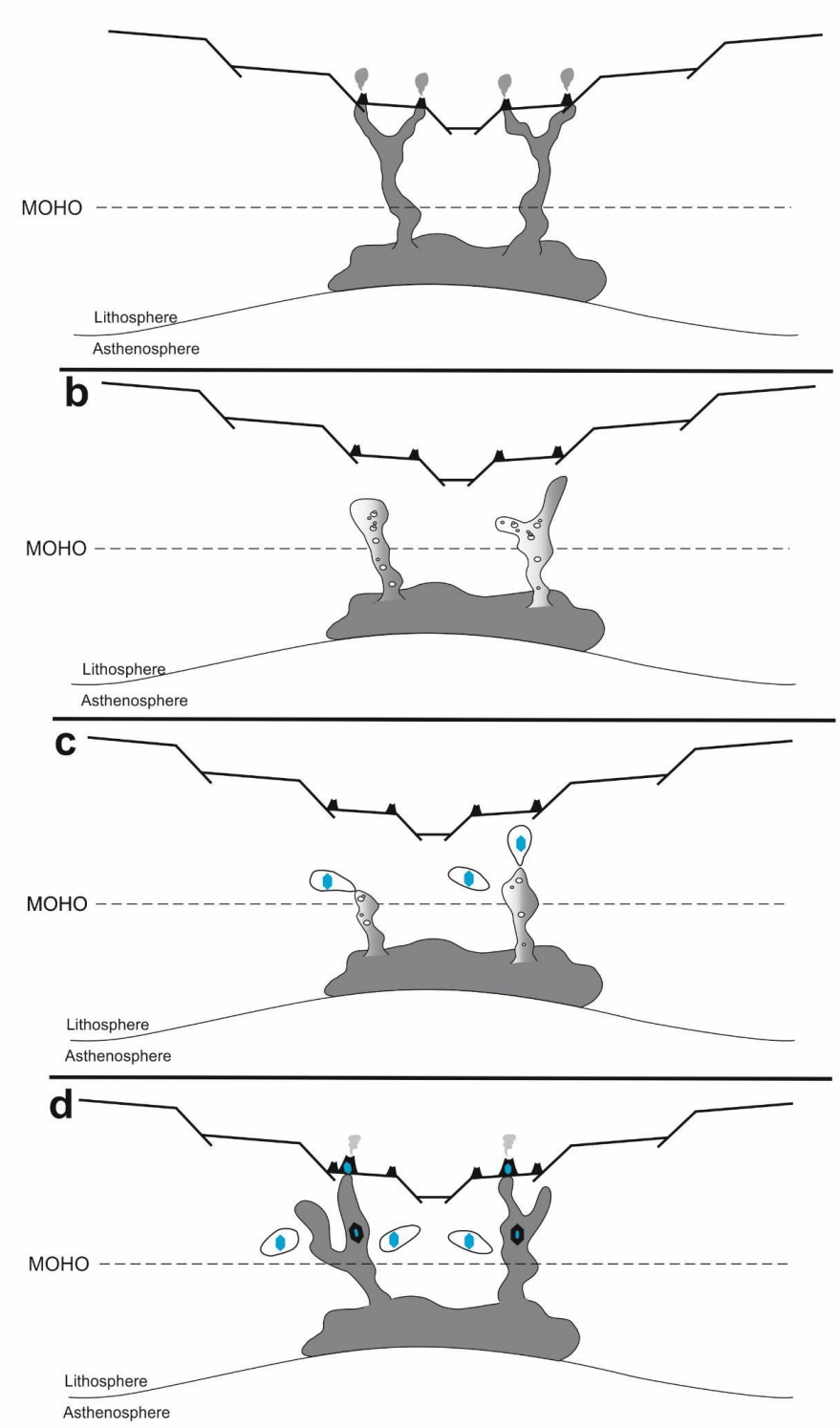

Figure 45: Petrogenetic model for the Siebengebirge sapphires. a: Alkaline basaltic volcanism is initiated in the SVF. b: Differentiation of alkaline mafic magmas leads to the formation of highly evolved phonolites, which is accompanied by a build-up of pCO_2 in the melt. c: Is the highly evolved phonolite saturated in CO_2, a carbonatitic melt exsolves and separates from the nephelinite. Sapphires precipitate from the carbonatite after physical separation. d: fresh pulses of alkaline mafic melts rise. When encountering the carbonatite lenses, the alkaline mafic melts decompose the carbonatite, incorporate the sapphires and carry them to the surface.

4.4. Implications for the Siebengebirge Volcanism

As discussed in the Geological Overview in this study, the SVF is comprised of an exceptionally broad range of SiO_2 saturated and SiO_2 undersaturated mafic and evolved melts (e.g., Kolb et al., 2012). The most evolved SiO_2 saturated volcanics reported from the SVF are tephriphonolites. Evidence for a differentiation of SiO_2 undersaturated magma suites to phonolitic compositions have not been reported yet. However, the phonolitic glass inclusions in one sapphire from the SVF that was investigated in this study (sample PE25) indicate that the SiO_2 undersaturated volcanic magmas in the SVF did differentiate towards phonolitic compositions, and that these phonolites expelled carbonatitic melts at the latest stage of magmatic differentiation. A similar case has been reported from the nearby East Eifel Volcanic Field (EEVF) (e.g., Schmitt et al., 2010) that is also part of the Central European Volcanic Province (CEVP). The volcanic suites from the Laacher See Complex (LSC) of the EEVF (e.g., Wörner and Schmincke, 1984a, 1984b; Bourdon et al., 1994; Schmitt et al., 2010) represent a suiting analogue to the magmatic evolution of the SVF SiO_2 undersaturated melts, as implicated by the Siebengebirge sapphires. The LSC is comprised of a stratified highly evolved phonolite tephra (Lower, Middle, Upper Laacher See Tephra: LLST, MLST, ULST) that becomes increasingly crystal rich from the bottom towards the top of the deposit (e.g., Wörner and Schmincke, 1984a, b). At the boundary between the LLST and the MLST, rare intrusive carbonatites associated with syenites occur. According to Bourdon et al. (1994), the phonolites from the LSC formed via differentiation from basanites, and the carbonatites were proposed by Schmitt et al. (2010) to have formed via immiscibility from the phonolites. This example from the East Eifel Volcanic Complex provides evidence for that the implications for the magmatic evolution of the Siebengebirge Volcanic Field undersaturated magmatic suite is indeed probable. Furthermore, the study of the Siebengebirge sapphires provides insights into the timescale of magmatic evolution. As indicated, the sapphires precipitated from a carbonatitic melt that exsolved from a highly

differentiated phonolitic melt. This is confirmed by glass inclusions of phonolitic composition. Yet, the sapphires were carried to the surface by alkaline basalts. As shown in Fig. 46, the phonolite in the sapphires and the alkaline mafic rocks that host the sapphires are end-members of two distinct differentiation trends, with the phonolite being the most evolved endmember of basanitic/tephritic primary magmas, and alkaline basalts being the most primitive of the basalt – trachyte differentiation trend.

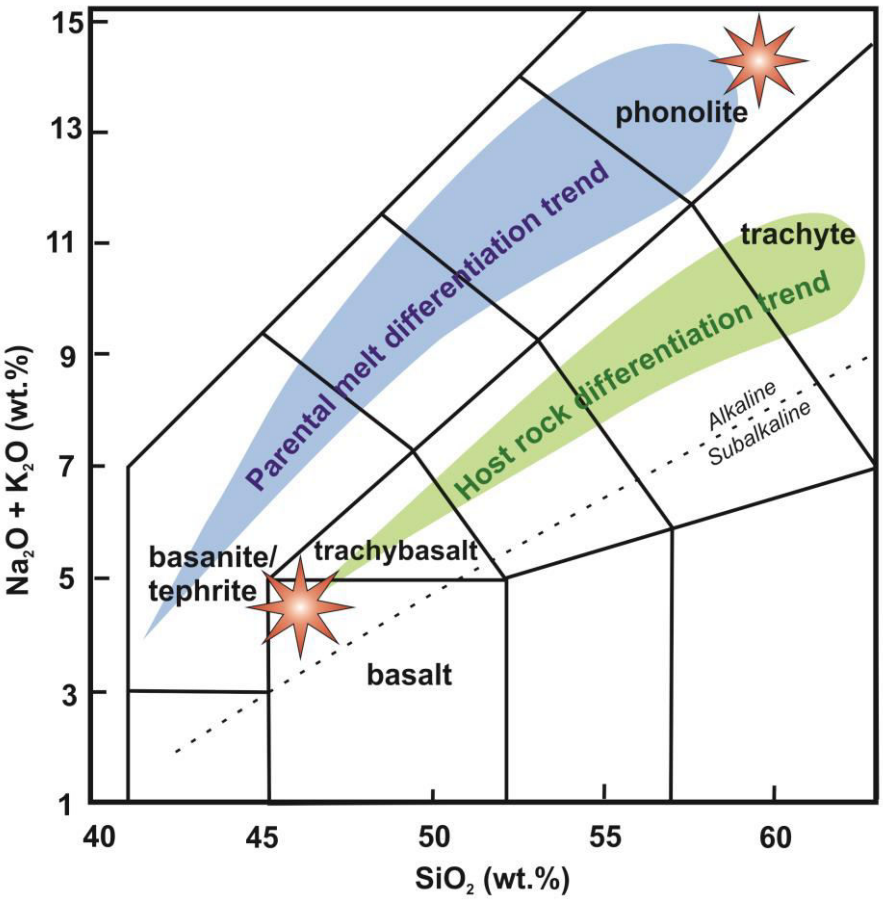

Figure 46: Schematic diagram showing the differentiation trends for the sapphire phonolite glass inclusion (red star in the phonolite field) and for the sapphire host rocks (red star in the basalt field). Though both events have the same age, the compositions represent endmembers of two different differentiation trends, indicating that magma generation and evolution in the SVF occurred on a very rapid time-scale.

Geochronological studies (this study for the sapphire precipitation and Przybyla (2013) for the alkaline mafic rocks of the SVF) show that the differentiation of a basanite to a phonolite and subsequent exsolution of a carbonatite and precipitation of sapphires, and the generation and eruption of alkaline basalts must have occurred on a

geologically very short time-scale that is not resolvable with geochronological methods. The rapidity of these magmatic processes is also confirmed by the short residence time of the sapphires in the basaltic melt of only a few weeks to months.

From the Siebengebirge sapphires, further implications can be made about the composition of the mantle source of the alkaline mafic melts from the Siebengebirge Volcanic Field. The SVF is one of many intra-plate volcanic fields associated with alkaline volcanism around the world. A major question addressed to the genesis of intra-continental alkaline volcanism remains the identification of the source of these SiO_2-undersaturated melts. Such melts show similar trace element patterns and Sr-Nd-Pb isotopic compositions as Ocean Island Basalts (OIB), i.e., enrichment in most incompatible elements, and negative K and Pb anomalies relative to the primitive mantle. This geochemical similarity betwee OIBs and continental intra-plate alkaline volcanics suggests a similar mantle source for both magma-types (e.g., Wörner et al., 1986; Blusztajn and Hart, 1989; Wilson and Downes, 1991; Hegner et al., 1995; Wilson et al., 1995; Jung and Masberg, 1998; Wedepohl and Baumann, 1999; Jung and Hoernes, 2000). It has been inferred by many previous studies (e.g., Hirose, 1997; Green and Falloon, 1998; Dasgupta et al., 2007; Zeng et al., 2010) that the mantle source generating OIB and continental intra-plate alkaline volcanics must be either carbonate bearing, or metasomatically enriched by CO_2 bearing fluids. Also, the alkaline mafic melts from the SVF are suggested to be generated from refertilized carbonated spinel peridotite (Jung et al., 2012; Kolb et al., 2012).

The various alkaline mafic rocks are proposed to reflect variable melt degrees at various melting depths (Kolb et al., 2012; Schubert et al., 2015). Yet, the evidence for a carbonated peridotite to be the source of alkaline mafic rocks from the SVF is very scarce. The only hint was given by elevated Nb/Ta ratios and strongly variable Zr/Hf ratios compared to the Primitive Mantle and to MORB, suggesting a metasomatized source with carbonatites being the putative metasomatizing agent.

The Siebengebirge sapphires presented in this study provide direct evidence for that the mantle source of the alkaline basalts must have been highly enriched in volatiles such as CO_2, alkalis and sulfur. The fact that intra-plate alkaline mafic volcanics are frequently associated with magmatic sapphires, indicates that in general, intra-continental alkaline mafic magmas are produced via melting of a mantle source that is strongly metasomatized by volatile-rich carbonatitic melts, similar as for OIB.

4.5. Summary and conclusions

Magmatic sapphires are well known to occur associated with intra-continental alkaline mafic volcanism. Around the world, predominantly in Asia and Australia, many alkaline basalt fields are reported to carry megacrysts of magmatic sapphires. To date, many theories have been proposed to investigate the nature of these so-called BGY sapphires. Still, although these studies comprise detailed investigations on the sapphires including trace-element analyses, analyses of mineral inclusions as well as melt and/or fluid inclusion and oxygen isotope measurements, no consensus was reached about the sapphire genesis. Moreover, these studies failed to explain the association of Blue-Green-Yellow (BGY) sapphires with alkaline basaltic volcanism. This study on the BGY sapphires hosted by alkaline basalts from the Siebengebirge Volcanic Field (SVF) elucidates many yet unknown details about the formation of this special type of gemstones. The main conclusions from this study can be summarized as follows:

(1) Sapphire megacrysts are xenogenic to the host basalts, as indicated by the spinel corona surrounding each sapphire at the contact towards the basalt. With time series experiments, the reaction rate constant of the reaction of basaltic melt with corundum to form spinel could be constrained. This allowed to estimate

the residence time of the sapphires in the basaltic melt to be a few weeks to months.

(2) There is no evidence that the Siebengebirge sapphires crystallized from evolved silicate melts such as syenites, the favored scenario for BGY sapphires from other locations discussed in the literature. Reconnaissance experiments in the silicate – carbonatite system revealed that the interaction of a carbonatitic melt with a silicate melt indeed triggers an increase in the Alumina Saturation Index (ASI) within the silicate melt fraction, but this effect does not suffice to stabilize corundum as a liquidus phase. In contrast, there is evidence – most notably from the abundant carbonate inclusions - that the sapphires precipitated from carbonatitic melts that formed via liquid immiscibility from a highly evolved phonolitic melt due to an increase in pCO_2 in the melt during fractionation. The crystallization of corundum from the carbonatitic melt probably formed at late-stage magmatic evolution.

(3) Reconnaissance experiments showed that the Al_2O_3 solubility in carbonatites is low, i.e. < 1 wt. %. Corundum can only precipitate from a FeO - MO free, highly evolved carbonatitic melt, provided that latter is saturated in alumina. Carbonatite rich in FeO and MgO will rather stabilize spinel as alumina phase.

(4) Although corundum is chemically stable in carbonatitic melt, it will immediately migrate into a silicate melt if given the opportunity, as corundum is wetted far better by a silicate melt rather than a carbonatitic melt. As to the chemical disequilibrium between corundum and basaltic melt, the corundum will immediately become resorbed by the basaltic melt to form spinel coronas.

(5) There is a close genetical relationship between the sapphires and the hosting alkaline mafic rocks. The age of the Siebengebirge sapphires dated in this work and the age of the alkaline mafic volcanism in that area (Przybyla, 2013) overlap. The genetical link between magmatic sapphires and the hosting basalt that has been a puzzle, to date, bears upon CO_2. Only alkaline volcanic suites can build up enough CO_2 in the magma chamber upon fractionation so that at high degrees of fractionation a carbonatitic melt exsolves which in turn can crystallize sapphires. During ascent, fresh alkaline basaltic melt that encounters carbonatite melt pockets will decompose the carbonatite and incorporate the sapphires to carry them to the surface.

5. REFERENCES

Abduriyim A., Kitawaki H. (2006) Determination of the origin of blue sapphire using Laser Ablation Inductively Coupled Plasma Mass Spectrometry (LA-ICP-MS). Journal of Gemmology 30, 23-36.

Ackermand D., Herd R. K., Windley B. F. (1982) Chemographic relationships in sapphirine-bearing rocks of the Limpopo belt, South Africa. Revista Brasiliera de Geociencas, São Paulo 12, 292-300.

Ahorner L., Baier B., Bonjer K.-P. (1983) General patterns of seismotectonic dislocation and the earthquake-generating stress field in Central Europe between the Alps and the North Sea. In: Plateau Uplift (Fuchs K. ed.), pp. 187-197. Springer, Berlin.

Altherr R., Okrusch M., Bank H. (1982) Corundum and kyanite bearing anatexites from the Precambrian of Tanzania. Lithos 15, 191-197.

Aspen P., Upton B.G.J., Dicken A.P. (1990) Anorthoclase, sanidine and associated megacrysts in Scottish alkali basalts: high pressure syenitic debris from upper mantle sources? European Journal of Mineralogy 2, 503-517.

Aydogan M. S., Moazzen M. (2012) Origin and Metamorphism of Corundum-rich metabauxites at Mt. Ismail in the Southern Menderes Massif, SW Turkey. Resource Geology 62, 243-262.

Babuska V., Plomerova J., Granet M. (1990) The deep lithosphere in the Alps: a model inferred from P residuals. Tectonophysics 176, 137-165.

Babuska V., Plomerova J. (1992) The lithoshpere in central Europe - seismological and petrological aspects. Tectonophysics 207, 141-163.

Babuska V., plomerova J. (2006) European mantle lithosphere assembled from rigid microplates with inherited seismic anisotropy. Physics of the Earth and Planetary Interiors 158, 264-280.

Barr S. M., MacDonald A. S. (1981) Geochemistry and geochronology of late Cenozoic basalts of Southeast Asia. Geological Society of America Bulletin (II) 92, 1069-1142.

Beccaluva L., Barbieri M., Born H., Brotzu P., Coltorti M., Conte A., Garbarino C., Gomes G. C. B., Acciotta M., Morbidelli L., Ruberti E., Siena F., Traversa G. (1992) Fractional Crystallization and Liquid Immiscibility Processes in the Alkaline-Carbonatite Complex of Juquiá (São Paulo, Brazil). Journal of Petrology 33, 1371-1404.

Békri S., Thovert J. F., Adler P. M. (1995) Dissolution of porous media. Chemical Engineering Science 50, 2765-2791.

Berger J., Féménias O., Ohnenstetter D., Plissart G., Mercier J.-C. C. (2010) Origin and tectonic significance of corundum-kyanite-sapphirine amphibolites from the Variscan French Massif Central. Journal of Metamorphic Petrology 28, 341-360.

Bertrán J. F. (1983) Study of the Fermi doublet v_1-$2v_2$ in the Raman spectra of CO_2 in different phases. Spectrochimica Acta 39A, 119-121.

Blauwet D., Laurs B. M. (2005) New ruby and pink sapphire deposit in the Lake Baringo area, Kenya. Gems and Gemology 41, 177-178.

Blusztajn J., Hart S. R. (1989) Sr, Nd, and Pb isotopic character of tertiary basalts from southwest Poland. Geochimica et Cosmochimica Acta 53, 2689-2696.

Bluszajn J., Hegner E. (2002) Osmium isotopic systematic of melilitites from the Tertiary Central European Volcanic province in SW Germany. Chemical Geology 189, 91-103.

Bogaard P. J. F., Wörner G. (2003) Petrogenesis of basanitic to tholeitic volcanic rocks from the Miocene Vogelsberg, Central Germany. Journal of Petrology 44, 569-602.

Bohlen S. R. (1982) The quartz = coesite transformation: A precise determination and the effects of other components. Journal of Geophysical Research 87, 7073-7078.

Bosshart G. (1995) Sapphires and rubies from Laos, 25th International Gemmological Conference Program Rayong, Thailand, pp. 209-228.

Bourdon B., Zindler A., Wörner G. (1994) Evolution of the Laacher See magma chamber: Evidence from SIMS and TIMS measurements of U-Th disequilibria in minerals and glasses. Earth and Planetary Science Letters 126, 75-90.

Brauns R. (1922) Die Mineralien der Niederrheinischen Vulkangebiete mit besonderer Berücksichtigung ihrer Bildung und Umbildung. Schweizerbart, Stuttgart, 225 p.

Brooker R. A. (1998) The Effect of CO_2 Saturation on Immiscibility between Silicate and Carbonate Liquids: An Experimental Study. Journal of Petrology 39, 1905-1915.

Brooker R. A., Hamilton D. L. (1990) Three-liquid immiscibility and the origin of carbonatites. Nature 346, 459-462.

Brooker R. A., Kjarsgaard B. A. (2010) Silicate-carbonate liquid immiscibility and phase relations in the system SiO_2-Na_2O-Al_2O_3-CaO-CO_2 at 0.1 - 2.5 GPa with applications to carbonatite genesis. Journal of Petrology 52, 1281-1305.

Brousse R., Varet J. (1966) Les trachytes du Mont-Dore et du Cantal septentrional et leurs enclaves. Bulletin of the Geological Society of France 7 (VIII), 246-262.

Brownlow A. H., Komorowski J.-C. (1988) Geology and Origin of the Yogo sapphire deposit, Montana. Economic Geology 83, 875-880.

Cartwright I., Barnicoat A. (1986) The generation of quartz normative melts and corundum-bearing restites in crustal anatexis, petrogenetic modelling based on an example from the Lewisian of North West Scotland. Journal of Metamorphic Geology 3, 79-99.

Che X-D., Wu F-Y, Wang R-Ch, Gerdes A., Ji W-Q, Zhao Z-H., Yang J-H., Zhu Z-Y. (2015) In situ U-Pb isotopic dating of columbite-tantalite by LA-ICP-MS. Ore Geology Reviews 65, 979-989.

Chualaowanich T., Sutthirat C., Harzenberger C., Pisutha-Arnond V. (2005) Another constraint on Thai-corundum genesis: new evidence from ruby-bearing xenoliths from the eastern gem field, Thailand. International conference on geology, geotechnology and mineral resources of Indochina (GEOINDO 2005), Khon Kaen, Thailand. 345 pp.

Church A. A., Jones A. P. (1994) Hollow natrocarbonatite lapilli from the 1992 eruption of Oldoinyo Lengai, Tanzania. Journal of the Geological Society 151, 118-120.

Coenraads R. R., Sutherland F. L., Kinny P. D. (1990) The origin of sapphires: U-Pb dating of zircon inclusions shed new light. Mineralogical Magazine 54, 113-122.

Coenraads R. R., Vivhit P., Sutherland F. L. (1995) An unusual sapphire-zircon-magnetite xenolith from the Chanthaburi Gem Province, Thailand. Mineralogical Magazine 59, 465-479.

Coetze C. B. (1940) Sillimanite-corundum rock: A metamorphosed bauxite in Namaqualand. Transactions of the Royal Society of South Africa 28, 199-205.

Cooper A. F., Gittins J., Tuttle O. F. (1975) The system $Na_2CO_3 – K_2CO_3 – CaCO_3$ at 1 kbar and its significance in carbonatite petrogenesis. American Journal of Science 275, 534-560.

Dahanayake K. (1980) Modes of occurrence and provenance of gemstones of Sri Lanka. Mineralium Deposita 15, 81-86.

Dalton J. A., Wood B. J. (1993) The compositions of primary carbonate melts and their evolution through wallrock reaction in the mantle. Earth and Planetary Science Letters 119, 511-525.

Dannenberg A.

(1895) Studien an Einschlüssen in den vulcanischen Gesteinen des Siebengebirges. Tschermaks mineralogische und petrographische Mitteilungen 14, 17-84.

Dasgupta R., Hirschmann M. M., Dellas N. (2005) The effect of bulk composition on the solidus of carbonated eclogite from partial melting experiments at 3 GPa. Contributions to Mineralogy and Petrology 149, 288-305.

Dasgupta R., Hirschmann M. M., Smith N. D. (2007) Partial Melting Experiments of Peridotite + CO_2 at 3 GPa and Genesis of Alkalic Ocean Island Basalts. Journal of Petrology 48, 2093-2124.

De Maesschalck A. A., Oen I. S. (1989) Fluid and mineral inclusions in corundum from gem gravels in Sri Lanka. Mineralogical Magazine 53, 539-545.

Deer W. A., Howie R. A., Zussman J. (1992) An Introduction tot he Rock-Forming Minerals. Longman Scientific and Technical, New York. 696 pp.

Dill H. G., Gerdes A., Weber B. (2007) Cu-Fe-U phosphate mineralization of the Hagendorf-Pleystein pegmatite province, Germany: with special reference to laser-ablation-inductive-coupled-plasma mass spectrometry (LA-ICP-MS) of limonite-cored torberite. Mineralogical Magazine 71, 423-439.

Dobson D. P., Jones A.P., Rabe R., Toshimori S., Kurita K., Taniguchi T., Kondo T., Kato T., Shimomura O., Urakawa S. (1996) In-situ measurement of viscosity and density of carbonate melts at high pressure. Earth and Planetary Science Letters 143, 207-215.

Droop G. T. R. (1989) Reaction history of garnet-sapphirine granulite-facies metamorphism in the Central Limpopo Mobile Belt, Zimbabwe. Journal of Metamorphic Geology 7, 383-403.

Droop G. T. R., Bucher-Nurminen K. (1984) Reaction textures and metamorphic evolution of sapphirine-bearing granulites from the Gruf Complex, Italian Central Alps. Journal of Petrology 25, 766-803.

Fall A., Tattitch B., Bodnar R. J. (2011) Combined microthermometric and Raman spectroscopic technique to determine the salinity of H_2O-CO_2-NaCl fluid inclusions based on clathrate melting. Geochimica et Cosmochimica Acta 75, 951-964.

Feenstra A. (1996) An EMP and TEM-AEM Study of Margarite, Muscovite and Paragonite in Polymetamorphic Metabauxites of Naxos (Cyclades, Greece) and the Implications of Fine-scale Mica Interlayering and Multiple Mica Generations. Journal of Petrology 37, 201-233.

Ferguson J., Fielding P. E. (1971) The origin of the colours of yellow, green and blue sapphire. Chemical Physics Letter 10, 262-265.

Ferguson J., Fielding P. E. (1972) The origins of the colours of natural yellow, blue, and green sapphire. Australian Journal of Chemistry 25, 1371-1385.

Floyd P. A. (1965) Metasomatic Hornfelses of the Land's End Aureole at Tarter-du, Cornwall. Journal of Petrology 6, 223-245.

Frechen J., Vieten K. (1970a) Petrographie der Vulkanite des Siebengebirges. Die peralkalische Gesteinsreihe Alkalitrachyt-Sanidinbasanit. Decheniana 122, 357-377.

Frechen J., Vieten K. (1970b) Petrographie der Vulkanite des Siebengebirges. Die subalkalische Gesteinsreihe Quarztrachyt-Latitbasalt. Decheniana 122, 337-356.

Freestone I. C., Hamilton D. L. (1980) The role of Liquid Immiscibility in the Genesis of Carbonatites – An Experimental Study. Contributions to Mineralogy and Petrology 73, 105-117.

Gabudianu Radulescu I., Compagnioni R., Lombardo B. (2011) Polymetamorphic history of a relict Permian hornfels from the central Gran Paradiso Massif (Western Alps, Italy): a microstructural and thermodynamic modelling study. Journal of Metamorphic Geology 29, 851-874.

Garnier V. (2003) Les gisements de rubis associés aux marbres de l'Asie Centrale et du Sud-est: Genèse et caractérisation isotopique (Ph.D. thesis): Nancy, France, Institut National Polytechnique de Lorraine, 371 p.

Garrabos Y., Tufeu R., Le Neindre B., Zalczer G., Beysens D. (1980) Rayleigh and waman scattering near the critical point of carbon dioxide. The Journal of Chemical Physics 72, 4637 – 4651.

Garnier V., Giuliani G., Ohnestetter D., Schwarz D. (2004) Les gisements de corindon, classification et genèse. Le Règne Minéral 55, 36-44.

Garnier V, Ohnenstetter D., Giuliani G., Fallick A.E., Phan Trong T., Hoang Quang V., Pham Van L., Schwarz D. (2005) Basalt petrology, zircon ages and sapphire genesis from Dak Nong, southern Vietnam. Mineralogical Magazine 69, 21-38.

Garnier V., Giuliani G., Ohnestetter D., Fallick A. E., Dubessy J., Banks D., Vinh H. Q., Lhomme T., Maluski H., Pêcher A., Bakhsh K. A., Van Long P., Trinh P. T., Schwarz D. (2008) Marble-hosted ruby deposits from Central and Southeast Asia: Towards a new genetic model. Ore Geology Reviews 34, 169-191.

Genge M. J., Price G. D., Jones A. P. (1995) Molecular dynamics simulations of $CaCO_3$ melts to mantle pressures and temperatures: implications for carbonatite magmas. Earth and Planetary Science Letters 131, 225-238.

Gerdes A., Zeh A. (2006) Combined U-Pb and Hf isotope LA-(MC-)-ICP-MS analyses of detrital zircons: Comparison with SHRIMP and new constraints for the provenance and age of an Armorican metasediment in Central Germany. Earth and Planetary Science Letters 249, 47-61.

Gerdes A., Zeh A. (2009) Zircon formation versus zircon alteration – New insights from combined U-Pb and Lu-Hf in-situ LA-ICP-MS analyses, and consequences for the interpretation of Archean zircon from the Central Zone of the Limpopo Belt. Chemical Geology 261, 230-243.

Giannuzzi L. A., Stevie F. A. (1999) A review of focused ion beam milling techniques for TEM specimen preparation. Micron 30, 197-204.

Gittins J. (1989) The origin and evolution of carbonatite magmas. In: Carbonatites: Genesis and Evolution (Bell K., ed.), pp. 580-600. Unwin Hyman, London.

Gittins J., Jago B. C. (1998) Differentiation of natrocarbonatite magma at Oldoinyo Lengai volcano, Tanzania. Mineralogical Magazine 62, 759-568.

Giuliani G., Fallick A. E., Garnier V., France-Lanord Ch., Ohnestetter D., Schwarz D. (2005) Oxygen isotope composition as a tracer for the origin of ruby and sapphires. Geology 33, 249-252.

Giuliani G., Pivin M., Fallick A. E., Ohnestetter D., Song Y., Demaiffe D. (2015) Geochemical and oxygen isotope signatures of mantle corundum megacrysts from the Mbuji-Mayi kimberlite, Democratic Republic of Congo, and the Changle alkali basalt, China. Comptes Rendus Geoscience 347.1, 24-34.

Giuliani G., Fallick A. E., Rakotondrazafy M., Ohnestetter D., Andriamamonjy A., Rakotosamizanay S., Ralantoarison Th., Razanatseheno M., Dungaigre

Ch., Schwarz D. (2007) Oxygen isotope systematic of gem corundum deposits in Madagascar: relevance for their geological origin. Mineralium Deposita 42, 251-270.

Giuliani G., Fallick A., Ohnestetter D., Pegere G. (2009) Oxygen isotopes composition of sapphires from the French Massif Central: implications for the origin of gem corundum in basaltic fields. Mineralium Deposita 44, 221-231.

Goes S., Spakman W., Bijwaard H. (1999) A lower mantle source for Central European Volcanism. Science 286, 1928-1930.

Golani P. R. (1989) Sillimanite-corundum deposits of Sonapahar, Meghalaya, India: a metamorphosed Precambrian paleosol. Precambrian Research 43, 175-189.

Goscombe B. (1992) Silica-undersaturated sapphirine, spinel and kornerupine granulite facies rocks, NE Strangways Range, Central Australie. Journal of Metamorphic Petrology 10, 181-201.

Graham I. T., Sutherland F. L., Web G. B., Fanning C. M. (2004) Polygenetic corundums from New South Wales gemfields. In: Metallogeny of the Pacific Northwest: Tectonics, magmatism and metallogeny of active continental margins. (Khanchuk A.I., Gonevchuk G.A., Mitrokhin A.N., Simaneko I.F., Cook N.J., Seltmann R., eds.), pp.336-339, Dalnauka, Vladivostok.

Graham I., Sutherland L., Zaw K., Nechav V., Khanchuk A. (2008) Advances in our understanding of the gem corundum deposits of the West Pacific continental margins intraplate basaltic fields. Ore Geology Reviews 34, 200-215.

Granet M., Wilson M., Achauer U. (1995) Imaging a mantle plume beneath the French Massif Central. Earth and Planetary Science Letters 136, 281-296.

Grapes R., Palmer K. (1996) (Ruby-Sapphire)-Chromian Mica-Tourmaline Rocks from Westland, New Zealand. Journal of Petrology 37, 293-315.

Green T. H., Wass S. Y., Ferguson J. (1978) Experimental study of corundum stability in basalts (abstract). Abstr Programme 3rd Ausralian Geology Convention, Townsville, pp. 34.

Guo J., O'Reilly S. Y., Griffin W. L. (1996) Corundum from basaltic terrains: A mineral inclusion approach to the enigma. Contribution to Mineralogy and Petrology 122, 368-386.

Haase K. M., Goldschmidt B., Garbe-Schönberg C.-D. (2004) Petrogenesis of Tertiary Continental Intra-plate Lavas from the Westerwald Region, Germany. Journal of Petrology 45, 883-905.

Halama R., Vennemann T., Siebel W., Markl G. (2005) The Gronnedal-Ika carbonatite syenite complex, South Greenland: carbonatite formation by liquid immiscibility. Journal of Petrology 46, 191-217.

Hamilton D. L., Freestone I. C. (1979) Origin of carbonatites by liquid immiscibility. Nature 279, 52-54.

Harley S. L., Green D. H. (1982) Garnet-orthopyroxene barometry for granulites and peridotites. Nature 300, 697-701.

Harmer R. E., Gittins J. (1998) The Case for Primary, Mantle-derived Carbonatite Magma. Journal of Petrology 39, 1895-1903.

Harmer R. E., Lee C. A., Eglington B. M. (1998) A deep mantle source for carbonatite magmatism; evidence from the nephelinites and carbonatites of the Buhera district, SE Zimbabwe. Earth and Planetary Science Letters 158, 131-142.

Harper D. (2015) Online etymology dictionary. www.etymonline.com.

Hegner E., Walter H. J., Satir M. (1995) Pb-Sr-Nd isotopic compositions and trace element geochemistry of megacrysts and melilitites from the Tertiary Urach volcanic field: source composition of small volume melts under SW Germany. Contributions to Mineralogy and Petrology 122, 322-335.

Helz R. T., Thornber C. R. (1987) Geothermometry of Kilauea Iki lava lake, Hawaii. Bulletin of Volcanology 49, 651-668.

Henn U., Milisenda C. C. (1997) Neue Edelsteinvorkommen in Tansania, Die Region Tunduru-Songea. Zeitschrift der Deutschen Gemmologischen Gesellschaft 46, 29-43.

Hoernle K., Zhang Y. S., Graham D. (1995) Seismic and geochemical evidence for large-scale mantle upwelling beneath the eastern Atlantic and western and central Europe. Nature 374, 34-39.

Hoernle K., Zhang Y.-S., Graham D. (1995) Seismic and geochemical evidence for large-scale mantle upwelling beneath the eastern Atlantic and western and central Europe. Nature 374, 34-39.

Holland T. J. B. (1980) The reaction albite = jadeite+quartz determined experimentally in the range 600-1200 degrees C. American Mineralogist 65, 129-134.

Horn I., Foley S. F., Jackson S. E., Jenner G. A. (1994) Experimentally determined partitioning of high field strength- and selected transition elements between spinel and basaltic melt. Chemical Geology 117, 193-218.

Horrocks P. C. (1983) A corundum and sapphirine paragenesis from the Limpopo Mobile Belt, southern Africa. Journal of Metamorphic Geology 1, 13-23.

Hughes R. W. (1997) Ruby and Sapphire. R. W. H. Publishing, Boulder, Colorado. 512 pp.

Irving A. J., Price R. C. (1981) Geochemistry and evolution of lherzolite-bearing phonolitic lavas from Nigeria, Australia, East Germany and New Zealand. Geochimica et Cosmochimica Acta 45, 1309-1320.

Irving A. J. (1986) Polybaric magma mixing in alkali basalts and kimberlites: evidence from corundum, zircon and ilmenite megacrysts. 4th International Kimberlite Conference, Perth, Geological Society of Australia Abstr. Ser., vol. 16. Blackwell Scientific, Oxford, pp. 262–264.

Illies J. H., Prodehl C., Schmincke H.-U., Semmel A. (1979) The quarternary uplift of the rhenish shield in germany. Tectonophysics 61, 197-225.

Illies H., Baumann H., Hoffers B. (1981) Stress pattern and strain release in the Alpine foreland. Tectonophysics 71, 157-172.

Illies H., Baumann H. (1982) Crustal dynamics and morphodynamics of the Western European Rift System. Zeitschrift für Geomorphologie, NF 42, 135-165.

Izokh A. E., Smirnov S. Z., Egorova V. V., Anh T. T., Kovyazin S. V., Phuong N. T., Kalinina V. V. (2010) The conditions of formation of sapphire and zircon in the areas of alkali-basaltoid volcanism in Central Vietnam. Russian Geology and Geophysics 51, 719-733.

Jackson S. E., Pearson N. J., Griffin W. L., Belousova E. A. (2004) The application of laser ablation-inductively coupled plasma-mass spectrometry to in situ U-Pb zircon geochronology. Chemical Geology 211, 47-69.

Jacob D. E. (2004) Nature and origin of eclogite xenoliths from kimberlites. Lithos 77, 295-316.

Johannes W., Puhan D. (1971) The Calcite-Aragonite Transition, Reinvestigated. Contributions to Mineralogy and Petrology 31, 28-38.

Jung S. (1999) The Role of Crustal Contamination During the Evolution of Continental Rift-Related Basalts: A Case Study from the Vogelsberg Area (Central Germany). Geolines 9, 48-58.

Jung S., Hoernes S. (2000) the major- and trace-element and isotope (Sr, Nd, O) geochemistry of Cenozoic alkaline rift-type volcanic rocks from the Rhoen area (central Germany): petrology, mantle source characteristics and implications for asthenosphere-lithosphere interactions. Journal of Volcanology and Geothermal Research 99, 27-53.

Jung S., Pfänder J. A., Brügmann G., Stracke A. (2005) Sources of primitive alkaline volcanic rocks from the Central European Volcanic Province (Rhön, Germany) inferred from Hf, Os and Pb isotopes. Contributions to Mineralogy and Petrology 150, 546-559.

Jung C., Jung S., Hoffer E., Berndt J. (2006) Petrogenesis of Tertiary Mafic Alkaline Magmas in the Hocheifel, Germany. Journal of Petrology 47, 1637-1671.

Jung S., Vieten K., Romer R. L., Mezger K., Hoernes S., Satir M. (2006) Petrogenesis of Tertiary Alkaline Magmatism in the Siebengebirge, Germany. Journal of Petrology 53, 2381-2409.

Jung S., Vieten K., Romer R. L., Mezger K., Hoernes S., Satir M. (2012) Petrogenesis of Tertiary Alkaline Magmas in the Siebengebirge, Germany. Journal of Petrology 53, 2381-2409.

Kawaki Y., Yamamoto J., Kagi H. (2003) Micro-Raman densimeter for CO_2 inclusions in mantle-derived minerals. Applied Spectroscopy 37, 1333-1339.

Keller P. C. (1982) The Chanthaburi-Trat gem field, Thailand. Gems and Gemmology 18, 186-196.

Keller P. C., Koivula J. I., Jara G. (1985) Sapphire from the Mercaderes-Rio Mayo ore, Cauca, Columbia. Gems and Gemmology 21, 20-25.

Khamloet P., pisutha-Arnond V., Sutthirat C. (2014) Mineral inclusions in sapphire from the basalt-related deposit in Bo Phloi, Kanchanaburi, western Thailand: indication of their genesis. Russian Geology and Geophysics 55, 1087-1102.

Khanchuk A., Zalishchak B., Pakhomova V., Odarichenko E., Sapin V. (2003) Genesis and gemmology of sapphire from the Nezametnoye deposit, Primorye Region, Russia. Australian Gemmologist 21, 329-335.

Kiefert L., Schmetzer K. (1987) Blue and yellow sapphire from Kaduna Province, Nigeria. Journal of Gemmology 20, 427-442.

Kjarsgaard B., Hamilton D. L. (1988) Liquid immiscibility and the origin of alkali-poor carbonatites. Mineralogical Magazine 52, 43-55.

Kjarsgaard B., Hamilton D. L. (1989) The genesis of carbonatites by immiscibility. In: Carbonatites; Genesis and Evolution. (Bell K., ed), p. 388-404, Unwin Hyman, London.

Kjarsgaard B., Peterson T. (1991) Nephelinite-carbonatite liquid immiscibility at Shombole volcanoe, East Africa: Petrographic and experimental evidence. Mineralogical Petrology 43, 293-314.

Klein C., Hurlbut C. S. (1993) Manual of Mineralogy. John Wiley and Sons, New York. 681 pp.

Kolb M., Paulik H., Kirchenbaur M., Münker C. (2012) Petrogenesis of Mafic to Felsic Lavas from the Oligocene Siebengebirge Volcanic Field (Germany): Implications for the Origin of Intracontinental Volcanism in Central Europe. Journal of Petrology 53, 2349-2379.

Kornprobst J., Piboule M., Roden M., Tabit A. (1990) Corundum-bearing Garnet Clinopyroxenites at Beni Bousera (Morocco): Original Plagioclase-rich Gabbros Recrystallized at Depth within the Mantle? Journal of Petrology 31, 717-745.

Koster van Groos A. K., Wyllie P. J. (1963) Experimental Data bearing on the Role of Liquid Immiscibility in the Genesis of Carbonatites. Nature 199, 801-802.

Koster van Groos A. K., Wyllie P. J. (1966) Liquid immiscibility in the system Na_2O-Al_2O_3-SiO_2-CO_2 at pressures to 1 kilobar. American Journal of Science 264, 234-255.

Koster van Groos A. K. (1975) The effect of high CO_2 pressures on alkali rocks and its bearing on the formation of alkali ultrabasic rocks and the associated carbonatites. American Journal of Science 275, 163-185.

Kriegsman L. M., Schumacher J. C. (1999) Petrology of Sapphirine-bearing and Associated Granulites from Central Sri Lanka. Journal of Petrology 40, 1211-1239.

Krzemnicki M., Hänni H. A., Guggenheim R., Mathys D. (1996) Investigations on sapphires from alkali basalt, South West Rwanda. Journal of Gemmology 25, 90-106.

Kushiro I. (1975) On the nature of silicate melt and its significance in magma genesis: regularities in the shift of the liquidus boundaries involving olivine, pyroxene, and silica minerals. American Journal of Science 29, 71-107.

Lacroix A. (1901) Corindon. In: Minéralogie de la France et de ses colonies. Librairie polytechnique Baudry et Cie, Paris, vol 3, pp. 237-243.

Lasaulx A. v. (1885) Ueber das optische Verhalten und die Mikrostructur des Korund. Zeitschrift für Kistallographie 10, 346-365.

Laspeyres H. (1900) Das Siebengebirge am Rhein. Verhandlungen des naturhistorischen Vereins der preussischen Rheinlande und Westfalens 57, 119-596.

Leake B. E., Skirrow G. (1960) The Pelitic Hernfelded of the Cashel-Lough Wheelaub Intrusion, County Galway, Eire. The Journal of Geology 68, 23-40.

Le Maitre R. W. (1984) A proposal by the IUGS Subcommission on the Systematics of Igneous Rocks for a chemical classification of volcanic rocks based on the total alkali silica (TAS) diagram. Australian Journal of Earth Sciences: An International Geoscience Journal of the Geological Scociety of Australia 31, 243-255.

Le Maitre R. W. (2002) A Classification and Glossary of Terms; Recommendations of the International Union of Geological Sciences: Subcommision on the Systematics of Igneous Rocks. Cambridge: Cambridge University Press.

Lee W-J., Wyllie P. J. (1994) Experimental data bearing on liquid immiscibility, crystal fractionation, and the origin of calciocarbonatites and natrocarbonatites. International Geology Review 36, 797-819.

Lee W-J., Wyllie P. J. (1997) liquid immiscibility between nephelinite and carbonatite from 1.0 to 2.5 GPa compared with mantle melt compositions. Contributions to Mineralogy and Petrology 127, 1-16.

Lee W-J., Wyllie P. J. (1998) Process of Crustal Carbonatite Formation by Liquid Immiscibility and Differentiation, Elucidated by Model Systems. Journal of Petrology 39, 2005-2013.

Lee J-H., Seo J-K., Park J-W. (2006) Characterization of natural corundum (rubies and sapphires) and beryllium diffused corundum. ECS Meeting Abstracts, no. 58, 209th ECS Meeting.

Limtrakun P., Zaw K., Ryan C. G., Mernagh T. P. (2001) Formation of the Denchai gem sapphires, northern Thailand: evidence from mineral chemistry and fluid/melt inclusion characteristics. Mineralogical Magazine 65, 725-735.

Linthout K., Paulick H., Wijbrans J. R. (2009) Provenance of basalt blocks from Roman sites in Vleuten-De Meern (The Netherlands) traced to the Tertiary Siebengebirge (Germany): A geoarcheological quest using petrological and geochemical methods. Geologie en Mijnbouw 88, 78-99.

Lippolt H. (1982) K-Ar determinations and the correlation of tertiary volcanic activity in Central Europe. Geologisches Jahrbuch Hannover, D52, 113-135.

Liu T.-C., Presnall D. C. (1990) Liquidus phase relationships on the join anorthite-forsterite-quartz at 20 kbar with applications to basalt petrogenesis and igneous sapphirine. Contributions to Mineralogy and Petrology 104, 735-742.

Liu T.-C., Presnall D. C. (2000) Liquidus Phase Relations in the System CaO-MgO-Al_2O_3-SiO_2 at 2.0 GPa: Applications to Basalt Fractionation, Eclogites, and Igneous Sapphirine. Journal of Petrology 41, 3-20.

Ludwig K. R. (2012) Isoplot 3.75 A Geochronological Toolkit for Microsoft Excel. Berkeley Geochronology Center Special Publication No. 5.

MacNevin A. A. (1972) Sapphires in the New England district, New South Wales. Records of the Geological Survey of New South Wales 14, 19-35.

Maliková P. (1999) Origin of sapphires from the Jizerská Louka alluvial deposit in North Bohemia, Czech Republic, Euope. Austalian Gemmology 20, 202-206.

Markl G. (2005) Mullite-corundum-spinel-cordierite-plagioclase xenoliths in the Skaergaard Marginal Border Group: multi-stage interaction between metasediments and basaltic magma. Contributions to Mineralogy and Petrology 149, 169-215.

Mazzone P., Haggerty S. E. (1989) Peraluminous xenoliths in kimberlite: metamorphosed restites produced by partial melting of pelites. Geochimica et Cosmochimica Acta 53, 1551-1561.

McColl D. H., Warren R. G. (1980) First discovery of ruby in Australia. Mineral Record 11, 371-79.

McGee, B. M. (2005) Characteristics and origin of the Weldborough sapphire, NE Tasmania. (Unpublished BSc thesis): Hobart, Australia, University of Tasmania, School of Earth Science, 118 pp.

Mehnert K. (1986) Migmatites and the Origin of Granitic Rocks. Elsevier, Amsterdam. 391 pp.

Melcher F., Sitnikova M. A., Graupner T., Martin N., Oberthür T. (2008) Analytical fingerprint of columbite-tantalite (coltan) mineralization in pegmatites: focus on Africa. In: Proceedings, ninth international congress for applied mineralogy (ICAM) pp. 615-624.

Melcher F., Graupner T., Gäbler H-E., Sitnikova M., Henjes-Kunst F., Oberthür T., Gerdes A., Dewaele S. (2015) Tantalum-(niobium-tin) mineralisation in African pegmatites and rare metal granites: Constraints from Ta-Nb

oxide mineralogy, geochemistry and U-Pb geochronology. Ore Geology Reviews 64, 667-719.

Mengel K., Sachs P. M., Stosch H. G., Wörner G., Look, G. (1991) Crustal Xenoliths from Cenozoic volcanic fields of West Germany: implications for structure and composition of the crust. Tectonophysics 195, 271-289.

Meyer H. O. A.; Mitchell R. H. (1988) Sapphire-bearing ultramafic lamprophyre from Yogo, Montana: A ouachitite. Canadian Mineralogist 26, 81-88.

Meyer W., Stets J. (2002) Pleistocene to Recent tectonics in the Rhenish Massif (Germany). Netherlands Journal of Geosciences/ Geologie en Mijnbouw 81, 217-221.

Meyer R., Abratis M., Viereck-Götte L., Mädler J., Hertogen J., Romer R. L. (2003) Mantelquellen des Vulkanismus in der thüringischen Rhön. Beiträge zur Geologie von Thüringen 9, 75-105.

Middlemost E. A. K. (1974) Petrogenetic model for the origin of carbonatites. Lithos 7, 275-278.

Milholland C. S. and Presnall D. C. (1998) Liquidus Phase Relations in the CaO-MgO-Al_2O_3-SiO_2 System at 3.0 GPa: the Aluminous Pyroxene Thermal Divide and High-pressure Fractionation of Picritic and Komatiitic Magmas. Journal of Petrology 39, 3-27.

Mitchell R. H. and Brunfelt A. O. (1975) Rare earth element geochemistry of the Fen alkaline complex, Norway. Contributions to Mineralogy and Petrology 52, 247-259.

Moyd L. (1949) Petrology of the nepheline and corundum rocks of south eastern Ontario. American Mineralogist 34, 736-751.

Münker C., Pfänder J.A., Weyer S., Büchl A., Kleine T., Mezger K. (2003) Evolution of Planetary Cores and the Earth-Moon System from Nb/Ta Systematics. Science 301, 84-87.

Nechaev V. P., Nechaeva E. V., Chashchin A. A., Vysotskiy S. V., Graham I. T., Sutherland F. L. (2009) New Isotopic Data on Late Cenozoic Age and Mantle Origin of Gem zircon and Corundum from Placers of Primorye, Russia. Doklady Earth Sciences 2009, 1426-1429.

Noeggerath J. (1827) Der Bergschlüpf vom 20. December 1846 an den Unkeler Basaltsteinbrüchen bei Oberwinter, geognostisch geschildert und geologisch erläutert. Henry und Cohen. Bonn, 1827.

Oakes G. M., Barron L. M., Lishmund S. R. (1996) Alkali basalts and associated volcaniclastic rocks as a source of sapphire in eastern Australia. Australian Journal of Earth Sciences 43, 289-298.

Okrusch M., Bunch T. E., Bank H. (1976) Paragenesis and Petrogenesis of a corundum-bearing marble at Hunza (Kaishmir). Mineralium Deposita 11, 278-297.

Oncken O., Winterfeld C., Dittmar U. (1999) Accretion of a rifted passive margin: The Late Paleozoic Rhenohercynian fold and thrust belt (Middle European Variscides). Tectonics 18, 75-91.

Operta M., Pamić J., Balen D., Tropper P. (2002) Corundum-bearing amphibolites from the metamorphic basement of the Krivaja-Konjuh ultramafic massif (Dinaride Ophiolite Zone, Bosnia). Mineralogy and Petrology 77, 287-295.

Ouzegane K., Guiraud M., Kienast J. R. (2002) Prograde and Retrograde Evolution in High-temperature Corundum Granulites (FMAS and KFMASH Systems) from In Ouzzal Terrane (NW Hoggar, Algeria). Journal of Petrology 44, 517-545.

Pakhomova V. A., Zalishchak B. L., Odarichenko E. G., Lapina M. I., Karmanov N. S. (2006) Study of melt inclusions in the Nezametnoye corundum deposit, Primorsky region of the Russian Far East: Petrogenetic consequences. Journal of Geochemical Exploration 89, 302-305.

Panina L. I. (2008) Liquid immiscibility in deep-seated magmas and the generation of carbonatite melts. Geochemistry International 46, 448-464.

Paton C., Hellstrom J., Paul B., Woodhead J., Hergt J. (2011) Iolite: Freeware for the visualization and processing of mass spectrometric data. Journal of Analytical Atomic Spectrometry 26, 2508-2518.

Petrelli M., Poli G., Perugini D., Peccerillo A. (2005) PetroGraph: A new software to visualize, model, and present geochemical data in igneous petrology. Geochemistry, Geophysics, Geposystems.

Petrus J. A., Kamber B. S. (2012) VizualAge: A Novel Approach to Laser Ablation ICP-MS U-Pb Geochronology Data Reduction. Geostandards and Geoanalytical Research 36, 247-270.

Peucat J. J., Ruffault P., Fritsch E., Bouhnik-Le Coz M., Simonet C., Lasnier B. (2007) Ga/Mg ratio as a new geochemical tool to differentiate magatic from metamorphic blue sapphires. Lithos 98, 261-274.

Pfänder J. A., Jung S., Münker C., Stracke A., Mezger K. (2012) A possible high Nb/Ta reservoir in the continental lithospheric mantle and consequences on the global Nb budget – Evidence from continental

basalts from Central Germany. Geochimica et Cosmochimica Acta 77, 232 – 251.

Pisutha-Arnond V., Intasopa S., Wathanakul P., Griffin W. L., Atichat W., Sutthirat C. (2005) Corundum xenocrysts in basalt from Bo Phloi gem field, Kanchanaburi, western Thailand. In: International conference on Geology, Geotechnology and Mineral Resources of Indochina (GEOINDO 2005), Khon Kaen, Thailand, pp. 338-344.

Pitzer K. S., Sterner S. M. (1994) Equations of state valid continuously from zero to extreme pressures for H_2O and CO_2. The Journal of Chemical Physics 101, 3111-3116.

Prodehl C., Mueller S., Glahn A., Gutscher M., Haak V. (1992) Lithospheric cross sections of the European Cenozoic rift system. Tectonophysics 208, 113-138.

Przybyla M. (2013) $^{40}Ar/^{39}Ar$-Datierungen an Vulkaniten des Siebengebirges. (Msc thesis): Cologne, Germany, Institut für Geologie und Mineralogie, Universität zu Köln, 123 pp.

Putnis A. (2002) Mineral replacement reactions: from macroscopic observations to microscopic mechanisms. Mineralogical Magazine 66, 689-708.

Rakatondrazafy A. F. M., Giuliani G., Ohnestetter D., Falllick A. E., Rakotosamizanany S., Andriamamonjy A., Ralantoarison T., Razanatseheno M., Offant Y., Garnier V., Maluski H., Dunaigre C., Schwarz D., Ratrimo V. (2008) Gem corundum deposits of Madagascar: A review. Ore Geology Reviews 34, 134-154.

Regenauer-Lieb K. (1998) Dilatant plasticity applied to Alpine collision: ductile void growth in the intraplate area beneath the Eifel volcanic field. Journal of Geodynamics 27, 1-21.

Ritter J. R. R., Jordan M., Christensen U. R., Achauer U. (2001) A mantle plume beneath the Eifel volcanic fields, Germany. Earth and Planetary Science Letters 186, 7-14.

Roberts D. L., Sutherland F. L., Hollis J. D., Kennewell P., Graham I. T. (2004) Gemstone characteristics, North-East Barrington Plateau, NSW. Journal of Proceedings of the Royal Society of New South Wales 137, 99-122.

Robertson A. D. C., Sutherland F. L. (1992) Possible origins and ages for sapphire and diamond from the central Queensland gemfields. Records of the Australian Museum Supplement 15, 45-54.

Rossman G. R., Smyth J. R. (1990) Hydroxyl contents of accessory minerals in eclogites and related rocks. American Mineralogist 75, 775-780

Rosso K. M., Bodnar R. J. (1995) Microthermometric and Raman spectroscopic detection limits of CO_2 in fluid inclusions and the Raman spectroscopic characterization of CO_2. Geochimica et Cosmochimica Acta 59, 3961-3975.

Saminpanya S. (2001) Ti-Fe mineral inclusions in star sapphires from Thailand. Australian Gemmologist 21, 125-128.

Saminpanya S., Manning D. A. C., Droop G. T. R., Henderson C. M. B. (2003) Trace elements in Thain gem corundums. Journal of Gemmology 28, 399-415.

Saminpanya S., Sutherland F. L. (2011) Different origins of Thai area sapphire and ruby, derived from mineral inclusions and co-existing minerals. European Journal of Mineralogy 23, 683-694.

Sanchez-Viscaíno V. L. (2002) Reaction zones developed between corundum metapelite and marble, Alborán Sea basement, western mediterranean: origin and phase relations.

Schmetzer K., Bank H. (1980) Explanations of the absorption spectra of natural and synthetic Fe- and Ti-containing corundums. Neues Jahrbuch für Mineralogie - Abhandlungen 139, 216-225.

Schmetzer K., Bank H. (1981) The color of natural corundum. Neues Jahrbuch für Mineralogie - Monatshefte 2, 59-68.

Schmitt A. K., Wetzel F., Cooper K. M., Zou H., Wörner G. (2010) Magmatic Longevity of Laacher See Volcano (Eifel, Germany) Indicated by U-Th Dating of Intrusive Carbonatites. Journal of Petrology 51, 1053-1085.

Schubert S., Jung S., Pfänder J. A., Hauff F., Garbe-Schönberg D. (2015) Petrogenesis of Tertiary continental intra-plate lavas between Siebengebirge and Westerwald, Germany: Constraints from trace element systematics and Nd, Sr and Pb isotopes. Journal of Volcanology and Geothermal Research 305, 84-99.

Shimpo M., Tsunogae T., Santosh M. (2006) First report of garnet-corundum rocks from southern India: Implications for prograde high-pressure (eclogite-facies?) metamorphism. Earth and Planetary Science Letters 242, 111-129.

Simonet C. (2000) Géologie des gisements de saphir et de rubis. L'exemple de la John Saul mine, Mangari, Kenya. Thèse de Doctorat, Université de Nantes, France, p 349.

Simonet C., Paquette J. L., Pin C., Lasnier B., Fritsch E. (2004) The Dusi (Garba Tula) sapphire deosit, Central Kenya – a unique Panafrican corundum-bearing monzonite. Journal of African Earth Sciences 38, 401-410.

Simonet C., Fritsch E., Lasnier B. (2008) A classification of gem corundum deposits aimed towards gem exploration. Ore Geology Reviews 34, 127-133.

Smith C. P., Kammerling R. C., Keller A. S., Peretti A., Scarratt K. V., Khoa N. D., Repetto S. (1995) Sapphires from Southern Vietnam. Gems and Gemology 31.3, 168-186.

Smith S. R., Foster G. L., Romer R. L., Tindle A. G., Kelley S. P., Noble S. R., Horstwood M., Breaks F. W. (2004) U-Pb columbite-tantalite chronology of rare-element pegmatites using TIMS and Laser Ablation-Multi-Collector-ICP-MS. Contributions to Mineralogy and Petrology 147, 549-564.

Song Y., Hu W., Zhang W. (2008) Microthermometry and Raman density analysis of fluid and melt inclusions in corundum megacrysts from basalts in Changle, Shandong province. Acta Petrologica et Mineralogica 27, 489-504.

Song Y., Chou I. M., Hu W., Burruss R., Lu W. (2009a) CO_2 density-Raman shift relation derived from synthetic inclusions in fused silica capillaries and its application. Acta Geologica Sinica 83, 932-938.

Song Y., Hu W. (2009) Carbonates und sulfates-bearing melt inclusions in corundum megacrysts from Changle basalts of Shandong province and their implications. Acta Petrologica et Mineralogica 28, 349-363.

Srithai B., Rankin A. H. (1999) Fluid inclusion characteristics of sapphires from Thailand. In: Stanley, et al. (Ed.), Mineral Deposits: Processes to Processing. Balkema, Rotterdam, pp. 107-110.

Stacey J. S., Kramers J. D. (1975) Approximation of terrestrial lead isotope evolution by a two-stage model. Earth and Planetary Science Letters 26, 207-221.

Steiger R. H., Jäger E. (1977) Subcommission on geochronology: Convention on the use of decay constants in geo- and cosmochronology. Earth and Planetary Science Letters 36, 359-362.

Stephenson P. J. (1976) Sapphire and zircon in some basaltic rocks from Queensland, Australia. Abstracts of the 25th International Geological Congress 2, 602-603.

Strogi L., Warner M. E., Lutz T. M. (1993) Dehydration partial melting and disequilibrium in the granulite-facies Wilmington Complex, Pennsylvania Delaware Piedmont. American Journal of Science 293, 405-462.

Sugawara T. (2000) Empirical relationships between temperature, pressure, and MgO content in olivine and pyroxene saturated liquid. Journal of Geophysical Research 105, 8457-8472.

Sutherland F. L. (1996) Alkaline rocks and gemstones, Australia: a review and synthesis. Australian Journal of Earth Sciences 43, 323-343.

Sutherland F. L., Schwarz D., Jobbins E. A., Coenraads R. R., Webb G. (1998a) Distinctive gem corundum suites from discrete basalt fields: a comparative study of Barrington, Australia, and West Pailin, Cambodia, gemfields. Journal of Gemmology 26, 65-85.

Sutherland F. L., Hoskin P. O.W., Fanning C. M., Coenraas R. R. (1998b) Models of corundum origin from alkali basaltic terrains: a reappraisal. Contributions to mineralogical petrology 133, 356-372.

Sutherland F. L., Schwarz D. (2001) Origin of gem corundums from basaltic fields. Australian Gemmology 21, 30-33.

Sutherland F. L., Bosshart G., Fanning C. M., Hoskin P. W. O., Coenraads R. R. (2002a) Sapphire crystallization, age and origin, Ban Huai Sai, Laos: age based on zircon inclusions. Journal of Asian Earth Sciences 20, 841-849.

Sutherland F. L., Graham I. T., Pogson R. E., Schwarz D., Webb G. B., Coenraads R. R., Fanning C. M., Hollis J. D., Allen T. C. (2002b) The Tumbarumba Basaltic Gem Field, New South Wales: In Relation to Sapphire-Ruby Deposits of Eastern Australia. Records of the Australian Museum 54, 215-248.

Sutherland F. L., Coenraads R. R., Schwarz D., Raynor L. R., Barron B. J., Webb G. B. (2003) Al-rich diopside in alluvial ruby and corundum-bearing xenoliths, Australian and SE Asian basalt fields. Mineralogical Magazine 67, 717-732.

Sutherland L., Graham I., Webb G., Pogson R., Giuliani G. (2005) New ruby-sapphire sources, Yarrowitch basalt field, eastern NSW. SGGMP – Port Macquire 2005. Geological Society of Australia Abstracts 76, 133-136.

Sutherland F. L., Duroc-Danner J. M., Meffre S. (2008) Age and origin of gem corunudum and zircon megacrysts from the Mercaferes-Rio Mayo area, South-west Colombia, South America. Ore Geology Reviews 34, 155-168.

Sutherland F. L., Giuliani G., Fallick A. E., Garland M., Webb G. (2008b) Sapphire-ruby characteristics, West Palin, Cambodia: Clues to their origin based on trace element and O isotope analysis. The Australian Gemmologist 23, 329-368.

Sutherland F. L., Giuliani G., Fallick A. E., Garland M., Webb G. (2009) Sapphire-ruby characteristics, West Palin, Cambodia: clues to their origin based on trace element and O isotope analysis. Australian Gemmologist 23, 373-432.

Sutthirat C., Saminpanya S., Droop G. T. R., Henderson C. M. B., Manning D. A. C. (2001) Clinopyroxene-corundum assemblages from alkali basalts and alluvium, eastern Thailand: constraints on the origin of Thai rubies. Mineralogical Magazine 65, 277-295.

Srivastava R. K., Heaman L. M., Sinha A. K., Shihua S. (2005) Emplacement age and isotope geochemistry of Sung Valley alkaline-carbonatite complex, Shillong Plateau, northeastern India: Implications for primary carbonate melt and genesis of the associated silicate rocks. Lithos 81, 33-54.

Sweeney R. J. (1994) Carbonatite melt composition in the Earth's mantle. Earth and Planetary Science Letters 128, 259-270.

Tamman G. (1920) Über Anlauffarben von Metallen. Zeitschrift für anorganische und allgemeine Chemie 111, 78-89.

Tera F., Wasserburg G. J. (1972) U-Th-Pb systematic in three Apollo 14 basalts and the problem of initial Pb in lunar rocks. Earth and Planetary Science Letters 14, 281-304.

Thibault Y., Edgar A. D., Lloyd F. E. (1992) Experimental investigation of melts from a carbonated phlogopite lherzolite: Implications for metasomatism in the continental lithospheric mantle. American Mineralogist 77, 784-794.

Todt W., Lippolt H. J. (1980) K-Ar age determinarion on tertiary volcanic rocks: V. Siebengebirge, Siebengebirge-Graben, Journal of Geophysics 48, 18-27.

Uher, P.; Giuliani, G.; Szakall, S.; Fallick, A.; Strunga, V.; Vaculovic, T.; Ozdin, D.; Greganova, M. (2012) Sapphires related to alkali basalts from the Cerová Highlands, Wesatern Carpathians (southern Slovakia): composition and origin. Geologica Carpathica 63, 71-82.

Upton B. G. L., Hinton R.W., Aspen P., Finch A., Valles J. W. (1999) Megacrysts and associated xenoliths: evidence for migration of geochemically enriched melts in the upper mantle beneath Scotland. Journal of Petrology 40, 935 – 956.

Van Long P., Quang Vinh H., Garnier V., Giuliani G., Ohnestetter D., Lhomme T., Schwarz D., Fallick A. E., Dubessy J., Trong Trinh P. (2004) Gem corundum deposits in Vietnam. Journal of Gemmology 29, 129-147.

Vichit P. (1987) The distribution and some characteristics of corundum bearing basalts in Thailand. Journal of the Geological Society of Thailand 3, M4.1-M4.38.

Vieten K. (1983) Tertiary volcanism in the Siebengebirge mountains. In: Plateau Uplift – The Rhenish Shield – A Case History. (Fuchs., von Gehlen K., Mälzer H., Murawski H., Semmel A., eds), pp. 131-132. Springer, Berlin.

Vieten K., Hamm H. M., Grimmeisen W. (1988). Tertiärer Vulkanismus des Siebengebirges. Fortschritte der Mineralogie, Beihefte 66, 1-42.

Vysotskiy S. V., Shcheka G. G., Lehmann B. (2002) First Finding of Platinum Group Minerals in the Gold- and Sapphire-Bearing Placer of the Kedrovka River (Bol'shaya Ussurka River Basin, Primorye Region). Doklady Earth Sciences 387, 890-894.

Wallace M. E. and Green D. H. (1988) An experimental determination of primary carbonatite magma composition. Nature 335, 343-346.

Wang X., Chou I.-M., Hu W., Burruss R. C., Sun Q., Song Y. (2011) Raman spectroscopic measurements of CO_2 density: Experimental calibration with high-pressure optical cell (HPOC) and fused silica capillary capsule (FSCC) with application to fluid inclusion observations. Geochimcia et Cosmochimica Acta 75, 4080-4093.

Wang L. Z. (2000) Transmission Electron Microscopy of Shape-Controlled Nanocrystals and Their Assemblies. The Journal of Physical Chemistry B 104, 1153-1175.

Warren R. G. (1983) PRograde and retrograde sapphirine in metamorphic rocks of central Australia. B.M.R. Journal of Australian Geology and Geophysics 8, 139-145.

Wathanakul P., Atichat W., Pisutha-Arnond V., Win T. T., Singbamroong S. (2004) Evidences of the unusually high Be, Sn, Nb and Ta content in some

trapiche-like sapphires from basaltic origins. Proceedings of the 29th International Gemmological Conference, Wuhan, China, pp.114-118.

Watson E. B., Price J. D. (2002) Kinetrics of the reaction $MgO + Al_2O_3 \rightarrow MgAl_2O_4$ and Al-Mg interdiffusion in spinel at 1200 to 2000°C and 0.1 to 4.0 GPa. Geochimica et Cosmochimica Acta 66, 2123-2138.

Whalen J. B., Curie K. L., Chappell B. W. (1987) A-type granites: geochemical characteristics, discrimination and petrogenesis. Contributions to Mineralogy and Petrology 95, 407-419.

Windley B. F., Ackermand D., Herd R. K. (1984) Sapphirine/kornerupine-bearing rocks and crustal uplift history of the Limpopo belt, Southern Africa. Contributions to Mineralogy and Petrology 86, 342-358.

Wedepohl K. H., Gohn E., Hartmann G. (1994) Cenozoic alkali basaltic magmas of western Germany and their products of differentiation. Contributions to Mineralogy and Petrology 115, 253-278.

Wedepohl K. H., Baumann A. (1999) Ventral European Cenozoic plume volcanism with OIB characteristics and indications of a lower mantle source. Contributions to Mineralogy and Petrology 136, 225-239.

Whitney W. P., Stubican V. S. (1971) Interdiffusion studies in the system MgO-Al_2O_3. Journal of Physics and Chemistry of Solids 32, 305-312.

Wildschrey E. (1911) Neue und wenig bekannte Mineralien aus dem Siebengebirge und seiner Umgebung. (Dissertation): Bonn, Germany, Institut für Geologie, Mineralogie und Paläontologie, Rheinische Friedrich-Wilhelms-Universität Bonn, pp. 61.

Wilson M., Downes H. (1991) Tertiary-Quarternary extension related alkaline magmatism in western and central Europe. Journal of Petrology 32, 811-849.

Wilson M., Patterson R. (2001) Interplate magmatism related to short-wavelength convective instabilities in the upper mantle: evidence from the Tertiary-Quarternary volcanic province of western and Central Europe. In: Mantle Plumes; Their Identification Through Time. (Ernst R.E., Buchan K.L., eds.), Geological Society of America, Special Paper 352, 37-58.

Wirth R. (2004) Focused Ion Beam (FIB) A novel technology for advanced application of micro- and nanoanalysis in geosciences and applied mineralogy. European Journal of Mineralogy 16, 863-876.

Wirth R. (2009) Focused Ion Beam (FIB) combined with SEM and TEM: Advanced analytical tools for studies of chemical composition, microstructure and crystal structure in geomaterials on a nanometre scale. Chemical Geology 261, 217-229.

Wolff J. A. (1994) Physical properties of carbonatite magmas inferred from molten salt data, and application to extraction patterns from carbonatite-silicate magma chambers. Geological Magazine 131, 145-153.

Wörner G., Schmincke H.-U. (1984a) Mineralogical and chemical zonation oft he Laacher See tephra sequence (East Eifel, W. Germany). Journal of Petrology 25, 805-835.

Wörner G., Schmincke H.-U. (1984b) Petrogenesis oft he zoned Laacher See tephra. Journal of Petrology 25, 836-851.

Wörner G., Zindler A., Staudigel H., Schmincke H.-U. (1986) Sr, Nd, and Pb isotope geochemistry of Tertiary and Quarternary alkaline volcanics from West Germany. Earth Planetary Science Letters 79, 107-119.

Yamomoto J., Kagi H. (2006) Extended micro-Raman densimeter for CO_2 applicable to mantle-originated fluid inclusions. Chemistry Letters 35, 610-611.

Ying J., Zhou X., Zhang H. (2004) Geochemical and isotopic investigation of the Laiwu-Ziob carbonatites from western Shandong Province, China, and implications for their petrogenesis and enriched mantle source. Lithos 75, 413-426.

Yui, T. F.; Zaw, K.; Limtrakun, P. (2003) Oxygen isotope composition of the Denchai sapphire, Thailand: a clue to its enigmatic origin. Lithos 67, 153-161.

Yui, T. F., Wu, C. M., Limtrakum P., Sricharn W., Boonsoog A. (2006) Oxygen isotope studies on placer sapphire and ruby in the Chantaburi-Trat alkali basaltic gemfield, Thailand. Lithos 86, 197-211.

Zaw K., Sutherland F. L., Dellapasqua F., Ryan C. G., Yui T.-F., Mernagh T. P., Duncan D. (2006) Contrasts in gem corundum characteristics, eastern Australian basaltic fields: trace elements, fluid/melt inclusions and oxygen isotopes. Mineralogical Magazine 70, 669-687.

Zehler J.G. Das Siebengebirge und seine Umgebungen nach den interessanten Beziehungen dargestellt. J.H. Funk'sche Buchhandlung. Krefeld, 1937.

Zhang P., DebRoy T., Seetharaman S. (1996) Interdiffusion in the MgO-Al_2O_3 spinel with or without some dopants. Metallurgical and Materials Transections A 27, 2105-2114.

Zhang R. Y., Liou J. G., Zheng J. P. (2004) Ultrahigh-pressure corundum-rich garnetite in garnet peridotite, Sulu terrane, China. Contributions to Mineralogy and Petrology 147, 21-31.

Ziegler P. A. (1992) European Cenozoic rift system. Tectonophysics 208, 91-111.

Zirkel F. (1903) Über Urausscheidungen in Rheinischen Basalten. Abhandlungen der königlich sächsischen Gesellschaft der Wissenschaften zu Leipzig, mathematisch-physische Classe 28, 101-198. Teubner, Leipzig.

Table A-1: Composition of the host basalt constituting major minerals

sample	3				15			26	
	Diopside	**Olivine**	**Labradorite**	**Anorthoclase**	**Diopside**	**Labradorite**	**Sanidine**	**Diopside**	**Labradorite**
	(n = 5)	*(n = 4)*	*(n = 9)*	*(n = 1)*	*(n =9)*	*(n =9)*	*(n = 1)*	*(n =10)*	*(n =10)*
SiO_2	46.8	39.2	51.9	63.5	48.6	53.2	64.5	48.2	51.9
TiO_2	2.29	0.02	0.18	0.28	2.14	0.16	0.15	2.05	0.13
Al_2O_3	7.25	0.05	29.4	20.9	5.63	29.5	19.8	6.54	30.3
FeO	6.82	19.2	0.67	0.37	7.48	0.77	0.36	6.56	0.64
MnO	0.12	0.42	0.03	0.04	0.20	0.03	0.01	0.15	0.04
MgO	13.1	41.9	0.06	0.02	13.3	0.06	0.01	13.8	0.05
CaO	22.1	0.30	11.7	1.72	21.9	11.0	2.2	22.2	12.45
Na_2O	0.62	0.02	3.93	3.8	0.68	4.33	4.41	0.56	3.8
K_2O	0.01	0.01	0.42	7.47	0.02	0.43	8.6	0.01	0.31
Cr_2O_3	0.30	0.02	0.02	0.02	0.20	0.02	n.d.	0.36	0.02
Total	99.5	101.1	98.3	99.2	100.1	99.8	100.0	100.3	99.7
Wo	44	**Fo** 80	**An** 59	11	**Wo** 41	**An** 56	8	**Wo** 45	**An** 62
En	46	**Fa** 20	**Ab** 36	40	**En** 46	**Ab** 39	41	**En** 46	**Ab** 35
Fs	10		**K** 3	44	**Fs** 13	**K** 3	50	**Fs** 9	**K** 2

sample	ÖL25				ÖL60			ÖL61		
	Diopside	**Labradorite**	**Andesine**	**Anorthoclase**	**Diopside**	**Olivine**	**Labradorite**	**Diopside**	**Olivine**	**Labradorite**
	(n =10)	*(n = 6)*	*(n = 1)*	*(n = 3)*	*(n = 3)*	*(n = 7)*	*(n = 10)*	*(n = 14)*	*(n = 11)*	*(n = 10)*
SiO_2	48.1	52.7	56.0	50.6	48.2	38.7	52.7	47.8	38.6	52.9
TiO_2	2.18	0.17	0.17	0.99	2.01	0.20	0.17	2.15	0.03	0.16
Al_2O_3	5.58	29.9	27.7	17.5	7.20	0.04	29.9	5.79	0.03	29.4
FeO	7.16	0.65	0.56	4.09	6.58	21.9	0.74	6.96	21.3	0.63
MnO	0.26	0.02	n.d.	0.10	0.11	0.51	0.03	0.15	0.47	0.02
MgO	13.6	0.03	0.03	6.97	14.0	39.7	0.05	13.7	40.1	0.04
CaO	21.4	12.0	9.26	17.2	20.9	0.35	12.2	21.5	0.33	12.0
Na_2O	0.67	4.14	5.19	2.13	0.74	0.03	3.96	0.82	0.06	4.13
K_2O	0.01	0.31	0.63	0.17	0.01	0.01	0.43	0.01	0.01	0.30
Cr_2O_3	0.07	0.02	0	0.08	0.17	0.01	0.02	0.17	0.03	0.01
Total	99.0	99.9	99.5	99.8	99.9	101.3	100.2	99.1	100.9	90.9
Wo	41	**An** 59	46	53	**Wo** 41	**Fo** 76	**An** 60	**Wo** 42	**Fo** 77	**An** 59
En	47	**Ab** 37	47	37	**En** 51	**Fa** 23	**Ab** 36	**En** 47	**Fa** 23	**Ab** 38
Fs	12	**K** 2	4	9	**Fs** 9		**K** 3	**Fs** 11		**K** 2

Table A-1 (continued): Composition of the host basalt constituting major minerals

sample	PE21				KS21				S52					
	Diopside		**Labradorite**	**Andesine**	**Diopside**		**Labradorite**		**Diopside**		**Olivine**		**Labradorite**	
	(n = 10)		*(n = 8)*	*(n = 2)*	*(n =10)*		*(n =10)*		*(n = 3)*		*(n = 7)*		*(n = 10)*	
SiO_2	48.4		54.4	56.2	49.4		51.8		48.2		38.7		51.9	
TiO_2	2.28		0.17	0.14	1.82		0.17		1.85		0.05		0.12	
Al_2O_3	5.06		28.9	27.9	4.71		30.4		5.86		0.03		30.3	
FeO	7.57		0.53	0.43	7.37		0.80		7.55		22.4		0.66	
MnO	0.17		0.02	0.04	0.18		0.03		0.16		0.48		0.03	
MgO	13.2		0.06	0.04	13.9		0.07		12.8		39.3		0.05	
CaO	21.8		10.8	9.74	21.6		12.8		22.1		0.36		12.5	
Na_2O	0.70		4.52	5.04	0.64		3.62		0.79		0.03		2.69	
K_2O	0.02		0.37	0.54	0.02		0.32		0.01		0.01		0.29	
Cr_2O_3	0.15		0.01	0.02	0.16		0.01		0.26		0.02		0.02	
Total	99.3		99.8	100.0	99.8		99.9		99.6		101.5		99.6	
Wo	40	**An**	53	48	**Wo**	43	**An**	63	**Wo**	43	**Fo**	75	**An**	63
En	45	**Ab**	42	47	**En**	40	**Ab**	33	**En**	45	**Fa**	24	**Ab**	32
Fs	14	**K**	2	3	**Fs**	16	**K**	2	**Fs**	12			**K**	2

sample	PE25							UN31					
	Diopside		**Olivine**	**Labradorite**	**Andesine**	**Sanidine**		**Diopside**		**Olivine**		**Labradorite**	**Andesine**
	(n = 10)		*(n = 2)*	*(n = 4)*	*(n = 5)*	*(n = 1)*		*(n = 10)*		*(n = 10)*		*(n = 9)*	*(n = 1)*
SiO_2	49.4		36.8	53.9	55.9	65.2		47.2		38.2		53.0	58.7
TiO_2	2.02		0.04	0.16	0.17	0.17		2.37		0.04		0.15	0.17
Al_2O_3	4.58		0.01	29.0	27.7	20.5		6.29		0.04		29.4	25.7
FeO	7.59		26.6	0.61	0.66	0.32		7.30		22.8		0.64	0.41
MnO	0.17		0.62	0.04	0.03	0.03		0.17		0.52		0.03	0.06
MgO	13.9		34.6	0.08	0.15	0.01		13.0		38.5		0.04	0.02
CaO	21.7		0.42	10.9	9.39	1.22		21.6		0.34		11.6	6.88
Na_2O	0.63		0.02	4.55	4.83	4.95		0.69		0.04		2.32	0.17
K_2O	0.02		0.02	0.37	1.16	8.14		0.02		0.01		2.08	5.83
Cr_2O_3	0.24		0.02	0.02	0.02	0.02		0.15		0.01		0.02	n.d.
Total	100.1		99.2	99.6	99.9	100.5		98.9		100.5		99.4	99.2
Wo	**Wo**	40	**Fo** 69	**An**	54	46	7	**Wo**	41	**Fo**	75	**An**	57	35
En	**En**	46	**Fa** 30	**Ab**	41	44	44	**En**	45	**Fa**	25	**Ab**	38	53
Fs	**Fs**	14		**K**	2	7	47	**Fs**	15			**K**	2	9

Table B-1: Major composition of the sapphires and the spinel rims (Electron microprobe analyses

sample	3								15							
	corundum				spinel				corundum				spinel			
	1	2	3	**average**	1	2	3	**average**	1	2	3	**average**	1	2	3	**average**
MgO	n.d.	0.01	0.01	0.01	16.4	16.2	16.4	16.3	0.01	n.d.	0.07	0.04	16.2	16.1	15.9	16.1
FeO	1.65	1.30	1.53	1.49	18.1	18.0	16.9	17.6	2.18	2.03	1.84	2.02	18.5	18.3	18.2	18.3
MnO	n.d.	n.d.	0.01	0.01	0.29	0.28	0.25	0.27	0.01	0.03	n.d.	0.02	0.33	0.25	0.38	0.32
K_2O	0.01	n.d.	n.d.	0.01	n.d.	n.d.	n.d.	n.d.	n.d.	0.01	0.01	0.01	0.01	0.01	0.01	0.01
Na_2O	n.d.	n.d.	0.01	0.01	0.02	n.d.	0.02	0.02	0.02	0.01	0.01	0.01	n.d.	0.03	0.06	0.05
CaO	0.01	0.02	n.d.	0.02	0.04	n.d.	0.01	0.02	n.d.	n.d.	0.01	0.01	n.d.	0.05	0.01	0.03
TiO_2	0.64	0.46	0.29	0.46	0.05	0.11	0.15	0.10	0.16	0.04	0.19	0.13	0.11	0.11	0.10	0.10
Cr_2O_3	n.d.	n.d.	0.01	0.01	0.01	n.d.	0.02	0.02	n.d.	n.d.	n.d.	n.d.	0.01	0.03	0.04	0.03
Al_2O_3	98.6	99.0	97.5	98.4	65.9	65.8	65.7	65.8	98.1	97.9	98.1	98.0	65.6	65.3	65.8	65.6
SiO_2	0.04	0.04	0.02	0.03	0.01	0.03	0.03	0.02	0.02	0.02	0.02	0.02	0.07	0.04	0.02	0.04
Total	101.0	101.1	99.4	100.5	100.8	100.4	99.4	100.2	100.5	100.1	100.2	100.3	100.8	100.2	100.5	100.5

sample	KS21							ÖL61						
	corundum			spinel				corundum			spinel			
	1	2	**average**	1	2	3	**average**	1	2	**average**	1	2	3	**average**
MgO	n.d.	0.01	n.d.	14.2	14.1	14.2	14.2	0.00	0.01	0.00	14.2	14.1	14.2	14.2
FeO	0.02	0.03	0.02	0.01	0.00	0.00	0.00	0.02	0.03	0.02	0.01	0.00	0.00	0.00
MnO	1.75	1.28	1.52	21.2	20.8	21.4	21.1	1.75	1.28	1.52	21.2	20.8	21.4	21.1
K_2O	n.d.	n.d.	n.d.	0.01	n.d.	n.d.	n.d.	0.00	0.00	0.00	0.01	0.00	0.00	0.00
Na_2O	0.22	0.13	0.18	0.21	0.31	0.17	0.23	0.22	0.13	0.18	0.21	0.31	0.17	0.23
CaO	0.01	0.01	0.01	0.00	0.04	0.03	0.02	0.01	0.01	0.01	0.00	0.04	0.03	0.02
TiO_2	97.9	99.3	98.6	64.9	64.7	64.7	64.8	97.9	99.3	98.6	64.9	64.7	64.7	64.8
Cr_2O_3	n.d.	0.02	0.02	0.26	0.26	0.30	0.27	0.00	0.02	0.01	0.26	0.26	0.30	0.27
Al_2O_3	0.02	0.01	0.02	0.05	0.03	0.04	0.04	0.02	0.01	0.02	0.05	0.03	0.04	0.04
SiO_2	0.01	0.02	0.01	n.d.	0.01	0.01	0.01	0.01	0.02	0.01	0.00	0.01	0.01	0.01
Total	99.9	100.8	100.4	100.8	100.3	100.8	100.6	99.9	100.8	100.4	100.8	100.3	100.8	100.6

Table B-1 (continued): Major element composition of the sapphires and the spinel rims (Electron microprobe analyses).

sample	PE25							S52							
	corundum				spinel			corundum				spinel			
	1	2	3	**average**	1	2	**average**	1	2	3	**average**	rim 1	rim 2	rim 3	**average**
MgO	0.01	0.01	n.d.	0.01	14.1	14.1	14.1	0.02	0.01	n.d.	0.02	16.1	15.9	15.6	15.9
FeO	0.01	n.d.	0.02	0.01	0.04	0.01	0.02	1.71	1.71	1.60	1.67	18.0	18.2	18.7	18.3
MnO	0.90	0.90	0.95	0.92	21.2	21.3	21.3	n.d.	n.d.	n.d.	n.d.	0.27	0.36	0.28	0.30
K_2O	0.00	0.01	0.01	0.01	0.02	0.01	0.01	0.01	0.01	n.d.	0.01	n.d.	n.d.	n.d.	n.d.
Na_2O	0.11	0.28	0.36	0.25	0.07	0.23	0.15	0.01	n.d.	n.d.	0.01	n.d.	n.d.	0.05	0.05
CaO	0.03	0.04	0.00	0.02	0.03	0.06	0.05	n.d.	0.01	0.01	0.01	0.03	0.02	0.03	0.03
TiO_2	99.6	99.5	99.1	99.4	65.2	64.9	65.1	0.09	0.15	0.05	0.10	0.11	0.11	0.04	0.09
Cr_2O_3	0.01	n.d.	0.05	0.03	0.32	0.28	0.30	0.02	0.01	n.d.	0.01	n.d.	0.02	n.d.	0.02
Al_2O_3	0.01	n.d.	0.01	0.01	0.04	0.01	0.02	97.7	97.8	97.9	97.8	65.1	65.2	65.1	65.1
SiO_2	0.04	n.d.	0.01	0.02	0.00	0.04	0.02	0.04	0.02	0.00	0.02	0.03	0.03	0.02	0.03
Total	100.7	100.7	100.5	100.6	101.1	100.9	101.0	99.6	99.8	99.6	99.7	99.7	99.8	99.8	99.7

sample	UN31								26							
	corundum				spinel				corundum				spinel			
	1	2	3	**average**	1	2	3	**average**	1	2	3	**average**	1	2	3	**average**
MgO	0.02	0.02	n.d.	0.02	15.6	15.7	15.4	15.6	n.d.	n.d.	n.d.	n.d.	15.8	16.0	15.5	15.8
FeO	1.37	1.52	1.50	1.46	18.6	19.1	19.1	18.9	0.81	0.89	0.91	0.87	18.7	18.8	19.1	18.9
MnO	n.d.	n.d.	n.d.	n.d.	0.25	0.28	0.24	0.26	0.01	n.d.	0.04	0.03	0.24	0.32	0.35	0.30
K_2O	n.d.	0.01	0.01	0.01	0.01	n.d.	n.d.	0.01	0.01	n.d.	0.01	0.01	n.d.	n.d.	n.d.	n.d.
Na_2O	n.d.	n.d.	n.d.	n.d.	n.d.	n.d.	0.02	0.02	n.d.	n.d.	0.02	0.02	0.01	0.01	n.d.	0.01
CaO	0.01	0.01	0.02	0.01	0.01	0.01	0.02	0.01	0.03	0.01	n.d.	0.02	0.02	0.01	0.02	0.02
TiO_2	0.22	0.18	0.20	0.20	0.17	0.09	0.17	0.14	0.09	0.19	0.09	0.12	0.02	0.06	0.05	0.04
Cr_2O_3	n.d.	n.d.	0.01	0.01	n.d.	n.d.	n.d.	n.d.	0.01	n.d.	n.d.	0.01	n.d.	n.d.	n.d.	n.d.
Al_2O_3	98.2	98.4	98.1	98.2	65.4	64.6	65.1	65.0	99.7	99.2	99.7	99.5	65.5	65.5	65.4	65.5
SiO_2	0.01	0.02	0.01	0.01	0.01	n.d.	0.02	0.01	0.04	0.02	0.01	0.02	0.03	0.03	0.03	0.03
Total	99.8	100.2	99.9	99.9	99.8	99.8	100.0	99.9	100.7	100.3	100.8	100.6	100.4	100.7	100.5	100.5

sample	PE21					ÖL60							
	corundum	spinel				corundum				spinel			
	1	1	2	3	**average**	1	2	3	**average**	1	2	3	**average**
MgO	n.d.	14.0	14.3	14.2	14.2	n.d.	0.01	n.d.	0.01	16.7	16.7	16.7	16.7
FeO	0.88	20.4	20.9	20.7	20.7	0.39	0.43	0.48	0.43	17.5	18.2	17.3	17.7
MnO	n.d.	0.41	0.18	0.20	0.26	n.d.	n.d.	n.d.	n.d.	0.17	0.22	0.32	0.24
K_2O	n.d.	0.01	0.01	0.01	0.01	0.01	n.d.	0.01	0.01	n.d.	n.d.	n.d.	n.d.
Na_2O	n.d.	n.d.	0.01	n.d.	n.d.	0.07	0.02	n.d.	0.04	n.d.	0.01	n.d.	0.01
CaO	0.01	0.03	0.01	0.04	0.03	0.02	0.01	n.d.	0.02	n.d.	0.02	n.d.	0.02
TiO_2	0.48	0.29	0.22	0.29	0.27	0.03	0.02	0.13	0.06	0.05	0.07	0.10	0.07
Cr_2O_3	n.d.	0.03	0.04	0.00	0.02	0.01	n.d.	0.04	0.02	0.02	n.d.	n.d.	0.02
Al_2O_3	97.9	63.9	63.5	63.8	63.7	99.8	99.7	99.5	99.6	65.3	65.0	65.7	65.3
SiO_2	0.04	n.d.	0.01	0.02	0.01	0.01	0.02	0.01	0.02	0.03	0.02	0.03	0.03
Total	99.3	99.1	99.2	99.2	99.2	100.3	100.2	100.2	100.2	99.8	100.2	100.2	100.1

Table B-2: Trace element composition of the sapphires (LA-ICP-MS analyses).

sample	Be	Na	Mg	K	Ti	V	Cr	Mn	Fe	Zn	Ga	Sr	Y	Zr	Nb	Sn	Hf	Ta	W	Th	U	Nb/Ta	Zr/Hf	Ga/Mg	Fe/Ti
OL61-1	n.d.	n.d.	23.42	n.d.	277.39	7.09	n.d.	n.d.	8696.76	2.64	155.09	n.d.	n.d.	0.57	2.11	0.32	0.04	3.22	0.38	0.07	n.d.	0.66	16.01	6.62	31.35
OL61-2	0.35	n.d.	13.07	n.d.	707.55	6.92	n.d.	n.d.	7065.95	3.15	133.55	n.d.	n.d.	n.d.	1.55	0.50	0.00	2.79	n.d.	0.01	n.d.	0.56	-	10.22	9.99
OL61-3	0.10	11.78	15.93	n.d.	409.73	8.68	n.d.	2.75	9135.20	6.85	162.21	n.d.	n.d.	n.d.	0.43	0.27	n.d.	1.45	0.01	n.d.	n.d.	0.30	-	10.18	22.30
OL61-4	0.09	26.43	15.13	22.99	377.11	7.43	n.d.	n.d.	9010.84	3.80	154.01	0.18	n.d.	n.d.	1.37	0.20	0.00	1.09	0.01	n.d.	n.d.	1.26	-	10.18	23.89
OL61-5	0.09	8.45	12.76	n.d.	209.25	7.37	n.d.	n.d.	8682.96	4.48	145.97	n.d.	n.d.	n.d.	1.17	n.d.	0.00	0.27	0.01	n.d.	n.d.	4.37	-	11.44	41.50
OL61-6	n.d.	10.01	11.06	n.d.	193.75	6.50	n.d.	2.27	7887.84	4.12	134.13	n.d.	n.d.	n.d.	0.49	0.09	n.d.	0.25	0.00	n.d.	n.d.	1.99	-	12.13	40.71
OL61-7	0.09	n.d.	17.97	n.d.	193.06	7.06	4.04	n.d.	8777.46	5.39	150.15	n.d.	n.d.	n.d.	1.74	0.10	n.d.	0.72	0.00	n.d.	n.d.	2.43	-	8.36	45.47
OL61-8	0.08	n.d.	19.74	n.d.	287.70	8.51	n.d.	n.d.	10008.35	5.32	156.13	n.d.	n.d.	n.d.	1.69	0.11	n.d.	0.87	0.01	n.d.	n.d.	1.94	-	7.91	34.79
OL61-9	0.19	8.32	20.09	n.d.	412.76	8.64	n.d.	n.d.	9450.27	7.19	158.24	n.d.	n.d.	n.d.	8.89	0.27	n.d.	3.44	0.09	n.d.	n.d.	2.58	-	7.88	22.90
OL61-10	0.06	4.60	16.47	n.d.	357.55	9.65	n.d.	1.85	10727.98	5.47	166.87	n.d.	n.d.	n.d.	0.92	0.22	0.01	1.85	0.01	n.d.	n.d.	0.50	-	10.13	30.00
OL61-11	n.d.	65.39	19.47	30.57	640.44	7.56	n.d.	n.d.	10057.31	5.27	155.44	n.d.	n.d.	n.d.	0.37	0.15	n.d.	1.52	0.04	n.d.	n.d.	0.24	-	7.98	15.70
OL61-12	0.15	n.d.	13.10	n.d.	367.96	7.54	n.d.	n.d.	8778.40	3.35	140.69	n.d.	n.d.	n.d.	0.79	0.41	n.d.	3.96	n.d.	0.01	n.d.	0.20	-	10.74	23.86
OL61-13	0.09	n.d.	19.14	n.d.	1129.39	9.74	n.d.	n.d.	9936.48	5.35	156.67	n.d.	n.d.	n.d.	n.d.	0.45	n.d.	0.75	0.01	n.d.	n.d.	-	-	8.19	8.80
OL61-14	n.d.	469.21	45.22	732.44	1204.60	9.42	n.d.	9.92	10223.10	13.77	155.49	7.50	n.d.	n.d.	5.76	0.61	0.01	1.84	0.18	0.07	0.02	3.12	-	3.44	8.49
OL61-15	n.d.	60.66	21.49	69.99	991.94	8.49	n.d.	2.55	9794.60	7.06	145.11	0.39	n.d.	n.d.	2.22	0.54	0.00	1.46	0.05	n.d.	0.01	1.52	-	6.75	9.87
OL61-16	0.34	n.d.	14.57	16.74	880.38	7.22	n.d.	n.d.	7737.15	4.09	132.64	0.18	n.d.	n.d.	0.27	0.38	n.d.	0.17	n.d.	n.d.	n.d.	1.58	-	9.10	8.79
OL61-17	n.d.	9.22	24.95	10.26	1126.69	7.46	n.d.	2.33	8492.78	9.83	136.69	n.d.	n.d.	n.d.	1.68	0.47	0.00	0.14	n.d.	0.04	n.d.	12.35	-	5.48	7.54
OL61-18	0.18	n.d.	17.42	n.d.	471.41	8.43	n.d.	2.85	9293.33	6.36	153.17	n.d.	n.d.	n.d.	0.77	0.20	n.d.	0.26	n.d.	n.d.	n.d.	2.92	-	8.79	19.71
OL61-19	0.68	n.d.	12.28	n.d.	345.21	6.82	n.d.	n.d.	7468.60	3.17	129.91	n.d.	n.d.	0.18	1.47	0.17	0.01	0.63	n.d.	n.d.	n.d.	2.32	22.47	10.58	21.63
OL61-20	n.d.	n.d.	13.86	n.d.	386.45	7.03	n.d.	n.d.	7723.56	2.75	133.04	n.d.	n.d.	n.d.	1.61	0.09	n.d.	0.74	0.02	n.d.	n.d.	2.18	-	9.60	19.99
OL61-21	n.d.	n.d.	25.59	n.d.	719.84	6.50	1.55	1.35	4597.71	4.37	106.76	n.d.	n.d.	n.d.	n.d.	0.49	n.d.	0.11	n.d.	n.d.	n.d.	-	-	4.17	6.39
OL61-22	0.06	n.d.	41.85	n.d.	206.97	7.01	1.23	n.d.	5374.33	2.43	116.63	n.d.	n.d.	n.d.	0.20	0.24	n.d.	2.19	n.d.	n.d.	n.d.	0.09	-	2.79	25.97
OL61-23	0.27	n.d.	16.42	n.d.	188.13	6.90	n.d.	n.d.	5543.38	2.49	123.53	n.d.	n.d.	n.d.	0.18	0.26	n.d.	2.30	n.d.	n.d.	n.d.	0.08	-	7.52	29.46
OL61-24	n.d.	3.88	17.84	n.d.	321.90	8.96	1.03	1.10	6410.27	3.40	133.80	n.d.	n.d.	n.d.	7.38	0.26	n.d.	3.22	n.d.	n.d.	n.d.	2.29	-	7.50	19.91
OL61-25	n.d.	23.15	17.53	7.27	90.29	7.12	n.d.	2.09	6031.64	3.77	135.81	n.d.	n.d.	n.d.	2.21	0.17	n.d.	0.32	n.d.	n.d.	n.d.	6.88	-	7.75	66.80
OL61-26	0.05	6.30	16.07	n.d.	74.95	7.13	0.89	1.10	6211.50	4.48	141.38	n.d.	n.d.	n.d.	4.54	0.20	n.d.	1.29	n.d.	n.d.	n.d.	3.51	-	8.80	82.88
OL61-27	0.04	n.d.	13.72	n.d.	140.22	7.16	1.31	1.18	5515.65	3.54	124.92	n.d.	n.d.	n.d.	0.75	0.12	n.d.	0.31	n.d.	n.d.	n.d.	2.42	-	9.10	39.34
OL61-28	0.06	n.d.	9.56	n.d.	206.97	7.56	n.d.	1.52	5605.45	2.70	116.53	n.d.	n.d.	n.d.	n.d.	0.09	n.d.	0.12	n.d.	n.d.	n.d.	n.d.	-	12.19	27.08
OL61-29	0.23	n.d.	15.68	n.d.	635.18	9.08	0.84	1.33	6442.50	3.87	130.85	n.d.	n.d.	n.d.	0.92	0.27	n.d.	0.69	n.d.	n.d.	n.d.	1.35	-	8.35	10.14
OL61-30	0.05	n.d.	42.89	n.d.	273.82	8.53	1.64	1.07	6842.02	4.18	142.53	n.d.	n.d.	n.d.	7.93	0.26	n.d.	3.18	n.d.	n.d.	n.d.	2.50	-	3.32	24.99
OL61-average	0.16	54.41	19.48	127.18	460.95	7.78	1.56	2.35	7917.45	4.82	140.93	2.06	n.d.	0.38	2.20	0.27	0.01	1.37	0.05	0.02	n.d.	2.07	4.28	8.24	26.01
UN31-1	n.d.	59.55	83.54	23.49	1072.26	27.72	n.d.	n.d.	8663.06	n.d.	158.88	0.54	n.d.	n.d.	n.d.	0.85	n.d.	0.50	0.33	0.04	0.04	-	-	1.90	8.08
UN31-2	0.19	n.d.	68.53	n.d.	953.42	28.77	n.d.	n.d.	8596.82	n.d.	150.11	n.d.	n.d.	n.d.	n.d.	0.98	0.01	0.13	n.d.	n.d.	n.d.	-	-	2.19	9.02
UN31-3	n.d.	n.d.	91.67	n.d.	1468.06	32.34	n.d.	n.d.	8675.70	n.d.	152.71	n.d.	n.d.	n.d.	n.d.	1.39	n.d.	0.58	n.d.	n.d.	n.d.	-	-	1.67	5.91
UN31-4	0.28	n.d.	91.04	n.d.	1420.92	36.69	n.d.	n.d.	9237.49	4.01	147.75	n.d.	n.d.	n.d.	n.d.	1.12	0.05	0.33	n.d.	n.d.	n.d.	-	-	1.62	6.50
UN31-5	n.d.	n.d.	93.43	n.d.	1432.77	34.50	n.d.	n.d.	8059.71	4.35	172.65	n.d.	n.d.	n.d.	2.19	1.27	0.03	1.27	n.d.	0.03	n.d.	1.73	-	1.85	5.63
UN31-6	n.d.	n.d.	106.80	n.d.	1814.08	39.56	n.d.	n.d.	8101.49	4.96	163.55	n.d.	n.d.	n.d.	1.53	1.62	0.07	1.70	n.d.	0.01	n.d.	0.90	-	1.53	4.47
UN31-7	0.29	n.d.	168.43	n.d.	1511.38	49.93	13.34	n.d.	9507.94	5.96	190.62	n.d.	n.d.	1.08	289.50	4.23	0.25	96.25	0.69	7.29	n.d.	3.01	4.35	1.13	6.29
UN31-8	n.d.	n.d.	161.37	n.d.	1458.96	48.99	14.90	n.d.	9426.99	7.56	184.13	n.d.	n.d.	2.56	584.72	7.52	0.55	168.07	1.15	19.57	0.01	3.48	4.64	1.14	6.46
UN31-9	0.56	n.d.	174.35	n.d.	1394.07	65.81	18.43	n.d.	11321.96	8.59	205.42	n.d.	n.d.	1.03	517.37	5.33	0.22	104.64	1.36	9.37	0.01	4.94	4.66	1.18	8.12
UN31-10	1.40	n.d.	172.26	n.d.	1552.39	60.47	9.08	n.d.	10480.10	5.39	201.28	n.d.	n.d.	2.58	748.18	8.62	0.40	166.20	1.77	21.32	0.01	4.50	6.45	1.17	6.75
UN31-11	n.d.	n.d.	131.32	n.d.	1001.56	53.45	9.55	n.d.	9977.77	5.33	196.61	n.d.	n.d.	n.d.	247.66	2.49	n.d.	27.74	0.61	0.84	n.d.	8.93	-	1.50	9.96
UN31-12	n.d.	n.d.	83.10	n.d.	645.96	39.94	21.86	n.d.	7774.43	2.30	159.06	n.d.	n.d.	n.d.	31.89	0.33	0.01	4.65	0.06	0.16	n.d.	6.85	-	1.91	12.04
UN31-13	0.24	n.d.	85.96	n.d.	1246.28	34.03	n.d.	n.d.	7986.82	5.43	162.02	n.d.	n.d.	n.d.	3.76	1.38	0.02	1.07	n.d.	0.05	n.d.	3.51	-	1.88	6.41
UN31-14	n.d.	n.d.	87.92	n.d.	1334.96	33.41	n.d.	n.d.	8270.43	3.44	157.04	n.d.	n.d.	n.d.	1.71	0.99	0.02	0.78	0.01	0.02	n.d.	2.20	-	1.79	6.20
UN31-15	0.21	n.d.	134.63	n.d.	1987.73	58.45	n.d.	n.d.	10728.60	9.86	173.78	n.d.	n.d.	n.d.	4.15	1.46	0.02	1.22	0.01	0.02	n.d.	3.41	-	1.29	5.40
UN31-16	n.d.	n.d.	129.82	n.d.	1932.12	58.63	11.57	3.68	9970.46	6.86	180.58	n.d.	n.d.	n.d.	6.02	1.57	0.04	1.94	0.01	0.03	n.d.	3.11	-	1.39	5.16
UN31-17	0.23	n.d.	126.08	n.d.	2148.65	52.30	n.d.	n.d.	9350.56	5.70	158.09	n.d.	n.d.	n.d.	4.19	1.75	0.04	1.57	0.03	0.02	n.d.	2.67	-	1.25	4.35
UN31-18	0.18	n.d.	115.56	n.d.	1568.31	45.32	n.d.	n.d.	9259.46	4.81	147.98	n.d.	n.d.	n.d.	4.08	0.83	0.02	1.82	0.01	0.02	n.d.	2.24	-	1.28	5.90
UN31-19	n.d.	n.d.	97.95	n.d.	1364.52	40.30	n.d.	n.d.	10180.87	5.62	159.66	n.d.	n.d.	n.d.	0.76	1.24	n.d.	0.30	n.d.	n.d.	n.d.	2.57	-	1.63	7.46
UN31-20	n.d.	n.d.	108.57	n.d.	1237.73	44.65	n.d.	n.d.	12701.15	11.49	190.18	n.d.	n.d.	n.d.	0.51	1.05	n.d.	0.23	n.d.	n.d.	n.d.	2.20	-	1.75	10.26
UN31-21	0.36	n.d.	140.88	n.d.	934.04	51.69	9.14	n.d.	8207.06	4.27	167.01	n.d.	n.d.	n.d.	440.38	5.65	n.d.	147.02	n.d.	n.d.	n.d.	3.00	-	1.19	8.79
UN31-22	0.36	n.d.	150.89	n.d.	1160.30	55.60	12.86	n.d.	8354.88	4.41	167.19	n.d.	n.d.	n.d.	228.82	2.90	n.d.	73.20	n.d.	n.d.	n.d.	3.13	-	1.11	7.20
UN31-23	1.13	n.d.	140.42	n.d.	1002.37	51.27	18.94	n.d.	8279.56	4.97	167.11	n.d.	n.d.	n.d.	594.49	7.23	n.d.	169.34	n.d.	n.d.	n.d.	3.51	-	1.19	8.26
UN31-24	0.24	n.d.	91.41	n.d.	706.38	51.33	9.15	n.d.	7939.61	3.20	155.99	n.d.	n.d.	n.d.	9.89	0.33	n.d.	2.45	n.d.	n.d.	n.d.	4.04	-	1.71	11.24
UN31-25	n.d.	n.d.	60.52	n.d.	640.75	31.60	1.39	n.d.	6544.91	2.80	134.78	n.d.	n.d.	n.d.	0.17	0.64	n.d.	0.10	n.d.	n.d.	n.d.	1.78	-	2.23	10.21
UN31-26	n.d.	n.d.	70.13	n.d.	848.87	32.11	1.71	1.58	7320.25	2.34	134.82	n.d.	n.d.	n.d.	n.d.	0.96	n.d.	0.15	n.d.	n.d.	n.d.	-	-	1.92	8.62
UN31-27	0.14	n.d.	81.12	n.d.	1042.38	41.07	5.14	n.d.	6811.19	2.96	139.68	n.d.	n.d.	n.d.	9.97	1.21	n.d.	2.01	n.d.	n.d.	n.d.	4.97	-	1.72	6.53
UN31-28	n.d.	n.d.	72.11	n.d.	892.38	32.43	2.31	n.d.	7423.57	2.18	132.61	n.d.	n.d.	n.d.	0.37	0.92	n.d.	0.23	n.d.	n.d.	n.d.	1.59	-	1.84	8.32
UN31-29	0.14	11.01	83.38	n.d.	948.72	36.01	3.08	n.d.	8383.81	3.90	139.99	n.d.	n.d.	n.d.	2.76	0.90	n.d.	1.31	n.d.	n.d.	n.d.	2.11	-	1.68	8.84
UN31-30	0.15	n.d.	95.75	n.d.	1214.70	42.54	1.73	n.d.	8973.21	3.67	159.93	n.d.	n.d.	n.d.	0.66	1.40	n.d.	0.56	n.d.	n.d.	n.d.	1.19	-	1.67	7.39
UN31-average	0.38	35.28	109.96	23.49	1264.57	43.70	9.66	2.63	8883.66	5.05	163.71	0.54	n.d.	1.81	149.43	2.27	0.12	32.58	0.50	3.46	0.01	2.72	1.34	1.58	7.53

Table B-2 (continued): Trace element composition of the sapphires (LA-ICP-MS analyses).

sample	Be	Na	Mg	K	Ti	V	Cr	Mn	Fe	Zn	Ga	Sr	Y	Zr	Nb	Sn	Hf	Ta	W	Th	U	Nb/Ta	Zr/Hf	Ga/Mg	Fe/Ti
OL25-1	0.62	65.44	23.06	31.21	1498.67	8.22	n.d.	8.44	8484.93	4.26	122.75	n.d.	0.12	n.d.	1.72	0.69	0.02	2.14	0.04	0.03	0.02	0.80	-	5.32	5.66
OL25-2	0.40	83.78	9.32	40.75	282.18	5.71	n.d.	7.76	6569.89	n.d.	109.02	n.d.	n.d.	n.d.	1.61	0.22	0.01	0.47	0.12	0.11	0.05	3.41	-	11.70	23.28
OL25-3	n.d.	n.d.	9.91	n.d.	257.24	5.85	n.d.	n.d.	6400.10	n.d.	110.79	n.d.	n.d.	n.d.	0.56	0.16	n.d.	0.19	0.01		0.00	2.98	-	11.18	24.88
OL25-4	n.d.	58.87	15.46	14.92	474.09	8.23	n.d.	4.26	7342.16	2.16	108.23	n.d.	n.d.	0.16	1.39	0.18	n.d.	0.49	0.02	0.03	0.02	2.86	-	7.00	15.49
OL25-5	0.24	16.28	17.10	n.d.	404.71	7.42	n.d.	3.86	8405.28	3.30	128.46	n.d.	n.d.	n.d.	1.31	0.18	n.d.	0.35		0.01	0.03	3.79	-	7.51	20.77
OL25-6	0.61	n.d.	8.79	n.d.	269.88	6.09	n.d.	n.d.	6909.14	n.d.	112.83	0.22	n.d.	n.d.	0.77	n.d.	n.d.	0.40	0.02	0.01	0.00	1.94	-	12.84	25.60
OL25-7	2.12	99.90	54.77	57.27	4107.85	10.29	n.d.	17.08	9350.57	3.95	104.51	0.22	0.09	0.49	72.64	2.08	0.14	42.28	0.67	5.31	0.06	1.72	3.59	1.91	2.28
OL25-8	1.96	23.52	60.48	16.47	4460.87	11.86	n.d.	14.50	9530.67	5.29	101.99	n.d.	0.06	0.62	78.92	2.17	0.09	44.15	0.63	4.08	0.11	1.79	6.95	1.69	2.14
OL25-9	1.77	8.04	74.46	n.d.	5153.98	15.59	n.d.	11.64	12107.86	6.99	119.56	n.d.	n.d.	0.55	86.38	2.17	0.05	39.42	0.75	2.33	0.03	2.19	10.85	1.61	2.35
OL25-10	0.90	13.85	89.67	n.d.	4249.02	18.53	n.d.	34.28	12122.34	8.28	140.82	n.d.	n.d.	0.33	95.97	2.16	0.04	23.90	0.46	1.82	0.06	4.02	9.25	1.57	2.85
OL25-11	2.01	173.95	52.18	94.79	3887.58	8.99	n.d.	18.27	8626.40	2.37	86.81	n.d.	n.d.	0.61	68.52	1.83	0.12	27.40	0.37	1.31	0.12	2.50	5.19	1.66	2.22
OL25-12	0.96	n.d.	17.36	12.21	577.62	7.30	n.d.	n.d.	7199.36	n.d.	127.51	n.d.	n.d.	n.d.	49.48	0.43	0.01	33.71	0.01	0.09	0.00	1.47	-	7.34	12.46
OL25-13	0.72	8.61	22.67	n.d.	891.81	9.45	n.d.	n.d.	8356.16	2.05	129.69	n.d.	n.d.	n.d.	13.06	0.26	n.d.	8.87	0.01	0.03	0.01	1.47	-	5.72	9.37
OL25-14	1.15	6.02	30.55	n.d.	1445.20	10.57	n.d.	8.05	9313.07	3.48	125.33	n.d.	0.06	n.d.	39.34	0.62	0.02	26.78	0.15	0.21	0.02	1.47	-	4.10	6.44
OL25-15	1.21	n.d.	23.85	n.d.	468.00	6.00	n.d.	n.d.	8318.26	3.15	127.52	n.d.	n.d.	n.d.	27.62	0.35	0.02	45.70	0.00	0.12	0.00	0.60	-	5.35	17.77
OL25-16	1.45	30.28	36.18	22.54	2344.74	10.17	n.d.	22.86	9281.82	2.60	120.40	n.d.	0.16	n.d.	13.56	1.05	0.05	9.96	0.15	0.41	0.10	1.36	-	3.33	3.96
OL25-17	1.06	34.25	36.55	13.93	2171.62	14.06	n.d.	19.68	11598.81	5.97	146.02	n.d.	n.d.	n.d.	9.46	1.03	0.02	3.95	0.07	0.12	0.12	2.39	-	4.00	5.34
OL25-18	1.21	15.38	44.56	10.60	2929.31	14.83	n.d.	18.03	11804.91	6.40	146.72	n.d.	n.d.	0.25	12.23	1.32	0.05	8.41	0.15	0.12	0.07	1.46	4.94	3.29	4.03
OL25-19	0.49	10.67	34.30	6.57	2103.87	14.10	n.d.	8.30	10674.71	5.59	129.30	n.d.	n.d.	n.d.	5.48	0.82	n.d.	3.35	0.05	0.02	0.04	1.64	-	3.77	5.07
OL25-20	0.09	n.d.	20.11	n.d.	491.36	7.54	n.d.	4.47	8638.59	4.94	125.57	0.12	n.d.	n.d.	7.07	0.40	0.02	15.50	0.01	0.02	0.00	0.46	-	6.25	17.58
OL25-21	n.d.	61.44	6.71	60.06	76.37	5.25	n.d.	8.42	3176.98	n.d.	95.96	n.d.	n.d.	n.d.	2.57	0.08	n.d.	0.13	n.d.	n.d.	n.d.	20.27	-	14.31	41.60
OL25-22	1.43	34.73	43.24	25.03	2998.80	11.82	n.d.	41.01	5832.81	9.71	92.24	n.d.	n.d.	n.d.	21.01	1.53	n.d.	12.24	n.d.	n.d.	n.d.	1.72	-	2.13	1.95
OL25-23	n.d.	359.45	24.85	222.11	675.69	9.47	n.d.	35.10	5776.93	7.58	121.55	n.d.	n.d.	n.d.	51.10	0.48	n.d.	17.42	n.d.	n.d.	n.d.	2.93	-	4.89	8.55
OL25-24	n.d.	13.96	9.63	7.70	188.49	5.90	n.d.	6.62	4611.03	1.91	100.98	n.d.	n.d.	n.d.	5.51	0.18	n.d.	0.78	n.d.	n.d.	n.d.	7.08	-	10.48	24.46
OL25-25	0.98	9.70	21.41	n.d.	754.22	10.13	1.28	6.78	6547.20	6.60	122.46	n.d.	n.d.	n.d.	34.30	0.53	n.d.	25.34	n.d.	n.d.	n.d.	1.35	-	5.72	8.68
OL25-26	n.d.	108.89	19.49	25.05	476.38	9.06	n.d.	13.37	7427.41	5.11	136.19	n.d.	n.d.	n.d.	18.53	0.29	n.d.	7.63	n.d.	n.d.	n.d.	2.43	-	6.99	15.59
OL25-27	0.12	30.80	8.07	9.30	95.12	4.59	n.d.	4.08	4380.60	2.39	93.70	n.d.	n.d.	n.d.	1.22	n.d.	n.d.	0.29	n.d.	n.d.	n.d.	4.16	-	11.61	46.05
OL25-28	0.12	60.50	7.49	35.96	141.46	5.45	1.63	7.90	4359.18	n.d.	93.02	n.d.	n.d.	n.d.	1.61	0.08	n.d.	0.22	n.d.	n.d.	n.d.	7.19	-	12.42	30.82
OL25-29	0.12		8.87	7.78	134.57	6.05	1.96	n.d.	5873.60	n.d.	104.63	n.d.	n.d.	n.d.	n.d.	n.d.	n.d.	0.02	n.d.	n.d.	n.d.	-	-	11.79	43.65
OL25-30	2.26	64.84	59.97	43.56	2818.65	16.61	n.d.	48.51	11584.00	8.50	144.61	n.d.	n.d.	n.d.	83.83	1.09	n.d.	20.55	n.d.	n.d.	n.d.	4.08	-	2.41	4.11
OL25-average	1.00	58.05	29.70	37.89	1560.98	9.50	1.62	15.55	8020.16	4.90	117.64	0.19	0.10	0.43	27.82	0.83	0.05	14.07	0.19	0.85	0.04	3.05	2.91	6.33	14.50
OL60-1	26.06	n.d.	4.82	n.d.	641.74	1.71	n.d.	n.d.	3098.96	7.90	197.91	n.d.	n.d.	0.41	814.13	1.27	0.21	262.83	0.60	9.96	0.01	3.10	2.02	41.03	4.83
OL60-2	1.32	n.d.	2.91	n.d.	492.40	3.06	n.d.	2.93	2487.14	4.39	168.53	n.d.	n.d.	n.d.	68.96	0.14	n.d.	10.03	0.04	0.12	0.00	6.87	-	57.98	5.05
OL60-3	0.93	n.d.	2.93	n.d.	197.98	2.94	n.d.	n.d.	2600.15	2.83	163.79	n.d.	n.d.	n.d.	26.45	0.11	0.01	5.07	0.03	0.07	0.01	5.21	-	55.97	13.13
OL60-4	0.45	n.d.	1.78	n.d.	65.34	2.53	n.d.	n.d.	2461.26	n.d.	156.70	n.d.	n.d.	n.d.	5.81	n.d.	n.d.	7.61	0.01	0.04	0.00	0.76	-	88.13	37.67
OL60-5	0.26	n.d.	3.11	n.d.	231.12	4.18	n.d.	n.d.	3722.74	4.21	209.71	n.d.	n.d.	n.d.	1.91	0.09	0.00	5.79	0.00	0.01	0.01	0.33	-	67.51	16.11
OL60-6	0.42	n.d.	23.84	n.d.	240.34	4.16	n.d.	3.27	4451.76	4.68	203.20	n.d.	n.d.	n.d.	2.05	n.d.	n.d.	1.90	0.01	0.02	0.01	1.08	-	8.52	18.52
OL60-7	0.98	23.42	12.21	n.d.	633.84	4.02	n.d.	2.85	3557.40	5.43	179.23	n.d.	n.d.	n.d.	3.87	n.d.	0.01	3.11	0.03	0.05	0.02	1.25	-	14.67	5.61
OL60-8	0.94	40.81	3.80	22.21	324.23	3.94	n.d.	3.89	3568.39	3.29	176.23	n.d.	n.d.	n.d.	1.51	n.d.	0.01	0.82	n.d.	0.08	0.01	1.85	-	46.38	11.01
OL60-9	0.41	21.44	3.60	n.d.	413.36	3.96	n.d.	2.54	3422.25	5.29	175.11	n.d.	n.d.	n.d.	2.26	0.11	n.d.	2.27	0.03	0.03	0.00	1.00	-	48.64	8.28
OL60-10	0.74	18.65	9.23	17.41	573.35	3.27	n.d.	n.d.	3262.98	4.32	166.69	n.d.	n.d.	n.d.	0.79	0.12	0.01	0.68	0.01	0.02	0.01	1.17	-	18.05	5.69
OL60-11	2.30	n.d.	49.96	n.d.	658.77	12.41	0.77	5.57	8549.35	2.12	193.40	n.d.	n.d.	n.d.	720.65	9.68	n.d.	370.15	n.d.	n.d.	n.d.	1.95	-	3.87	12.98
OL60-12	0.53	15.53	859.26	n.d.	622.72	3.91	1.86	18.47	2528.70	10.53	140.54	n.d.	n.d.	n.d.	0.64	0.13	n.d.	0.86	n.d.	n.d.	n.d.	0.74	-	0.16	4.06
OL60-13	n.d.	9.90	117.05	n.d.	131.11	2.51	n.d.	3.05	2055.26	4.00	135.50	n.d.	n.d.	n.d.	2.42	0.09	n.d.	5.44	n.d.	n.d.	n.d.	0.44	-	1.16	15.68
OL60-14	0.33	8.00	54.28	n.d.	317.93	3.59	n.d.	3.00	2081.39	3.57	148.23	n.d.	n.d.	n.d.	0.64	n.d.	n.d.	1.08	n.d.	n.d.	n.d.	0.59	-	2.73	6.55
OL60-15	n.d.	n.d.	228.75	n.d.	59.77	2.49	n.d.	5.10	1875.19	3.01	134.56	n.d.	n.d.	n.d.	0.35	n.d.	n.d.	0.17	n.d.	n.d.	n.d.	1.99	-	0.59	31.37
OL60-16	0.46	93.56	47.98	38.69	361.88	3.76	0.97	7.78	2302.09	5.31	159.02	n.d.	n.d.	n.d.	1.09	n.d.	n.d.	1.22	n.d.	n.d.	n.d.	0.89	-	3.31	6.36
OL60-average	2.58	28.91	89.09	26.10	372.87	3.90	1.20	5.31	3251.56	4.73	169.27	n.d.	n.d.	0.41	103.35	1.31	0.04	42.44	0.08	1.04	0.01	1.83	0.34	28.67	12.68

Table B-2 (continued): Trace element composition of the sapphires (LA-ICP-MS analyses).

sample	Be	Na	Mg	K	Ti	V	Cr	Mn	Fe	Zn	Ga	Sr	Y	Zr	Nb	Sn	Hf	Ta	W	Th	U	Nb/Ta	Zr/Hf	Ga/Mg	Fe/Ti
PE21-1	8.35	37.45	25.23	29.69	1869.53	18.13	7.10		5129.09	n.d.	171.25	n.d.	0.51	18.17	2157.72	17.43	4.04	800.98	20.24	166.40	0.42	2.69	4.50	6.79	2.74
PE21-2	5.55	71.64	25.26	46.01	1588.93	22.46	n.d.	7.15	5004.33	n.d.	165.42	n.d.	n.d.	13.52	2162.79	15.72	3.62	886.69	19.19	91.85	0.23	2.44	3.73	6.55	3.15
PE21-3	4.66	65.60	30.01	44.49	1546.85	29.95	n.d.	6.73	5435.10	3.72	171.20	n.d.	n.d.	9.02	2412.83	14.16	1.96	918.09	25.98	29.31	0.16	2.63	4.59	5.70	3.51
PE21-4	6.09	56.55	33.54	37.48	1606.48	32.84	n.d.	4.28	6076.94	3.44	177.78	n.d.	n.d.	8.62	2405.47	13.99	2.02	904.43	26.51	25.36	0.10	2.66	4.26	5.30	3.78
PE21-5	10.11	79.42	28.85	51.66	2100.34	29.76	8.18	n.d.	5709.72	3.98	167.82	n.d.	n.d.	22.37	3817.85	20.75	4.83	1573.80	33.67	68.88	0.22	2.43	4.64	5.82	2.72
PE21-6	10.28	n.d.	30.34	16.72	2203.33	28.87	9.72	n.d.	5605.15	4.44	161.51	0.19	0.14	18.92	3939.63	20.15	3.72	1699.17	35.01	49.74	0.19	2.32	5.09	5.32	2.54
PE21-7	7.48	n.d.	29.26	n.d.	2153.81	27.97	n.d.	n.d.	5308.13	3.04	159.93	n.d.	n.d.	20.73	3802.79	18.68	4.28	1664.58	33.01	64.48	0.21	2.28	4.84	5.47	2.46
PE21-8	9.76	n.d.	33.59	n.d.	2286.50	36.79	n.d.	n.d.	6303.83	5.22	192.89	n.d.	n.d.	18.52	3998.21	21.01	4.19	1503.90	40.70	59.95	0.25	2.66	4.42	5.74	2.76
PE21-9	0.93	n.d.	20.60	n.d.	3992.39	13.98	14.28	n.d.	4147.13	3.92	126.85	n.d.	n.d.	1.38	413.21	5.44	0.36	158.94	3.08	5.89	0.03	2.60	3.87	6.16	1.04
PE21-10	1.81	20.16	30.95	13.49	5183.38	24.60	15.95	n.d.	5335.56	4.82	162.55	n.d.	n.d.	1.45	447.09	5.81	0.31	133.24	3.69	22.04	0.05	3.36	4.68	5.25	1.03
PE21-11	1.06	17.89	18.81	20.70	4178.45	15.52	n.d.	n.d.	3957.54	3.40	126.08	n.d.	n.d.	1.18	235.24	4.32	0.20	82.40	1.68	5.67	0.03	2.85	6.04	6.70	0.95
PE21-12	1.14	11.56	23.84	n.d.	5030.89	16.13	n.d.	n.d.	4343.68	n.d.	128.90	n.d.	n.d.	0.53	99.78	4.79	0.24	49.62	1.03	4.66	0.01	2.01	2.16	5.41	0.86
PE21-13	1.18	10.53	30.22	n.d.	6231.23	22.52	6.90	5.37	5310.54	3.75	140.82	n.d.	n.d.	0.63	139.08	5.98	0.21	73.42	1.07	14.50	0.01	1.89	3.02	4.66	0.85
PE21-14	1.43	20.26	28.44	n.d.	5935.54	18.60	6.54	4.86	4947.81	n.d.	134.89	n.d.	n.d.	2.65	246.54	6.79	0.35	108.43	1.79	76.41	0.09	2.27	7.65	4.74	0.83
PE21-15	2.95	n.d.	29.35	n.d.	5752.79	17.66	7.61	n.d.	4807.85	3.49	130.79	n.d.	n.d.	3.58	377.15	7.04	0.71	172.50	2.63	105.87	0.13	2.19	5.06	4.46	0.84
PE21-16	0.18	n.d.	23.42	n.d.	3578.54	15.32	n.d.	n.d.	4442.93	n.d.	137.49	n.d.	n.d.	0.86	85.39	3.34	0.24	57.85	1.25	7.93	0.00	1.48	3.54	5.87	1.24
PE21-17	n.d.	n.d.	18.39	n.d.	3750.49	14.33	n.d.	n.d.	4500.54	n.d.	122.95	n.d.	n.d.	0.44	113.82	3.15	0.11	51.43	1.00	1.62	0.01	2.21	3.90	6.69	1.20
PE21-18	0.98	n.d.	28.62	n.d.	3504.22	16.47	8.07	n.d.	4932.59	3.28	121.68	n.d.	n.d.	0.74	199.40	3.31	0.15	75.36	1.70	1.33	0.02	2.65	4.86	4.25	1.41
PE21-19	3.47	n.d.	29.59	n.d.	5351.02	20.84	11.09	n.d.	6693.28	3.56	142.76	n.d.	0.13	4.41	962.91	8.39	0.75	358.36	6.06	106.90	0.20	2.69	5.85	4.83	1.25
PE21-20	3.15	8.40	31.18	n.d.	5199.77	19.84	18.69	4.53	6378.52	3.90	149.37	n.d.	n.d.	2.05	682.73	7.19	0.42	202.44	4.48	111.52	0.20	3.37	4.91	4.79	1.23
PE21-21	1.97	n.d.	26.04	n.d.	4568.73	18.02	10.30	n.d.	4450.53	n.d.	116.83	n.d.	n.d.	n.d.	229.00	5.82	n.d.	110.43	n.d.	n.d.	n.d.	2.07	-	4.49	0.97
PE21-22	1.89	n.d.	24.72	n.d.	4368.24	18.19	14.00	4.45	3927.00	n.d.	117.83	n.d.	n.d.	n.d.	257.66	5.93	n.d.	113.56	n.d.	n.d.	n.d.	2.27	-	4.77	0.90
PE21-23	2.93	n.d.	25.31	n.d.	3660.80	16.67	15.51	2.34	4052.92	n.d.	118.24	n.d.	n.d.	n.d.	484.93	6.07	n.d.	217.43	n.d.	n.d.	n.d.	2.23	-	4.67	1.11
PE21-24	5.16	n.d.	21.34	n.d.	3491.44	15.99	5.78	n.d.	3907.82	n.d.	131.95	n.d.	n.d.	n.d.	414.62	6.25	n.d.	188.24	n.d.	n.d.	n.d.	2.20	-	6.18	1.12
PE21-25	n.d.	n.d.	16.93	n.d.	3064.57	14.89	3.40	n.d.	3398.91	n.d.	127.04	n.d.	n.d.	n.d.	23.84	2.87	n.d.	14.72	n.d.	n.d.	n.d.	1.62	-	7.50	1.11
PE21-26	0.50	n.d.	9.57	n.d.	1748.00	12.95	3.00	n.d.	3301.53	n.d.	124.63	n.d.	n.d.	n.d.	3.28	1.77	n.d.	4.10	n.d.	n.d.	n.d.	0.80	-	13.02	1.89
PE21-27	1.89	n.d.	26.32	n.d.	4038.49	16.46	7.17	3.05	3919.94	n.d.	113.49	n.d.	n.d.	n.d.	460.98	5.78	n.d.	180.24	n.d.	n.d.	n.d.	2.56	-	4.31	0.97
PE21-28	9.85	44.92	25.77	40.26	1610.88	26.38	15.59	n.d.	4687.06	n.d.	137.93	n.d.	n.d.	n.d.	2929.08	14.84	n.d.	1349.61	n.d.	n.d.	n.d.	2.17	-	5.35	2.91
PE21-29	6.81	16.80	22.63	12.79	1234.13	24.73	20.14	32.78	4105.13	n.d.	138.87	n.d.	n.d.	n.d.	2347.57	11.99	n.d.	1146.10	n.d.	n.d.	n.d.	2.05	-	6.14	3.33
PE21-30	8.48	n.d.	18.74	n.d.	1045.65	24.92	10.10	196.03	4048.12	n.d.	143.71	n.d.	n.d.	n.d.	2116.90	11.65	n.d.	1022.74	n.d.	n.d.	n.d.	2.07	-	7.67	3.87
PE21-average	4.29	35.47	25.56	31.33	3395.85	21.06	10.43	24.69	4805.64	3.85	142.11	0.19	0.26	7.49	1265.58	9.35	1.64	527.43	13.19	51.02	0.13	2.32	4.58	5.82	1.82
PE25-1	6.68	n.d.	17.76	n.d.	875.56	19.54	n.d.	n.d.	4992.67	3.07	174.88	n.d.	n.d.	11.20	1743.25	10.46	2.76	976.96	15.67	39.06	0.08	1.78	4.06	9.85	5.70
PE25-2	9.73	n.d.	18.33	n.d.	1076.74	20.29	n.d.	n.d.	4812.97	1.95	167.48	n.d.	n.d.	12.13	1918.43	10.57	2.73	907.63	16.15	100.50	0.26	2.11	4.43	9.14	4.47
PE25-3	7.44	n.d.	19.68	n.d.	1290.71	20.31	n.d.	n.d.	5104.47	3.52	173.46	n.d.	0.22	13.44	2149.86	11.27	2.98	883.72	17.64	130.87	0.44	2.43	4.52	8.82	3.95
PE25-4	9.21	6.11	25.28	n.d.	1615.40	27.32	5.66	3.89	6168.35	5.03	187.76	n.d.	0.20	13.50	2770.76	13.86	2.88	913.07	22.84	140.29	0.52	3.03	4.69	7.43	3.82
PE25-5	8.61	n.d.	25.17	n.d.	1590.19	29.32	n.d.	2.98	5679.26	5.68	183.29	n.d.	0.23	13.16	2710.45	13.84	2.72	915.76	22.36	129.37	0.56	2.96	4.83	7.28	3.57
PE25-6	9.66	7.04	243.41	n.d.	1430.20	23.93	n.d.	2.73	5052.82	3.27	166.79	n.d.	0.23	14.00	2441.97	12.08	2.81	917.51	21.29	131.33	0.45	2.66	4.98	0.69	3.53
PE25-7	9.49	n.d.	79.24	n.d.	1321.49	29.06	6.34	2.74	5750.23	5.05	188.42	n.d.	n.d.	11.53	2585.92	13.75	2.45	924.38	22.24	67.50	0.33	2.80	4.70	2.38	4.35
PE25-8	7.32	n.d.	25.46	n.d.	1229.86	24.92	9.35	2.40	5142.94	4.20	175.08	n.d.	n.d.	11.84	2473.58	13.44	2.68	978.09	20.75	62.26	0.21	2.53	4.41	6.88	4.18
PE25-9	11.29	n.d.	21.05	8.58	1701.70	20.32	11.75	n.d.	4472.08	3.35	155.93	n.d.	0.48	22.01	2473.50	14.33	3.99	956.13	19.05	226.91	0.63	2.59	5.51	7.41	2.63
PE25-10	7.69	n.d.	21.72	n.d.	1311.12	20.92	10.28	n.d.	4813.62	3.37	158.77	n.d.	0.23	18.85	2267.46	13.25	4.09	1010.76	17.70	129.34	0.30	2.24	4.61	7.31	3.67
PE25-11	7.85	n.d.	20.89	n.d.	1039.34	21.31	6.21	n.d.	4561.53	4.77	153.34	n.d.	n.d.	12.94	1983.09	10.68	3.19	1002.87	16.85	53.12	0.11	1.98	4.06	7.34	4.39
PE25-12	0.69	n.d.	14.51	n.d.	1088.13	14.12	9.37	n.d.	4043.18	n.d.	145.33	n.d.	n.d.	0.26	75.16	0.40	0.03	28.87	0.54	0.58	0.00	2.60	7.84	10.02	3.72
PE25-13	0.89	n.d.	23.58	n.d.	1288.20	19.16	12.47	n.d.	5072.29	4.37	160.31	n.d.	n.d.	0.53	183.15	1.18	0.08	56.78	1.18	5.39	0.01	3.23	6.95	6.80	3.94
PE25-14	4.10	149.46	26.19	108.71	4019.75	16.22	8.23	5.33	4786.24	3.40	146.70	0.17	n.d.	3.68	674.08	6.81	0.71	275.50	3.92	80.55	0.15	2.45	5.18	5.60	1.19
PE25-15	5.28	21.94	22.60	19.77	3969.51	14.13	10.75	n.d.	4203.38	n.d.	140.62	n.d.	n.d.	4.35	612.82	7.96	0.80	282.02	4.12	98.42	0.14	2.17	5.46	6.22	1.06
PE25-16	3.09	43.19	23.26	23.22	4537.55	16.78	8.90	4.21	4268.02	5.22	139.04	n.d.	n.d.	3.22	430.15	6.35	0.52	183.62	3.00	99.91	0.17	2.34	6.16	5.98	0.94
PE25-17	2.96	12.77	32.87	n.d.	5955.62	24.68	16.19	3.62	5787.59	5.52	167.55	n.d.	0.10	3.10	560.67	8.61	0.68	165.79	3.64	85.72	0.20	3.38	4.59	5.10	0.97
PE25-18	3.28	11.84	29.75	n.d.	5699.53	23.34	20.75	n.d.	5456.99	5.22	152.75	n.d.	n.d.	3.01	484.28	7.37	0.47	159.48	3.48	86.02	0.15	3.04	6.36	5.13	0.96
PE25-19	4.22	n.d.	28.93	n.d.	5794.85	20.94	18.43	n.d.	4808.23	5.18	148.70	n.d.	n.d.	2.68	419.99	7.11	0.49	147.58	3.01	99.97	0.18	2.85	5.51	5.14	0.83
PE25-20	3.39	n.d.	31.89	n.d.	6226.24	23.92	17.86	3.01	5564.30	6.85	154.52	n.d.	n.d.	3.18	414.71	8.56	0.50	133.28	3.50	109.06	0.19	3.11	6.30	4.84	0.89
PE25-21	2.49	n.d.	24.70	n.d.	4793.14	15.82	18.62	n.d.	4691.04	n.d.	136.69	n.d.	n.d.	3.13	222.36	5.93	0.46	104.27	1.56	91.15	0.10	2.13	6.77	5.53	0.98
PE25-22	1.09	n.d.	12.90	n.d.	2636.61	12.02	n.d.	2.69	3956.65	3.30	129.55	n.d.	n.d.	0.53	12.06	2.14	0.18	8.25	0.12	1.48	0.00	1.46	2.90	10.05	1.50
PE25-23	2.08	n.d.	17.73	n.d.	3327.77	13.24	n.d.	n.d.	4270.12	n.d.	150.17	n.d.	n.d.	0.53	122.37	3.57	0.25	62.15	0.91	25.67	0.01	1.97	2.15	8.47	1.28
PE25-24	2.93	n.d.	19.98	n.d.	3452.38	16.16	n.d.	n.d.	4326.80	2.63	151.29	n.d.	n.d.	1.21	242.97	3.87	0.30	95.48	1.37	52.43	0.04	2.54	4.02	7.57	1.25
PE25-25	3.13	n.d.	19.88	n.d.	3638.14	14.98	n.d.	n.d.	4082.85	3.71	142.50	n.d.	n.d.	1.80	359.64	4.98	0.46	158.94	2.33	57.67	0.07	2.26	3.90	7.17	1.12
PE25-26	2.03	n.d.	26.99	n.d.	3650.52	16.61	7.41	n.d.	4406.67	4.19	140.33	n.d.	n.d.	2.11	555.30	5.19	0.49	220.26	4.21	50.32	0.07	2.52	4.32	5.20	1.21
PE25-27	8.85	n.d.	17.55	n.d.	888.20	22.94	2.91	n.d.	4548.80	1.82	161.15	n.d.	n.d.	n.d.	1909.55	9.82	n.d.	922.01	n.d.	n.d.	n.d.	2.07	-	9.18	5.12
PE25-28	8.77	14.61	19.31	11.89	909.89	26.55	5.42	2.53	5176.19	2.50	169.45	n.d.	n.d.	n.d.	2295.36	10.89	n.d.	951.30	n.d.	n.d.	n.d.	2.41	-	8.78	5.69
PE25-29	6.72	n.d.	17.89	n.d.	1021.77	23.44	5.88	1.87	4512.28	2.41	153.61	n.d.	n.d.	n.d.	2026.69	10.21	n.d.	932.91	n.d.	n.d.	n.d.	2.17	-	8.59	4.42
PE25-30	n.d.	n.d.	19.55	n.d.	1555.64	18.40	14.14	n.d.	4357.51	n.d.	132.66	n.d.	n.d.	n.d.	23.47	0.80	n.d.	19.39	n.d.	n.d.	n.d.	1.21	-	6.79	2.80
PE25-31	1.15	34.18	23.65	18.13	3871.71	17.66	13.34	n.d.	4001.89	n.d.	120.87	n.d.	n.d.	n.d.	258.01	5.68	n.d.	116.50	n.d.	n.d.	n.d.	2.21	-	5.11	1.03
PE25-32	2.13	n.d.	24.06	n.d.	3897.70	17.49	13.89	5.32	3996.22	2.38	116.21	n.d.	n.d.	n.d.	157.99	4.63	n.d.	76.81	n.d.	n.d.	n.d.	2.06	-	4.83	1.03
PE25-33	3.48	20.48	21.55	17.17	3067.17	16.56	7.56	n.d.	3852.95	2.35	121.37	n.d.	n.d.	n.d.	364.77	4.08	n.d.	144.46	n.d.	n.d.	n.d.	2.52	-	5.63	1.26
PE25-34	2.42	11.42	22.12	12.12	3547.23	16.08	4.40	n.d.	3897.23	n.d.	124.18	n.d.	n.d.	n.d.	147.79	4.39	n.d.	61.56	n.d.	n.d.	n.d.	2.40	-	5.61	1.10
PE25-35	2.93	n.d.	25.73	n.d.	4486.15	17.97	13.97	n.d.	4208.05	2.92	118.61	n.d.	n.d.	n.d.	232.77	5.83	n.d.	93.07	n.d.	n.d.	n.d.	2.50	-	4.61	0.94
PE25-36	2.80	n.d.	21.17	n.d.	3150.84	15.67	6.64	3.05	3919.72	2.71	124.10	n.d.	n.d.	n.d.	468.79	5.61	n.d.	209.60	n.d.	n.d.	n.d.	2.24	-	5.86	1.24
PE25-average	5.02	30.27	30.18	27.45	2804.35	19.78	10.62	3.31	4687.39	3.79	150.93	0.17	0.24	7.23	1077.03	7.76	1.53	444.36	9.59	82.88	0.21	2.42	4.97	6.62	2.52

Table B-2 (continued): Trace element composition of the sapphires (LA-ICP-MS analyses).

sample	Be	Na	Mg	K	Ti	V	Cr	Mn	Fe	Zn	Ga	Sr	Y	Zr	Nb	Sn	Hf	Ta	W	Th	U	Nb/Ta	Zr/Hf	Ga/Mg	Fe/Ti
S52-1	n.d.	n.d.	69.73	n.d.	225.52	7.60	n.d.	5.84	10434.45	n.d.	65.80	n.d.	n.d.	n.d.	n.d.	n.d.	n.d.		n.d.	0.02	0.01	-	-	0.94	46.27
S52-2	n.d.	n.d.	59.28	n.d.	256.15	7.43	5.09	5.45	9725.53	n.d.	60.95	n.d.	n.d.	n.d.	n.d.	0.13	n.d.	0.01	n.d.	0.02	0.02	-	-	1.03	37.97
S52-3	n.d.	n.d.	71.86	n.d.	302.58	9.16	n.d.	7.78	10021.77	1.66	59.52	n.d.	n.d.	n.d.	1.24	0.09	n.d.	0.03	n.d.	0.17	0.06	47.74	-	0.83	33.12
S52-4	0.11	n.d.	66.60	n.d.	246.11	8.02	n.d.	5.67	9988.12	2.25	58.76	n.d.	n.d.	n.d.	1.06	n.d.	0.01	0.01	n.d.	0.08	0.05	74.31	-	0.88	40.58
S52-5	0.22	n.d.	57.35	n.d.	229.62	6.83	n.d.	n.d.	8096.82	n.d.	63.95	n.d.	n.d.	n.d.	n.d.	n.d.	n.d.		n.d.	n.d.	0.01	-	-	1.11	35.26
S52-6	n.d.	34.09	59.56	13.65	250.67	6.37	n.d.	n.d.	8081.42	n.d.	63.57	n.d.	n.d.	n.d.	n.d.	0.07	0.01	0.01	0.02	n.d.	n.d.	-	-	1.07	32.24
S52-7	n.d.	13.61	66.80	n.d.	243.73	8.71	n.d.	n.d.	10381.37	4.70	63.98	n.d.	n.d.	0.18	n.d.	n.d.	0.01		n.d.	n.d.	0.01	-	17.39	0.96	42.59
S52-8	n.d.	1644.17	151.84	426.61	489.83	11.53	n.d.	33.26	9159.47	3.29	76.53	10.76	3.69	0.95	18.56	0.10	0.01	0.32	0.39	3.26	0.74	57.25	68.05	0.50	18.70
S52-9	0.11	17.01	80.22	n.d.	315.44	8.85	n.d.	4.34	8756.22	2.01	61.36	n.d.	n.d.	n.d.	0.60	n.d.	0.00		n.d.	0.03	0.02	-	-	0.76	27.76
S52-10	n.d.	204.18	76.96	50.92	286.47	9.34	n.d.	4.39	8631.17	2.65	63.13	0.77	0.15	n.d.	2.78	n.d.	0.00	0.03	0.09	0.18	0.09	81.61	-	0.82	30.13
S52-11	0.83	155.28	77.02	38.62	287.00	8.19	n.d.	6.23	8866.24	2.02	55.90	0.40	n.d.	n.d.	3.42	n.d.	n.d.	0.06	0.04	0.20	0.13	57.41	-	0.73	30.89
S52-12	n.d.	45.75	62.69	16.22	349.68	7.32	n.d.	n.d.	7157.50	2.42	68.71	n.d.	n.d.	n.d.	0.83	n.d.	n.d.	0.01	0.03	0.01	0.03	88.49	-	1.10	20.47
S52-13	n.d.	62.76	64.32	20.43	391.93	6.99	n.d.	3.61	7481.78	2.81	70.35	0.64	0.17	0.87	0.91	n.d.	0.01	0.03	0.02	0.09	0.03	33.29	66.46	1.09	19.09
S52-14	n.d.	65.49	77.28	31.13	429.16	8.90	n.d.	3.98	8408.78	3.29	76.34	0.60	n.d.	n.d.	0.50	n.d.	n.d.	0.13	0.08	0.01	0.01	3.75	-	0.99	19.59
S52-15	n.d.	n.d.	86.19	n.d.	332.44	9.09	n.d.	n.d.	8593.65	2.83	77.55	n.d.	n.d.	n.d.	0.27	n.d.	n.d.	0.17	0.03	0.00	n.d.	1.57	-	0.90	25.85
S52-16	0.50	n.d.	84.80	n.d.	392.40	9.71	n.d.	n.d.	9548.34	2.60	81.70	n.d.	n.d.	n.d.	0.64	0.11	n.d.	0.59	n.d.	0.01	n.d.	1.08	-	0.96	24.33
S52-17	n.d.	n.d.	85.03	n.d.	341.82	10.99	3.81	2.56	9960.27	4.11	84.79	n.d.	n.d.	n.d.	n.d.	n.d.	0.00	0.27	0.00	n.d.	n.d.	-	-	1.00	29.14
S52-18	n.d.	n.d.	72.85	n.d.	343.60	8.92	n.d.	n.d.	8794.51	2.76	81.41	n.d.	n.d.	n.d.	n.d.	n.d.	n.d.	0.02	0.02	n.d.	n.d.	-	-	1.12	25.60
S52-19	n.d.	n.d.	58.70	n.d.	320.33	7.66	n.d.	n.d.	8041.04	2.45	75.46	n.d.	n.d.	n.d.	n.d.	0.08	n.d.	0.01	n.d.	n.d.	n.d.	-	-	1.29	25.10
S52-20	0.17	n.d.	78.57	n.d.	414.10	10.70	n.d.	n.d.	9099.28	2.19	77.68	n.d.	n.d.	n.d.	n.d.	n.d.	n.d.	n.d.	0.02	n.d.	n.d.	-	-	0.99	21.97
S52-21	0.17	n.d.	85.88	n.d.	468.09	12.32	n.d.	n.d.	10398.89	n.d.	90.23	n.d.	n.d.	n.d.	n.d.	n.d.	n.d.	n.d.	n.d.	n.d.	n.d.	-	-	1.05	22.22
S52-22	n.d.	n.d.	74.78	n.d.	374.42	9.14	n.d.	n.d.	7921.30	n.d.	71.74	n.d.	n.d.	n.d.	n.d.	n.d.	n.d.	0.32	n.d.	n.d.	n.d.	-	-	0.96	21.16
S52-23	0.16	n.d.	79.85	n.d.	364.46	9.57	1.96	n.d.	8307.66	n.d.	72.98	n.d.	n.d.	n.d.	1.42	n.d.	n.d.	1.99	n.d.	n.d.	n.d.	0.71	-	0.91	22.79
S52-24	n.d.	n.d.	54.59	n.d.	224.70	7.46	n.d.	n.d.	7567.96	n.d.	64.21	n.d.	n.d.	n.d.	n.d.	n.d.	n.d.	n.d.	n.d.	n.d.	n.d.	-	-	1.18	33.68
S52-25	n.d.	n.d.	51.61	n.d.	246.71	7.72	n.d.	n.d.	7010.35	n.d.	56.95	n.d.	n.d.	n.d.	n.d.	0.09	n.d.	n.d.	n.d.	n.d.	n.d.	-	-	1.10	28.42
S52-26	n.d.	n.d.	45.43	n.d.	159.57	6.50	n.d.	n.d.	7028.52	n.d.	47.74	n.d.	n.d.	n.d.	0.18	0.08	n.d.	n.d.	n.d.	n.d.	n.d.	-	-	1.05	44.05
S52-27	0.10	n.d.	61.97	n.d.	212.10	7.55	n.d.	n.d.	7615.31	n.d.	52.04	n.d.	n.d.	n.d.	n.d.	n.d.	n.d.	0.15	n.d.	n.d.	n.d.	-	-	0.84	35.91
S52-28	n.d.	n.d.	45.36	n.d.	201.61	8.03	n.d.	n.d.	6800.01	n.d.	57.78	n.d.	n.d.	n.d.	n.d.	n.d.	n.d.	0.02	n.d.	n.d.	n.d.	-	-	1.27	33.73
S52-29	n.d.	n.d.	42.03	n.d.	149.63	6.37	n.d.	n.d.	6859.68	n.d.	52.23	n.d.	n.d.	n.d.	n.d.	n.d.	n.d.	n.d.	n.d.	n.d.	n.d.	-	-	1.24	45.84
S52-30	n.d.	n.d.	60.81	n.d.	306.40	7.69	n.d.	n.d.	7581.65	n.d.	70.67	n.d.	n.d.	n.d.	n.d.	n.d.	n.d.	n.d.	n.d.	n.d.	n.d.	-	-	1.16	24.74
S52-31	n.d.	n.d.	50.19	n.d.	152.00	5.75	n.d.	n.d.	6519.05	n.d.	55.55	n.d.	n.d.	n.d.	n.d.	0.07	n.d.	0.01	n.d.	n.d.	n.d.	-	-	1.11	42.89
S52-average	0.26	249.15	69.68	85.37	300.27	8.40	3.62	7.56	8478.65	2.75	67.08	2.63	1.34	0.67	2.49	0.09	0.01	0.16	0.06	0.27	0.08	24.42	18.99	1.00	30.39
3-1	1.01	n.d.	33.83	n.d.	1922.79	7.79	n.d.	n.d.	8989.47	n.d.	204.91	n.d.	n.d.	0.54	35.55	2.30	0.18	42.49	0.10	0.95	n.d.	0.84	3.02	6.06	4.68
3-2	0.87	n.d.	34.42	n.d.	1954.73	8.99	n.d.	n.d.	8645.78	2.46	193.99	n.d.	n.d.	0.65	35.94	1.98	0.21	41.84	0.09	0.74	n.d.	0.86	3.09	5.64	4.42
3-3	0.83	39.28	37.35	22.71	1908.80	9.41	n.d.	4.82	9093.75	3.48	195.69	n.d.	n.d.	n.d.	23.94	2.08	0.11	30.36	0.09	0.44	n.d.	0.79	-	5.24	4.76
3-4	0.28	n.d.	25.14	n.d.	1145.51	7.56	n.d.	n.d.	8288.00	n.d.	190.93	n.d.	n.d.	n.d.	4.64	1.33	0.12	7.06	0.03	0.05	n.d.	0.66	-	7.59	7.24
3-5	1.90	n.d.	48.79	n.d.	2827.76	9.08	n.d.	n.d.	9399.17	2.74	204.48	n.d.	n.d.	1.38	92.55	5.59	0.31	99.62	0.29	5.71	n.d.	0.93	4.37	4.19	3.32
3-6	1.00	n.d.	50.84	n.d.	2879.71	9.95	n.d.	n.d.	9576.96	3.06	212.68	n.d.	0.07	1.94	176.10	6.09	0.60	133.80	0.19	7.03	0.01	1.32	3.23	4.18	3.33
3-7	n.d.	n.d.	40.95	n.d.	1252.77	10.21	n.d.	6.44	10383.26	n.d.	238.27	n.d.	n.d.	n.d.	17.08	0.79	0.01	9.95	n.d.	0.11	n.d.	1.72	-	5.82	8.29
3-8	0.47	n.d.	4528.14	n.d.	1333.49	12.06	n.d.	91.80	14231.93	75.43	234.62	n.d.	n.d.	n.d.	8.75	0.75	0.01	5.69	0.01	0.09	n.d.	1.54	-	0.05	10.67
3-9	0.18	n.d.	192.98	n.d.	290.80	14.56	7.62	4.67	6783.11	3.69	197.38	n.d.	n.d.	0.56	89.09	1.83	0.11	47.69	0.18	0.64	0.01	1.87	5.02	1.02	23.33
3-10	n.d.	n.d.	10803.41	n.d.	802.94	10.59	n.d.	212.23	18294.52	211.66	200.96	n.d.	n.d.	n.d.	7.00	0.41	0.02	3.50	0.02	0.14	n.d.	2.00	-	0.02	22.78
3-11	2.30	n.d.	1629.51	n.d.	2230.48	9.83	n.d.	21.39	12614.26	21.21	188.60	n.d.	n.d.	n.d.	109.35	3.85	0.12	39.32	0.24	0.57	n.d.	2.78	-	0.12	5.66
3-12	n.d.	n.d.	158.29	n.d.	2364.83	10.74	n.d.	5.12	10482.51	4.72	235.24	n.d.	n.d.	n.d.	25.78	3.74	0.15	10.54	0.07	0.19	n.d.	2.45	-	1.49	4.43
3-13	0.13	n.d.	63.58	n.d.	2105.63	10.42	n.d.	4.12	10657.49	5.25	224.27	n.d.	n.d.	0.11	24.64	3.39	0.06	11.64	0.03	0.10	n.d.	2.12	1.88	3.53	5.06
3-14	0.57	n.d.	73.61	n.d.	2287.44	9.93	n.d.	3.45	10344.68	4.89	205.67	n.d.	n.d.	n.d.	29.38	3.59	0.09	14.10	0.04	0.15	n.d.	2.08	-	2.79	4.52
3-15	0.66	n.d.	52.54	n.d.	2011.07	10.27	n.d.	3.68	11213.96	3.26	208.54	n.d.	n.d.	n.d.	20.13	3.01	0.07	9.32	0.03	0.07	n.d.	2.16	-	3.97	5.58
3-16	0.85	n.d.	126.61	n.d.	1228.62	10.84	n.d.	3.16	9845.21	6.77	220.84	n.d.	n.d.	0.52	110.12	2.87	0.13	53.15	0.15	0.36	n.d.	2.07	4.07	1.74	8.01
3-17	0.32	78.98	54.78	54.14	2056.67	11.01	n.d.	4.84	10750.52	4.95	192.49	0.24	n.d.	0.19	10.89	2.98	0.07	6.24	0.15	0.04	0.01	1.74	2.84	3.51	5.23
3-18	n.d.	n.d.	493.51	n.d.	757.30	12.20	n.d.	10.96	8754.14	8.57	129.91	n.d.	n.d.	n.d.	4.48	0.35	n.d.	2.32	0.04	0.01	n.d.	1.93	-	0.26	11.56
3-19	0.51	n.d.	56.28	n.d.	157.62	14.13	n.d.	n.d.	8021.21	3.16	171.01	n.d.	n.d.	n.d.	2.34	n.d.	0.01	0.83	n.d.	n.d.	n.d.	2.82	-	3.04	50.89
3-20	n.d.	n.d.	169.68	n.d.	180.48	14.02	n.d.	3.11	9062.81	8.11	175.18	n.d.	n.d.	n.d.	0.75	0.13	n.d.	0.43	0.01	n.d.	n.d.	1.76	-	1.03	50.21
3-21	0.52	23.87	37.45	n.d.	241.83	12.10	n.d.	n.d.	7710.01	2.12	149.51	n.d.	n.d.	n.d.	25.11	0.47	0.01	7.10	0.09	0.09	n.d.	3.54	-	3.99	31.88
3-22	n.d.	n.d.	33.39	n.d.	1402.94	9.55	n.d.	n.d.	10567.98	3.39	180.97	n.d.	n.d.	n.d.	2.88	1.77	0.07	3.32	0.03	0.02	n.d.	0.87	-	5.42	7.53
3-23	0.15	n.d.	134.15	n.d.	1068.03	8.12	1.47	5.25	6141.42	6.17	162.55	164.14	n.d.	n.d.	3.98	2.28	n.d.	6.59	n.d.	n.d.	n.d.	0.60	-	1.21	5.75
3-24	0.27	16.88	28.53	n.d.	1012.82	8.23	n.d.	1.21	6421.06	1.99	162.77	168.63	n.d.	n.d.	3.59	1.79	n.d.	4.45	n.d.	n.d.	n.d.	0.81	-	5.71	6.34
3-25	0.96	n.d.	43.41	n.d.	1713.58	10.17	n.d.	4.19	7308.10	2.06	170.06	177.42	n.d.	n.d.	30.11	3.66	n.d.	39.95	n.d.	n.d.	n.d.	0.75	-	3.92	4.26
3-26	0.42	197.86	37.82	94.53	1150.55	9.54	n.d.	7.01	7246.05	4.07	172.71	180.17	n.d.	n.d.	7.72	2.39	n.d.	6.51	n.d.	n.d.	n.d.	1.19	-	4.57	6.30
3-27	0.18	33.95	35.79	20.06	1311.31	12.15	0.95	3.06	8128.84	2.55	197.52	204.04	n.d.	n.d.	2.99	2.27	n.d.	3.02	n.d.	n.d.	n.d.	0.99	-	5.52	6.20
3-28	0.17	14.68	36.18	5.67	1008.86	11.27	0.93	2.61	8431.01	2.84	195.22	208.22	n.d.	n.d.	1.21	1.66	n.d.	1.24	n.d.	n.d.	n.d.	0.98	-	5.40	8.36
3-29	0.22	89.36	41.91	40.82	1215.87	8.71	1.29	5.68	6928.62	1.90	165.69	166.70	n.d.	n.d.	3.39	2.15	n.d.	2.28	n.d.	n.d.	n.d.	1.48	-	3.95	5.70
3-30	0.06	19.54	22.17	10.99	206.36	13.72	1.90	1.58	5559.08	n.d.	126.56	127.99	n.d.	n.d.	2.00	0.45	n.d.	0.92	n.d.	n.d.	n.d.	2.17	-	5.71	26.94
3-31	n.d.	n.d.	38.95	n.d.	1709.54	10.30	n.d.	1.45	7812.31	2.63	173.02	179.19	n.d.	n.d.	8.24	3.30	n.d.	10.39	n.d.	n.d.	n.d.	0.79	-	4.44	4.57
3-32	2.28	n.d.	48.99	n.d.	719.03	12.85	1.24	3.92	8141.40	2.29	192.97	196.27	n.d.	n.d.	705.95	8.99	n.d.	362.02	n.d.	n.d.	n.d.	1.95	-	3.94	11.32
3-average	0.69	57.15	600.41	35.56	1389.38	10.63	2.20	17.32	9244.64	14.48	189.85	161.18	0.07	0.74	50.80	2.52	0.12	31.80	0.09	0.88	n.d.	1.58	1.38	3.60	11.54

Table B-2 (continued): Trace element composition of the sapphires (LA-ICP-MS analyses).

sample	Be	Na	Mg	K	Ti	V	Cr	Mn	Fe	Zn	Ga	Sr	Y	Zr	Nb	Sn	Hf	Ta	W	Th	U	Nb/Ta	Zr/Hf	Ga/Mg	Fe/Ti
15-1	n.d.	n.d.	84.27	n.d.	848.11	13.46	n.d.	n.d.	9926.50	n.d.	113.78	n.d.	n.d.	n.d.	n.d.	0.49		0.33	n.d.	n.d.	n.d.	-	-	1.35	11.70
15-2	n.d.	n.d.	68.46	n.d.	792.26	11.81	n.d.	n.d.	9740.81	n.d.	112.58	n.d.	n.d.	n.d.	n.d.	0.43	0.01	0.03	0.01	n.d.	n.d.	-	-	1.64	12.29
15-3	n.d.	n.d.	55.87	n.d.	419.69	11.62	13.71	n.d.	9152.21	3.95	106.82	n.d.	n.d.	n.d.	n.d.	n.d.	0.01	0.00	n.d.	n.d.	n.d.	-	-	1.91	21.81
15-4	0.30	n.d.	54.36	n.d.	437.18	7.47	n.d.	n.d.	9474.95	n.d.	106.23	n.d.	n.d.	n.d.	n.d.	n.d.	n.d.	0.00	0.01	n.d.	n.d.	-	-	1.95	21.67
15-5	n.d.	n.d.	58.98	n.d.	474.02	10.50	n.d.	n.d.	10874.64	5.13	118.29	n.d.	n.d.	n.d.	1.53	0.19	0.01	0.00	0.05	n.d.	n.d.	369.03	-	2.01	22.94
15-6	n.d.	n.d.	86.36	n.d.	630.99	16.28	n.d.	n.d.	14042.53	5.57	130.15	n.d.	n.d.	n.d.	n.d.	0.26	0.01	0.01	n.d.	n.d.	n.d.	-	-	1.51	22.25
15-7	n.d.	n.d.	84.95	n.d.	772.60	14.91	n.d.	3.27	13368.09	6.27	127.72	n.d.	n.d.	n.d.	n.d.	n.d.	0.01	0.02	n.d.	n.d.	n.d.	-	-	1.50	17.30
15-8	n.d.	n.d.	76.93	n.d.	688.01	10.74	n.d.	8.93	10602.64	n.d.	103.91	0.96	n.d.	n.d.	n.d.	0.57	n.d.	0.12	0.02	0.02	n.d.	-	-	1.35	15.41
15-9	n.d.	17.19	87.36	n.d.	866.49	11.44	n.d.	n.d.	11057.95	n.d.	99.55	n.d.	n.d.	n.d.	n.d.	0.41	n.d.	0.34	n.d.	0.01	n.d.	-	-	1.14	12.76
15-10	n.d.	n.d.	116.60	n.d.	1182.14	17.49	n.d.	6.06	14957.70	9.77	122.59	n.d.	n.d.	n.d.	n.d.	0.51	0.04	0.34	n.d.	0.02	n.d.	-	-	1.05	12.65
15-11	n.d.	n.d.	70.71	n.d.	557.65	11.48	14.75	9.79	10986.15	n.d.	103.29	n.d.	n.d.	n.d.	n.d.	0.24		0.08	n.d.	0.02	0.04	-	-	1.46	19.70
15-12	n.d.	n.d.	78.01	n.d.	694.39	9.28	n.d.	21.90	12342.08	n.d.	116.26	n.d.	n.d.	0.51	9.73	0.69	0.01	5.18	0.09	0.82	0.20	1.88	66.29	1.49	17.77
15-13	0.23	n.d.	89.21	n.d.	440.29	11.34	n.d.	5.74	11544.93	3.81	113.30	n.d.	n.d.	0.43	23.33	0.59	0.07	9.71	0.09	0.85	0.07	2.40	6.11	1.27	26.22
15-14	6.88	n.d.	61.80	n.d.	235.44	8.16	n.d.	n.d.	10134.83	n.d.	105.14	n.d.	n.d.	n.d.	0.59	n.d.	n.d.	0.36	n.d.	n.d.	0.01	1.64	-	1.70	43.05
15-15	n.d.	18.78	41.08	n.d.	171.41	7.30	n.d.	n.d.	8564.56	n.d.	99.04	n.d.	n.d.	n.d.	n.d.	n.d.	n.d.	0.04	0.01	0.01	n.d.	-	-	2.41	49.97
15-16	n.d.	n.d.	39.09	n.d.	248.97	6.93	n.d.	n.d.	9211.90	3.25	99.70	n.d.	0.23	n.d.	n.d.	n.d.	0.02	0.01	n.d.	0.01	n.d.	-	-	2.55	37.00
15-17	n.d.	n.d.	62.55	n.d.	459.45	11.15	8.77	6.57	12407.60	5.56	110.01	n.d.	n.d.	n.d.	3.36	0.15	0.01	0.16	n.d.	0.06	0.06	21.30	-	1.76	27.01
15-18	n.d.	143.61	91.34	78.31	588.00	10.71	n.d.	28.91	11948.06	6.55	116.68	n.d.	n.d.	0.43	3.40	n.d.	0.04	1.34	0.13	0.19	0.07	2.55	9.99	1.28	20.32
15-19	n.d.	n.d.	82.55	n.d.	511.84	8.62	n.d.	7.53	11599.60	n.d.	111.75	n.d.	n.d.	n.d.	4.84	n.d.	n.d.	2.73	n.d.	0.15	0.02	1.77	-	1.35	22.66
15-20	0.18	29.10	105.90	14.56	549.10	15.21	n.d.	13.32	14643.57	7.82	138.42	0.44	n.d.	n.d.	3.80	0.26	n.d.	1.57	0.05	0.17	0.04	2.42	-	1.31	26.67
15-21	0.21	n.d.	59.76	n.d.	533.52	11.18	1.08	n.d.	9610.17	3.10	96.12	n.d.	n.d.	n.d.	0.16	0.32	n.d.	0.03	n.d.	n.d.	n.d.	5.08	-	1.61	18.01
15-22	0.11	n.d.	87.98	n.d.	998.41	12.12	n.d.	1.98	10218.26	3.79	99.92	n.d.	n.d.	n.d.	0.21	0.76	n.d.	0.30	n.d.	n.d.	n.d.	0.70	-	1.14	10.23
15-23	0.17	76.49	150.27	1151.66	679.31	14.08	n.d.	8.51	12269.19	5.64	108.54	n.d.	n.d.	n.d.	57.05	1.38	n.d.	26.46	n.d.	n.d.	n.d.	2.16	-	0.72	18.06
15-24	0.15	15.36	47.96	10.19	281.70	8.88	1.68	16.38	8795.41	1.90	91.22	n.d.	n.d.	n.d.	0.68	0.11	n.d.	0.15	n.d.	n.d.	n.d.	4.43	-	1.90	31.22
15-25	0.09	n.d.	72.02	n.d.	388.05	10.16	n.d.	n.d.	9664.88	1.99	98.46	n.d.	n.d.	n.d.	5.17	0.11	n.d.	2.38	n.d.	n.d.	n.d.	2.17	-	1.37	24.91
15-26	0.27	n.d.	68.32	n.d.	545.45	10.36	n.d.	2.72	9234.90	3.44	90.51	n.d.	n.d.	n.d.		0.23	n.d.	0.14	n.d.	n.d.	n.d.	0.00	-	1.32	16.93
15-27	0.33	n.d.	79.93	n.d.	727.50	12.46	n.d.	n.d.	10477.15	2.62	102.66	n.d.	n.d.	n.d.	7.22	0.29	n.d.	3.14	n.d.	n.d.	n.d.	2.30	-	1.28	14.40
15-28	n.d.	4.01	68.91	n.d.	535.29	11.78	2.38	6.97	9483.18	4.19	95.22	n.d.	n.d.	n.d.		0.21	n.d.	0.09	n.d.	n.d.	n.d.	0.00	-	1.38	17.72
15-29	0.06	n.d.	61.26	n.d.	411.75	11.21	1.22	7.90	10081.00	2.84	102.86	n.d.	n.d.	n.d.	0.17	0.23	n.d.	0.03	n.d.	n.d.	n.d.	5.94	-	1.68	24.48
15-30	n.d.	6.15	58.05	n.d.	335.54	10.15	1.20	15.18	9182.83	3.01	95.06	n.d.	n.d.	n.d.	0.97	0.11	n.d.	0.23	n.d.	n.d.	n.d.	4.29	-	1.64	27.37
15-average	0.75	38.84	75.03	313.68	566.82	11.28	5.60	10.10	10853.28	4.51	107.86	0.70	0.23	0.46	7.64	0.39	0.02	1.84	0.05	0.19	0.05	14.33	7.49	1.53	22.15
26-1	n.d.	37.63	11.75	35.58	81.19	4.66	n.d.	18.79	4070.84	n.d.	256.09	n.d.	n.d.	n.d.	1.49	n.d.	n.d.	0.96	0.09	0.02	0.01	1.56	-	21.80	50.14
26-2	0.18	20.39	9.43	20.17	109.28	5.92	n.d.	15.59	4196.60	n.d.	221.19	n.d.	n.d.	n.d.	1.39	n.d.	0.01	1.13	0.07	0.03	0.01	1.23	-	23.46	38.40
26-3	0.19	15.03	12.64	n.d.	199.36	8.60	n.d.	21.33	5961.60	n.d.	222.10	n.d.	n.d.	n.d.	2.56	n.d.	0.01	6.68	0.03	0.07	0.02	0.38	-	17.57	29.90
26-4	n.d.	30.63	8.89	14.41	161.73	7.13	n.d.	16.64	6435.60	9.17	205.95	n.d.	n.d.	n.d.	1.65	n.d.	0.01	1.53	0.12	0.00	0.01	1.08	-	23.17	39.79
26-5	0.18	n.d.	9.83	n.d.	160.94	4.19	n.d.	n.d.	5020.51	3.30	189.95	n.d.	n.d.	n.d.	13.29	n.d.	0.02	9.84	0.03	0.06	n.d.	1.35	-	19.32	31.19
26-6	2.38	122.48	8.67	74.23	195.04	3.96	7.67	8.64	5059.76	4.58	189.23	n.d.	n.d.	n.d.	47.93	0.27	0.02	24.67	0.12	0.34	n.d.	1.94	-	21.82	25.94
26-7	1.33	77.20	11.31	40.43	126.46	4.52	n.d.	n.d.	5565.87	3.92	203.99	n.d.	n.d.	n.d.	48.23	0.25	0.02	21.74	0.13	0.30	n.d.	2.22	-	18.03	44.01
26-8	0.54	41.80	10.57	39.87	218.45	5.60	n.d.	6.44	6045.20	4.71	211.58	n.d.	0.11	n.d.	16.39	0.15	0.01	8.54	0.05	0.09	n.d.	1.92	-	20.01	27.67
26-9	n.d.	95.70	7.61	42.77	285.52	5.21	n.d.	10.77	5562.79	5.76	197.96	n.d.	n.d.	n.d.	9.88	0.19	0.01	2.45	0.17	0.07	n.d.	4.04	-	26.03	19.48
26-10	n.d.	172.88	6.71	134.95	150.13	2.31	n.d.	7.16	3928.68	5.06	166.57	n.d.	n.d.	n.d.	2.22	n.d.	0.01	1.49	0.06	0.04	n.d.	1.49	-	24.83	26.17
26-11	n.d.	36.25	253.42	35.58	176.23	5.51	n.d.	10.25	4871.36	n.d.	196.42	n.d.	n.d.	n.d.	0.89	n.d.	n.d.	0.50	0.06	0.02	n.d.	1.79	-	0.78	27.64
26-12	1.29	372.87	51.46	282.80	632.54	7.08	n.d.	18.60	5558.33	n.d.	227.25	n.d.	n.d.	n.d.	10.08	0.27	0.04	4.72	0.04	0.21	0.01	2.14	-	4.42	8.79
26-13	n.d.	72.81	15.07	37.06	491.53	6.44	n.d.	15.18	4653.92	4.70	204.93	n.d.	n.d.	n.d.	2.47	0.23	n.d.	1.16	0.02	0.14	0.00	2.13	-	13.60	9.47
26-14	0.96	264.82	21.77	223.47	527.10	7.55	n.d.	59.50	5127.53	5.67	225.30	0.29	n.d.	n.d.	20.51	0.38	0.03	9.92	0.08	0.89	0.03	2.07	-	10.35	9.73
26-15	0.93	22.05	10.22	22.80	491.68	n.d.	n.d.	28.72	4556.22	5.52	201.42	n.d.	n.d.	n.d.	3.68	0.22	n.d.	3.31	0.06	0.19	0.01	1.11	-	19.71	9.27
26-16	n.d.	n.d.	15.72	n.d.	1291.97	9.14	n.d.	91.64	16746.38	n.d.	238.19	n.d.	n.d.	2.42	709.66	1.75	0.13	11.70	0.56	0.33	0.47	60.64	18.12	15.16	12.96
26-17	n.d.	12.79	9.35	n.d.	690.67	7.01	n.d.	10.26	5534.44	4.86	223.94	n.d.	n.d.	n.d.	5.72	0.25	n.d.	1.25	0.03	0.06	0.01	4.58	-	23.95	8.01
26-18	n.d.	n.d.	6.62	n.d.	298.03	6.77	n.d.	n.d.	4969.23	n.d.	212.34	n.d.	n.d.	n.d.	1.15	n.d.	0.01	0.14	n.d.	0.01	n.d.	8.01	-	32.09	16.67
26-19	0.21	59.38	105.70	56.01	377.84	6.93	n.d.	5.95	4962.24	n.d.	191.75	0.40	n.d.	n.d.	0.51	0.11	n.d.	0.28	n.d.	0.03	n.d.	1.81	-	1.81	13.13
26-20	n.d.	70.10	63.71	55.80	195.47	9.03	n.d.	18.20	6142.08	4.80	243.27	n.d.	n.d.	n.d.	1.21	0.10	n.d.	0.13	0.01	0.05	0.01	9.60	-	3.82	31.42
26-21	0.58	n.d.	9.74	n.d.	244.48	10.75	n.d.	6.64	5702.31	5.92	235.39	n.d.	n.d.	n.d.	n.d.	n.d.	n.d.	0.68	n.d.	0.03	0.01	-	-	24.17	23.32
26-22	n.d.	n.d.	148.35	n.d.	177.54	11.97	n.d.	6.64	3924.02	n.d.	210.90	n.d.	n.d.	n.d.	1.41	n.d.	n.d.	0.90	n.d.	n.d.	n.d.	1.56	-	1.42	22.10
26-23	0.26	125.21	20.59	84.53	238.96	6.95	2.75	16.29	3760.80	2.59	182.90	n.d.	n.d.	n.d.	3.66	n.d.	n.d.	2.08	n.d.	n.d.	n.d.	1.76	-	8.88	15.74
26-24	0.50	n.d.	6.03	n.d.	235.25	5.06	2.41	10.60	3357.28	2.95	167.97	n.d.	n.d.	n.d.	0.46	0.10	n.d.	0.35	n.d.	n.d.	n.d.	1.29	-	27.85	14.27
26-25	0.61	n.d.	8.12	n.d.	291.18	6.80	n.d.	8.00	3993.16	2.25	186.18	n.d.	n.d.	n.d.	2.05	0.31	n.d.	6.83	n.d.	n.d.	n.d.	0.30	-	22.92	13.71
26-26	0.55	8.10	8.13	12.22	234.89	6.90	2.54	10.22	4153.07	1.95	186.30	n.d.	n.d.	n.d.	1.55	0.21	n.d.	7.67	n.d.	n.d.	n.d.	0.20	-	22.93	17.68
26-27	0.09	14.08	6.61	n.d.	102.84	4.09	n.d.	8.19	2966.51	3.58	149.13	n.d.	n.d.	n.d.	1.99	0.11	n.d.	0.47	n.d.	n.d.	n.d.	4.23	-	22.55	28.85
26-28	0.64	30.91	8.54	28.52	86.05	3.79	n.d.	4.18	3570.86	1.92	157.75	n.d.	n.d.	n.d.	24.70		n.d.	12.45	n.d.	n.d.	n.d.	1.98	-	18.47	41.50
26-29	0.26	49.05	4.68	33.16	77.56	3.58	n.d.	6.26	3425.12	1.85	157.31	n.d.	n.d.	n.d.	1.75	0.16	n.d.	1.22	n.d.	n.d.	n.d.	1.43	-	33.62	44.16
26-30	n.d.	22.49	6.68	n.d.	101.08	6.60	2.03	7.42	3385.99	2.15	191.49	n.d.	n.d.	n.d.	1.62	0.09	n.d.	0.46	n.d.	n.d.	n.d.	3.54	-	28.68	33.50
26-31	0.37	14.81	10.87	n.d.	618.20	6.49	1.71	48.45	3819.69	3.62	178.24	n.d.	n.d.	n.d.	6.68	0.32	n.d.	4.39	n.d.	n.d.	n.d.	1.52	-	16.39	6.18
26-average	0.63	74.56	28.67	67.07	299.01	6.35	3.18	17.73	5065.42	4.13	201.06	0.35	0.11	2.42	31.56	0.29	0.02	4.83	0.10	0.14	0.03	4.16	1.39	18.37	23.90

Table B-2 (continued): Trace element composition of the sapphires (LA-ICP-MS analyses).

sample	Be	Na	Mg	K	Ti	V	Cr	Mn	Fe	Zn	Ga	Sr	Y	Zr	Nb	Sn	Hf	Ta	W	Th	U	Nb/Ta	Zr/Hf	Ga/Mg	Fe/Ti
KS21-1	1.14	n.d.	25.82	n.d.	865.67	8.35	n.d.	3.87	12516.43	n.d.	213.65	n.d.	n.d.	3.26	428.88	14.03	0.35	226.58	1.04	13.54	0.01	1.89	9.26	8.27	14.46
KS21-2	2.71	n.d.	28.82	n.d.	1091.73	9.68	n.d.	4.86	13676.35	3.00	216.19	n.d.	n.d.	3.51	581.37	18.31	0.53	341.75	1.05	11.42	0.01	1.70	6.62	7.50	12.53
KS21-3	2.49	n.d.	36.49	n.d.	1201.60	12.35	n.d.	3.22	15527.13	4.97	235.83	n.d.	n.d.	1.74	487.80	14.86	0.27	281.60	1.13	3.40	0.01	1.73	6.48	6.46	12.92
KS21-4	1.55	9.43	36.70	n.d.	1051.95	13.67	n.d.	3.91	15966.85	5.62	245.34	n.d.	n.d.	2.47	590.37	16.97	0.34	272.13	1.16	8.14	0.01	2.17	7.18	6.69	15.18
KS21-5	1.64	n.d.	37.01	n.d.	1273.38	13.74	n.d.	6.01	15236.97	5.02	217.13	n.d.	n.d.	1.86	637.58	16.56	0.33	287.14	1.35	6.14	0.01	2.22	5.71	5.87	11.97
KS21-6	1.39	n.d.	34.34	n.d.	1178.85	13.66	n.d.	5.04	14522.52	4.39	222.31	n.d.	n.d.	1.86	624.14	16.57	0.31	239.63	1.37	8.00	0.02	2.60	6.05	6.47	12.32
KS21-7	1.74	n.d.	37.99	n.d.	1309.98	14.75	n.d.	3.89	14771.12	4.74	228.78	n.d.	n.d.	2.39	765.41	18.92	0.37	335.15	1.47	6.41	0.01	2.28	6.40	6.02	11.28
KS21-8	1.42	n.d.	39.33	n.d.	1315.65	14.94	n.d.	3.26	14954.69	5.56	236.10	n.d.	n.d.	2.72	805.84	20.31	0.38	319.06	1.73	8.89	0.01	2.53	7.22	6.00	11.37
KS21-9	1.49	n.d.	33.99	n.d.	1089.70	14.27	n.d.	4.97	13964.74	4.71	236.17	n.d.	n.d.	1.75	672.56	17.00	0.28	244.85	1.60	7.79	0.01	2.75	6.28	6.95	12.82
KS21-10	0.93	n.d.	31.94	n.d.	810.81	14.48	n.d.	2.87	12973.81	5.09	232.92	n.d.	n.d.	1.20	406.89	10.64	0.14	136.24	1.12	4.25	0.01	2.99	8.32	7.29	16.00
KS21-11	2.19	n.d.	31.93	n.d.	1189.22	11.20	n.d.	4.58	11123.97	2.27	202.18	n.d.	n.d.	3.10	662.50	19.00	0.60	336.68	1.26	12.27	0.01	1.97	5.14	6.33	9.35
KS21-12	n.d.	n.d.	24.87	n.d.	914.42	8.54	n.d.	n.d.	14092.37	6.26	141.55	n.d.	n.d.	0.43	430.59	6.37	0.08	140.07	0.78	1.47	n.d.	3.07	5.32	5.69	15.41
KS21-13	0.83	n.d.	18.00	n.d.	799.90	7.16	n.d.	n.d.	8439.32	2.98	202.23	n.d.	n.d.	n.d.	48.40	2.16	0.02	12.39	0.15	0.12	n.d.	3.91	-	11.24	10.55
KS21-14	n.d.	n.d.	17.31	n.d.	724.99	10.59	n.d.	n.d.	12195.17	5.34	199.63	n.d.	n.d.	n.d.	287.02	4.46	0.06	70.52	0.49	0.68	n.d.	4.07	-	11.53	16.82
KS21-15	n.d.	n.d.	9.78	n.d.	485.30	6.52	n.d.	n.d.	8303.27	n.d.	220.28	n.d.	n.d.	n.d.	53.86	1.41	0.02	13.28	0.08	0.11	n.d.	4.06	-	22.53	17.11
KS21-16	n.d.	n.d.	5.85	n.d.	273.96	5.18	n.d.	n.d.	6579.48	n.d.	194.55	n.d.	n.d.	n.d.	10.68	0.63	n.d.	3.31	0.02	0.04	n.d.	3.23	-	33.27	24.02
KS21-17	n.d.	n.d.	4.20	n.d.	204.88	5.55	n.d.	3.82	6010.20	n.d.	197.79	n.d.	0.11	n.d.	0.47	0.18	n.d.	0.16	n.d.	n.d.	n.d.	2.92	-	47.15	29.34
KS21-18	n.d.	n.d.	4.23	n.d.	205.07	3.49	n.d.	n.d.	6078.51	n.d.	210.80	n.d.	n.d.	n.d.	n.d.	0.42	n.d.	0.05	n.d.	n.d.	n.d.	-	-	49.81	29.64
KS21-19	n.d.	n.d.	3.76	n.d.	203.01	6.76	n.d.	n.d.	5532.70	n.d.	212.75	n.d.	n.d.	n.d.	n.d.	0.43	0.01	0.03	n.d.	n.d.	n.d.	-	-	56.54	27.25
KS21-20	n.d.	n.d.	4.49	n.d.	242.93	6.64	n.d.	n.d.	6824.96	3.31	244.87	n.d.	n.d.	n.d.	n.d.	0.42	n.d.	0.05	n.d.	n.d.	n.d.	-	-	54.52	28.09
KS21-21	n.d.	11.20	4.92	n.d.	288.85	7.36	n.d.	4.13	6776.02	5.12	251.72	n.d.	n.d.	n.d.	1.17	0.59	n.d.	0.16	0.01	0.02	0.01	7.42	-	51.12	23.46
KS21-22	n.d.	n.d.	3.94	n.d.	249.06	5.02	n.d.	n.d.	5427.37	714.01	198.83	n.d.	n.d.	n.d.	n.d.	0.49	n.d.	0.11	n.d.	n.d.	n.d.	-	-	50.51	21.79
KS21-23	0.08	9.44	5.85	n.d.	264.46	5.94	2.04	6.22	4598.66	n.d.	190.75	n.d.	n.d.	n.d.	1.22	0.68	n.d.	0.45	n.d.	n.d.	n.d.	2.71	-	32.62	17.39
KS21-24	0.32	n.d.	5.51	n.d.	406.16	6.23	1.62	2.48	4665.94	1.26	230.29	n.d.	n.d.	n.d.	0.34	0.49	n.d.	0.75	n.d.	n.d.	n.d.	0.45	-	41.79	11.49
KS21-25	0.07	n.d.	4.40	n.d.	321.16	6.57	n.d.	2.35	5393.78	2.02	197.62	n.d.	n.d.	n.d.	0.14	0.68	n.d.	0.42	n.d.	n.d.	n.d.	0.33	-	44.94	16.79
KS21-26	0.06	n.d.	3.61	n.d.	190.71	6.00	1.48	1.87	5422.91	1.25	186.47	n.d.	n.d.	n.d.	n.d.	0.39	n.d.	0.04	n.d.	n.d.	n.d.	-	-	51.60	28.44
KS21-27	0.08	n.d.	3.60	n.d.	178.71	5.69	n.d.	1.44	5123.77	n.d.	164.38	n.d.	n.d.	n.d.	n.d.	0.29	n.d.	0.04	n.d.	n.d.	n.d.	-	-	45.61	28.67
KS21-28	n.d.	143.80	3.71	69.20	157.90	4.71	1.18	13.32	5023.66	2.12	160.09	n.d.	n.d.	n.d.	0.16	0.25	n.d.	0.04	n.d.	n.d.	n.d.	3.96	-	43.20	31.81
KS21-29	n.d.	n.d.	4.25	n.d.	191.32	5.38	n.d.	1.35	5350.54	1.38	163.02	n.d.	n.d.	n.d.	n.d.	0.28	n.d.	0.04	n.d.	n.d.	n.d.	-	-	38.35	27.97
KS21-30	n.d.	n.d.	8.40	n.d.	441.79	5.54	n.d.	2.39	5945.07	1.44	137.55	n.d.	n.d.	n.d.	n.d.	0.82	n.d.	0.15	n.d.	n.d.	n.d.	-	-	16.38	13.46
KS21-31	0.17	n.d.	8.95	n.d.	433.08	6.01	n.d.	n.d.	6158.73	1.44	135.07	n.d.	n.d.	n.d.	0.35	0.51	n.d.	0.53	n.d.	n.d.	n.d.	0.65	-	15.09	14.22
KS21-32	0.13	n.d.	6.19	n.d.	232.69	6.10	0.96	1.30	5954.38	1.15	164.82	n.d.	n.d.	n.d.	n.d.	0.17	n.d.	0.09	n.d.	n.d.	n.d.	-	-	26.63	25.59
KS21-average	1.07	43.47	16.57	69.20	618.40	8.50	1.46	3.96	9222.86	33.10	202.86	n.d.	0.11	2.19	325.99	6.42	0.26	101.98	0.83	5.15	0.01	1.93	5.00	25.75	18.73

APPENDIX C: PM AND MANTLE NORMALIZED HFSE CONTENT

Table C-1: Element correlations of the Siebengebirge sapphires.

KS21	Be	Mg	Ti	V	Fe	Zn	Ga	Nb	Sn	Hf	Ta	W
Be	1											
Mg	0.86	1										
Ti	0.90	0.98	1									
V	0.71	0.94	0.90	1								
Fe	0.85	0.97	0.94	0.91	1							
Zn	0.61	-0.22	-0.22	-0.24	-0.22	1						
Ga	0.63	0.44	0.41	0.55	0.45	-0.02	1					
Nb	0.80	0.96	0.95	0.91	0.92	0.56	0.40	1				
Sn	0.89	0.96	0.95	0.90	0.91	-0.18	0.48	0.98	1			
Hf	0.71	0.71	0.75	0.49	0.54	-0.45	0.30	0.78	0.91	1		
Ta	0.93	0.95	0.94	0.86	0.91	-0.18	0.44	0.97	0.99	0.93	1	
W	0.24	0.96	0.93	0.91	0.90	-0.40	0.19	0.98	0.96	0.71	0.93	1

ÖL25												
Be	1											
Mg	0.73	1										
Ti	0.79	0.95	1									
V	0.55	0.88	0.79	1								
Fe	0.52	0.78	0.72	0.84	1							
Zn	0.26	0.55	0.43	0.72	0.34	1						
Ga	0.03	0.29	0.11	0.58	0.69	0.33	1					
Nb	0.76	0.84	0.77	0.63	0.52	0.45	0.13	1				
Sn	0.74	0.94	0.99	0.72	0.64	0.42	-0.01	0.77	1			
Hf	0.82	0.53	0.72	0.17	0.15	-0.24	-0.64	0.55	0.75	1		
Ta	0.70	0.62	0.60	0.36	0.42	0.19	0.10	0.81	0.60	0.44	1	
W	0.76	0.84	0.91	0.53	0.51	0.40	-0.32	0.86	0.92	0.72	0.65	1

ÖL60												
Be	1											
Mg	-0.10	1										
Ti	0.38	0.19	1									
V	-0.22	-0.01	0.39	1								
Fe	0.00	-0.18	0.44	0.92	1							
Zn	0.37	0.67	0.49	-0.32	-0.28	1						
Ga	0.34	-0.48	0.33	0.35	0.62	-0.07	1					
Nb	0.77	-0.13	0.52	0.46	0.58	0.08	0.44	1				
Sn	0.04	-0.11	0.45	0.94	0.96	-0.38	0.36	0.70	1			
Hf	1.00	-0.14	0.51	-0.86	-0.25	0.87	0.41	1.00	1.00	1		
Ta	0.59	-0.11	0.50	0.65	0.73	-0.04	0.43	0.97	0.86	1.00	1	
W	1.00	-0.14	0.47	-0.72	-0.11	0.83	0.32	1.00	1.00	1.00	1.00	1

ÖL61												
Be	1											
Mg	-0.30	1										
Ti	0.28	0.29	1									
V	-0.33	0.26	0.39	1								
Fe	-0.10	0.02	0.39	0.54	1							
Zn	-0.24	0.44	0.64	0.50	0.56	1						
Ga	-0.27	0.04	0.15	0.60	0.90	0.47	1					
Nb	-0.15	0.43	0.04	0.43	0.01	0.30	0.20	1				
Sn	0.25	0.40	0.80	0.26	0.17	0.50	0.03	0.19	1			
Hf	0.69	0.16	-0.34	-0.21	-0.04	-0.29	0.27	0.11	-0.17	1		
Ta	-0.02	0.31	-0.10	0.23	0.12	-0.07	0.24	0.50	0.26	0.61	1	
W	0.65	0.54	0.11	-0.08	-0.01	0.10	0.15	0.35	0.39	0.93	0.71	1

Table C-1 (continued): Element correlations of the Siebengebirge sapphires.

PE21	Be	Mg	Ti	V	Fe	Zn	Ga	Nb	Sn	Hf	Ta	W
Be	1											
Mg	0.28	1										
Ti	-0.68	0.20	1									
V	0.75	0.65	-0.46	1								
Fe	0.38	0.83	0.07	0.66	1							
Zn	0.36	0.32	-0.05	0.44	0.29	1						
Ga	0.66	0.56	-0.44	0.83	0.72	0.54	1					
Nb	0.93	0.42	-0.68	0.86	0.50	0.29	0.77	1				
Sn	0.93	0.50	-0.60	0.84	0.56	0.32	0.81	0.97	1			
Hf	0.95	0.34	-0.77	0.69	0.39	0.26	0.78	0.94	0.97	1		
Ta	0.93	0.37	-0.70	0.84	0.44	0.24	0.71	0.99	0.95	0.94	1	
W	0.94	0.49	-0.80	0.87	0.51	0.31	0.85	0.99	0.97	0.93	0.98	1

PE25												
Be	1											
Mg	0.30	1										
Ti	-0.61	-0.09	1									
V	0.69	0.28	-0.27	1								
Fe	0.50	0.23	-0.08	0.84	1							
Zn	-0.12	0.05	0.45	0.41	0.61	1						
Ga	0.71	0.22	-0.47	0.76	0.85	0.33	1					
Nb	0.95	0.28	-0.66	0.76	0.58	-0.03	0.79	1				
Sn		0.26	-0.35	0.77	0.64	0.16	0.73	0.93	1			
Hf	0.92	0.21	-0.66	0.55	0.35	-0.26	0.64	0.94	0.89	1		
Ta	0.94	0.22	-0.70	0.68	0.49	-0.15	0.74	0.98	0.89	0.97	1	
W	0.94	0.34	-0.67	0.72	0.52	-0.11	0.81	1.00	0.91	0.93	0.97	1

S52												
Be	1											
Mg	0.25	1										
Ti	0.02	0.76	1									
V	-0.10	0.77	0.78	1								
Fe	0.07	0.51	0.40	0.62	1							
Zn	0.03	0.19	0.06	0.28	0.29	1						
Ga	-0.08	0.57	0.83	0.73	0.44	0.39	1					
Nb	0.76	0.90	0.52	0.66	0.21	0.42	0.23	1				
Sn		0.39	0.50	0.54	0.76	0.46	0.36	0.46	1			
Hf	-1.00	0.28	0.43	-0.21	-0.28	0.28	0.13	0.60	1.00	1		
Ta	-0.11	0.29	0.26	0.28	0.10	0.43	0.24	0.02	0.40	0.11	1	
W	1.00	0.92	0.63	0.48	0.10	0.29	0.12	0.97	0.77	0.46	0.65	1

3												
Be	1											
Mg	0.11	1										
Ti	0.40	-0.12	1									
V	-0.09	0.05	-0.59	1								
Fe	0.34	0.79	0.28	-0.04	1							
Zn	0.03	1.00	-0.15	0.03	0.80	1						
Ga	0.22	0.17	0.53	-0.16	0.55	0.20	1					
Nb	0.67	-0.07	0.00	0.19	-0.04	-0.09	0.13	1				
Sn	0.73	-0.25	0.54	-0.12	-0.06	-0.30	0.29	0.77	1			
Hf		-0.25	0.62	-0.33	-0.24	-0.26	0.14	0.78	0.77	1		
Ta	0.70	-0.10	0.11	0.11	-0.07	-0.11	0.15	0.98	0.82	0.92	1	
W	0.71	-0.24	0.42	-0.10	-0.23	-0.28	0.07	0.79	0.67	0.56	0.77	1

Appendix C-1 (continued): Element correlations of the Siebengebirge sapphires.

15

	Be	Mg	Ti	V	Fe	Zn	Ga	Nb	Sn	Hf	Ta	W
Be	1											
Mg	0.11	1										
Ti	0.40	-0.12	1									
V	-0.09	0.05	-0.59	1								
Fe	0.34	0.79	0.28	-0.04	1							
Zn	0.03	1.00	-0.15	0.03	0.80	1						
Ga	0.22	0.17	0.53	-0.16	0.55	0.20	1					
Nb	0.67	-0.07	0.00	0.19	-0.04	-0.09	0.13	1				
Sn	0.73	-0.25	0.54	-0.12	-0.06	-0.30	0.29	0.77	1			
Hf		-0.25	0.62	-0.33	-0.24	-0.26	0.14	0.78	0.77	1		
Ta	0.70	-0.10	0.11	0.11	-0.07	-0.11	0.15	0.98	0.82	0.92	1	
W	0.71	-0.24	0.42	-0.10	-0.23	-0.28	0.07	0.79	0.67	0.56	0.77	1

26

	Be	Mg	Ti	V	Fe	Zn	Ga	Nb	Sn	Hf	Ta	W
Be	1											
Mg	-0.05	1										
Ti	0.20	-0.05	1									
V	-0.15	0.27	0.37	1								
Fe	0.35	-0.01	0.74	0.36	1							
Zn	0.39	0.14	0.25	0.30	0.74	1						
Ga	0.23	0.09	0.35	0.59	0.49	0.56	1					
Nb	0.78	-0.07	0.72	0.25	0.93	0.04	0.27	1				
Sn	0.47	-0.09	0.82	0.47	0.93	0.27	0.42	0.98	1			
Hf	0.49	0.30	0.94	0.47	0.92	-0.44	0.51	0.95	0.98	1		
Ta	0.76	-0.22	0.09	-0.24	0.27	-0.11	-0.04	0.29	0.30	0.27	1	
W	0.75	-0.11	0.67	0.26	0.91	0.35	0.19	0.95	0.94	0.88	0.31	1

UN31

	Be	Mg	Ti	V	Fe	Zn	Ga	Nb	Sn	Hf	Ta	W
Be	1											
Mg	0.59	1										
Ti	0.02	0.47	1									
V	0.49	0.87	0.40	1								
Fe	0.31	0.58	0.52	0.56	1							
Zn	0.14	0.58	0.57	0.56	0.88	1						
Ga	0.60	0.82	0.39	0.72	0.75	0.70	1					
Nb	0.89	0.79	-0.01	0.59	0.26	0.21	0.61	1				
Sn	0.89	0.80	0.15	0.59	0.28	0.28	0.62	0.98	1			
Hf	0.87	0.76	0.04	0.45	0.42	0.34	0.70	0.92	0.95	1		
Ta	0.82	0.78	0.01	0.56	0.20	0.21	0.55	0.97	0.98	0.97	1	
W	0.88	0.76	-0.12	0.47	0.53	0.26	0.81	0.99	0.94	0.86	0.93	1

Acknowledgements

First and foremost, I would like to thank my advisor **Prof. Dr. Christian Ballhaus** who is one of the cleverest, if not the cleverest person I have ever met. He has been supporting me ever since I was an undergraduate student. Not only that he accepted a pregnant woman as a PhD student without hesitation, he also gave me any time that I needed at home as a young mother, never doubting that I would do my best at work when time was ready. His extraordinary ability to filter the most substantial information out of a large pool was of invaluable use that I would not have wanted to miss. As a supervisor he always gave me the freedom to do what I believed was right, but guided me towards the right direction when I lost myself somewhere in the big universe of science.

I am furthermore highly grateful to **Prof. Dr. Thorsten Geisler-Wierwille** to accept being my second supervisor on a quite short notice. Due to his profound expertise in Raman spectroscopy and fluid inclusion barometry, his suggestions and comments were of great help to extend the frame of this work and to improve its quality.

My very special thank is dedicated to **Dr. Frank 'FTom' Tomaschek**, the most thorough and modest person I know. He got involved into the project somewhere half the way and was immediately very helpful and enthusiastic and always gave me the feeling that helping me was rather a pleasure to him than work. Without his patient guidance through the world of U-Pb dating, today I would probably still sit at my desk, wondering how to figure out the age of my samples. I thank him a lot for all the discussions in which he taught me to think more critical without criticising me, but by asking the right questions. His comments on the first draft of this work helped me a lot to improve the work.

I thank **Dr. Raúl Fonseca** for his advice on the experimental part of this work and for his help at the LA-ICP-MS. I would also like to thank him for inspiring discussion and for his support and encouragement in times of doubt.

Thank you to **Prof. Dr. Thorsten Nagel** for having taught me how to use the Electron Microprobe.

Thank you **to Dr. Renate Schumacher** for providing the samples from the Mineralogical Museum of the University of Bonn.

I thank **Thomas Schulz** and **Dieter Lülsdorf** for their technical support and **Nils Jung** for sample preparation.

I thank **Dr. Axel Gerdes** from the University of Frankfurt for his assistance with the columbite U-Pb dating.

Dr. Michael Wirth from the University of Potsdam deserves my special thanks for that he conducted Transmission Electron Microscope analyses of one of the samples, on a very short note. These final analyses filled the last major gap in the work.

Thank you to **Christoph Lenting** for cross-reading and commenting one subchaper of this work.

Thank you to **Dagmar Hambach**, **Daniela Bungartz** and **Viktoria Kußerow**, the ‘women behind the scenes‘ for all the small things that you do every day to keep the every-day business running.

I would like to thank **Georg Oleschinsky** for the beautiful pictures of the sapphires.

Thank you **’HARI‘-Bo Elfers** and **Maria ’Kirchenabu‘** for your always refreshing and amusing company as office-mates. Also thank you **Peter Sprung** for finally joining into the fat people office!

My special thanks also to **Aurelia Zirner**, my fellow PhD student who was so kind to help me with the experiments when I had a broken foot from my "base jumping accident". I also thank her for her mental support and for always listening to my problems.

Special thanks to **Alessandro Bragagni** for his mental support in the finishing-period of this work. Thank you also for guiding me through all the byrocracy. And thank you for your companionship during the printing-marathon! I hope you will keep page 38 in awe.

I would also like to thank all the other fellow PhD students from the Steinmann Institute, and from the University of Cologne (Isotope Geochemistry work group) for being team players through and through. The group dynamics and solidarity within this group was and still is amazing. In the end, we are all sitting in the same boat…..

Finally, I would like to thank my family. **Simon**: I probably don´t need to tell you because you could always read my mind, anyway. Without you, I would have certainly not made it to where I am now. The unconditional support and endless patience you showed me day after day is incredible. Thank you for showing to the world that a woman is more than a housewife and mother. **Paul**: Thank you for being wisest, most tolerant and adorable three-year-old kid in the world. Even with your young age, you were able to support and comfort me. I will never forget the moment when I told you that I am so sorry that I have to work so much and don't have that much time for you, and you answered: "It's OK, mummy, I am happy, anyway". Thank you for calling me your "best friend ever".

CURRICULUM VITAE

Personal Details

Career

Education

Research interests

Petrology of magmatic rocks and of asteroidal bodies; Experimental Petrology; Genesis of noble-metal phases; U-Pb dating; Mineral reaction mechanisms; petrogenesis and differentiation processes of carbonatites

Publications

Baldwin L. C., Ballhaus C., Bischoff A., Fonseca R. O. C., Helmy H. M., Hecht L. (2015) The structure of the CK chondrites parent body: Evidence for a "rubble-pile" structure from base-metal and noble-metal sulfide paragenesis. *Submitted at Meteoritics and Planetary Science Letters.*

Conference Abstracts

08/2015 **Baldwin, L.C.**; Tomaschek, F.; Gerdes, A.; Fonseca, R.O.C.; Ballhaus, C. Implications for a Carbonated Peridotite Source for Intra-Continental Alkaline

Mafic Lavas from the Siebengebirge Volcanic Field (Germany). Goldschmidt Abstracts 2015, 183.

09/2014 **Baldwin, L.C**.; Ballhaus, C.; Fonseca, R.O.C.; Nagel, T.; Heuser, A. Petrogenesis and evolution of phenocrystic sapphire in alkaline basalts from the Siebengebirge Volcanic Field, SW Germany. 92. annual meeting of the german mineralogical society, 21. - 25.09.14, Jena.

06/2014 **Baldwin, L.C.**; Ballhaus, C.; Fonseca, R.O.C.. The origin of sapphire megacrysts from alkaline basalts in the Siebengebirge Volcanic Field, SW Germany. Annual meeting of the petrology/ geochemistry section of the german mineralogical society, 27. - 28.06.14, Hannover.

06/2013 **Baldwin, L.C.**; Ballhaus, C.; Fonseca, R.O.C.; Helmy, H.M.; Hecht, L. A critical reappraisal of thermal metamorphism of the CK chondrites. Annual meeting of the petrology section of the german mineralogical society, 7. - 8.06.14, Bonn.

Other qualifications

Since 04/2014 Foundation and organization of the Bonn – Cologne geoscience PhD student seminar

2007-2008 Member of the student council of the geological/petrological department.

Bonn, 11th of January, 2016

Lisa Baldwin